Science with the Einstein Telescope: a comparison of different designs

Journal of Cosmology and Astroparticle Physics
An IOP and SISSA journal

Science with the Einstein Telescope: a comparison of different designs

Marica Branchesi,[1,2,*] Michele Maggiore,[3,4,*] David Alonso,[5] Charles Badger,[6] Biswajit Banerjee,[1,2] Freija Beirnaert,[7] Enis Belgacem,[3,4] Swetha Bhagwat,[8,9] Guillaume Boileau,[10,11] Ssohrab Borhanian,[12] Daniel David Brown,[13] Man Leong Chan,[14] Giulia Cusin,[15,3,4] Stefan L. Danilishin,[16,17] Jerome Degallaix,[18] Valerio De Luca,[19] Arnab Dhani,[20] Tim Dietrich,[21,22] Ulyana Dupletsa,[1,2] Stefano Foffa,[3,4] Gabriele Franciolini,[8] Andreas Freise,[23,16] Gianluca Gemme,[24] Boris Goncharov,[1,2] Archisman Ghosh,[7] Francesca Gulminelli,[25] Ish Gupta,[20] Pawan Kumar Gupta,[16,26] Jan Harms,[1,2] Nandini Hazra,[1,2,27] Stefan Hild,[16,17] Tanja Hinderer,[28] Ik Siong Heng,[29] Francesco Iacovelli,[3,4] Justin Janquart,[16,26] Kamiel Janssens,[10,11] Alexander C. Jenkins,[30] Chinmay Kalaghatgi,[16,26,31] Xhesika Koroveshi,[32,33] Tjonnie G.F. Li,[34,35] Yufeng Li,[36] Eleonora Loffredo,[1,2] Elisa Maggio,[22] Michele Mancarella,[3,4,37,38] Michela Mapelli,[39,40,41] Katarina Martinovic,[6] Andrea Maselli,[1,2] Patrick Meyers,[42] Andrew L. Miller,[43,16,26] Chiranjib Mondal,[25] Niccolò Muttoni,[3,4] Harsh Narola,[16,26] Micaela Oertel,[44] Gor Oganesyan,[1,2] Costantino Pacilio,[8,37,38] Cristiano Palomba,[45] Paolo Pani,[8] Antonio Pasqualetti,[46] Albino Perego,[47,48] Carole Périgois,[39,40,41] Mauro Pieroni,[49,50] Ornella Juliana Piccinni,[51] Anna Puecher,[16,26] Paola Puppo,[45] Angelo Ricciardone,[52,39,40] Antonio Riotto,[3,4] Samuele Ronchini,[1,2] Mairi Sakellariadou,[6] Anuradha Samajdar,[21] Filippo Santoliquido,[39,40,41] B.S. Sathyaprakash,[20,53,54] Jessica Steinlechner,[16,17] Sebastian Steinlechner,[16,17] Andrei Utina,[16,17] Chris Van Den Broeck[16,26] and Teng Zhang[9,17]

[1]Gran Sasso Science Institute (GSSI), I-67100 L'Aquila, Italy
[2]INFN, Laboratori Nazionali del Gran Sasso, I-67100 Assergi, Italy

*Corresponding author.

https://doi.org/10.1088/1475-7516/2023/07/068

JCAP07(2023)068

[3]Département de Physique Théorique, Université de Genève,
24 quai Ansermet, CH-1211 Genève 4, Switzerland
[4]Gravitational Wave Science Center (GWSC), Université de Genève,
CH-1211 Geneva, Switzerland
[5]Department of Physics, University of Oxford, Denys Wilkinson Building,
Keble Road, Oxford OX1 3RH, United Kingdom
[6]Theoretical Particle Physics and Cosmology Group, Physics Department,
King's College London, University of London, Strand, London WC2R 2LS, United Kingdom
[7]Department of Physics and Astronomy, Ghent University, 9000 Ghent, Belgium
[8]Dipartimento di Fisica, "Sapienza" Università di Roma & Sezione INFN Roma1,
Piazzale Aldo Moro 5, 00185, Roma, Italy
[9]Institute for Gravitational Wave Astronomy & School of Physics and Astronomy,
University of Birmingham, Edgbaston, Birmingham B15 2TT, U.K.
[10]Universiteit Antwerpen, Prinsstraat 13, 2000 Antwerpen, Belgium
[11]Université Côte d'Azur, Observatoire de la Côte d'Azur, CNRS, ARTEMIS,
06304 Nice, France
[12]Theoretisch-Physikalisches Institut, Friedrich-Schiller-Universität Jena,
07743, Jena, Germany
[13]ARC Centre of Excellence for Gravitational Wave Discovery, School of Physical Sciences,
University of Adelaide, 5005 Adelaide, Australia
[14]Department of Physics and Astronomy, The University of British Columbia,
Vancouver, BC V6T 1Z4, Canada
[15]Sorbonne Université, CNRS, UMR 7095, Institut d'Astrophysique de Paris,
75014 Paris, France
[16]Nikhef — National Institute for Subatomic Physics,
Science Park 105, 1098 XG Amsterdam, The Netherlands
[17]Department of Gravitational Waves and Fundamental Physics,
Maastricht University, 6200 MD Maastricht, The Netherlands
[18]Université Lyon, Université Claude Bernard Lyon 1, CNRS,
Laboratoire des Matériaux Avancés (LMA), IP2I Lyon/IN2P3,F-69622 Villeurbanne, France
[19]Center for Particle Cosmology, Department of Physics and Astronomy,
University of Pennsylvania 209 S. 33rd St., Philadelphia, PA 19104, U.S.A.
[20]Institute for Gravitation and the Cosmos, Department of Physics,
The Pennsylvania State University, University Park, PA 16802, U.S.A.
[21]Institut für Physik und Astronomie, Universität Potsdam,
Haus 28, Karl-Liebknecht-Str. 24/25, 14476, Potsdam, Germany
[22]Max Planck Institute for Gravitational Physics (Albert Einstein Institute),
D-14476 Potsdam, Germany
[23]Department of Physics and Astronomy, VU Amsterdam,
De Boelelaan 1081, 1081, HV, Amsterdam, The Netherlands
[24]INFN, Sezione di Genova, I-16146 Genova, Italy
[25]Normandie Univ, ENSICAEN, UNICAEN, CNRS/IN2P3, LPC Caen, 14000 Caen, France
[26]Institute for Gravitational and Subatomic Physics (GRASP), Utrecht University,
Princetonplein 1, 3584 CC Utrecht, The Netherlands
[27]INAF — Osservatorio Astronomico d'Abruzzo, Teramo, Italy

JCAP07(2023)068

[28]Institute for Theoretical Physics, Utrecht University,
Princetonplein 5, 3584 CC Utrecht, The Netherlands
[29]SUPA, School of Physics and Astronomy, University of Glasgow,
Glasgow G12 8QQ, United Kingdom
[30]Department of Physics and Astronomy, University College London,
London WC1E 6BT, United Kingdom
[31]Institute for High-Energy Physics, University of Amsterdam,
Science Park 904, 1098 XH Amsterdam, The Netherlands
[32]Institute of Technical Thermodynamics and Refrigeration: Refrigeration and Cryogenics,
Karlsruhe Institute of Technology (KIT), 76131 Karlsruhe, Germany
[33]Institute of Beam Physics and Technology, Karlsruhe Institute of Technology (KIT),
76344 Eggenstein-Leopoldshafen, Germany
[34]Institute for Theoretical Physics, Department of Physics and Astronomy, KU Leuven,
Celestijnenlaan 200D, B-3001 Leuven, Belgium
[35]STADIUS, Department of Electrical Engineering (ESAT), KU Leuven,
Kasteelpark Arenberg 10, B-3001 Leuven, Belgium
[36]Department of Astronomy, Beijing Normal University, Beijing 100875, China
[37]Dipartimento di Fisica "G. Occhialini", Università degli Studi di Milano-Bicocca,
Piazza della Scienza 3, 20126 Milano, Italy
[38]INFN, Sezione di Milano-Bicocca, Piazza della Scienza 3, 20126 Milano, Italy
[39]Physics and Astronomy Department Galileo Galilei, University of Padova,
Vicolo dell'Osservatorio 3, I-35122, Padova, Italy
[40]INFN — Padova, Via Marzolo 8, I-35131 Padova, Italy
[41]INAF — Osservatorio Astronomico di Padova,
Vicolo dell'Osservatorio 5, I-35122 Padova, Italy
[42]Theoretical Astrophysics Group, California Institute of Technology,
Pasadena, CA 91125, U.S.A.
[43]Université catholique de Louvain, B-1348 Louvain-la-Neuve, Belgium
[44]Laboratoire Univers et Théories, CNRS, Observatoire de Paris, Université PSL,
Université Paris Cité, 5 place Jules Janssen, 92195 Meudon, France
[45]INFN, Sezione di Roma, I-00185 Roma, Italy
[46]European Gravitational Observatory (EGO), I-56021 Cascina, Pisa, Italy
[47]Dipartimento di Fisica, Università di Trento, Via Sommarive 14, 38123 Trento, Italy
[48]INFN-TIFPA, Trento Institute for Fundamental Physics and Applications,
Via Sommarive 14, I-38123 Trento, Italy
[49]Theoretical Physics Department, CERN, 1211 Geneva 23, Switzerland
[50]Blackett Laboratory, Imperial College London,
South Kensington Campus, London, SW7 2AZ, U.K.
[51]Institut de Fisica d'Altes Energies (IFAE), The Barcelona Institute of Science
and Technology, Campus UAB, 08193 Bellaterra (Barcelona) Spain
[52]Dipartimento di Fisica "E. Fermi", Università di Pisa, I-56127 Pisa, Italy
[53]Department of Astronomy and Astrophysics, The Pennsylvania State University,
University Park, PA 16802, U.S.A.
[54]School of Physics and Astronomy, Cardiff University, Cardiff, CF24 3AA, U.K.

JCAP07(2023)068

E-mail: marica.branchesi@gssi.it, michele.maggiore@unige.ch

Received April 14, 2023
Revised June 15, 2023
Accepted June 17, 2023
Published July 28, 2023

Abstract. The Einstein Telescope (ET), the European project for a third-generation gravitational-wave detector, has a reference configuration based on a triangular shape consisting of three nested detectors with 10 km arms, where each detector has a 'xylophone' configuration made of an interferometer tuned toward high frequencies, and an interferometer tuned toward low frequencies and working at cryogenic temperature. Here, we examine the scientific perspectives under possible variations of this reference design. We perform a detailed evaluation of the science case for a single triangular geometry observatory, and we compare it with the results obtained for a network of two L-shaped detectors (either parallel or misaligned) located in Europe, considering different choices of arm-length for both the triangle and the 2L geometries. We also study how the science output changes in the absence of the low-frequency instrument, both for the triangle and the 2L configurations. We examine a broad class of simple 'metrics' that quantify the science output, related to compact binary coalescences, multi-messenger astronomy and stochastic backgrounds, and we then examine the impact of different detector designs on a more specific set of scientific objectives.

Keywords: gravitational wave detectors, gravitational waves / experiments, gravitational waves / sources

ArXiv ePrint: 2303.15923

JCAP07(2023)068

Contents

JCAP07(2023)068

1 Introduction

Thanks to the extraordinary discoveries of the LIGO-Virgo Collaboration (LVC) in the last few years [1–7], the field of gravitational waves (GWs) is blossoming. After three observing runs the current catalog of GW detections contains about 90 binary black hole (BBH) coalescences, which in the last run have been detected on a weekly basis, as well as two binary neutron stars (BNSs) and two neutron star-black hole (NSBH) binaries [5, 6]. These discoveries are already having a significant impact on our understanding of the population properties (see, e.g. ref. [7]) and provide first results on fundamental physics and cosmology (see, e.g. ref. [8, 9]). The tremendous potential of combining multi-messenger observations including gravitational waves has been shown by GW170817, the first gravitational-wave observation from the merger of a binary neutron-star system which was detected in all the electromagnetic bands

JCAP07(2023)068

from gamma rays (GRB 170817A), X-ray, ultraviolet-optical-near infrared (AT2017gfo), to radio [4]. This event had important implications in many fields of astrophysics, from relativistic astrophysics, nuclear physics, nucleosynthesis in the Universe, and cosmology.

However, the current infrastructures have intrinsic limitations, and for more than a decade the European community has been preparing the jump toward a 'third-generation' (3G) European GW detector. The Einstein Telescope (ET) [10–12] is the European observatory designed to detect gravitational-wave sources along the cosmic history up to the early Universe. The U.S. community is participating in the efforts toward 3G detectors, with the Cosmic Explorer (CE) project [13, 14]. Third-generation detectors such as ET and CE will provide an improvement in sensitivity by one order of magnitude and a significant enlargement of the bandwidth, both toward low and high frequencies, and will have extraordinary potential for discoveries in astrophysics, cosmology, and fundamental physics. Building on many previous works, the science case for ET has been summarized in [15, 16], while a recent comprehensive study of the ET capabilities can be found in [17] and, for multi-messenger observations, in [18]. For CE and for a more general discussion of 3G detectors see also [19, 20].

The current design of ET is based on several innovative concepts, with respect to the (second-generation) LIGO-Virgo detectors. In particular, ET is currently planned to be a single observatory, located 200-300 meters underground, in order to significantly reduce seismic noise; to have a triangular shape, consisting of three nested detectors, providing redundancy, the possibility of resolving the GW polarizations, and a null stream, i.e. a combination of outputs where the GW signal cancels, that can act as a veto against disturbances; and it will feature a 'xylophone' configuration, in which each of the three detectors actually consists of two interferometers, one tuned toward high frequencies, and therefore using high laser power, and one tuned toward low-frequency, working at cryogenic temperatures and low laser power. The first ET Conceptual Design Report dates back to 2011, and laid down the basic structure mentioned above. It has been updated in 2020, in the context of the successful proposal for including ET in the ESFRI Roadmap, the roadmap of large scientific European infrastructures.[1] However, a detailed comparison of different alternatives in the design and on their impact on the science output has never been performed. The concept of ET was proposed well before the first observations of GWs. Unlike then, all the knowledge about GW sources that has accumulated in recent years makes such a study with astrophysically motivated GW source populations possible, and mandatory, today.

The aim of this work is twofold. First, we want to examine the effect of variations in the geometry, comparing a single triangle to a configuration made of two well-separated L-shaped detectors, which we will refer to as the '2L' configuration, while maintaining all other innovative concepts of the ET design (underground, cryogenic, and in a xylophone configuration). Second, we want to study what the impact on the science output would be if some aspects of the design should turn out to be difficult to achieve, at least in the first stage of operations (both for a triangle and for a 2L configuration). In particular, we will study the situation in which the low-frequency (LF) instrument is not operative, and we only have the high-frequency (HF) instrument in each detector. This will allow us to quantify the impact of the LF instrument on the expected science output.

This study has been performed in the context of the activities of the Observational Science Board (OSB) of ET, which is in charge of developing the Science Cases and the

[1] See http://www.et-gw.eu/index.php/relevant-et-documents for a collection of documents on the ET design study and science case.

JCAP07(2023)068

analysis tools relevant for ET.[2] The study is structured as follows. In section 2 we will introduce and motivate the different detector geometries considered and we will give the corresponding strain sensitivities. We will then discuss the impact of different choices of geometry and design on the science that can be made with ET. The coalescence of compact binaries, such as binary black holes (BBHs) and binary neutron stars (BNSs), is a primary target of 3G detectors. The crucial properties here are the detection rates, the range and distribution in redshift of the detected events, and the accuracy in the reconstruction of the source parameters. Properties such as detection rate, range and accuracy in parameter estimation have the advantage of being very general and requiring minimal model-dependent assumptions (which are reported in the paper). Therefore, they already provide a first solid understanding of the relative advantages/disadvantages of different configurations. In section 3 we will then compare, from this point of view, the performance of the different ET configurations introduced in section 2. We will first consider ET observing as single detector (whether in its triangle or 2L configuration), discussing BBHs in section 3.1 and BNSs in section 3.2, and we will then perform in section 3.3 the same study when ET is part of a 3G detector network including one or two Cosmic Explorer detectors. The effect of the different choices of ET as single observatory on multi-messenger observations of BNSs is studied in section 4. In particular, section 4.1 discusses the sky-localization and pre-merger alerts, while sections 4.2 and 4.3 evaluate, respectively, the prospects of detecting short γ-ray bursts (GRB) and kilonovae associated with BNS mergers.

Stochastic backgrounds of GWs are another primary target of ET. The effect of different configurations on stochastic searches is studied in section 5. In particular, in section 5.1 we discuss the sensitivity to stochastic backgrounds (as expressed by the power-law integrated sensitivity, PLS) of the different configurations, while the angular resolution obtained from a multipole decomposition is discussed in section 5.2. A comparison of the different sensitivities with predictions for astrophysical backgrounds is performed in section 5.3, while the impact of correlated noise is discussed in section 5.4.

Beside the study of these rather general metrics, it is also important to investigate how these differences in detection rates, parameter estimation, or sensitivity to stochastic backgrounds, reflect on specific scientific targets of ET around which the ET Science Case is structured [15], even if this, unavoidably, may introduce some extra model-dependent assumptions. In section 6 we will then discuss the impact of the different configurations on a broad set of specific scientific targets of ET in the domains of astrophysics, fundamental physics and cosmology. Finally, in section. 7 we will discuss the properties of the null stream for the triangular configuration and its potential benefits. A summary of the main results of this study is presented in section 8 and, in particular, our conclusions are discussed in section 8.3. More technical material is collected in four appendices; in particular, several tables with useful figures of merits for BBHs and BNSs are collected in appendix C. We also provide, at the end of the paper, a list of acronyms used in the text.

2 Detector geometries and sensitivity curves

The ET initial design included high laser power at the interferometer input, leading to high optical power in the cavity of the order of several MW, optimisation of signal recycling, frequency-dependent light squeezing, increase of the beam size, and heavier mirrors compared

[2] See https://www.et-gw.eu/index.php/observational-science-board for a public repository of papers produced within the ET Observational Science Board.

JCAP07(2023)068

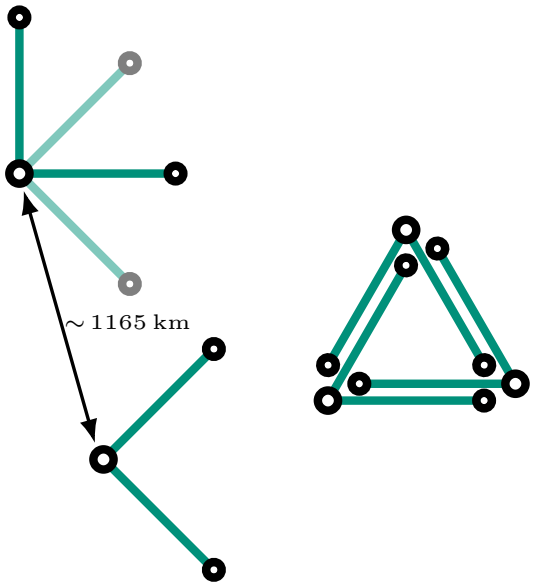

Figure 1. A schematic picture of the different geometries considered: two widely separated L-shaped detectors (either parallel or at 45°), or a triangle made of three nested detectors.

to 2G detectors. These specifications led to the so-called ET-B sensitivity curve [10]. This design, however, neglected the fact that high circulating power is difficult to reconcile with cryogenic test masses. This has led to a 'xylophone' concept, in which a detector is actually composed of two different interferometers, one optimized for low frequencies (LF) and one for high frequencies (HF); the LF instrument has low power (since laser power is only needed to beat down the shot noise in the high-frequency range) and cryogenic mirrors, while the HF instrument has high power and mirrors at room temperature. This has led to the ET-C sensitivity curve and, after further refinement of some noise models, to the ET-D sensitivity curve [12]. The ET-B and ET-C sensitivities must be considered as obsolete, and should not be used. The ET-D sensitivity has been the basis for all recent ET studies. Actually, we will use a further refinement of the ET-D sensitivity curve, recently developed in the context of the ET Instrument Science Board (ISB), see below.

As far as the geometry is concerned, we will study triangular configurations, in which three detectors (each one made of a LF and a HF interferometer) are nested into a triangular shape, as well as a network of two well-separated L-shaped detectors (that we will denote as the '2L' configuration), and will we examine different options for the arm length and, for the 2L configuration, different relative orientations between their arms. A schematic picture of the different geometries considered is shown in figure 1. For a single triangular configuration, currently the candidate sites are the Sos Enattos site in Sardinia, and the Meuse-Rhine three-border region across Belgium, Germany and the Netherlands. When considering a single triangle, we will locate it for definiteness in Sardinia, but there will be no significant difference in the results considering ET in the Meuse-Rhine region. When considering the 2L configuration, we will locate one detector in Sardinia and one in the Meuse-Rhine region. However, at the current level of precision, the analysis will be valid, with minor changes, for any pair of interferometers located at a comparable distance.

For two L-shaped detectors, in the coplanar limit the setting with parallel arms maximizes the sensitivity to stochastic backgrounds and the range to compact binaries, while it

JCAP07(2023)068

is the least favorable in terms of the accuracy on angular localization and reconstruction of the distance of compact binary coalescences (or other individual sources). Conversely, the setting with arms at 45° is basically blind to stochastic backgrounds, while it maximizes the performances in terms of angular localization and distance of compact binaries, see section 5.1. When taking into account the Earth's curvature, the relative orientation between the two detectors is usually defined with reference to the great circle that connects the two detectors [21, 22]. Denoting by β the angle describing the relative orientation of the two detectors, defined with reference to this great circle, $\beta = 0°$ corresponds to the case where the arms of the two interferometers make the same angle with respect to the great circle, while $\beta = 45°$ is when one of the two interferometers is rotated by 45° from the $\beta = 0°$ orientation. For $\beta = 45°$, the sensitivity to stochastic backgrounds is minimized, to the extent that it becomes exactly zero in the limit $f\Delta x \to 0$, where f is the GW frequency and Δx the distance between the two detectors. In this work, we aim at studying the performance of the 2L configurations close to these limiting cases; however, setting exactly $\beta = 45°$ is not a convenient choice because it would send practically to zero the sensitivity to stochastic backgrounds; instead, as we will see, even a small deviation from $\beta = 45°$ allows us to reach an interesting sensitivity to stochastic backgrounds, without essentially affecting the performances for angular localization and parameter estimation of compact binary coalescences.

We decide to focus on two examples for the relative orientation of the interferometers arms in the 2L configurations, representatives of choices favoring, respectively, either the angular localization and distance determination of compact binaries, or the detection of stochastic backgrounds, but avoiding the limit in which the sensitivity to compact binaries is optimized at the expenses of sending to zero the sensitivity to stochastic backgrounds. We thus consider a simpler definition of the angles that uses the local North at the two detector sites as reference for the orientations. Denoting by α the relative angle defined in this way, and by β the relative angle defined with reference to the great circle connecting the detectors in Sardinia and in the Netherlands, we have $\alpha \simeq \beta + 2.51°$.[3] We will study the cases $\alpha = 0°$ and $\alpha = 45°$, that corresponds to introducing a small offset with respect to the 'perfectly' parallel ($\beta = 0°$) and maximally misaligned ($\beta = 45°$) configurations. The results for compact binary coalescence (CBC) parameter estimation depends minimally on the precise value of this offset, as long as this misalignment angle is small. We have indeed checked that the results shown in section 3 are unaffected, for all practical purposes, by this small offset; e.g. the differences between the cases $\alpha = 45°$ and the truly optimal orientation $\alpha = 47.51°$ would be invisible on the scale of the plots shown in section 3, and are below the variability due to the specific sample realization of the population. In contrast, the sensitivity to stochastic backgrounds strongly depends on it, as we will discuss in appendix B. In the following, we will refer to these choices as parallel (by which we mean $\alpha = 0°$) and misaligned ($\alpha = 45°$).[4]

In particular, we will consider (with the definition of parallel and at 45° specified above, i.e. with respect to the local Norths at the two detector sites):

1. a triangle with 10 km arms (the current baseline ET geometry)

2. a triangle with 15 km arms

[3] For the Sardinia site we take (latitude 40° 31', longitude 9° 25'), while for the Meuse-Rhine site we take (latitude 50° 43' 23", longitude 5° 55' 14").

[4] If a 2L option should be retained, it will be important to perform a more detailed study of the trade-offs between accuracy in the localization of compact binaries and sensitivity to stochastic backgrounds, as a function of the misalignment angle; such a study, however, cannot be performed abstractly but, especially when discussing misalignment at the $(1-2)°$ level, will have to integrate constraints from the geography and the geology of the candidate sites. For instance, underground tunnels have to follow optimized paths avoiding as much as possible fractures or water springs.

JCAP07(2023)068

3. a 2L with 15 km arms, with parallel arms
4. a 2L with 15 km arms, with a relative orientation of 45°
5. a 2L with 20 km arms, with parallel arms
6. a 2L with 20 km arms, with a relative orientation of 45°

We will also occasionally compare with the results that can be obtained with the most advanced network of 2G detectors (LIGO Hanford, LIGO Livingston, Virgo, KAGRA and LIGO India), in order to better appreciate the improvement due to 3G detectors. We use the publicly available best sensitivities that are planned to be achieved by LIGO, Virgo and KAGRA by the end of the O5 run [23]. We will denote this network LVKI O5. LIGO India is expected to join the 2G network late in this decade. Both the Virgo and LIGO collaborations are currently discussing plans for further upgrades of the detectors to be implemented after the O5 run by developing and testing key technologies critical for the 3G detectors [24]. We will also show some results for a single L-shaped detector of 20 km (denoted as '1L'), that we will locate for definiteness in the Meuse-Rhine region.

It is clear that the configurations considered have different financial costs, so some configurations might be obviously better than others. The aim of this work is to provide scientific input to a broader cost-benefit analysis.[5]

In figure 2 we show the different noise Amplitude Spectral Densities (ASDs) used in this work to characterise the various detector configurations considered. In particular, in the left panel we show, for various arm lengths, the noise curve attainable in the full design, in which there is a xylophone configuration with an instrument tuned toward high-frequencies (HF) and one tuned toward low frequencies (LF), and the LF instrument works at cryogenic temperatures. In the right panel we show the ASDs resulting from exploiting only the HF instruments. These curves have been computed in the context of the activities of the ET Instrument Science Board (ISB).[6] In particular, the line corresponding to the 10 km length in the panel labelled "HFLF cryogenic" updates the sensitivity curve known as ET-D, available at https://apps.et-gw.eu/tds/?content=3&r=14065, and shown as a reference as the black line in both panels of figure 2, and reflects more detailed data on the technology used in the ET-D design. It should be stressed that, in this phase where the design of ET is being more deeply analyzed, the sensitivity curves necessarily evolve, and will continue to evolve. The two curves shown, for the full sensitivity and for the HF instrument only, must be taken as representative curves, within other possibilities currently under study. Further intermediate sensitivities could also be studied (for instance, corresponding to a possible intermediate stage where the LF instrument is present, but operates at room temperature), and would give results in between those obtained with the HF-only and the HFLF-cryo sensitivities.

[5] An analysis of the costs of the different configurations is well beyond the scope of this study. We note, however, that in the comparison between geometries, the total linear arm length is not the only relevant parameter for estimating the relative costs. For instance, another significant parameter is the diameter of the tunnels. In an L-shaped configuration there will be only one detector per tunnel, compared to two in the triangle configuration with nested interferometers. As a result, in an L-shaped detector the diameter of the tunnels will be smaller, approximately 6.5 m, to be compared with 8 m for the triangle. Already just for what concerns the relative excavation costs, several other factors must be included for a realistic comparison, such as the fact that, in the triangle configuration, extra tunnel length is needed to displace the end towers of a detector with respect to the input towers of the other, as well as differences in the number and size of auxiliary caverns, and in the tunnels serving them. All these aspects can only be evaluated with a detailed dedicated study.

[6] These curves are available at https://apps.et-gw.eu/tds/ql/?c=16492, see in particular the Annex files. They obtained with the help of PyGWINC package [25].

JCAP07(2023)068

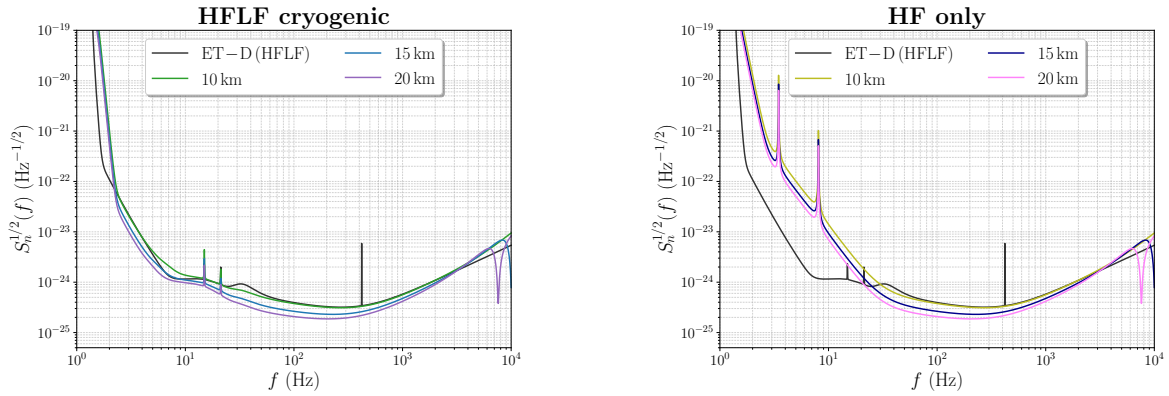

Figure 2. Amplitude spectral densities (ASDs, single-sided), used in the present work for different scenarios. In both panels we show the ASD for an interferometer with 10, 15 and 20 km arms. The left panel shows the full sensitivity curves (obtained from the HF instrument and the cryogenic LF instrument, in a xylophone configuration); the right panel is the sensitivity obtained with the HF instrument only. For comparison, in both panels we also show the ASD of the 10 km ET-D interferometer (which, by definition, includes the full HFLF sensitivity). Note that the ASD are plotted as a single nested detector (each one made of a LF and a HF interferometer left plot and each one made of HF only right plot). See the text on how to take into consideration the angle between the arms and the number of interferometers for the triangular shape.

When comparing a triangle to an L-shaped interferometer with the same instrument-noise ASD, one must take into account that the triangle is made of three nested detectors (a detector being an LF and HF interferometer pair), with an opening angle of 60°. For the triangle configuration, one must then project the GW tensor of the incoming wave onto each of these three components [see e.g. eqs. (9)–(11) of [26] for explicit expressions], and then combine the results at the level of the signal-to-noise ratio (SNR) and parameter estimation to obtain the ET capabilities. The accurate evaluations of detection horizons and parameter-estimation capabilities require the above calculation of GW-tensor projections onto the three ET components, as is done for all the results of the present paper, and in all Fisher matrix codes mentioned below. However, to have a simple and approximate rule-of-thumb for comparing the SNR of a triangle to that obtained, for the same signal, by an L-shaped detector with the same ASD, one must first of all take into account that, for each given component, the opening angle gives an extra factor $\sin(60^\circ) = \sqrt{3}/2$, see again eqs. (9)–(10) of [26]. In a first approximation, one can also assume that the three components of the triangle see the signal with the same SNR (which, however, is only approximately true). Then, since the SNR of the three components of the triangle add up in quadrature, the SNR^2 in a triangle is approximately larger than the SNR^2 in a L-shaped detector with the same ASD, by a factor $3\times(\sqrt{3}/2)^2 = 9/4$. For this reason, when comparing graphically the ASD of a triangle to that of an L-shaped detector, a more fair comparison is obtained dividing the ASD of the triangle by a factor 3/2. Since some source of noise, such as Newtonian noise, are such that the SNR scales as the length of the arms, in a first approximation one could further be tempted to estimate that, for a triangle, SNR $\propto L\sqrt{3}\sin(60^\circ) = 1.5L$, while for a 2L network with the same arm-length SNR $\propto L\sqrt{2}\sin(90^\circ) \simeq 1.41L$.[7] However, one must be careful not to infer

[7] In fact, not all noise relevant for 3G detectors are such that the SNR scales linearly with L. Examples of noise whose SNR do not scale with L include coating thermal noise (since it also depends on beam size, which increases with L), shot noise (since one needs to adjust the arm-cavity finesse depending on L), controls noise

JCAP07(2023)068

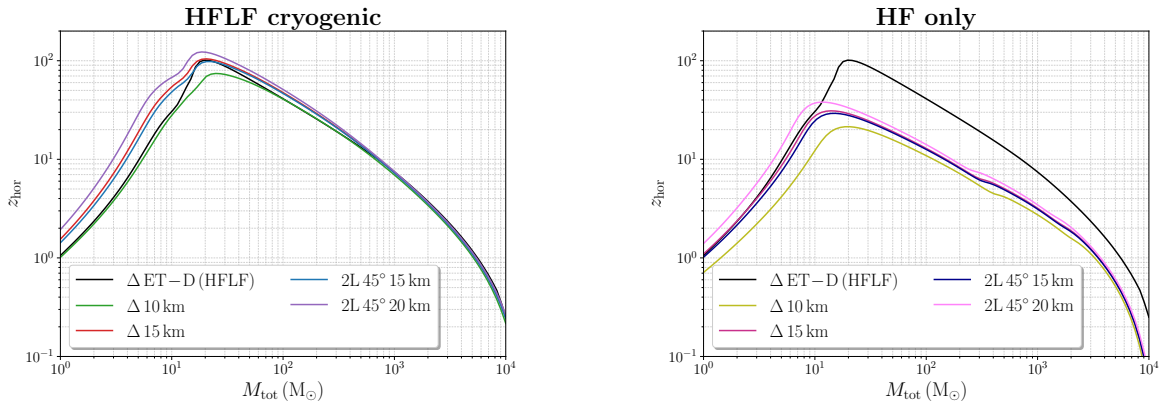

Figure 3. Detection horizons for monochromatic populations of equal-mass non-spinning binaries, for the various detector configurations considered. For comparison, we also show in each panel the curve obtained using a triangular detector with the 10 km ET-D ASD (which, by definition, includes the full HFLF sensitivity).

from this that a 2L and a triangle configurations with similar arm lengths necessarily perform comparably. The scientific performance is determined basically by the quality of parameter estimation, which does not depend just on the SNR. As an obvious counter-example, for an ensemble of compact binary coalescence signals, and fixed ASD, 2L parallel have a higher SNR than 2L at 45°; however, as far as parameter estimation is concerned, 2L at 45° perform significantly better (as we will see explicitly for ET in section 3), exactly the contrary of what would be inferred using an SNR-only argument. Similarly, for angular localization, the baseline between the detectors is another crucial factor. A comparison between the performances of different geometries can only be obtained with a parameter-estimation study, as we will perform below, and cannot be obtained from considerations based only on the SNR.

In figure 3 we show the corresponding detection horizons for equal-mass non-spinning binaries, as a function of their source frame total mass, for the various detector configurations considered. These are defined as the maximum redshift out to which a binary with the chosen characteristics, with optimal location and inclination, can be observed by a given detector configuration with a network SNR ≥ 8. This computation is performed using the IMRPhenomHM waveform model [28], and accounting for the effect of Earth rotation, which can give a contribution in the range of masses typical of BNS systems. For comparison, we also show the results obtained for a triangular-shaped detector using the 'older' ET-D ASD, which reproduces the result in figure 1 of [29].

In figure 4, left panel, we show the ratios of the redshift horizons for three different geometries (triangle 15 km, 2L-15km-45° and 2L-20km-45°), all in their HFLF-cryo configurations, with respect to the 10 km triangle, also taken in its HFLF-cryo configuration. In the right panel we show the same ratios for triangle 15 km, triangle 10 km, 2L-15km-45° and 2L-20km-45°, now all in their HF-only configuration, again with respect to the horizon of the 10 km HFLF-cryo triangle. We can appreciate that, especially for total masses below

(since L can change stability conditions of the opto-mechanical system, which requires adjustment of control filters) and suspension thermal noise (since one needs larger mirrors in longer detectors, which means higher suspended mass), see [27] for discussions. Therefore, the correct comparison is between detectors at fixed ASD, as discussed above, rather than at fixed L, and the scaling of SNR $\propto L$ is a further approximation, to be used only for a first orientation.

JCAP07(2023)068

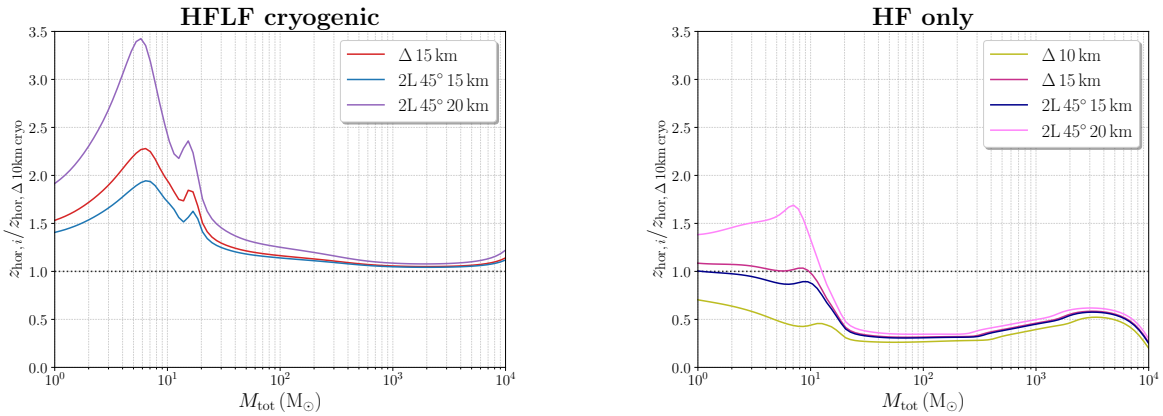

Figure 4. Ratios of the detector horizons for the different geometries. Left panel: full HFLF-cryo sensitivities, normalized to the horizon for the HFLF-cryo sensitivity of the 10 km triangle (i.e. to the green line in the left panel of figure 3). Right: HF sensitivities (still normalized to the full HFLF-cryo sensitivity of the 10 km triangle).

$\sim 10M_\odot$, arm-length has a very important effect on the detection horizon: for these masses, the 15 km triangle has a range that, in terms of redshift, is larger by a factor $1.5-2.2$ than that of the 10 km triangle, and the 2L-15km-45° is larger by a factor $1.4-1.8$; as we see from the right panel, in this range of masses this increase in arm-length would basically compensate the loss of the LF instrument (especially for the 15 km triangle). Once again, however, it is important to recall that the detection horizon is determined just by the SNR. More important, for the science case, is the quality of parameter estimation. For instance, the 2L-15km-45°, compared to the 2L-15km-0°, has a smaller horizon reach, but better capacity to determine the parameters of the sources, as we will quantify in the next section.

3 Coalescence of compact binaries

In this section we study the impact of the different detector geometries and different ASDs on the detection and parameter estimation of BBHs and BNSs. Several parameter estimation codes, tuned toward 3G detectors, have been developed recently, in particular `GWBENCH` [19, 30], `GWFISH` [31], `GWFAST` [17, 32], `TiDoFM` [33, 34] and the code used in [35]. In the context of the activities of the Observational Science Board (OSB) of ET, we have performed extended cross-checks between these codes, finding very good consistency. The results presented in this section have been obtained with `GWFAST` which, thanks to its vectorization properties, is quite convenient for dealing with the large number of runs required, while those presented in section 4 have been obtained with `GWFISH`, which is also tuned toward multi-band and multi-messenger observations [18, 31]. These codes are based on the Fisher matrix formalism. The Fisher matrix formalism has well-known limitations (see e.g. [36, 37] for extensive discussion) but is currently the only computationally practical way of dealing with parameter estimation for large populations. We refer to the original papers [17, 19, 30–32] for technical details on the application of the Fisher matrix formalism to parameter estimation for 3G detectors. It should also be observed that 3G detectors will observe a large number of events with very large SNR. As we will see for instance in figure 5 below, ET, in any of its configurations, will detect $\mathcal{O}(10^3-10^4)$ BBH/yr with SNR >100. These events will largely dominate the

JCAP07(2023)068

performance of a detector configuration for most aspects of the science case, and for large SNR the Fisher matrix approach becomes more and more reliable.

We use state-of-the-art waveforms and population models. For the waveforms, we use IMRPhenomXPHM for BBHs, which includes precessing spins and higher-order modes [38], and IMRPhenomD_NRTidalv2 [39, 40] for BNSs, which includes tidal effects. The parameters of the waveform are $\{\mathcal{M}_c, \eta, d_L, \theta, \phi, \iota, \psi, t_c, \Phi_c, \chi_{1,x}, \chi_{2,x}, \chi_{1,y}, \chi_{2,y}, \chi_{1,z}, \chi_{2,z}, \Lambda_1, \Lambda_2\}$, where $\mathcal{M}_c$ denotes the detector-frame chirp mass, η the symmetric mass ratio, d_L the luminosity distance to the source, θ and ϕ are the sky position coordinates (defined as $\theta = \pi/2 - \delta$ and $\phi = \alpha$, with α and δ right ascension and declination, respectively), ι the angle between the orbital angular momentum of the binary and the line of sight, ψ the polarisation angle, t_c the time of coalescence, Φ_c the phase at coalescence, $\chi_{i,c}$ the dimensionless spin of the object $i = \{1, 2\}$ along the axis $c = \{x, y, z\}$ of the coordinate system, chosen with the z axis pointing along the orbital angular momentum (we use the same conventions as in section IID of [41]), and Λ_i the dimensionless tidal deformability of the object i (which is present only for systems containing a NS). Instead of Λ_1, Λ_2, we will actually use the two combinations $\tilde{\Lambda}$ and $\delta\tilde{\Lambda}$ defined in [42], which have the advantage that $\tilde{\Lambda}$ is the combination that enters the inspiral waveform at 5 PN, while $\delta\tilde{\Lambda}$ first enters at 6 PN. In particular,

$$\tilde{\Lambda} = \frac{8}{13}\left[(1 + 7\eta - 31\eta^2)(\Lambda_1 + \Lambda_2) + \sqrt{1 - 4\eta}\,(1 + 9\eta - 11\eta^2)(\Lambda_1 - \Lambda_2)\right] . \tag{3.1}$$

For BBHs we will perform the inference on all parameters (except, of course, Λ_1, Λ_2, that vanish for BHs) and, as in LVK parameter estimations, rather than ι and $\chi_{i,c}$, we will use θ_{JN} (i.e. the angle between the *total* angular momentum and the line of sight; note that this is the same as ι only in the absence of precession), the spin magnitudes and angles, namely χ_1, χ_2, $\theta_{s,1}$, $\theta_{s,2}$, ϕ_{JL}, $\phi_{1,2}$.[8] For BNSs, instead, we include tidal deformability but, given the small expected values of their spin magnitudes, we only consider the aligned spin components in the analysis, thus performing estimation on $\chi_{1,z}$ and $\chi_{2,z}$. The labels '1' and '2' always refer, respectively, to the heaviest and lightest component of the binary system. After the inversion of the Fisher matrix, we compute the sky localisation area for the events at 90% c.l., $\Delta\Omega_{90\%}$. As in [17, 18], we assume an uncorrelated 85% duty cycle in each L-shaped detector, and in each of the three instruments composing the triangle. All technical details of the inference process for the results of this section are as described in [17].

We generated the catalogs of binary neutron stars (BNSs) with the population synthesis code MOBSE [43, 44]. MOBSE evolves isolated binary stars until they possibly become binary compact objects. For the models used here, we have evolved 1.8×10^8 binary systems with 12 different metallicities, ranging from $Z = 10^{-4}$ to 0.02. Primary masses are drawn from a Kroupa initial mass function [45] between 5 and 150 $M_\odot$, while mass ratios, initial orbital periods and eccentricities follow the distributions presented in [46]. MOBSE adopts up-to-date models for stellar winds [44]. We model electron-capture, and (pulsational) pair-instability supernovae according to [47] and [48], respectively. For core-collapse supernovae, we use the rapid model by [49], which enforces a mass gap between neutron stars and black holes. The main difference with respect to [49] is that we model neutron star masses according to an uniform distribution between $m_{\rm min} = 1.1$ $M_\odot$ and $m_{\rm max} = 2.5$ $M_\odot$, which is a better match to current LIGO-Virgo results [7]. We draw natal kicks from a Maxwellian distribution with one-dimensional root-mean-square $\sigma = 265$ km s^{-1}, rescaled by the mass of the compact

[8] This choice has the advantage of using quantities which are less degenerate among each other, leading to better conditioning of the Fisher matrices, thus improving the reliability of this approach.

JCAP07(2023)068

remnant and by the mass of the ejecta, see [50] for more details. During binary evolution we treat mass transfer, tidal evolution, gravitational-wave decay, and common envelope as described in [51]. For the common envelope, we assume an efficiency parameter $\alpha = 3$. We describe the evolution with redshift by accounting for the metallicity-dependent star formation rate across cosmic time, as described in [52]. The value for the local merger rate for this model turns out to be $R_0 \simeq 250\,\mathrm{Gpc}^{-3}\,\mathrm{yr}^{-1}$, which is consistent with the range $[10, 1700]\,\mathrm{Gpc}^{-3}\mathrm{yr}^{-1}$ obtained from the LVK results [7].

We generated the catalogs of binary black holes (BBHs) by mixing the isolated evolution channel (obtained as described above for BNSs) with the dynamical formation channel. We used the code FASTCLUSTER [53, 54], which evolves binary black holes in young, globular and nuclear star clusters, by accounting for their dynamical pair-up and for hierarchical mergers. In our catalogs, 55% of all BBHs come from isolated binary evolution, while 28, 15 and 2% come from dynamical formation in young, globular, and nuclear star clusters. We chose these mixing fractions because they ensure the best agreement with LIGO-Virgo black hole masses in the local Universe, see [54] for more details on the methodology. The BBH and BNS catalogs used for this study are publicly available at https://apps.et-gw.eu/tds/?content=3&r=18321.

3.1 Binary Black Holes

In this section we present the results obtained for BBHs. The data correspond to one year of data taking. With the assumed BBH population, the total number of BBHs coalescing in one year is about 1.2×10^5. We first study the effect of varying the geometry, for detectors all with their full HFLF-cryo sensitivity, and we then discuss the effect of varying the ASD.

3.1.1 Comparison between geometries

In the upper-left panel of figure 5 we show the cumulative distribution of the events with a network SNR larger than a given value, while in all other panels, involving parameter estimation, we restrict to events that pass a detection threshold SNR ≥ 12, and we show the corresponding cumulative distribution of events with an error smaller than a given value.[9]

[9]More precisely, when performing parameter estimation, we restrict to events that, besides passing the threshold on the SNR, also have a well-defined inversion of the Fisher matrix. In some cases, the Fisher matrix is ill-conditioned, so its inversion can lead to large errors and we then discard the corresponding event, see [17] for details. For BBHs, the fraction of ill-conditioned Fisher matrices is of order 1%, so has very little impact at this level, and is anyhow about the same percentage for different configurations, so this has essentially no impact on the comparison between configurations. For BNS, between 4% and 10% of the events are discarded, with the higher percentages appearing in the analyses using the ASD including only the HF instrument. There is also a slight dependence on the geometry especially in the HF-only case, with the 2L configurations resulting in worse conditioned matrices as compared to the triangular ones. However, the events discarded in these cases correspond preferentially to the situation when there is only one detector operating due to the duty cycle, in which case the Fisher matrix provides a poorer approximation. The ill-conditioned Fisher matrices often correspond at the population level to the events that would have anyhow large errors in parameter reconstruction (while the science output of the detectors depends mostly on the events with good reconstruction), but could also be related to events having a strong degeneracy between some parameters. In particular for BNS systems, where a higher percentage of events has ill-conditioned matrices as compared to BBH, the solution of discarding events, despite being conservative, might then leave a bias in the observed population, especially for specific science cases (as an example, events close to face-on/off are preferentially discarded due to the strong degeneracy present in this case between the inclination angle and the luminosity distance, but they are relevant e.g. for multi-messenger studies with GRBs). Another solution, adopted for the results presented in section 4, is to regularize the close-to-singular matrices according to the procedure described in [31]. This allows us to analyze the non-degenerate parameters of a larger number of the events,

JCAP07(2023)068

In each panel of this figure we show the results for the six geometries considered, all taken with their best ASD, i.e. in the xylophone configuration with the HF instrument and the cryogenic LF instrument (we use the label 'HFLF-cryo' for this ASD).

We see from the figure that even if, by itself, the performance of the 10 km triangle is extraordinary, the other geometries considered in general provide a further improvement (except for angular localization, where the 2L configurations with parallel arms have the worst performance). This is particularly evident in the reconstruction of the luminosity distance. In our population of 1.2×10^5 events (and in the specific sample drawn from it), the 10 km triangle can reach an accuracy on d_L equal or better than 1% for 28 events; this raises to 202 events for 2L with 15 km arms at 45°, and 365 events for 2L with 20 km arms at 45°, which is the configuration that provides the best results (a set of tables with the explicit number of events with SNR above given thresholds, or errors on various parameters below given values, is collected in appendix C). In general (not surprisingly), the 2L configuration with the longest arm length, 20 km, and relative arm orientation of 45°, is the one that performs better for all the parameters.

We can also appreciate from figure 5 that the configurations of 2L with parallel arms performs quite poorly (comparatively) for angular localization. While this was generally expected because of the parallel arms, it is quite interesting to see that, in terms of angular resolution, even the 2L with 20 km parallel arms performs somewhat less well than a single 10 km triangle, despite the longer arm length and the possibility of performing triangulation (even if only partial, since just two detectors are involved). Again, the best results are obtained with the 2L at 45°. For example, with our choices for the population and in our sample, the 10 km triangle can detect 35 BBH/yr with angular resolution below $1\,\mathrm{deg}^2$, to be compared with 92 BBH/yr for the 15 km 2L at 45° and 155 BBH/yr for the 20 km 2L at 45° (see table 40 in appendix C for a more extended set of examples). For the chirp mass reconstruction, the arm length sets the hierarchy among these configurations (see also table 41 in appendix C) so, again, among the configurations considered, the 10 km triangle is the least accurate. The results for the reconstruction of the symmetric mass ratio and of the spins show, instead, less pronounced differences among these configurations (note, however, the logarithmic scale, that visually flattens the differences; see again table 41 in appendix C for numerical values).

From figure 5 and tables 40, 41 we also see that the 15 km triangle has performances very similar to the 15 km 2L at 45°, except for the accuracy on the luminosity distance, where the 15 km 2L at 45° is clearly superior; for instance, the 15 km 2L at 45° would detect 202 BBH/yr with error on the luminosity distance better than 1%, to be compared with 77 for the 15 km triangle. In appendix D we examine the correlations between the various parameters for typical well-measured events and we find that, for the triangle, the error on d_L is more sensitive to the error on the localization, polarization angle and orbit inclination, so that errors on these parameters have a larger effect on the marginalized error on d_L, compared to the 2L configuration. We also note that this large improvement is specific to the 2L configurations with arms at 45°. For instance, we see from table 40 that the number of events/yr with d_L measured to better than 1% is 28 for the 10-km triangle, raising to 77 for the 15 km triangle; for the 15 km 2L with arms at 0° this number is 79, and jumps to 202 for the 15 km 2L at 45°. Therefore, the raise from 28 to 77 (or 79) events/yr can be traced to the increase in arm length, from

at the price of introducing a dependence on the adopted regularisation threshold. For a recent discussion and comparison of these intrinsic limitations of the Fisher approach related to the inversion procedure see e.g. appendices B and C of [17]. Each method has its own benefits, and it is reassuring that both have been used in the present analysis producing consistent results.

JCAP07(2023)068

10 km to 15 km; the fact that the 15 km triangle and the 15 km 2L with parallel arms have a very similar performance (on this metric) means that, for a given arm length, the three nested detectors of the triangle configuration approximately compensate the large baseline of the 2L configuration with parallel arms; the further increase to order 200 events/yr is due to the better capability of the 2L configuration at 45° to measure the source location, polarization and inclination angles, and therefore disentangle them from the luminosity distance.

We can also appreciate the overall similar performance of the different geometries in the reconstruction of the intrinsic parameters (masses and spins). This is due to the fact that their reconstruction is mostly influenced by the loudness of the signal in the detector, rather than by the localization capability, and is therefore largely determined by the SNR. As we see from the SNR panel in figure 5, all configurations have similar distributions of the SNR, except for the 10 km triangle, which is disfavored, and this is reflected in the estimation of masses and spins.

Finally, it is interesting to show the joint distribution of the events with respect to $\Delta d_L/d_L$ and $\Delta\Omega_{90\%}$, since this determines the overall localization volume. To avoid a proliferation of plots, here we limit ourselves to a comparison between the 10 km triangle and 15 km 2L at 45°, which is shown in the left panel of figure 6, and between the 15 km triangle and 15 km 2L at 45°, shown in the right panel. We see that the 15 km 2L at 45° has many more events than the triangle in the region of the $(\Delta d_L/d_L, \Delta\Omega_{90\%})$ plane corresponding to an interesting three-dimensional localization, e.g., $\Delta d_L/d_L \leq 1\%$ and *as far as these metrics are concerned, one can conclude that, while the performance of the 10 km triangle is by itself remarkable, the* 2L *configuration with 15 km arms, oriented at* 45°*, provides a further improvement (as the* 2L *configuration with 20 km arms or the 15 km triangle). In contrast, the* 2L *with parallel arms looks quite disfavoured, because of a comparatively poor angular localization capability. The 15 km 2L at* 45° *and the 15 km triangle provide results quite comparable, except for the accuracy on luminosity distance, for which the 15 km 2L at* 45° *is clearly superior.*

Finally, in figure 7 we study the performance of a single L-shaped detector with 20 km arms in the full HFLF cryo configuration, and we compare it with the 10 km triangle and with the 15 km 2L at 45°, also at their full sensitivity, as well as with LVKI O5. The most apparent feature is that, *in terms of angular resolution and reconstruction of luminosity distance, a single* L *is clearly performing very poorly, and is even way below the LVKI O5 forecast. This shows that a single* L*-shaped detector, not inserted in a global network, is basically useless for those aspects of the Science Case, such as multi-messenger astronomy or cosmology, that require good estimates of sky-localization and distance of the sources. For the other parameters, however, a single* L *of 20 km, although it provides worse estimates, can be comparable to the 3G networks that we have considered.*[10]

3.1.2 Effects of a change in the ASD

We next investigate how these results are affected by changes in ASD. In figure 8 we show, for the 10 km triangle, the cumulative distributions of the SNR and of parameter estimation (where again, for the SNR we show the cumulative distribution of events with SNR *larger* than a given value, while for parameter estimation we restrict to events with SNR ≥ 12 and we show the cumulative distribution of events with error *smaller* than a given value) for the full ASD including the HF instrument and a cryogenic LF instruments (denoted

[10]This, of course, assumes that spurious transient noise and glitches could be vetoed and eliminated reliably since, for a single detector, it would not be possible to reduce them by using the coincidence between independent detectors, or (as for the triangle) the null stream. In particular, the detection of unmodeled burst signals could not be reliably claimed with a single detector.

JCAP07(2023)068

'HFLF cryo'), and for the ASD in which the LF instrument is completely missing and only the HF instrument is operative (denoted 'HF only'). We also show, for comparison, our forecasts for LVKI O5. In order to be consistent with the ET results, the analysis for LVKI O5 is obtained following exactly the same Fisher-Matrix analysis used for ET. For a more precise and realistic forecast, we refer to [23] which uses a Bayesian framework close to real analysis applied to the current gravitational-wave observations.

An important message that emerges from figure 8 is that even if, at least in the first stage of operations, the LF instrument were not operational, still ET in its 10 km triangle configuration and HF-only sensitivity would provide a significant jump from 2G detectors, in terms of a number of detections, distribution of SNR and parameter reconstruction of BBHs, with the exception of angular localization (as expected, for a single infrastructure that cannot rely on triangulation). It is also worth noting that a single observatory, such as the 10-km ET triangle, at its best sensitivity, can localize a comparable number of sources with an accuracy as good as that of a network comprising five 2G detectors at full O5 sensitivity.

Note that, on a single event basis, the events observed by LVKI are almost always better localized than by ET, showing that localization benefits more from the network triangulation than from ET's higher SNR (with fluctuations due to the assumed duty cycle). Nonetheless, the number of detections by ET is more than 10 times higher, and comprises high SNR events with low masses and/or high mass ratios. The high-SNR low-mass BBH mergers can be optimally localized accessing low frequencies and using the imprint of Earth's rotation in the longer observed signal. The localization of high-SNR events with large mass ratio benefits from the detection of higher-order modes. This results in a similar number of optimally localized sources in the cumulative distribution up to a sky-localization of about 6 square degrees, see figure 8. The larger amount of BBHs localized with sky-localization uncertainty larger than this threshold by ET compared to LVKI network depends on the detection efficiency; ET has much higher detection efficiency, reaches higher z and has many more distant events where LVKI is no more able to detect sources. Going to larger and larger redshifts, on average the SNR decreases, and the ET localization worsen.

Figure 9 shows the corresponding results for the 2L configuration with 15 km arms at 45°, with the two different ASDs. For comparison, in this figure we also show both the results for the 10 km triangle in the full HFLF-cryo configuration, and the results for LVKI O5. It is interesting to observe that, even in the configuration in which the LF instrument is completely missing, for BBHs the 2L with 15 km arms at 45° is superior to the 10 km triangle with its full (HFLF cryo) sensitivity for the accuracy on the luminosity distance (particularly for the number of events with very good accuracy, say $\Delta d_L/d_L \leq 1\%$, with 56 events against 28, see table 40 in appendix C) and gives basically equivalent results for angular localization, spins and orbit inclination. In contrast, for the chirp mass and symmetric mass reconstruction, the full HFLF-cryo triangle is better than the HF-only 2L-15km-45°. In the comparison with LVKI O5 we see that, even in the HF-only configuration, the 2L with 15 km arms at 45° provides a remarkable jump from 2G detectors on BBH detection number, SNR distribution and parameter reconstruction, except that the angular localization of the best-localized events would no longer be better than that of the five-detector LVKI network at O5 sensitivities (although the number of events with $\Delta\Omega_{90\%} < 10^2\,\mathrm{deg}^2$, relevant for multi-messenger studies, is a factor ~ 5 higher for the 2L with 15 km arms at 45°, compared to LVKI O5). See again tables 40 and 41 in appendix C for a compilation of number events for the different geometries and ASDs, and different cuts on the parameters.

JCAP07(2023)068

A main message that emerges from figure 9 is that, as far as BBH parameter reconstruction is concerned, even if in a first stage of operations the whole LF instrument should not be operative, a 2L *configuration with 15 km arms at* 45° *would still be a very competitive 3G instrument, in fact quite comparable to a 10 km triangle at full sensitivity (with better performance of luminosity distance, less good performance on mass reconstruction, and equivalent performances on all other parameters and in SNR distribution).*[11]

Finally, another important target of 3G detectors are intermediate massive black holes (IMBHs) binaries, with masses in the range $10^2 - 10^4 M_\odot$, In this case, there are currently no observational constraints, and thus we do not use any astrophysically motivated IMBH population. Going back to figure 3, which showed the horizons for monochromatic non-spinning populations of equal-mass binaries (or figure 4, that directly gives the relative differences with respect to the baseline 10 km triangle), it can be deduced that, with the best sensitivity curve (HFLF-cryo configuration), for total masses above about $(300-400)M_\odot$, the difference between the different ET geometries is at about 10% level. For masses around $100M_\odot$ the difference is larger, and for instance for $100M_\odot$ the detection horizon ranges between $z \simeq 42$ and $z \simeq 50$ for the different geometries; however, in this redshift range we do not even expect astrophysical IMBH. Much more significant is the dependence on ASD. The right panel of figure 3 show a significant reduction in the IMBH horizon for the HF-only configuration. *This shows the importance of the low-frequency sensitivity for IMBHs.*

3.1.3 Golden events

Another important metric to assess the performance of a detector, or of a detector network, is provided by the number and redshift distribution of 'golden events', i.e. events with especially good properties in terms of SNR (e.g. BBHs with SNR $\geq$ 100), or error on luminosity distance (e.g. BBHs with $\Delta d_L/d_L \leq 0.05$) or angular localization (e.g. BBHs localized to better than $10\,\mathrm{deg}^2$). Indeed, while for some aspects of the Science Case, such as population studies, the completeness of the sample is a key element, for other aspects, such as precision tests of General Relativity (GR) or cosmological studies, the result will be largely, if not uniquely, determined by these 'golden events' (see the discussion in section 5.4 of [17] and section VI of [19]). In figure 10 we show the redshift distribution of the BBHs detected with SNR $\geq$ 100, the distribution of events with $\Delta d_L/d_L \leq 5\%$, and the distribution of events with $\Delta\Omega_{90\%} \leq 10\ \mathrm{deg}^2$.[12] In the upper row we show the results for the six detector geometries that we are considering, all taken at full (HFLF cryo) sensitivity. The middle row focuses on the 10 km triangle and shows how the result changes with the ASD, while the lower row shows the same result for the 2L with 15km arms at 45° (comparing also with the reference

[11] It should also be observed that, in most studies where the accuracy on both volume localization and masses is relevant, as for instance in joint studies of population and cosmological parameters, the bottle-neck is in the accuracy on sky localization and luminosity distance, which are always much worse than the relative accuracy on the (detector-frame) masses. As we see e.g. from figure 9, the relative error on the (detector-frame) chirp mass and on the symmetric mass ratio is typically well below 10^{-4} and can be as low as 10^{-6} for the chirp mass and 10^{-8} for η, while, for d_L, it is difficult to go below the 1% accuracy. Therefore, having a better performance on d_L has a much stronger impact than having a better performance on the detector-frame masses, which in any case are very accurately measured. Note, furthermore, that at the large redshifts explored by 3G detectors, the accuracy of the reconstruction of the actual (source-frame) masses from the detector-frame masses will be determined by the accuracy of the reconstruction of the redshift.

[12] Of course, these distributions are correlated. For instance, events with large SNR typically have small errors on d_L. The correlation between luminosity distance and angular resolution is shown, for BBHs, in figure 6, and the analogous result for BNS will be shown in figure 12. See figures 12 and 17 of [17] and figures 5-9 of [18] for further scatter plots of the correlations among different parameters, for the ET triangle configuration.

JCAP07(2023)068

triangle configuration). In all plots, we show for comparison the redshift distribution of the BBH population that we have used and, for each detector configuration, the distribution of the events detected with SNR ≥ 8 (which, on this scale, is almost indistinguishable from the whole population, at least for $z \lesssim 2$).

From the left panel in the upper row, and table 39 in appendix C, we see that, in terms of detections of events with large SNR, the 10 km triangle by itself has remarkable performances, with (in our sample realization) 2298 BBH/yr detected with SNR ≥ 100, and a redshift distribution extending up to $z \sim 5$. However, this is further improved in the other configurations; in particular, in the 2L-15km configurations, the number of BBH/yr with SNR ≥ 100 is 4933 for the misaligned configuration (and 5143 for the aligned-arms configuration), more than twice as large, and extends up to $z \simeq 7$; this further raises to more than 8000 for the 2L-20km configurations. On the other hand, we already saw from figure 5 that, over the whole ensemble of detected events, the setting with parallel arms has comparatively poor performance for angular localization and accuracy on the luminosity distance; this remains true also when we restrict to golden events, as we see from the middle and the right panel in the first row of figure 10. In particular, the 2L configurations with parallel arms (whether with 15 or 20 km arm-length) are by far the less performing in terms of events with $\Delta\Omega \leq 10$ deg^2 (followed by the 10 km triangle) while, in terms of the events with errors smaller than 5% on d_L, the 10 km triangle is, comparatively, the less performing, followed by the 2L configurations with parallel arms, while the 2L configurations with arms at 45° give the best results.

These results indicate that, for BBH golden events, the 2L *configuration with arms at* 45°*, or the 15 km triangle, provide the best compromise between detecting many of them, and out to large redshift, and localizing them, further improving on the already remarkable performances of the 10 km triangle.*

The middle row of figure 10 shows how the results depend on the ASD, for the 10 km triangle. From these plots we infer that, *also for golden BBH events, a 10 km triangle would provide an extraordinary jump, compared to 2G detectors, even in the HF-only configuration.* Indeed, by comparison, at LVKI O5, even having assumed the best-planned sensitivities for all five detectors, with our BBH population and the specific sample that we have drawn from it, we find only 4 events with SNR ≥ 100, to be compared with about 3000 for the 10 km triangle with the full HFLF-cryo ASD, and almost 800 for the 10 km triangle with the HF-only ASD, see table 40 in appendix C.

The lower row of figure 10 shows the dependence on the ASD for the 2L geometry with 15 km arms at 45° (showing, for comparison, also the result for the 10 km triangle at full sensitivity). Once again, *a significant conclusion is that the* 2L *geometry with 15 km arms at* 45°*, even with the HF-only instrument, is comparable to the 10 km triangle at full sensitivity.*

JCAP07(2023)068

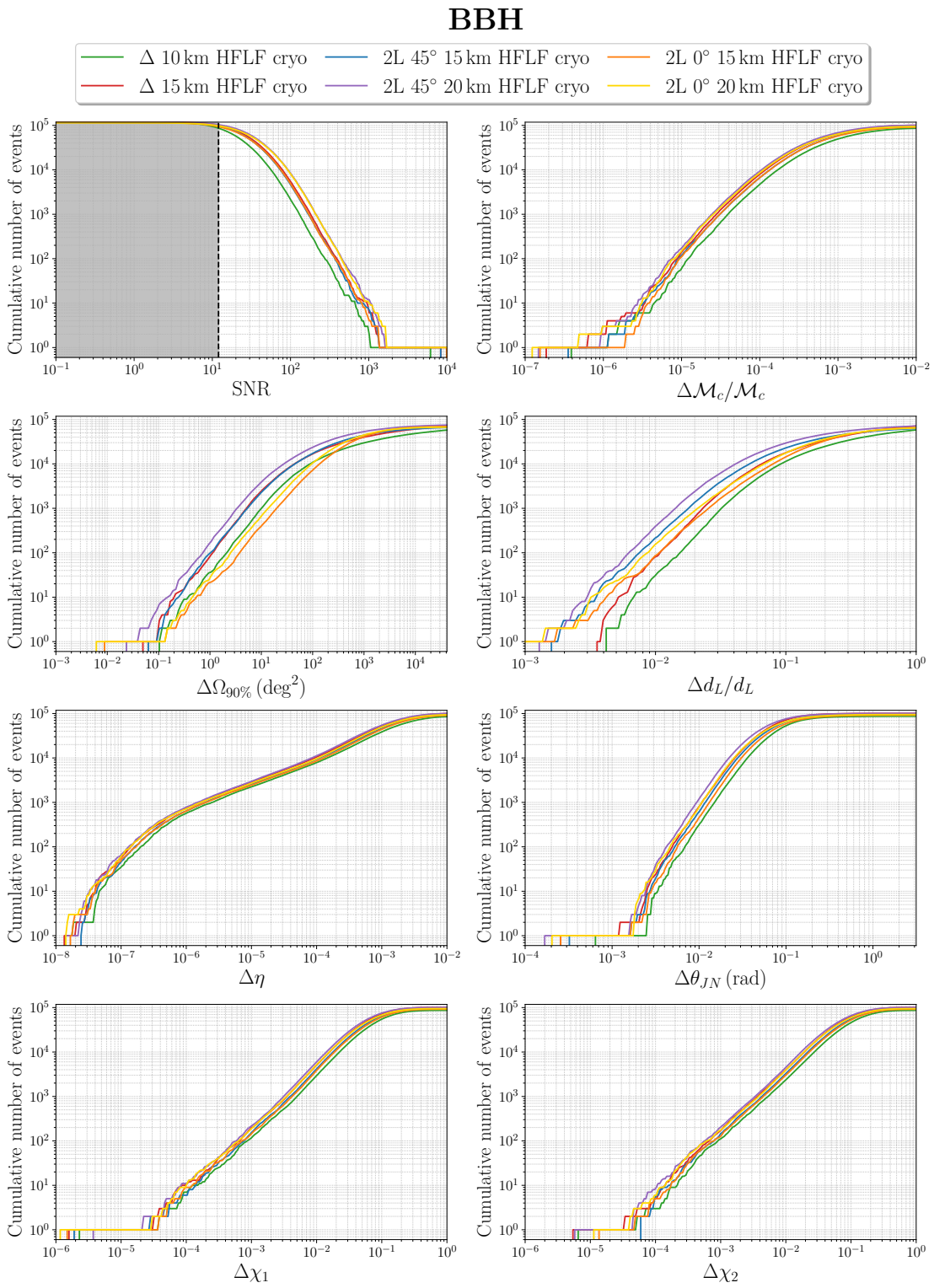

Figure 5. Cumulative distributions of the number of detections per year, for the SNRs and for the error on the parameters, for BBH signals, for the six considered geometries, all with their best ASD, including xylophone configuration and cryogenic LF instrument.

JCAP07(2023)068

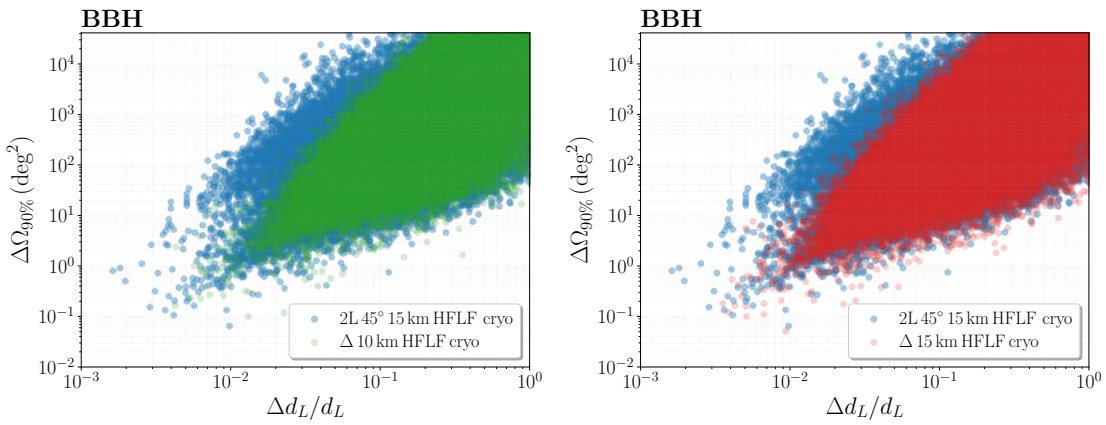

Figure 6. The joint accuracy on luminosity distance and angular resolution for BBHs. Left panel: the 15 km 2L at 45° (blue) compared to the 10 km triangle (green). Right panel: the 15 km 2L at 45° (blue) compared to the 15 km triangle (red).

JCAP07(2023)068

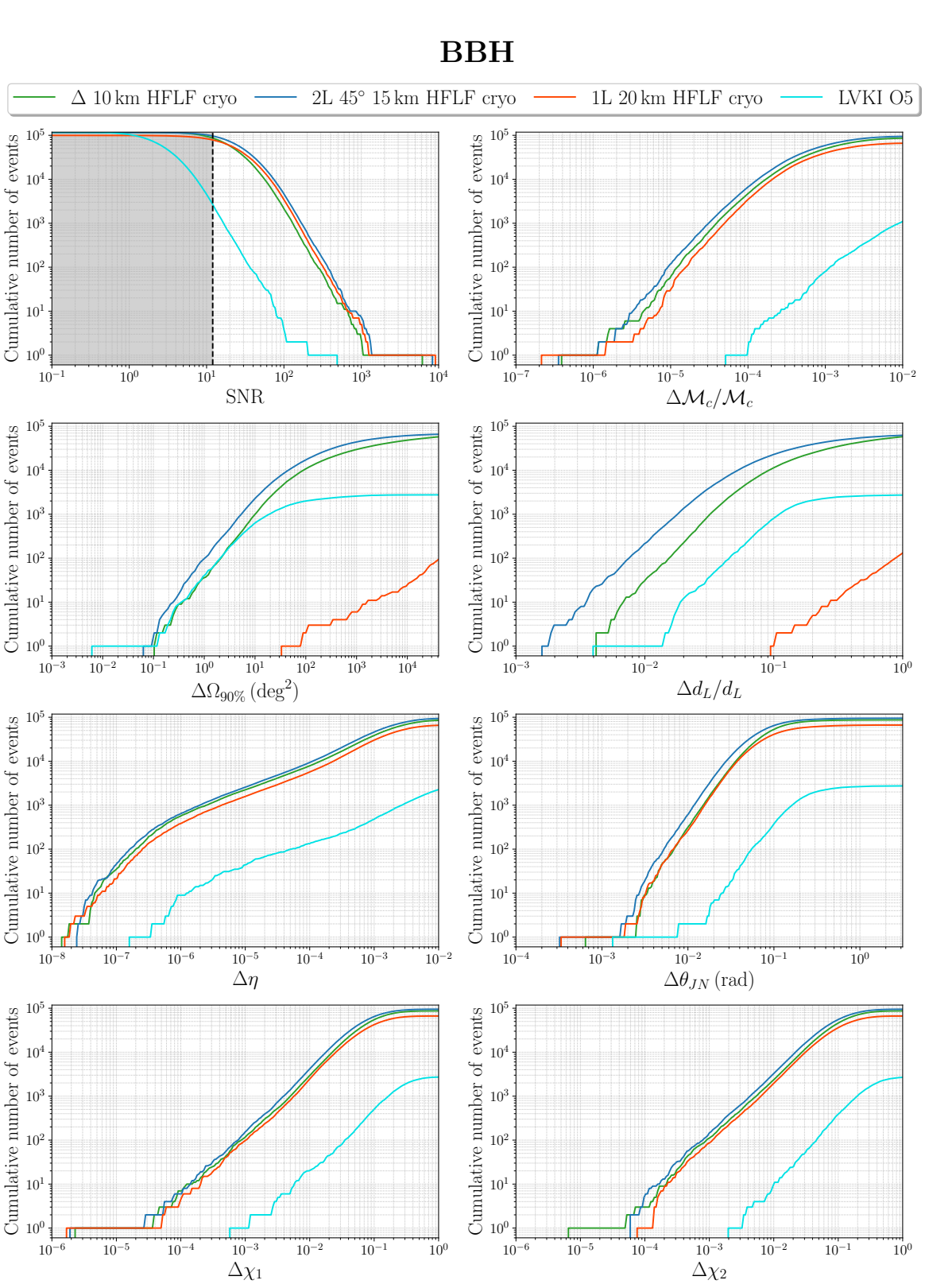

Figure 7. Comparison of SNR and parameter estimation error for the 10 km triangle, 15 km 2L misaligned and a single 20 km L with the HFLF-cryo ASD. By comparison, we also show the forecast for LVKI O5.

JCAP07(2023)068

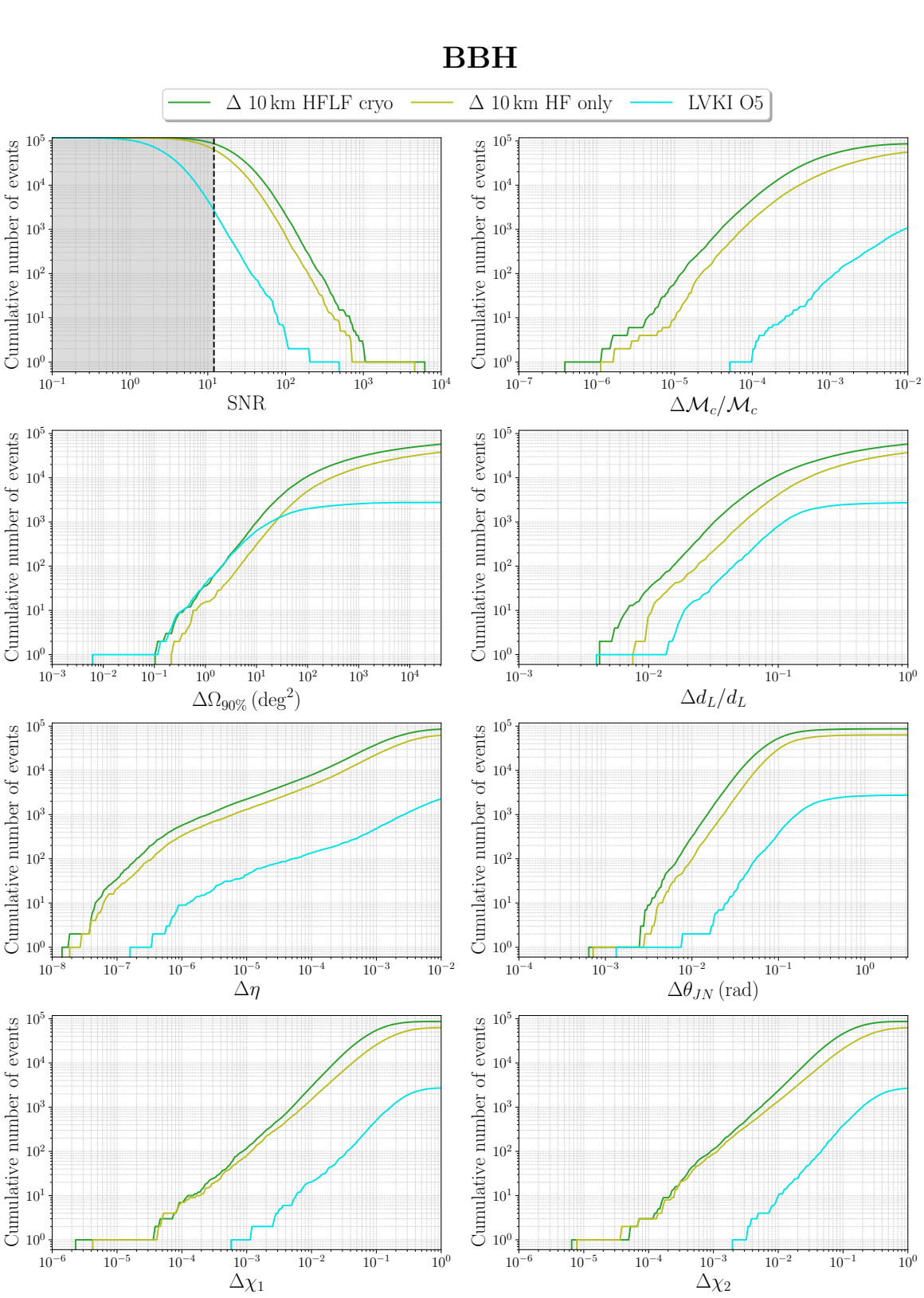

Figure 8. Comparison of SNR and parameter estimation error for the 10 km triangle with the HFLF-cryo and the HF-only ASDs. By comparison, we also show the forecast for LVKI O5.

JCAP07(2023)068

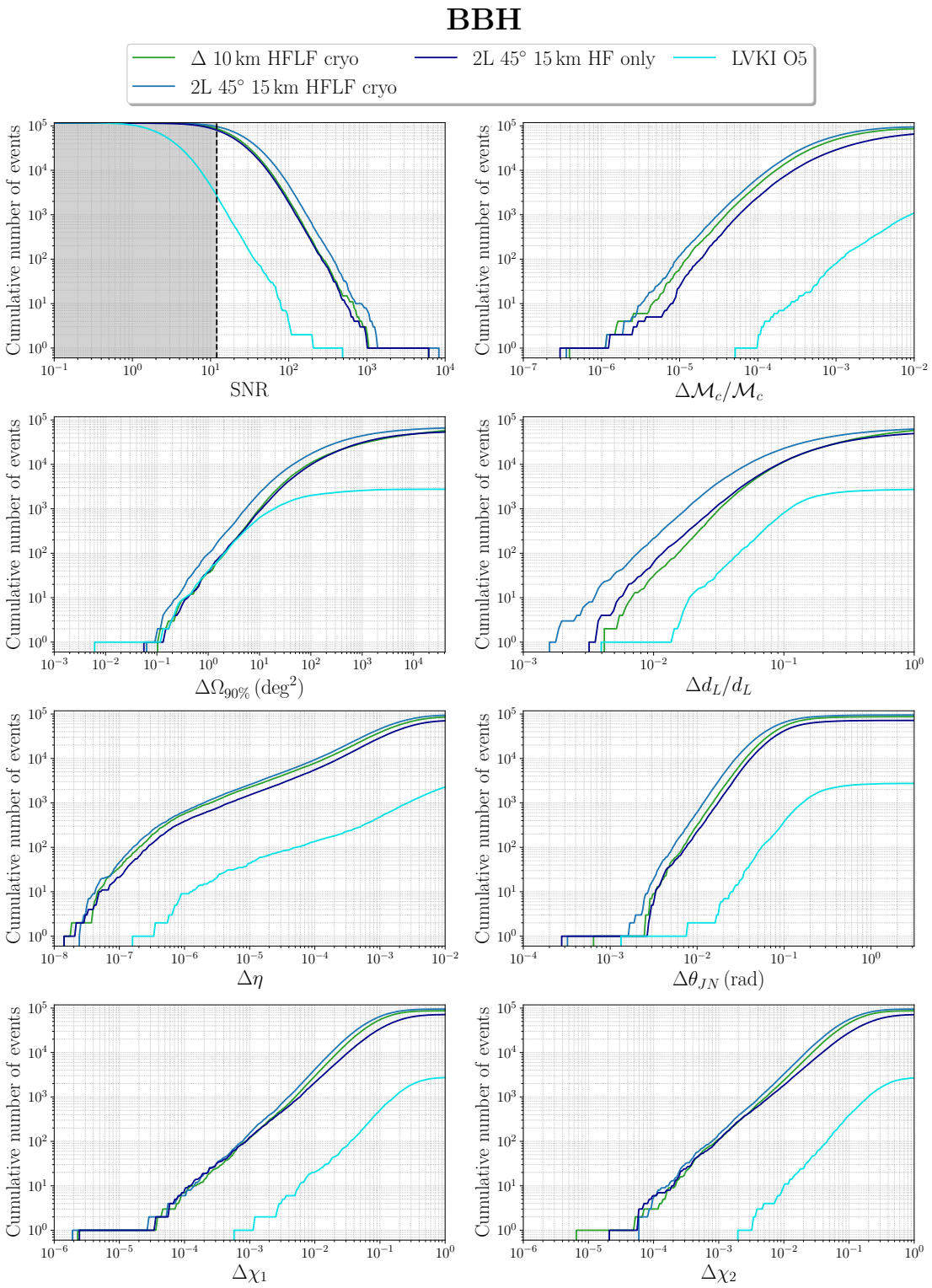

Figure 9. Comparison of SNR and parameter estimation error for the 15 km 2L misaligned with the HFLF-cryo and the HF-only ASDs. For comparison, we also show the result for the 10 km triangle in the HFLF-cryo configuration, and for LVKI O5.

JCAP07(2023)068

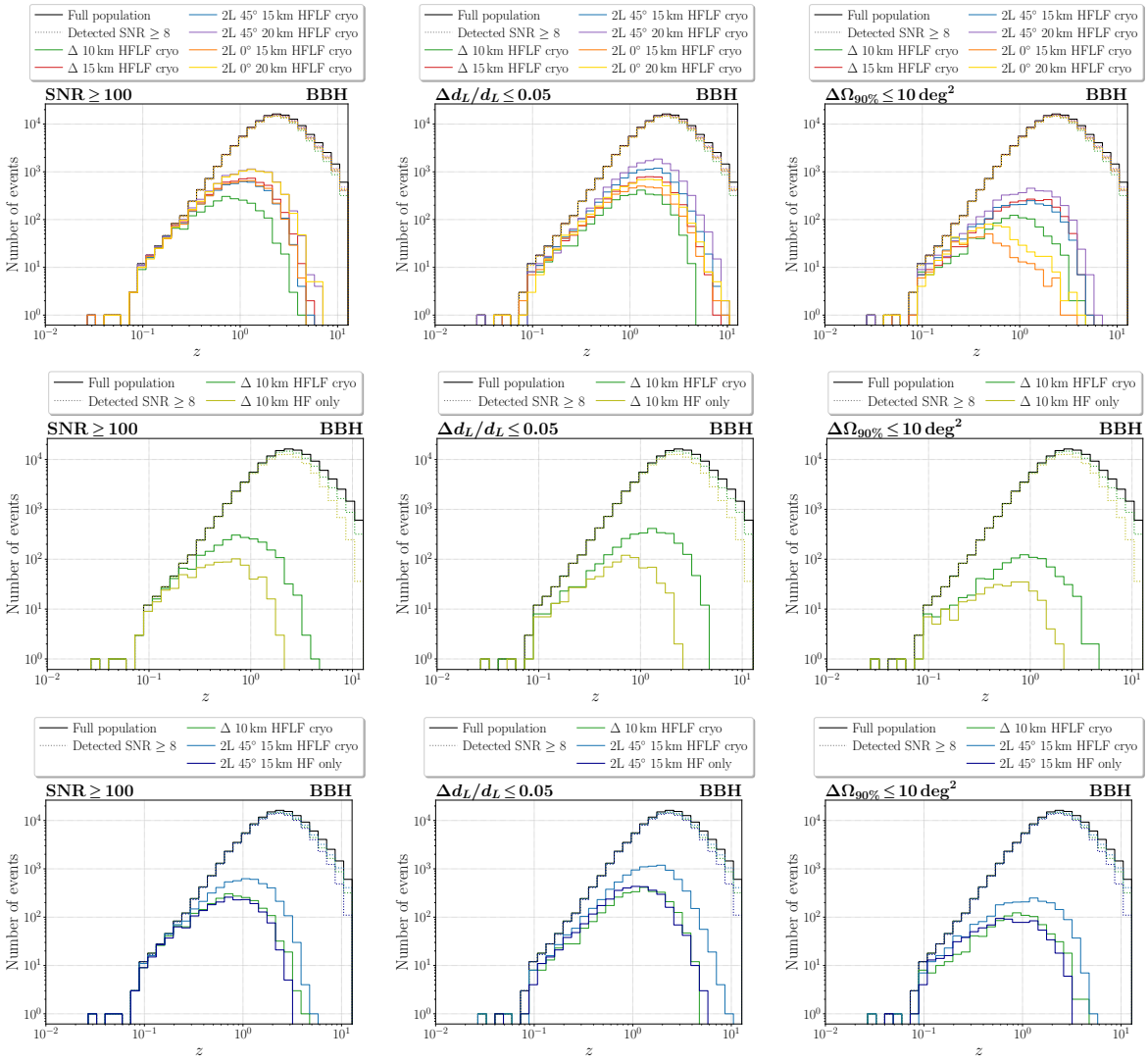

Figure 10. Redshift distribution of BBHs detected with SNR $\geq$ 100 (left column), or with relative error on the luminosity distance $\Delta d_L/d_L \leq 0.05$ (central column), or with sky location $\Delta\Omega \leq 10$ deg^2 (right column) for various detector geometries and sensitivity curves. The upper row shows the results for the six considered geometries, all with their best sensitivity, the central row for the 10 km triangle with the two considered ASDs, and the bottom row for the 2L with 15 km arms at 45° and the two considered ASDs (together with the 10 km triangle with the full ASD). In each panel we also show, for reference, the redshift distribution of the BBH population used (black solid line), and of the events detected in the various configurations with SNR $\geq$ 8 (dotted lines).

JCAP07(2023)068

3.2 Binary Neutron Stars

We now perform the same analysis for BNSs. The corresponding results are shown in figures 11–16. We discuss again separately the dependence on geometry, on ASD, and the 'golden events'.

3.2.1 Comparison between geometries

Figure 11 confirms the basic message obtained from BBHs in figure 5: the 10 km triangle has, in itself, remarkable performances and produces order-of-magnitudes improvements with respect to 2G detectors. However, a further improvement can be obtained from the other geometries that we have considered, on almost all parameters. The only exceptions are the inclination angle ι, for which the 2L configuration with parallel arms performs, comparatively, quite poorly, both for 15 km and 20 km arm-length,[13] and the luminosity distance, for which the 10 km triangle performs similarly to the 2L with 15 km parallel arms. Similarly to what we found for BBHs, also for BNSs *the* 2L *15 km with arms at* 45° *improves on the accuracy estimate of all the parameters with respect to the 10 km triangle.* Comparing instead the 2L 15 km at 45° to the 15 km triangle, we see that the two perform similarly on most parameters except for luminosity distance, for which the 2L 15 km at 45° is significantly better. The 15 km triangle, however, performs better than a 15 km 2L with arms at 45° for the inclination angle ι, while the 2L 15 km at 45° performs better for the polarization angle ψ. To understand better the causes of some differences between geometries, it is interesting to compare the 2L-15km with parallel arms to the triangle with the same arm length. The 2L-15km with parallel arms is significantly worse than the 15-km triangle for the reconstruction of the inclination angle ι. This is due to the fact that, for the 2L-15km with parallel arms, only a single combination of the two polarization amplitudes is accessible. On the other hand, the 2L-15km with parallel arms is better than the 15-km triangle on the angular localization because, thanks to its long baseline, it can partially triangulate. Both the reconstruction of ι and the angular localization influence the reconstruction of the luminosity distance. However, we see from the panel on the luminosity distance in figure 11 that the 2L-15km with parallel arms is still significantly worse than the 15-km triangle in the reconstruction of d_L, so the dominant effect is due to the (comparatively) poor reconstruction of ι.

For the parameter $\tilde{\Lambda}$ related to the tidal deformability of the two NSs, again the 10 km triangle already obtains remarkable performances, with 1040 events/yr with $\tilde{\Lambda}$ measured better than 10%, and the best events providing a measurement at a few percent level; however, all other geometries that we considered improve further on this; in particular, the 2L-15km-45° detects 2463 events/yr with $\tilde{\Lambda}$ measured better than 10%, so an improvement by a factor of 2.5, and the 15 km triangle 2783, see tables 42, 43 and 44 in appendix C.

Figure 12 shows the joint accuracy on luminosity distance and angular resolution for BNSs, comparing the 15 km 2L at 45° to the 10 km triangle (upper panel) and to the 15 km triangle (lower panel). Considering, for instance, the events with $\Delta d_L/d_L < 0.1$ and $\Delta\Omega_{90\%} \leq 10^2\,\mathrm{deg}^2$, we see that the figure 13 shows the performance of a single L-shaped detector of 20 km for BNSs, compared to other geometries, similarly to figure 7 for BBH. We observe that, with a single L-shaped detector, no BNS will have an angular resolution $\Delta\Omega_{90\%}$ below $10\,\mathrm{deg}^2$, and (in our sample realization) only 6 BNS/yr would have $\Delta\Omega_{90\%} \leq 10^2\,\mathrm{deg}^2$ (to be compared with 184 BNS/yr for the 10 km triangle and 559 BNS/yr for the 2L configuration

[13] The difference with respect to the angle θ_{JN} shown in the BBH case is that, for BBHs, higher-order modes and precessing spin significantly help to determine the inclination angle.

JCAP07(2023)068

with 15 km arms at 45°, see table 43 in appendix C.). The reconstruction of distances would also be comparatively poor, with just a handful of events measured to better than 10%; so, without other 3G detectors, a single L-shaped detector, even with 20 km arms, would miss all the aspects of the Science Case, such as multi-messenger astronomy or cosmology, that require good source localization.

3.2.2 Effects of a change in the ASD

Figure 14 shows the result for the two ASDs of the 10 km triangle and compares them with LVKI O5. Quite interesting results emerge from the panel on the angular resolution. A five-detector network, such as LVKI O5, would of course have excellent localization capabilities for some very close events, so that it can reach a localization below 1 $\deg^2$ on a few events per year, which a single 10 km triangle, even with the full ASD, cannot reach. However, this will be limited to a handful of particularly close events. What is also relevant, in the panel for $\Delta\Omega_{90\%}$ of figure 14, is the number of BNS with $\Delta\Omega_{90\%}$ below about $10^2\,\deg^2$. In fact, such an angular localization accuracy can already be sufficient to perform multi-messenger studies with wide field of view (FoV) electromagnetic observatories, as has been demonstrated by the current follow-up of gravitational-wave signals (see e.g. [4, 55]). In this case, the single triangle is quite superior to the LVKI O5 network, by detecting a number of well-localized sources higher by a factor ~ 3.6 (see table 43 in appendix C for a compilation of numerical values relative to these figures, and section 4 for a detailed discussion and implications for multi-messenger studies). However, this is true only for the triangle at full sensitivity, i.e. in the HFLF-cryo configuration. The ET full sensitivity localization significantly benefits from the use of the effect of Earth's rotation on the longer signal detected, thanks to the access to lower frequencies. The benefit is much larger for closer events where the BNS signal can be followed for a longer time. In terms of the number of BNSs with angular resolution below $10^2\,\deg^2$, the HF-only configuration is therefore much worse than LVKI O5. For most other parameters, in contrast, a 10 km triangle provides a significant jump with respect to LVKI O5 even in the HF-only configuration (except for luminosity distance and polarization, where it is worse; this is because these quantities are more correlated with angular localization). See again table 43 in appendix C for a compilation of numerical values.

Figure 15 show the analogous results for the 2L configurations with 15 km arms at 45°; for comparison, we also show both LVKI O5 and the 10 km triangle at full sensitivity. First of all, we see again that, at the level of full sensitivities, the configurations with 15 km arms at 45° is superior to the 10 km triangle for all parameters. We also see that, for angular localization, the HF-only configuration is much worse than LVKI O5, at least for events with $\Delta\Omega_{90\%} < 10^2\,\deg^2$, which are the relevant ones for multi-messenger studies, while, for all other parameters, even the HF-only configurations provides a remarkable jump compared to LVKI O5. However, contrary to the BBH case, the HF-only configuration is now very much inferior to the 10 km triangle with the full ASD, particularly for sky localization. This is due to the fact that the improvement of the low-frequency sensitivity allows a BNS to remain in the detector bandwidth for hours and even up to a day, as we already mentioned above (see also figure 2 of [17]), and then the rotation of the Earth improves the BNS localization. This is less relevant for BBHs since most of them have a total mass greater than about $\mathcal{O}(20\,M_\odot)$, and stay in the detector bandwidth for a time too short to appreciate the effect of Earth's rotation. Therefore, the low-frequency sensitivity, and therefore the LF instrument, is more important for the localization of BNSs compared to BBHs. *This shows the crucial importance of the LF instrument for BNSs.*

JCAP07(2023)068

3.2.3 Golden events

Figure 16 shows the redshift distribution of 'golden events' for BNSs, defined here either by the condition SNR ≥ 30, or by $\Delta d_L/d_L \leq 0.2$, or by $\Delta\Omega_{90\%} \leq 10^2\,\mathrm{deg}^2$. These conditions are less stringent than those used for BBHs in figure 10, reflecting the fact that BNSs are intrinsically less loud than BBHs. The upper row compares the different geometries, all taken with their best ASD, and basically confirms the picture obtained for BBH golden events, compare with the upper row of figure 10: for the SNR, the 10 km triangle gives the less good results, while the other configurations are comparable, with the 2L with 20 km parallel arms being the best; for luminosity distance and angular localization, the 2L configurations with arms at 45° give the best results and, overall, appears to provide the best compromise between having a large number of events with large SNR out to large distances, and localizing them well in volume.

The middle row quantifies the loss of performance of the 10 km triangle when the LF instrument is absent. The loss is particularly dramatic for the accuracy on luminosity distance and sky localization. *This confirms the crucial importance of the LF instrument for BNS,* as we already discussed when commenting figure 15.

From the bottom row we see that, also on this metric, the 2L configurations with arms at 45° and the HF-only ASD gives results basically identical to the 10 km triangle with full HFLF-cryo sensitivity for the SNR distribution; in contrast, we already remarked on the full ensemble of events that the LF instrument is crucial for angular localization and accuracy on luminosity distance for BNSs, and we see the same information emerging from golden events, where the HF-only configuration of the 2L configurations with arms at 45° is very much inferior to the full 10 km triangle, in contrast to what happens for BBHs, compare with figure 10. As already discussed, this is due to the fact that, with a good low-frequency sensitivity, BNSs can stay in the detector bandwidth for hours to about 1 day, with the corresponding benefit in angular localization and in all parameters correlated with it.

3.2.4 Dependence on the population model

Finally, it is interesting to discuss how these results depend on the model that we have used for the BNS population (and on the specific random sample extracted from it). First of all, we remark that the differences between designs that emerge from these plots, and the conclusions that we draw from them, are not driven by the tails of the distributions (that, even for a given population model, would also depend on the sample realization), but rather by their overall behavior, which in general involves hundreds of events; even for the 'golden events', there are several tens to several hundreds events per bin, see figure 16. To understand in full generality how the results depend on the population model used is quite difficult; the full set of runs, on all different detector configurations studied, is computationally expensive, and it is not feasible to explore a large parameter space of population models in a reasonable timeframe. Our strategy has rather been to use a state-of-the art population model [52] for BNS and NSBH (and [54] for BBHs), which are able to match the LVK rates. However, a useful check, for BNS, can be performed as follows. For the redshift distribution of the BNS rate, current models are quite sophisticated and we do not expect great variations (furthermore, we are not much interested in the absolute numbers of detections in a given configuration, but rather in the relative performances of the detectors). There is large uncertainty in the overall normalization, given by the local rate, which for BNS can be up a factor 10 higher or lower than the one that we use. However, while this will influence significantly the absolute number of detections per year, again it will not affect much the comparison between detectors, which

JCAP07(2023)068

is our main aim. For instance, if the local rate should turn out to be a factor of 2 smaller than the one that we use, the plots that we show will have to be understood as relative to 2 years of data, rather than 1 yr; however, the conclusions for the relative performances of the different design would be basically unaffected (of course, the tails of rare events will be affected for a given fixed observation time but, again, the conclusions are not really dependent on these tails). So, for our purposes the parameter that is most significant to vary, for BNS, is the mass distribution. As mentioned on page 10, the results for BNS presented above were obtained with a flat mass distribution between 1.1 and 2.5 solar masses. We have repeated the analysis using a Gaussian mass distribution, with mean $1.33M_{\odot}$ and standard deviation $0.09M_{\odot}$, sampled independently for both masses (we then impose that the heaviest one corresponds to m_1). The results, for the six considered geometries in their full HFLF-cryo configuration, are shown in figure 17. Comparing with figure 11, we see that the results are very consistent. There is a somewhat smaller number of overall detections (because in the gaussian distribution events with large masses are suppressed), but the parameter estimation is quite similar (with differences in the tails, expected because of sample variance), and the conclusions for the comparison between detector configurations are unchanged.

JCAP07(2023)068

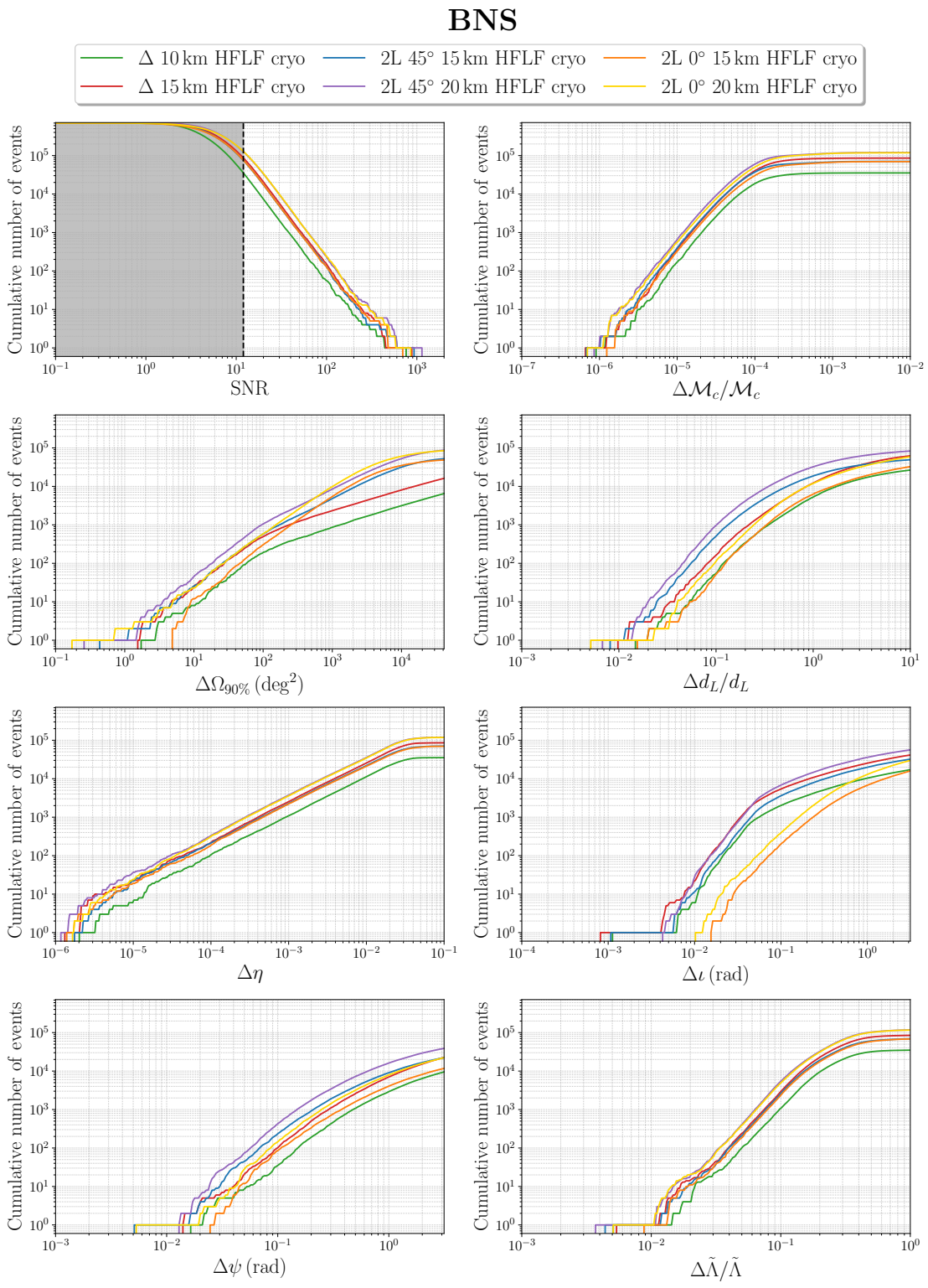

Figure 11. Cumulative distributions of the number of detections per year, for the SNRs and for the error on the parameters, for BNS signals, for the six considered geometries, all with their best ASD, including xylophone configuration and cryogenic LF instrument.

JCAP07(2023)068

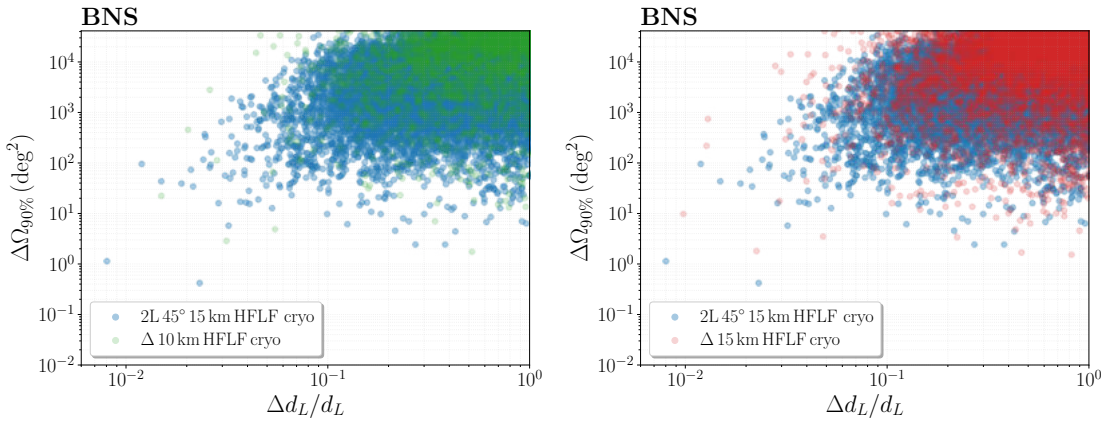

Figure 12. The joint accuracy on luminosity distance and angular resolution for BNSs. Left panel: the 15 km 2L at 45° (blue) compared to the 10 km triangle (green). Right panel: the 15 km 2L at 45° (blue) compared to the 15 km triangle (red).

JCAP07(2023)068

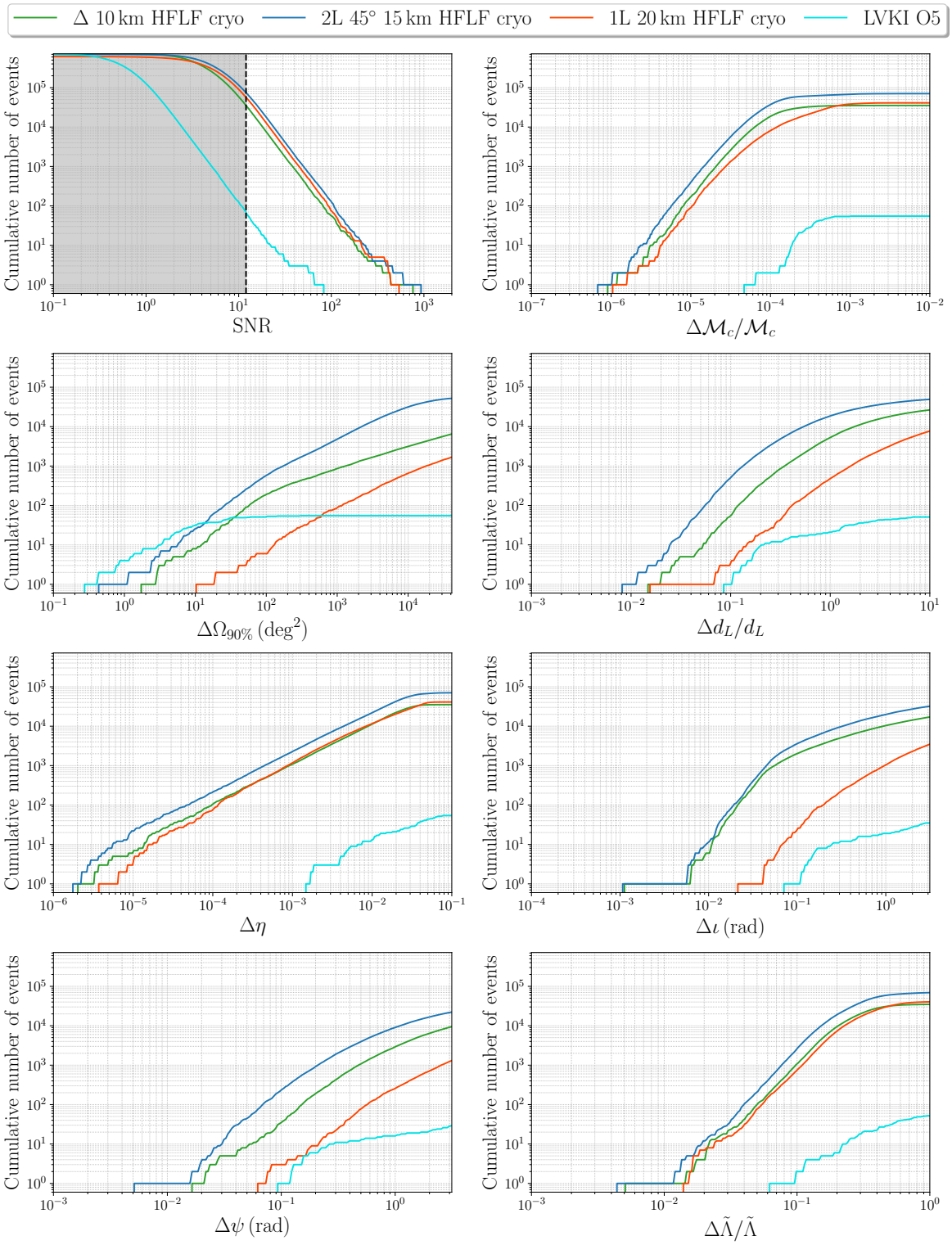

Figure 13. Comparison of SNR and parameter estimation error for a single 20 km L-shaped detector with the HFLF-cryo ASD, compared to the 10 km triangle, a 2L with 15 km arms at 45°, and the forecast for LVKI O5.

JCAP07(2023)068

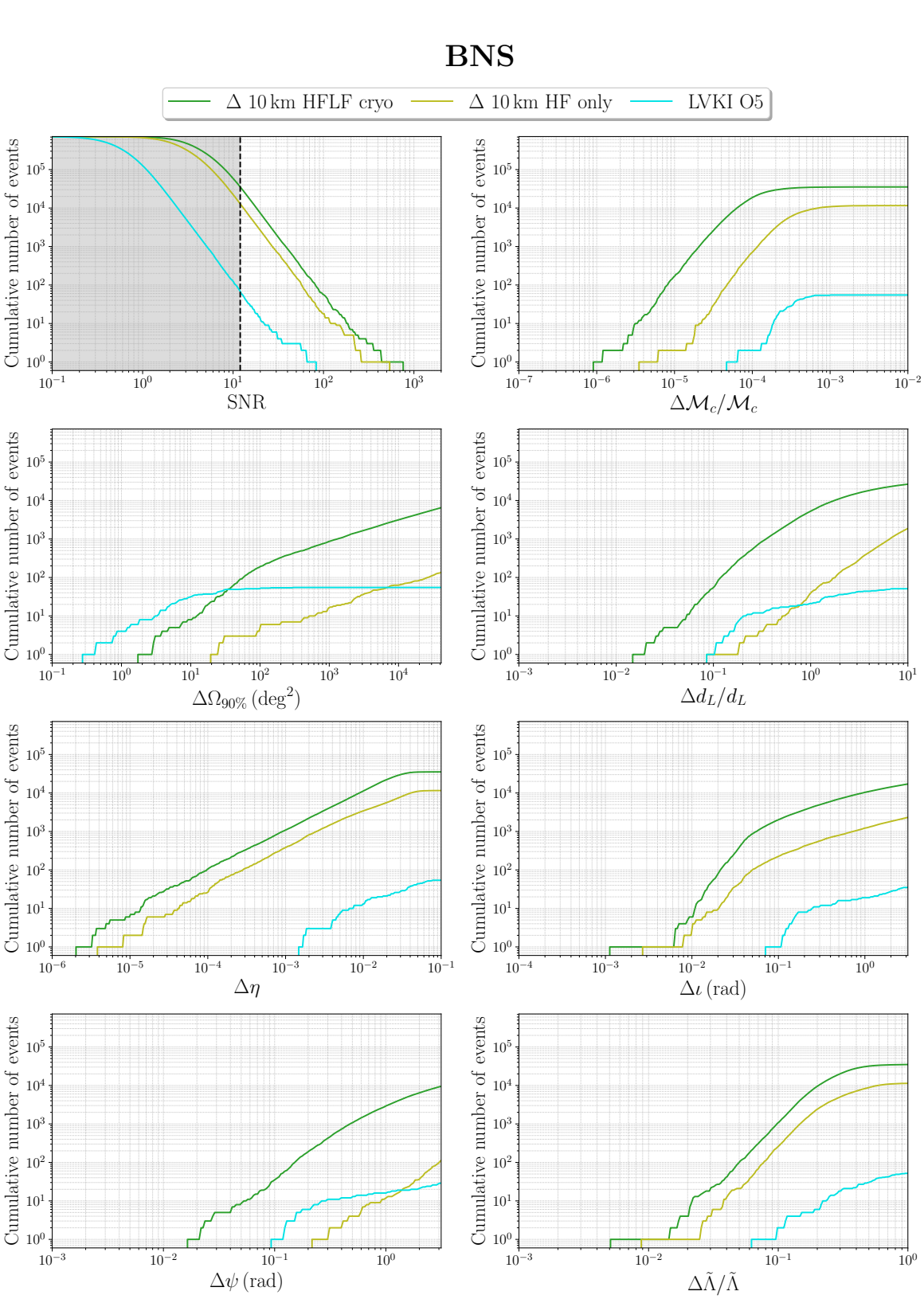

Figure 14. Comparison of SNR and parameter estimation error for the 10 km triangle with different ASDs. By comparison, we also show the forecast for LVKI O5.

JCAP07(2023)068

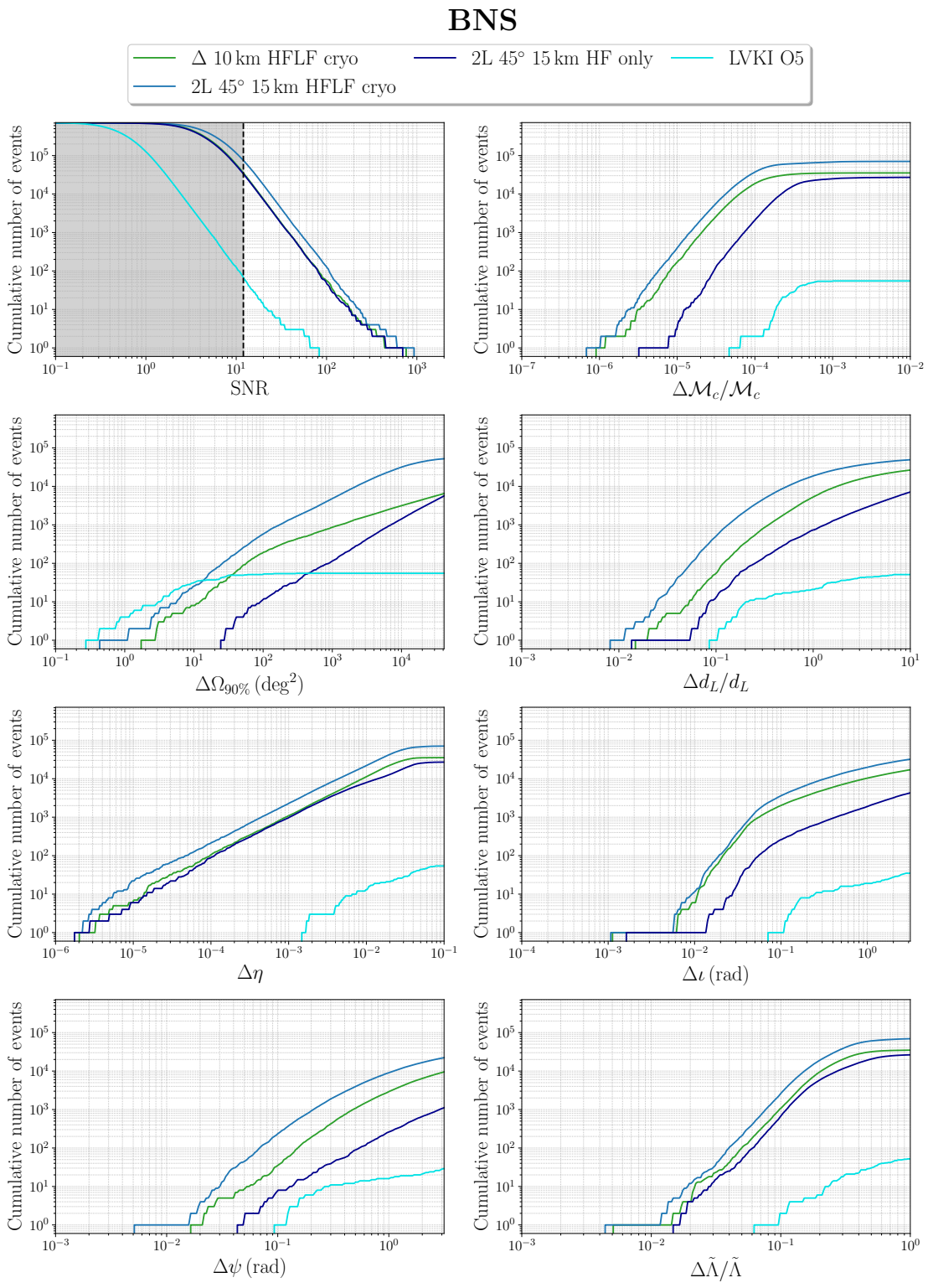

Figure 15. Comparison of SNR and parameter estimation error for the 2L with 15 km arms at 45°, with the two different ASDs. For comparison, we also show the 10 km triangle at full sensitivity, and the forecast for LVKI O5.

JCAP07(2023)068

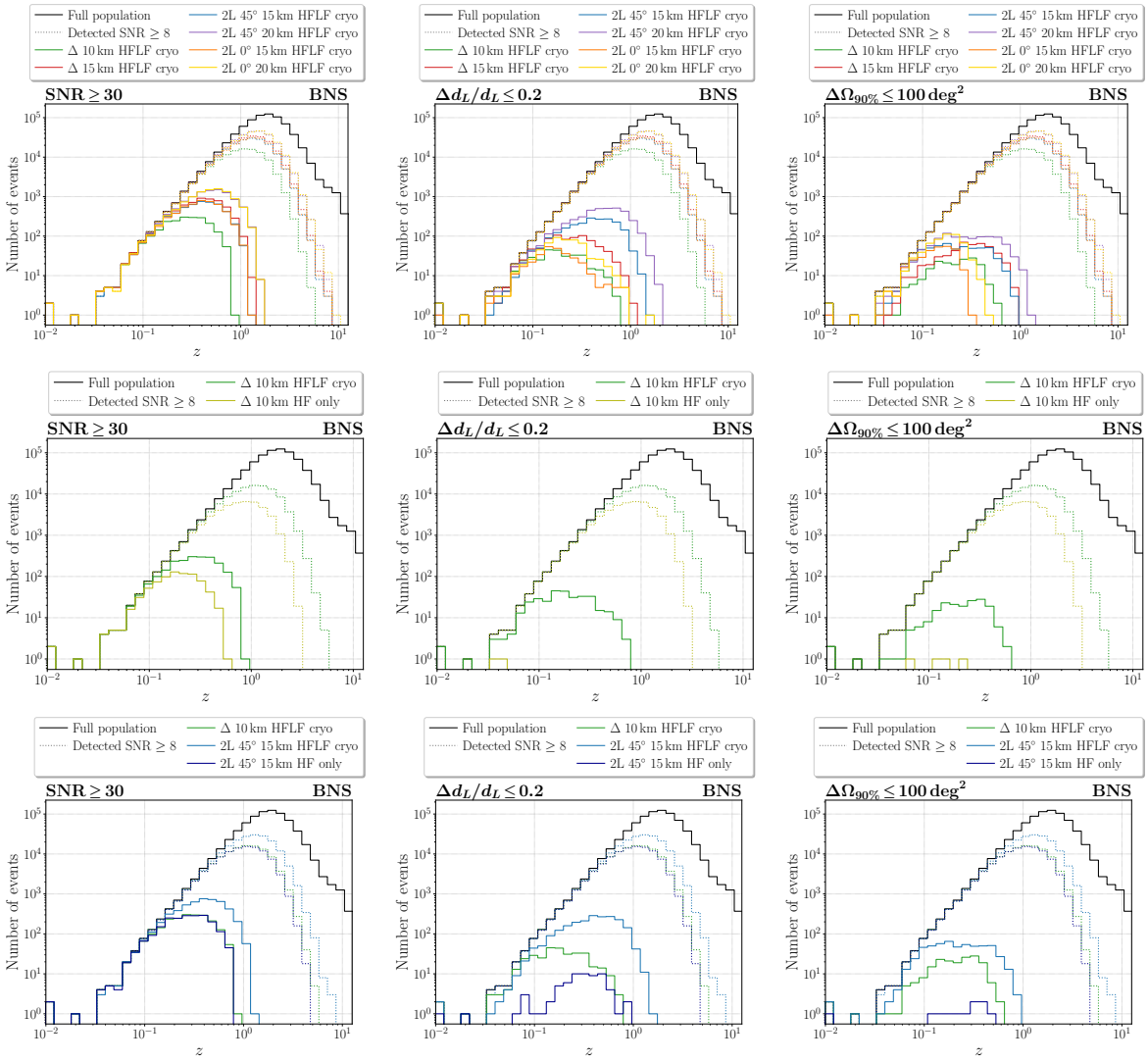

Figure 16. Redshift distribution of BNS detected with SNR $\geq$ 30 (left column), or relative error on the luminosity distance $\Delta d_L/d_L \leq 0.2$ (central column), or with sky location $\Delta\Omega \leq 100$ deg^2 (right column) for various detector configurations and sensitivity curves. The upper row shows the results for the six considered geometries, all with their best sensitivity, the central row for the 10 km triangle with the two considered ASDs, and the bottom row for the 2L with 15 km arms at 45° and the two considered ASDs. In each panel, we also show, for reference, the redshift distribution of the BNS population used (black solid line) and the events detected in the various configurations with SNR $\geq$ 8 (dotted lines).

JCAP07(2023)068

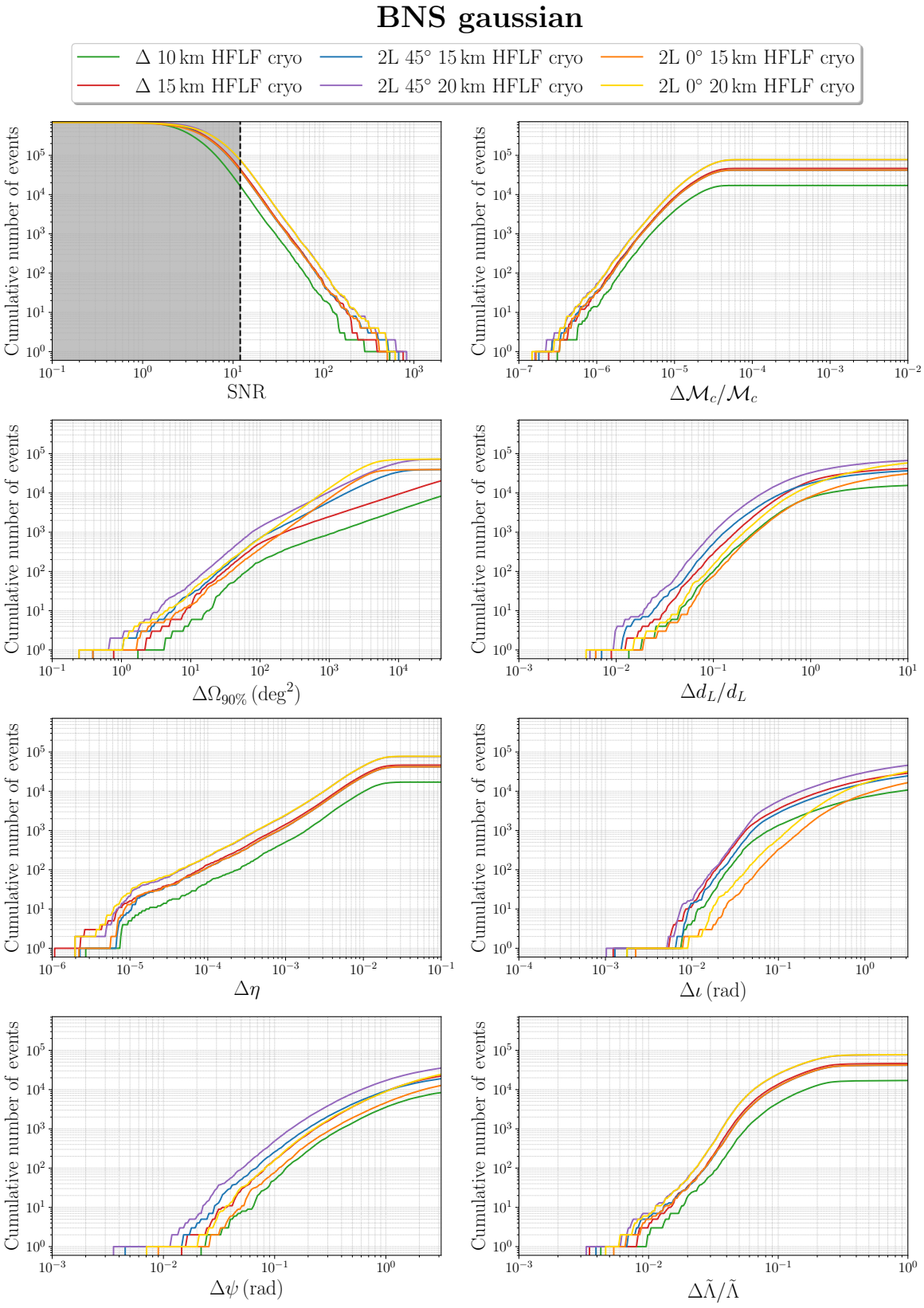

Figure 17. As in figure 11, for a gaussian mass distribution of the two component neutron stars.

JCAP07(2023)068

3.3 ET in a network of 3G detectors

The above analysis studied the capabilities of ET alone (whether consisting of a single-site triangle or of two L-shaped detectors on widely separated sites), comparing the results obtained with different possible geometries and sensitivity curves. We now study how the different geometries for ET (triangle or 2L) perform when they are included in a network of 3G detectors which includes Cosmic Explorer. The reference CE configuration currently consists of two L-shaped detectors (on the Earth's surface rather than underground), one with 40 km arms and one with 20 km arms [14]. We will refer to this configuration as '2CE' and we will study how different choices for the ET geometry affect the performance of a network made by ET and 2CE. Given the current uncertainties, it is also instructive to investigate what happens when ET (in a triangular or 2L geometry) is part of a network with a single CE detector, which we take to be the 40 km one ('1CE'). In order to avoid a proliferation of plots, we limit here to three options for ET: the 10 km triangle, and the 15 km 2L configurations, either with parallel arms or with arms at 45°. Therefore, we consider the following networks:

1. ET as a triangle with 10 km arms, together with 2CE (20+40 km)
2. ET as a 2L of 15 km and parallel arms, together with 2CE (20+40 km)
3. ET as a 2L of 15 km and arms at 45°, together with 2CE (20+40 km)
4. ET as a triangle with 10 km arms, together with 1CE (40 km)
5. ET as a 2L of 15 km and parallel arms, together with 1CE (40 km)
6. ET as a 2L of 15 km and arms at 45°, together with 1CE (40 km)

In particular, the last two options correspond to a global network of three L-shaped detectors, two of 15 km and with the ET ASD, and one of 40 km and the CE ASD. In all these configurations, for ET we will consider only the full sensitivity, corresponding to the ASD that we have labelled as 'HFLF-cryo' and, for CE, we use the latest publicly available official sensitivity curves.[14]

Figure 18 shows the SNR distribution and the errors on parameter estimation for BBHs for the six networks considered, while figure 19 shows the corresponding results for BNSs. From figure 18, to be compared with the green, blue and orange lines in figure 5 referring to ET alone, we see that, as expected, the overall performance of the network is significantly better than that of ET alone for angular localization and distance determination. As an example, the BBH/yr localized to better than $1\,\mathrm{deg}^2$ raise from a few tens (depending on the ET geometry) to a few times 10^3. On the other parameters, the gain from adding one or two CE detectors results typically in an increase by a factor of order 2 of the number of events with accuracy better than a given value of the chosen parameter; e.g., in our specific realization, for the symmetric mass ratio η, the number of events per year with $\Delta\eta \leq 10^{-6}$

[14]The most recent PSDs of CE can be found at https://dcc.cosmicexplorer.org/CE-T2000017/public. We used the locations and orientations reported in rows C and N of table III of [30]. In particular, the 40 km detector is placed in Idaho and the 20 km one in New Mexico. These orientations are such that the relative angle between the two CE detectors, measured with respect to the great circle that joins them, is about 56.0°. When ET is taken to be in the 2L configuration, with our choice of orientations the relative angle between the Sardinia detector and the CE-Idaho is about 191.2° and that between the Sardinia detector and the CE-New Mexico one is about 237.6°. As in the discussion in footnote 4, if a 2L configuration should be retained for ET, a careful study of the optimization of the relative orientations of the ET+2CE detector network will become necessary.

JCAP07(2023)068

raises from 559 for ET alone in the 10 km triangle configuration, to about 922 in a network with 1CE and 1018 with 2CE; similar results hold for the other parameters.

As we see from tables 39, 40 and 41 in appendix C (factors of 2 are difficult to appreciate on the logarithmic scale of figure 18), in a network with a 40km CE, for BBHs the different geometries chosen for ET induce overall differences in the results at the level of factors ~ 1.5 or smaller. As an example, the number of BBH/yr with d_L measured better than 1% raises from 2901 for the 10 km triangle+1CE, to 4301 for 2L-15km-45°+1CE, while the number of BBH/yr localized to better than $10\,\mathrm{deg}^2$ raises from 3.0×10^4 to 3.6×10^4.

For BNS, the effect of the ET geometry in a network with 1 or 2CE can be seen from figure 19, and especially from tables 42, 43 and 44. For instance, the number of BNS/yr with SNR ≥ 150 raises from 87 for the 10 km triangle+1CE, to 116 for 2L-15km-45°+1CE, while those with d_L measured better than 10% increases by about a factor of 2, from 4100 for the 10 km triangle+1CE to 7949 for 2L-15km-45°+1CE. Similar differences appear for the chirp mass, symmetric mass ratio and tidal deformability. For instance, the number of BNS/yr with tidal deformability measured to better than 10% raises from 2669 for the 10 km triangle+1CE to 4753 for 2L-15km-45°+1CE, and from 3847 for the 10 km triangle+2CE to 6319 for 2L-15km-45°+2CE.

So, among the three geometries considered here, the one that gives consistently the best results is, again, the 2L with 15 km arms at 45°, with typical improvement with respect to the 10 km triangle of about a factor of $\sim (1.5 - 2)$. The configuration 2L-15km-0°, when in a network with 1CE, gives similar performances to 2L-15km-45° for masses or tidal deformability, but is worse by a factor ~ 2.5 for angular localization and ~ 4 for luminosity distance. For instance, the number of BNS/yr with d_L measured better than 10% is 2079 for 2L-15km-0°+1CE and 7949 for 2L-15km-45°+1CE. In a network with 2CE the differences become smaller.

The overall conclusion is that the difference between the performances of the ET geometries remains visible, at the level of factors $\sim (1.5 - 2)$ *for BNSs, and somewhat smaller for BBHs, also when ET is in a network with 1 or 2 CE.*

JCAP07(2023)068

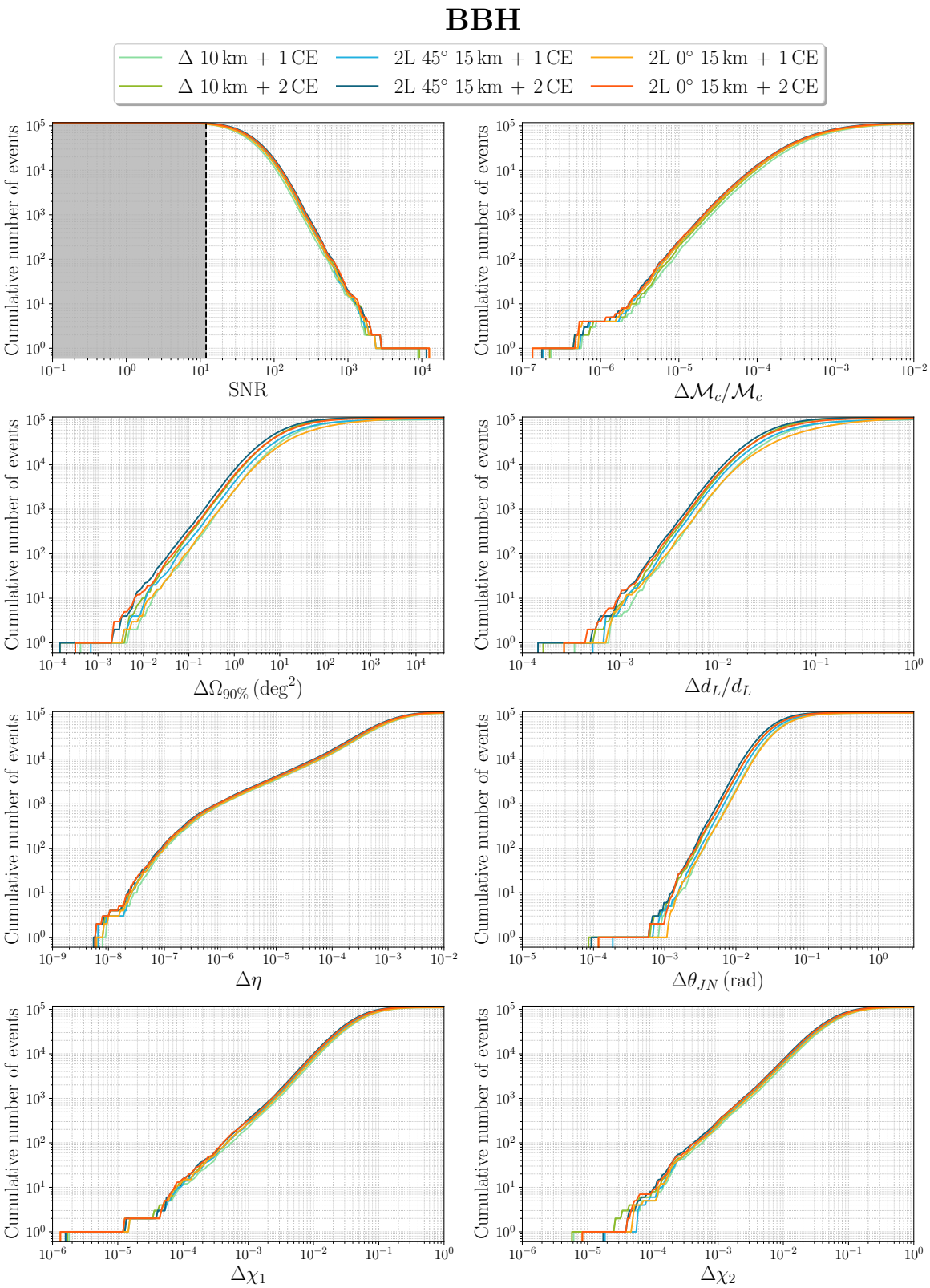

Figure 18. Comparison of SNR and parameter estimation error for BBHs, for the six 3G detector networks considered.

JCAP07(2023)068

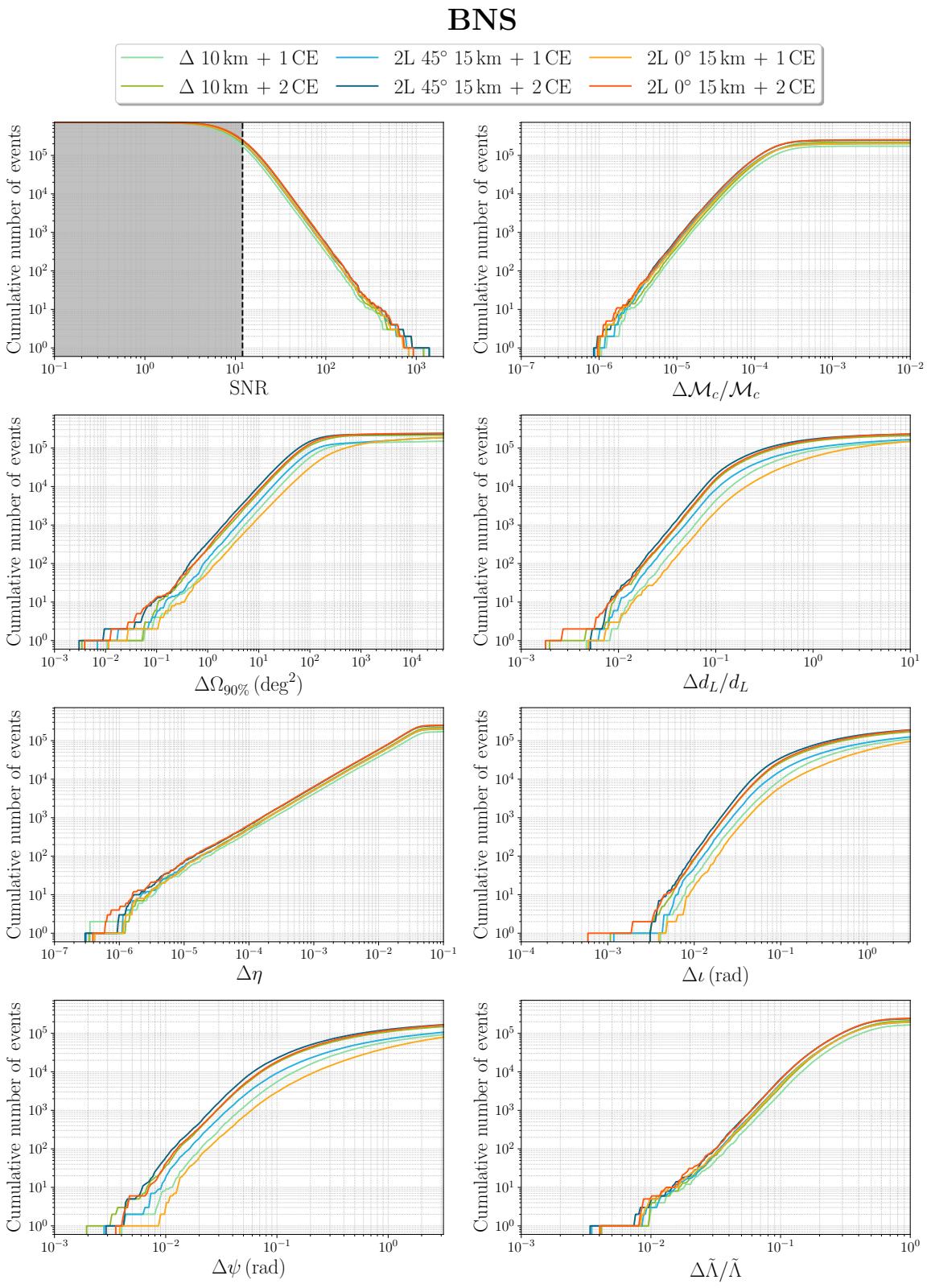

Figure 19. Comparison of SNR and parameter estimation error for BNSs, for the six 3G detector networks considered.

JCAP07(2023)068

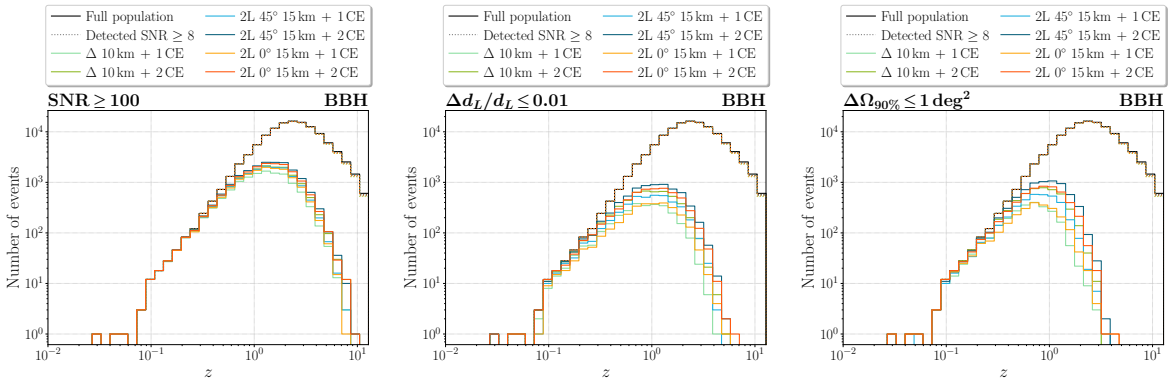

Figure 20. Redshift distribution of detected BBHs with SNR $\geq$ 100 (left column), or relative error on the luminosity distance $\Delta d_L/d_L \leq 0.01$ (central column), or sky location $\Delta\Omega \leq 1$ deg^2 (right column), for the six 3G the detector networks considered. In each panel, we also show, for reference, the redshift distribution of the BBH population used (black solid line), and of the events detected in the various configurations with SNR $\geq$ 8 (dotted lines, graphically almost indistinguishable from the full population on this scale).

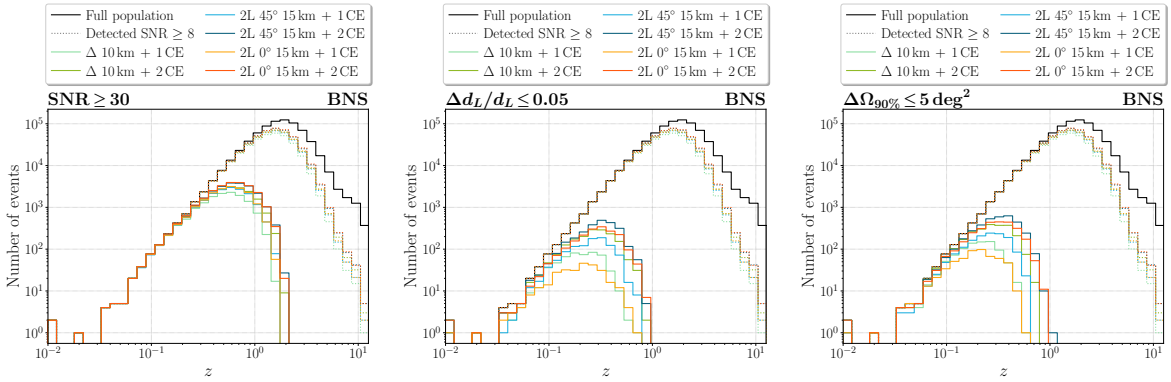

Figure 21. Redshift distribution of detected BNS with SNR $\geq$ 30 (left column), or relative error on the luminosity distance $\Delta d_L/d_L \leq 0.05$ (central column), or sky location $\Delta\Omega \leq 5$ deg^2 (right column) for the six 3G the detector networks considered. In each panel, we also show, for reference, the redshift distribution of the BNS population used (black solid line), and of the events detected in the various configurations with SNR $\geq$ 8 (dotted lines).

JCAP07(2023)068

4 Multi-messenger astrophysics

In this section we study the impact of the different detector geometries and different ASDs on the multi-messenger capabilities of ET operating in synergy with electromagnetic (EM) observatories. ET will observe together with a new generation of innovative EM observatories, such as CTA [56], Athena [57], the Vera Rubin Observatory [58], JWST [59], ELT [60], SKA [61] and with the possible mission concepts UVEX [62], THESEUS [63], HERMES [64], GRINTA, ASTROGAM [65] and AMEGO [66]. These observatories will probe the formation, evolution, and physics of BNS systems in connection with kilonovae (KNe) and short gamma-ray bursts (GRBs) along the star formation and chemical evolution of the Universe. The multi-messenger studies will tremendously benefit from the larger sample of joint GW/EM detections and, in the closer Universe, from the greatly improved parameter estimates of ET with respect to the current detectors.

Taking into account the sky-localization capability of ET and the fact that the KN emission is intrinsically fainter than that of GRBs, future multi-messenger astronomy will differ at closer redshifts ($< 0.3 - 0.4$), where it will be possible to detect KN emission using the wide-field telescopes, such as the Vera Rubin Observatory, from the distant Universe where the detectable counterparts at large redshift will be almost uniquely observed in the high-energy band through the beamed emission of GRBs. While the joint GW/KN detections will enable unprecedented studies of the enrichment of the Universe with heavy elements, of nuclear physics to constrain the equation of state (EoS) of NSs and cosmology estimating the expansion rate of the Universe, the joint GW/GRBs detections will unveil the structure and properties of relativistic jets, the emission mechanism of short GRBs, the role of merger remnants such as magnetars, and will make it possible to estimate cosmological parameters and test modified gravity at the cosmological scale.

The main parameters determining the joint GW/EM detections, and thus affecting the multi-messenger performance of ET, are the ability to localize the source and the volume of the Universe up to which ET will be able to detect the source in terms of achieved redshifts. Another important aspect of third-generation GW detectors is the ability to detect BNSs before the merger and send pre-merger alerts with a good estimate of the sky localization of the source. This is critical for detecting prompt and early emissions in EM bands where all-sky monitors are not operating.

Here, we examine the sky-localization capabilities as a function of redshift and the pre-merger alert scenarios, and we evaluate the joint detections for ET observation together with examples of high-energy satellites and optical wide-FoV telescopes. Differently from the other sections, in this section, we use an SNR detection threshold of 8 taking into account that the presence of a counterpart increases the significance of the source detection.

4.1 BNS sky-localization and pre-merger alerts

The sky-localization capability of GW detectors has a major impact in the efficiency of the search for a counterpart determining the number of pointings of the EM instruments to cover the GW signal location, the corresponding amount of observational time to be used and the search sensitivity, and the efficiency to select and remove contaminating transients. Starting from the BNS population described in section 3, `GWFISH` [31] is used to evaluate the localization capability and build table 1, which gives the expected number of detections (SNR ≥ 8) per year with sky-localization uncertainty (given as 90% c.l.) smaller than a threshold of 10, 40, 100, 1000 deg^2 for the different ET configurations (we do not consider the 2L aligned

JCAP07(2023)068

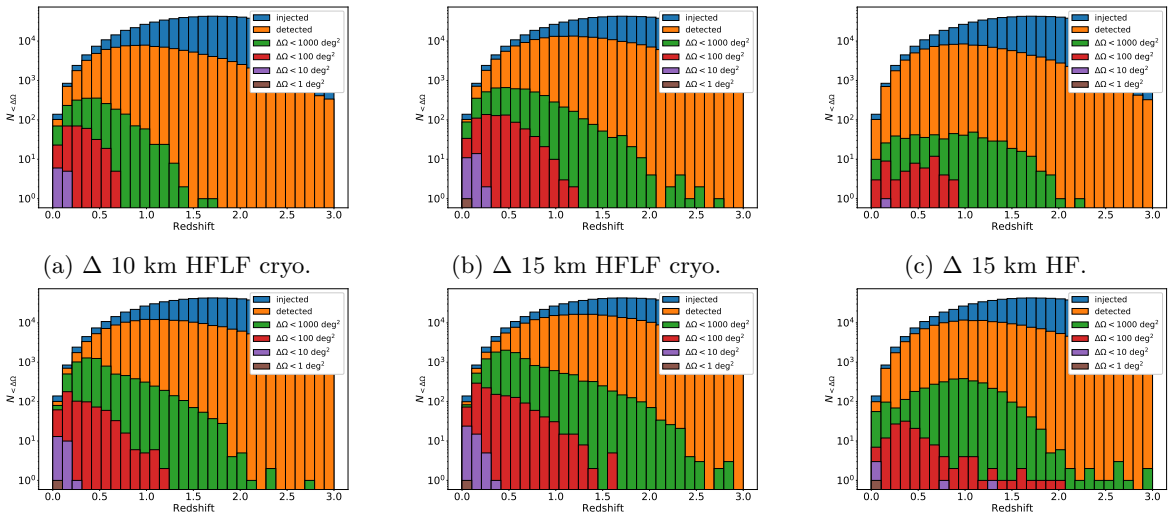

(a) Δ 10 km HFLF cryo. (b) Δ 15 km HFLF cryo. (c) Δ 15 km HF.

(d) 2L 15 km HFLF cryo. (e) 2L 20 km HFLF cryo. (f) 2L 20 km HF.

Figure 22. Redshift distribution of the sky-localization uncertainty (given as 90% credible region) of randomly oriented BNS systems as a function of redshift for four detector geometries: the 10 km triangle (Δ 10 km), the 15 km triangle (Δ 15 km), the 2L with 15 km misaligned arms (2L 15 km), and the 2L with 20 km misaligned arms (2L 20 km). The plots on left and central columns show the full (HFLF cryo) sensitivity detectors. In comparison, the plots on the right columns show the performance of the detectors operating only with the HF interferometers. The absolute numbers are relative to one year of observation and assuming a duty cycle of 0.85 as described in the text.

configurations because as shown in section 3.2 they yield worse localization capabilities with respect to the misaligned configurations). Figure 22 shows the redshift distribution of the sky-localization uncertainty for all the detected BNS events. The distribution is given as a function of redshift for four detector geometries; 10 km triangle, 15 km triangle, 2L with 15 km misaligned arms (i.e. arms at a relative orientation of 45°), and 2L with 20 km misaligned arms. The different colours show the detections localized within a certain threshold on the sky-localization uncertainty. Comparing the plots on the left and central columns of the figure, which show the full (HFLF cryo) sensitivity detectors, it emerges that *the 2L with 15 km misaligned arms performs better than the 10 km triangle and is comparable to 15 km triangle* (in agreement with the results shown in the panel for $\Delta\Omega_{90\%}$ in figure 11). Looking at the events localized with $\Delta\Omega_{90\%} < 10\,\mathrm{deg}^2$ ($100\ \mathrm{deg}^2$), the number of detection for the 2L with 15 km misaligned arms increases by factor 2 reaching z of 0.3 (1.2) with respect to the 10 km triangle, whose well-localized detections reach $z = 0.2\,(0.7)$. The 2L with 20 km misaligned arms increases the number of well-localized BNSs by a factor 4 with respect to the 10 km triangle reaching $z = 0.4\,(1.6)$ with events localized within $10\,\mathrm{deg}^2(100\,\mathrm{deg}^2)$. Table 1 shows also the expected number of detections per year within certain sky-localization uncertainty selecting events with a viewing angle, Θ_v,[15] smaller than 15°. A fraction of these events is expected to produce detectable high-energy emission powered by the GRB relativistic jet, assumed to be perpendicular to the orbital plane. *Also for on-axis events, the 2L with 15 km misaligned arms performs better than the 10 km triangle and is comparable to the 15 km triangle.*

[15]The viewing angle is defined as $\Theta_v = \iota$ for $0 \leq \iota \leq 90°$ and $\Theta_v = |\iota - 180°|$ for $90° < \iota < 180°$.

JCAP07(2023)068

Full (HFLF cryo) sensitivity detectors

$\Delta\Omega_{90\%}(\mathrm{deg}^2)$	All orientation BNSs				BNSs with viewing angle $\Theta_v < 15°$			
	Δ10	Δ15	2L 15	2L 20	Δ10	Δ15	2L 15	2L 20
10	11	27	24	45	0	1	2	5
40	78	215	162	350	8	22	20	33
100	280	764	644	1282	26	74	68	133
1000	2112	5441	7478	13482	272	632	1045	1725

Table 1. Expected number of detection (SNR $\geq$ 8) per year with sky-localization uncertainty $\Delta\Omega_{90\%}(\mathrm{deg}^2)$ smaller than the threshold indicated in the first column. While the columns 2-5 give the detections for BNS systems randomly oriented, the columns 5-9 give the detection of on-axis events, whose viewing angle is smaller than 15°. The numbers are relative to one year of observation assuming a duty cycle of 0.85 as described in the text.

HF sensitivity detectors

$\Delta\Omega_{90\%}(\mathrm{deg}^2)$	All orientation BNSs				BNSs with viewing angle $\Theta_v < 15°$			
	Δ10	Δ15	2L 15	2L 20	Δ10	Δ15	2L 15	2L 20
10	0	1	5	5	0	0	2	2
40	4	10	20	47	0	5	6	17
100	14	53	76	144	7	33	35	64
1000	145	548	1662	3378	80	336	672	1302

Table 2. Same as table 1 but considering the detectors operating with only the HF interferometers.

Losing the low-frequency interferometers, the HF GW detectors detect a significantly smaller number of well-localized events. However, as shown comparing table 1 and table 2,[16] *the decrease of detections of well-localized events is more severe for the triangle configurations than for 2L misaligned.* The right column of figure 22 shows the redshift distribution of the sky-localization uncertainty for the HF 15 km triangle and 2L with 20 km misaligned arms. The comparison with the corresponding configurations HFLF cryo shows that a large fraction of well-localized events is already missed at small redshifts. Focusing on the on-axis events, the use of only HF interferometers decreases the number of well-localized events but in a percentage of a smaller fraction with respect to the events randomly oriented. While the HF 2L with 15 km and 20 km misaligned arms localize worse than the HFLF-cryo 10 km triangle for randomly oriented systems, *for on-axis events, the HF 2L with 15 km misaligned arms localization capability is comparable to the HFLF-cryo 10 km triangle and the HF 2L with 20 km better than the HFLF-cryo 10 km triangle.*

The detection of prompt/early multi-wavelength emission from BNS mergers is critical to probe the central engine of GRBs, particularly to understand the jet composition, the particle acceleration mechanism, the radiation and energy dissipation mechanisms [see e.g.

[16]The different numbers, comparing tables 1 and 2 with table 43 in appendix C, reside in the different SNR threshold, assumed to be 8 for multi-messenger studies and 12 for the metrics of section 3 and appendix C. The larger difference on the HF-only estimates is also related to the different approach of `GWFISH` (used for the tables 1 and 2) which regularizes the close-to-singular matrices [31] instead of discarding the ill-conditioned Fisher matrix as `GWFAST` (used for the table 43) [17, 32]. As described in the footnote 9, for the HF-only case the percentage of discarded events approaches 10%.

JCAP07(2023)068

Full (HFLF cryo) sensitivity detectors

Configuration	$\Delta\Omega_{90\%}$	All orientation BNSs			BNSs with $\Theta_v < 15°$		
	[deg^2]	30 min	10 min	1 min	30 min	10 min	1 min
Δ10km	10	0	1	5	0	0	0
	100	10	39	113	2	8	20
	1000	85	293	819	10	34	132
	All detected	905	4343	23597	81	393	2312
Δ15km	10	1	5	11	0	1	1
	100	41	109	281	6	14	36
	1000	279	806	2007	33	102	295
	All detected	2489	11303	48127	221	1009	4024
2L 15 km misaligned	10	0	1	8	0	0	0
	100	20	54	169	2	7	26
	1000	194	565	1399	23	73	199
	All detected	2172	9598	39499	198	863	3432
2L 20 km misaligned	10	2	4	15	1	1	2
	100	39	118	288	7	19	47
	1000	403	1040	2427	47	128	346
	All detected	4125	17294	56611	363	1588	4377

Table 3. Number of BNS mergers per year detected (SNR ≥ 8) before the merger within $z = 1.5$ for the different full (HFLF cryo) sensitivity ET configurations. Three pre-merger scenarios (30, 10, and 1 minute(s) before the merger) are shown in different columns. For each detector configuration, the rows give the number of detections with sky-localization (90% c.l.) within 10, 100, 1000 deg^2, and all the detected sources. The numbers of GW detections per year take into account the ET duty cycle as described in the text.

67]. Regarding the kilonova emission, it has been shown that the early phase emission is particularly sensitive to the structure of the outer sub-relativistic ejecta (see, e.g., [68]) and can give rise to early UV emission detectable by wide-field satellites such as ULTRASAT [69], and mission concepts as UVEX [62] and Dorado [70] which can benefit of pre-merger alerts. Detecting a BNS signal before the merger makes it possible to eventually detect electromagnetic emission precursors. It makes it possible also to image the sky-localization before the merger that, especially for optical observations, is extremely useful to remove contaminating transients present before the merger. Considering all the benefits of pre-merger alerts for multi-messenger astronomy, here we explore the ET capabilities to detect BNSs and give a sky-localization before the merger.

JCAP07(2023)068

HF sensitivity detectors

Configuration	$\Delta\Omega_{90\%}$	All orientation BNSs			BNSs with $\Theta_v < 15°$		
	[deg^2]	30 min	10 min	1 min	30 min	10 min	1 min
Δ10km	100	0	0	0	0	0	0
	1000	0	0	4	0	0	1
	All detected	0	3	317	0	0	26
Δ15km	100	0	0	2	0	0	0
	1000	0	0	10	0	0	4
	All detected	2	8	891	0	1	84
2L 15 km misaligned	100	0	0	0	0	0	0
	1000	0	0	7	0	0	3
	All detected	0	7	743	0	1	69
2L 20 km misaligned	100	0	0	3	0	0	0
	1000	0	0	13	0	0	6
	All detected	2	11	1535	0	1	146

Table 4. Same as table 3 but for the HF sensitivity ET.

Table 3 shows the number of BNS mergers per year detected (SNR $\geq$ 8) before the merger within $z = 1.5$, for the different full (HFLF cryo) sensitivity ET configurations. We consider three pre-merger scenarios; 30, 10 and 1 minute(s) before the merger. For each ET configuration, we give the number of detection with sky-localization (90% c.l.) within 10, 100, 1000 deg^2, and all the detected sources. We show the results for the BNSs randomly oriented of our population (columns 3-5) and select among them the BNSs with viewing angles smaller than 15° (columns 6-8). The on-axis detections are particularly important to detect the prompt/early beamed emission associated with relativistic jets, for example the very high energy prompt emission never detected so far from GRBs (see [71] for the perspectives with the Cherenkov Telescope Array [72]). *Focusing on well-localized events detected pre-merger with a sky-localization smaller than 100* deg^2*, we highlight that the 15 km triangle turns out to perform better than the 10 km triangle and the 2L with 15 km misaligned arms, and its performance is similar to the 2L with 20 km misaligned arms. The 2L with 15 km misaligned arms performs better than the 10 km triangle. The results are similar for on-axis events.*

Table 4 shows the dramatic decrease of pre-merger alerts without low-frequency. *For all the ET configurations, there are no localized pre-merger detections, except a few events with sky localization smaller than* 1000 deg^2 *per year one minute before the merger (a few* $<$ 100 deg^2 *for* 2L20km*).*

4.2 Gamma-ray bursts: joint GW and high-energy detections

Following the approach described in [18], we evaluate the expected detections of prompt and afterglow emission of short GRBs associated with BNS mergers. We explore the joint

JCAP07(2023)068

INSTRUMENT	band MeV	$F_{\rm lim}$ ph cm^{-2} s^{-1}	FoV/4π	loc. acc.	Status
Fermi-GBM	0.01–25	0.5	0.75	5 deg	Operating mission
GECAM	0.006–5	2×10^{-8}(*)	1.0	1 deg	Operating mission
HERMES	0.05–0.3	0.2	1.0	1 deg	Mission concept Pathfinder next few yrs
GRINTA-TED	0.02–10	0.45	0.64	5deg(**)	Mission concept
ASTROGAM	0.03–200	0.29	0.27	<1.8 deg	Mission concept
THESEUS-XGIS	0.002–10	3×10^{-8}(*)	0.16	<15 arcmin	Mission concept Possible launch 2037

(*) expressed in ph erg cm^{-2} s^{-1}
(**) 65%(42%) of the TED/GW joint detections are detectable by the Hard X-ray Imager HXI on board of GRINTA by repointing HXI on the TED detection in 60s (5 min). HXI is expected to localize at order of 30 arcsec.

Table 5. Instruments characteristics.

detection capabilities of the different configurations of ET operating with gamma-ray and X-ray satellites. As reference instruments, we use some examples of current and upcoming satellites and mission concepts. We analyze different observational strategies: survey mode and target pointing.

4.2.1 Prompt emission

Starting from our astrophysically-motivated population of BNS mergers we model the high-energy signals associated with the mergers making the BNS population able to reproduce the rate and the properties of all the short GRBs observed so far (see [18] for details). For the fraction of BNS mergers in our population that are expected to produce a jet (about 20% of the BNS see [18]), we inject both the GW and EM signals and recover them based on the detection efficiency of the GW detector and EM satellites, respectively. We define a joint detection if the signal is above the detection threshold simultaneously in both the GW and EM observatories. To properly compare the capabilities of different ET configurations and avoid differences due to the uncertainties in the EM emission, for the whole set of GW simulations we associate to each BNS population the same realization of the EM signal derived from the MCMC.

For the detection of the prompt emission, we consider the following γ-ray instruments: the Gamma-ray Burst Monitor (GBM) on board of Fermi [73], the Gravitational wave high-energy Electromagnetic Counterpart All-sky Monitor [GECAM; 74], the High Energy Rapid Modular Ensemble of Satellites [HERMES; 64], the Transient Event Detector (TED) on board of the Gamma-Ray INternational Transient Array Observatory (GRINTA), ASTROGAM [65], and the X/Gamma-ray Imaging Spectrometer (XGIS) on board of the Transient High-Energy Sky and Early Universe Surveyor [THESEUS; 63]. The properties of these instruments are summarized in table 5.

Table 6 shows the numbers of joint GW+γ-ray detections during one year of observation for the different γ-ray satellites operating in survey mode together with different ET full sensitivity configurations. These numbers go from ten to one hundred depending on the satellite and ET configurations. We highlight that, while some satellites maximize the number of de-

JCAP07(2023)068

Full (HFLF cryo) sensitivity detectors								
Instrument	Δ10	Δ15	2L 15	2L 20	Δ10	Δ15	2L 15	2L 20
Fermi-GBM	31^{+9}_{-9}	42^{+11}_{-13}	39^{+11}_{-9}	44^{+13}_{-11}	$61^{+12}_{-11}\%$	$83^{+9}_{-10}\%$	$79^{+8}_{-11}\%$	$89^{+4}_{-8}\%$
GECAM	61^{+39}_{-25}	89^{+54}_{-34}	81^{+51}_{-32}	96^{+52}_{-36}	$51^{+5}_{-6}\%$	$74^{+5}_{-5}\%$	$70^{+3}_{-6}\%$	$80^{+4}_{-4}\%$
HERMES	86^{+31}_{-28}	120^{+40}_{-31}	117^{+37}_{-34}	132^{+34}_{-34}	$55^{+9}_{-7}\%$	$78^{+8}_{-7}\%$	$74^{+9}_{-9}\%$	$85^{+5}_{-6}\%$
GRINTA-TED	77^{+31}_{-25}	107^{+31}_{-28}	98^{+31}_{-25}	114^{+34}_{-28}	$57^{+10}_{-9}\%$	$79^{+8}_{-8}\%$	$74^{+9}_{-9}\%$	$85^{+5}_{-5}\%$
ASTROGAM	18^{+8}_{-5}	24^{+9}_{-7}	24^{+9}_{-6}	27^{+8}_{-7}	$59^{+11}_{-9}\%$	$80^{+8}_{-8}\%$	$77^{+8}_{-9}\%$	$86^{+6}_{-9}\%$
THESEUS-XGIS	10^{+3}_{-3}	13^{+3}_{-3}	13^{+3}_{-3}	15^{+3}_{-4}	$57^{+9}_{-10}\%$	$79^{+8}_{-9}\%$	$73^{+11}_{-7}\%$	$85^{+7}_{-5}\%$

Table 6. Columns 2-5 give the numbers of joint GW+γ-ray detections during one year of observation for different combinations of γ-ray instruments operating in survey mode together with different ET full sensitivity configurations. The absolute numbers do not assume duty cycle for the satellites. Columns 6-9 give the fraction of detected short GRBs which will have a GW counterparts.

JCAP07(2023)068

tections (which is useful for population studies) sacrificing the localization capability, others with a smaller number of detections give the sky-localization necessary to drive the ground-based and space-borne follow-up. This is critical for identifying the host galaxy, evaluating a redshift, and completely characterising the source and its environment. An important piece of information is given in columns 6-9, where we show what is the fraction of γ-ray bursts detected by each satellite which will have an associated GW signal. Here, we find that these fractions go from $51\% - 61\%$ for the 10 km triangle, $74\% - 83\%$ for the 15 km triangle, $70\% - 79\%$ for the 2L with 15 km misaligned arms, $80\% - 89\%$ for the 2L with 20 km misaligned arms. *The ET 10 km triangle will make possible remarkable results for GRB science by detecting GW signals for a large fraction of short GRBs observed by γ-ray satellites, and it represents an impressive step forward from the LIGO, Virgo and KAGRA network, whose BNS horizon strongly limits the ability to detect events with the relativistic jet aligned with the line-of-sight (see e.g. [75, 76]). Then, the percentage of GRBs with a GW counterpart significantly increases going from the 10 km triangle to 15 km and 20 km configurations.* The 15 km triangle is marginally better than the 2L with 15 km misaligned arms. Figure 23 takes as an example HERMES (full constellation) and shows the joint detections during one year. The plot shows that the most significant improvement is from the 10 km triangle to a 15 km configuration. *The 15 and 20 km configurations are able to increase the number of joint detection at redshift larger than 0.9 with respect to the 10 km triangle.* This is particularly important to estimate cosmological parameters or to test modified gravity at cosmological scales.

Considering the GW detectors operating with only the high-frequency instrument (see table 7), we find that the percentage of detected short GRBs with an associated GW signal significantly decreases for each configuration. The percentages become $29\% - 39\%$ for the 10 km triangle, $54\% - 64\%$ for the 15 km triangle, $49\% - 60\%$ for the 2L with 15 km misaligned arms, $66\% - 76\%$ for the 2L with 20 km misaligned arms. *In terms of percentage of short GRB with a GW signal, the performance of the 15 km triangle and* 2L15km *HF-only detectors is comparable to the 10 km triangle full sensitivity.* This is also shown in the left plot of figure 24. The right plot of figure 24 shows that 2L20km HF results to be better than the 10 km triangle full sensitivity, but again going to lower frequency significantly increase the 2L20km performance making possible to detect the GW signals associated with a large fraction (85%) of short GRBs detected by HERMES.

HF sensitivity detectors

Instrument	Δ10	Δ15	2L 15	2L 20	Δ10	Δ15	2L 15	2L 20
Fermi-GBM	20^{+8}_{-7}	33^{+9}_{-9}	29^{+11}_{-9}	38^{+12}_{-10}	$39^{+11}_{-8}\%$	$64^{+12}_{-11}\%$	$60^{+12}_{-11}\%$	$76^{+9}_{-9}\%$
GECAM	35^{+21}_{-15}	62^{+38}_{-22}	58^{+38}_{-22}	77^{+47}_{-30}	$29^{+4}_{-5}\%$	$54^{+4}_{-5}\%$	$49^{+4}_{-7}\%$	$66^{+4}_{-6}\%$
HERMES	52^{+21}_{-18}	91^{+30}_{-29}	83^{+28}_{-28}	107^{+40}_{-31}	$33^{+7}_{-8}\%$	$58^{+10}_{-8}\%$	$53^{+10}_{-8}\%$	$71^{+8}_{-8}\%$
GRINTA-TED	46^{+22}_{-16}	80^{+31}_{-25}	74^{+28}_{-25}	94^{+33}_{-23}	$34^{+9}_{-9}\%$	$61^{+9}_{-11}\%$	$55^{+9}_{-10}\%$	$72^{+9}_{-9}\%$
ASTROGAM	12^{+6}_{-5}	19^{+7}_{-5}	18^{+6}_{-6}	23^{+8}_{-7}	$37^{+11}_{-10}\%$	$62^{+9}_{-11}\%$	$57^{+10}_{-9}\%$	$74^{+9}_{-10}\%$
THESEUS-XGIS	6^{+2}_{-2}	10^{+3}_{-3}	9^{+3}_{-3}	12^{+3}_{-3}	$34^{+8}_{-9}\%$	$59^{+10}_{-8}\%$	$54^{+10}_{-9}\%$	$71^{+9}_{-9}\%$

Table 7. Same as 6 but considering the GW detectors operating with only the HF interferometers.

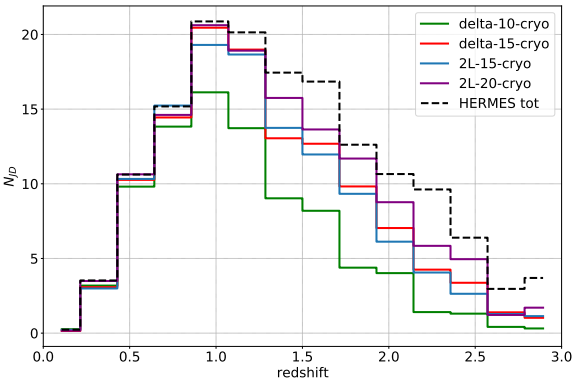

Figure 23. Histogram of the joint detection of ET and HERMES observing in survey mode during one year. The solid lines of different colors represent the different configurations of ET full sensitivity. The dashed line show the prompt emission of short γ-ray bursts expected to be detected by HERMES during one year of observations.

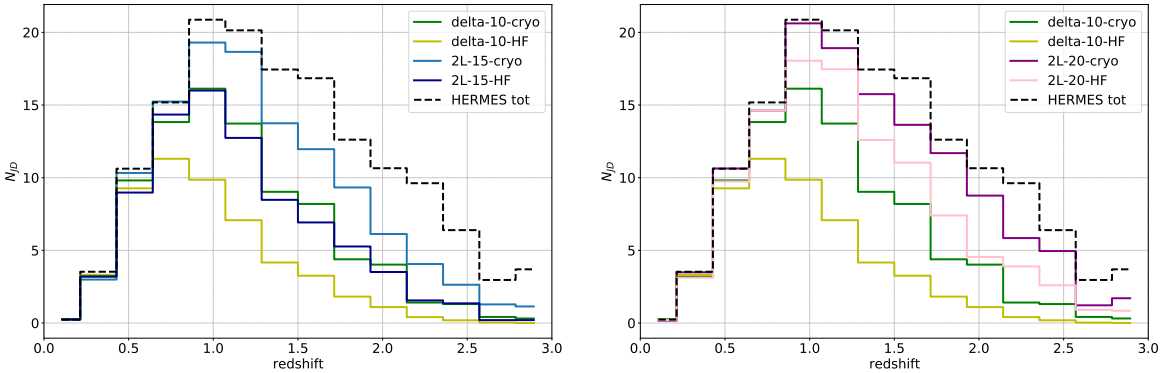

Figure 24. Histogram of the joint detection of ET and HERMES observing in survey mode during one year. The plot shows the comparison among ET full sensitivity and ET HF for Δ10km and 2L15km (left plot), and 2L20km (right plot). The dashed line show the prompt emission of short γ-ray bursts expected to be detected by HERMES during one year of observations.

4.2.2 Afterglow: survey and pointing modes

This section explores the capability of detecting X-ray short GRB afterglows associated with GWs. Using the approach described in [18], we model the afterglow taking into account both

JCAP07(2023)068

Full (HFLF cryo) sensitivity detectors

Instrument	Δ10	Δ15	2L 15	2L 20
THESEUS-SXI survey	10^{+3}_{-2}	13^{+3}_{-4}	12^{+3}_{-3}	12^{+3}_{-3}
THESEUS-(SXI+XGIS) survey	21^{+6}_{-7}	21^{+8}_{-6}	20^{+7}_{-5}	21^{+7}_{-7}

HF sensitivity detectors

Instrument	Δ10	Δ15	2L 15	2L 20
THESEUS-SXI survey	8^{+2}_{-3}	11^{+2}_{-4}	10^{+2}_{-3}	11^{+2}_{-2}
THESEUS-(SXI+XGIS) survey	16^{+6}_{-5}	19^{+8}_{-5}	19^{+4}_{-5}	21^{+8}_{-6}

Table 8. Numbers of joint GW+X-ray detections during one year of observation for THESEUS operating in survey mode considering the instrument SXI and the combination of SXI and XGIS.

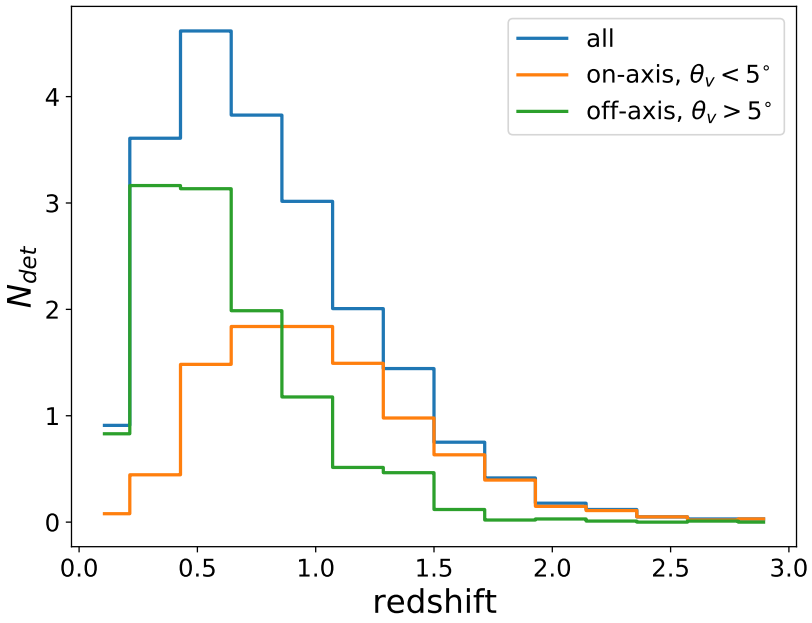

Figure 25. Redshift distribution of joint GW+EM detections with THESEUS-(SXI+XGIS) in survey mode, where we distinguish between on-axis and off-axis cases. The ET configuration considered here is 2L 20 km HFLF cryo.

the forward shock and the high-latitude emission [77, 78] and we evaluate the joint GW/X-ray detections by considering two observational strategies; the satellite observing in survey mode or the satellite slewing to point well-localized events. As an example of performance of X-ray wide FoV satellites, we consider the Soft X-ray Imager (SXI) planned to be on board the THESEUS mission [63]. SXI is a wide field of view instrument able to cover 0.5 steradians in one observation. It has a localization accuracy of 1-2 arcmin. Since also XGIS has good sensitivity down to 2 keV in a larger FoV of 2 steradians, We also consider the combination of SXI and XGIS.

Tables 8 show the numbers of X-ray afterglow detected in survey mode by SXI and the combination of SXI and XGIS on board of THESEUS which will have an associated GW sig-

JCAP07(2023)068

Instrument	Δ10 cryo	2L 20 km cryo	Δ10 HF	2L 20 km HF
THESEUS-SXI pointing	6^{+4}_{-4}	11^{+6}_{-5}	1^{+2}_{-1}	7^{+4}_{-4}

Table 9. Numbers of joint GW+X-ray detections during one year of observation for THESEUS-SXI operating in pointing mode. Only BNS localised better than 100 deg^2 are followed-up.

nal. While the top table shows the joint detection with the ET full sensitivity configurations, the bottom table shows the ones with ET HF. The number of joint detections is around 10 for SXI (20 for SXI+XGIS) per year independently of the arms lengths and the geometries, and the number remains almost the same also without accessing low-frequencies. Figure 25 shows a histogram of the joint GW+afterglow detections by THESEUS-(SXI+XGIS) in survey mode operating with full sensitivity 2L with 20 km misaligned arms as a function of redshift. The figure shows that the majority of the joint detections are within $z = 1$. This explains the reason why *both arm-length and accessible frequency do not change the joint GW/X-ray afterglow detection numbers;* the majority of the afterglows are detectable up to a redshift where there is no significant difference among the GW detection efficiency. The figure also shows that detecting the X-ray afterglow enables to observe events with a jet not aligned to the line of sight.

For the pointing strategy, we select events with a sky-localization uncertainty smaller than 100 deg^2, which is well-contained inside the SXI FoV, and we assume that SXI is able to be on target 100 s after the merger. This is a very optimistic scenario because 100 s should include the time to transmit the alert, respond to the trigger and re-point the instrument to the source position. Table 9 shows that a few detections are possible and going from the 10 km triangle to the full sensitivity 2L 20 km increases of a factor of about 2 the detections. As described in [18], there are two possible issues for the pointing strategy; being extremely fast to point to the source, and prioritising the events to be followed. No X-ray detection is possible being on source 1 hr after the merger with respect to 100 s because the X-ray afterglow emission is decaying fast. To detect a few events (see table 9) one needs to optimize the event selection among hundreds of events (see table 1) to be followed-up, to avoid to loose observational time. Selecting the sources localized better than 1000 deg^2, the number of joint GW+X-ray detections increases by a factor of 10 but the selection of the event to be followed becomes more complicated. As shown in table 1 the number of sources detected with sky-localization 1000 deg^2 are thousands. Also prioritizing the events on the basis of the viewing angle by excluding all the sources edge-on (for which the viewing angle estimate is more precise), the number of events to be followed up remains to be around several hundreds (for the 10 km triangle) to thausands (for the 2L 20 km). While the 10 km triangle gives fewer joint detections with respect to 2L 20 km full sensitivity, the trigger selection is easier because it is among a smaller number of events. The HF-only 2L with 20 km misaligned arms gives a number of joint detection comparable to the 10 km triangle.

In summary, for the detection of the X-ray afterglow emission associated with the GW BNS signals there are no significant differences for the different configurations of ET.

4.3 Kilonovae: joint GW and optical detections

This section explores the perspectives for the detection of KNe. The KN emission is not beamed as GRBs and is expected from all viewing angles. We consider as reference observatory, the Vera Rubin Observatory (VRO). VRO is the innovative 8.4-meter telescope

JCAP07(2023)068

Full (HFLF cryo) sensitivity detectors

Configuration	$N_{GW,VRO}$ $\Omega < 20\,deg^2$	VRO time	$N_{GW,VRO}$ $\Omega < 40\,deg^2$	VRO time	$N_{GW,VRO}$ $\Omega < 100\,deg^2$	VRO time
Δ10	14 (14)	1.1% (3.3%)	36 (39)	5.1% (15%)	96	40%
Δ15	38 (42)	3.3% (9.8%)	84 (101)	14.2% (42%)	163	>100%
2L 15	28 (28)	2.2% (6.5%)	62 (77)	10.6% (31%)	189	93%
2L 20	55 (64)	5% (14.9%)	115 (152)	23.1% (68%)	324	>100%

Table 10. Numbers of expected kilonovae detected by the VRO selecting the sources detected by the different configurations of ET with sky localization smaller than 20 deg^2 (column 2), 40 deg^2 (column 4) and 100 deg^2 (column 6). Columns 3, 5, and 7 give the percentage of the VRO time necessary to follow up all the sources with sky-localization smaller than the above thresholds and within the VRO visibility sky area. The observational time for each event is obtained considering 600 s for each pointing and a number of the pointing corresponding to the ratio between the sky-localization uncertainty and the VRO FoV plus one pointing to be more conservative. We consider observations in two filter (g and i) the first night after the merger and the two filter observations repeated during the second night after the merger. We add 60 s to take into account filter change, slew time and overheads each night. The percentage of VRO time is evaluated assuming 2600 hours as the total amount of observational time of the VRO in one year. The expected number of detected kilonovae and percentage of VRO time considering 1800 s for each pointing (instead of 600 s) are given in parentheses. For the 100 deg^2 threshold, assuming for each pointing of 1800 s entails that the number of hours requested to cover the entire sky-localization is larger than the ones available in one observing night. This makes our observational strategy unfeasible, and thus we exclude this case. It is also shown that to follow all events with sky-localization < 100 deg^2, the required observational time becomes prohibitively large and for Δ15 and 2L 20 larger than the entire VRO observational time.

HF sensitivity detectors

Configuration	$N_{GW,VRO}$ $\Omega < 20\,deg^2$	VRO time	$N_{GW,VRO}$ $\Omega < 40\,deg^2$	VRO time	$N_{GW,VRO}$ $\Omega < 100\,deg^2$	VRO time
Δ10	0 (0)	0% (0%)	2 (2)	0.3% (0.8%)	4	2%
Δ15	2 (2)	0.2% (0.5%)	3 (4)	0.7% (1.9%)	8	7.5%
2L 15	3 (4)	0.4% (1.2%)	7 (7)	1.3% (3.9%)	26	11%
2L 20	5 (4)	0.6% (1.6%)	15 (18)	3.1% (9.3%)	32	20.8%

Table 11. Same as 10 but for ET detectors without the low-frequency.

characterized by a wide field (9.6 deg^2) camera containing over three billion pixels of solid-state detectors [58]. Its compact shape enables to point and slew through large sky-region extremely fast. It represents the ideal instrument to observe the GW sky localizations obtaining deep observations of extremely high quality. In order to evaluate the number of possible joint optical/GW detections, we model the kilonova emission as in [79] taking the best-fit parameters obtained to reproduce the multi-filter optical observations of the kilonova AT2017gfo associated with GW170817. Our model includes cosmological and k-correction. We select all the BNS mergers detected with a sky-localization smaller than a threshold and we associate to each of them a GW17087-like kilonova taking into account the source distance and the viewing angle (our modeling starting from GW170817 reproduces the angular dependence of the expected emission). We assume three threshold on the sky-localization by selecting all the events with sky-localization $< 20\mathrm{deg}^2, < 40\mathrm{deg}^2,$ and $< 100\mathrm{deg}^2$. We

JCAP07(2023)068

consider a Target of Opportunity strategy similar to the ones described in [80–82]; we use observations in two filters (g and i) the first night after the merger and we repeat the two filter observations during the second night after the merger. We consider a detection when the kilonova emission is detected at 5σ the first and second night in both filters. Having observations in at least two filters is important to reduce the number of contaminating transients and identify the kilonova associated with the GW signal on the basis of the color evolution. The problem of contaminating transients is solved in real observations also using spectroscopy able to characterize the source, but here for the configurations comparison, this is not taken into account. Our counts take into account the visibility of the VRO.

Figure 26 shows the light-curves for GW170817-like signals associated with our population of BNSs detected with a sky-localization smaller than 40deg^2 by the full (HFLF cryo) sensitivity configurations and by the HF sensitivity configurations. The plots show the different numbers of events selected to be followed up for the different configurations. It is immediately clear the significant increase in the number of targets to be followed going from configurations with only high-frequency to the full sensitivity configurations.

Table 10 gives the number of expected kilonovae by following up all the events within the VRO visibility sky-area and with a sky-localization uncertainty smaller than 20 deg^2, 40 deg^2 and 100 deg^2, and the corresponding percentage of VRO time necessary for the follow-up. Enlarging the threshold on the sky-localization significantly increases the number of events to be followed-up and thus the number of joint detections but at the expense of more observational time. Also increasing the exposure from 600 s to 1800 s for each pointing tends to increase the number of detections but the percentage of time to be used becomes prohibitive. Looking at the full sensitivity detectors, *the 2L with 20 km misaligned arms is the best performing in detecting kilonovae. It enables to detect between several tens and a few hundred kilonova counterparts per year. The 15 km triangle is slightly better than the 2L with 15 km misaligned arms giving a number of detection about 30% larger.*[17] *The 15 km triangle is significantly better than the 10 km triangle giving about a factor 2 larger number of detections.*

The presence of low-frequency is critical for ET operating as single observatory to detect a large number of kilonovae counterparts. Table 11 shows the small number (a few) of detections per year expected with the triangle-HF configurations. This number increases to a few tens for the 2L-HF configurations.

We highlight that the absolute number per year of VRO detections is affected by the error on the BNS local rate normalization. The astrophysical rates inferred from the observations of the first, second and third run of observations of LIGO and Virgo give a BNS merger rate in the range 10 to 1700 Gpc^{-3}yr^{-1} [7]. Since our population corresponds to a local rate $R_0 \simeq 250\,\mathrm{Gpc}^{-3}\,\mathrm{yr}^{-1}$, the actual numbers could be up to one order of magnitude smaller or larger than the ones given in the tables.

[17] The scenario of following up all the events with sky-localization < 100 deg^2 case is not considered because the required observational time of VRO is prohibitive.

JCAP07(2023)068

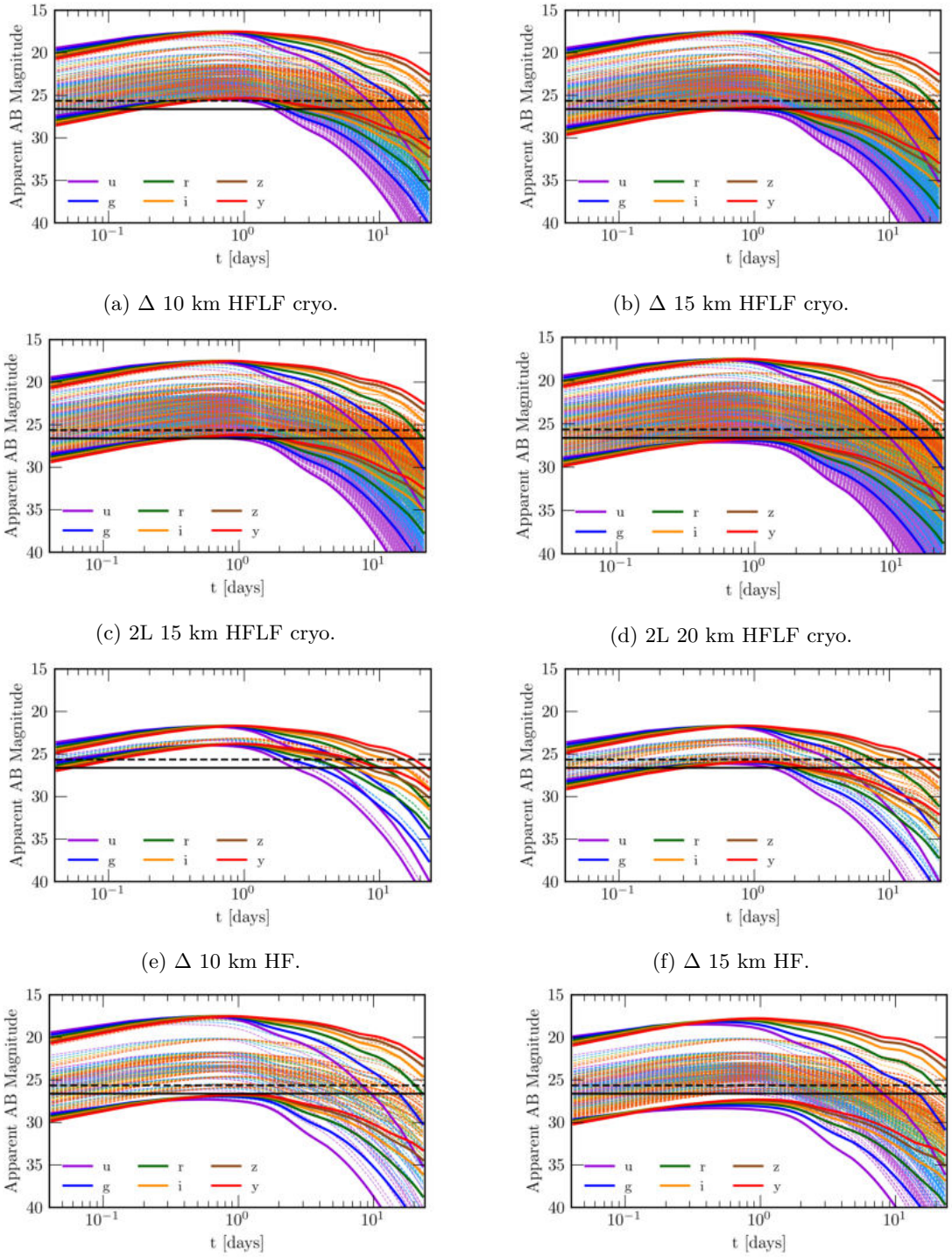

(a) Δ 10 km HFLF cryo.

(b) Δ 15 km HFLF cryo.

(c) 2L 15 km HFLF cryo.

(d) 2L 20 km HFLF cryo.

(e) Δ 10 km HF.

(f) Δ 15 km HF.

(g) 2L 15 km HF.

(h) 2L 20 km HF.

Figure 26. Light-curves for GW170817-like signals associated with BNS detected with a sky-localization smaller than 40 deg^2 by each of the full (HFLF cryo) sensitivity configurations (four top plot) and by each of the HF sensitivity configurations (four bottom plot). The black lines mark the (5σ point-source depth) limiting magnitudes corresponding to 600 s of exposure for each pointing in the g band (solid black line) and the i band (dashed black line).

JCAP07(2023)068

5 Stochastic backgrounds

The stochastic GW background (SGWB) is formed by the incoherent superposition of signals emitted by different GW sources in our Universe, primordial or astrophysical, at different redshifts, that we collect at our detector. Traditionally, we distinguish between an astrophysical GW background (AGWB) and a background of cosmological origin (CGWB). The latter are tensor modes produced by different processes in the early universe such as inflation, reheating, phase transitions, cosmic strings, or primordial black holes (see [83–85] for reviews). If detected, it would provide us with direct information about the very first instants of time of the evolution of our Universe. On the other hand, the AGWB is made of the superposition of all GWs emitted by different populations of astrophysical sources, from the onset of stellar activity until the present epoch. The CGWB and the AGWB are the gravitational counterparts of the Cosmic Microwave Background (CMB) [86] and of the Cosmic Infrared background (CIB) [87] in the electromagnetic context: in the same way as the CIB is a foreground for the CMB, which needs to be properly characterised and subtracted to access the CMB and its cosmological content, astrophysical backgrounds of gravitational waves represent foregrounds for primordial backgrounds of gravitational radiation. Typically it is expected that different GW sources are characterized by a different frequency profile, that can be used as a tool to disentangle them [88, 89]. As recalled in appendix A, a stochastic background is characterized by the quantity

$$\Omega_{\rm gw}(\hat{\mathbf{n}}, f) \equiv \frac{1}{\rho_c} \frac{d\rho_{\rm gw}(\hat{\mathbf{n}}, f)}{d\ln f d^2\hat{\mathbf{n}}}\,, \tag{5.1}$$

where $d\rho_{\rm gw}(\hat{\mathbf{n}}, f)/d\ln f d^2\hat{\mathbf{n}}$ is the energy density per unit logarithmic frequency and unit solid angle that reaches the observer from the direction $\hat{\mathbf{n}}$ and with frequency f, see eqs.(A.2)–(A.4). The isotropic (normalized) energy density is defined by

$$\Omega_{\rm gw}(f) \equiv \int d^2\hat{\mathbf{n}}\, \Omega_{\rm gw}(\hat{\mathbf{n}}, f)\,, \tag{5.2}$$

and gives the (normalized) energy density of the stochastic background reaching the observer from all directions. It is commonly assumed that it is possible to factorize the dependence on the frequency and that on the direction, i.e.

$$\Omega_{\rm gw}(\hat{\mathbf{n}}, f) = \mathcal{E}(f)\mathcal{P}(\hat{\mathbf{n}})\,. \tag{5.3}$$

Furthermore, for many cosmological backgrounds (but not, for instance, for the backgrounds generated by cosmological phase transitions) the scale of variation with frequency is such that, over the bandwidth of a ground-based or a space-borne GW detector, the frequency dependence can be approximated by a simple power-law $\mathcal{E}(f) = A_\beta\,(f/f_{\rm ref})^\beta$, where A_β is the amplitude at an arbitrarily chosen reference frequency $f_{\rm ref}$.

In the presence of statistical isotropy, the statistical properties of the background energy density can be characterised in terms of a frequency-dependent angular power spectrum as

$$\langle \Omega_{\rm gw}(\hat{\mathbf{n}}, f)\Omega_{\rm gw}(\hat{\mathbf{n}}', f)\rangle = \sum_\ell C_\ell(f) P_\ell(\hat{\mathbf{n}}\cdot\hat{\mathbf{n}}')\,, \tag{5.4}$$

where $P_\ell(\hat{\mathbf{n}}\cdot\hat{\mathbf{n}}')$ are Legendre polynomials, functions of the angular separation between the two directions $\hat{\mathbf{n}}$ and $\hat{\mathbf{n}}'$. The angular power spectrum and the frequency spectrum $\mathcal{E}(f)$

JCAP07(2023)068

encode most of the statistical properties of a given background component. Recently, it has been shown that, similarly to CMB photons, primordial GWs are also affected by large-scale anisotropies (i.e., Sachs-Wolfe and Integrated Sachs-Wolfe effects) [90–93]. Typical CGWB components are expected to have the same level of anisotropy as the CMB: a scale-invariant spectrum $\ell(\ell+1)C_\ell \propto$ constant, and a level of anisotropy of the order of $\sim 10^{-5}$ with respect to the monopole [91]. In contrast, extra-galactic AGWBs have a scaling given by clustering, resulting in $(\ell+1)C_\ell \propto$ constant, and a higher level of anisotropy, at the level of $\sim 10^{-2}$ with respect to the monopole [94–108] (see [109] for a recent public code to compute the anisotropies of the AGWB). Interestingly, both the CGWB and the AGWB anisotropies show a correlation with CMB anisotropies which can be used both as a source discriminator and for testing systematics [110–112].

While the production of tensor modes from the early universe can typically be described in terms of a continuous emission, varying on a time scale extremely small with respect to typical observation time-scales,[18] the AGWB in the frequency band of ET is expected to have a so-called *popcorn-like nature*, due to the discreteness of emissions in time. Indeed, in the Hz band, we expect the AGWB to be dominated by mergers of compact objects and, considering the short duration of the merger phase, events are expected to be separated in time and with a limited time overlap (some overlap is expected for BNS mergers). As a consequence, in the frequency band of ET, the angular power spectrum of the AGWB from mergers of compact binaries has an important popcorn component (due to the discrete emission in time), which adds to the clustering one (due to the discreteness of the spatial galaxy distributions) [97, 103, 104, 108]. Formally, the total angular power spectrum is given by $C_\ell^{\rm AGWB,tot} = C_\ell + N^{\rm pop}$, where the first term on the right-hand side is the contribution from clustering while the second component represents popcorn noise. The latter is flat in ℓ-space (it is just an offset) and it is expected to cover the clustering contribution, see [97, 103, 104, 108]. Even if popcorn noise contains astrophysical information, it does not provide any information about the spatial distribution of sources. A possible way to overcome this problem, i.e. to extract the clustering part out of the popcorn noise threshold, is to consider cross-correlations between an SGWB map and galaxy distributions, see e.g. [108]. The study of cross-correlations, besides being an independent observable interesting on its own, provides one with a powerful detection tool, as it typically has a higher SNR than the auto-correlation, see e.g. [96–98, 108, 113] in the context of the extra-galactic astrophysical background.

Finally, kinematic anisotropies induced by a peculiar motion of the observer with respect to the rest frame of emission are expected to be quite important and potentially detectable if the corresponding monopole has a sufficiently high SNR, see e.g. [114]. Recent studies to extract the cosmic dipole using next-generation detectors have been developed both for the AGWB [114, 115] and for resolved sources [116].

We conclude this section with a remark. Because of the discrete emission in time, the AGWB in the Hz band is not irreducible: with a perfect instrument with infinite sensitivity (and with infinite computational power), all events would be detectable individually. As the sensitivity of next-generation ground-based detectors will improve more and more events will be detectable individually: in this context, it is interesting to study the so-called *residual background*, i.e. the background contribution that remains after having filtered out resolvable objects. This observable can indeed provide us with a unique way of extracting information

[18] For this reason most of the CGWB components represent continuous and stationary background components and they are often referred to as *irreducible* backgrounds.

JCAP07(2023)068

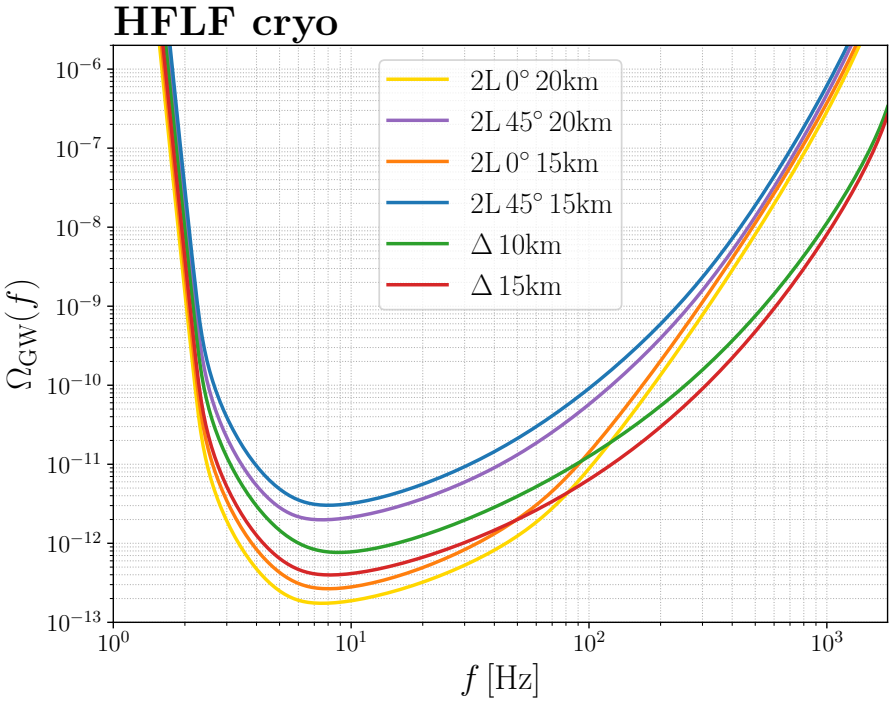

Figure 27. Power-law integrated sensitivity (PLS) to $\Omega_{\rm GW}(f)$ for different ET geometries, in the full HFLF-cryo configuration. We set $\mathrm{SNR}_{th} = 1$ and $T_{\rm obs} = 1$yr and we include only cross-correlations between detectors, excluding auto-correlations.

on a faint and distant population, that cannot be detected with a catalogue approach. We will get back to this point later in this section.

5.1 Sensitivity to isotropic stochastic backgrounds

We now study the sensitivity, in different configurations, to a SGWB. To this goal, we compute the Power-Law integrated Sensitivity curve (PLS), whose definition is recalled in appendix A, for the triangular and L-shaped detectors, in the configurations discussed in section 2, so for the triangular configuration we consider 10 and 15-km arm, while for the L-shaped we consider 4 configurations: 15 km and 20 km arms, aligned and misaligned (by 45 deg) detectors located one in Sardinia and one in the Netherlands. We then turn to the angular sensitivity for the same ET configurations, i.e. we present how well the various configurations can reconstruct the $C_\ell(f)$ (i.e., the angular power spectrum), defined in eq. (5.4).

The result is shown in figure 27 for the different geometries in the full HFLF-cryo configuration, and in figure 28 for the HF-only configuration.[19]

[19]Recall from section 2 that, for the 2L cases, the alignment between the two detectors has been defined using the relative angle α measured with respect to the north of the Sardinia site for both detectors, rather than with respect to the great circle passing through the two sites. Therefore the $\alpha = 0°$ and the $\alpha = 45°$ cases shown in the figures below do not correspond to the ideal and, respectively, the worst configurations for stochastic searches, but have slight offsets from it. In terms of the angle α, the ideally parallel and the perfectly misaligned for the configurations correspond to $\alpha = 2.51°$ and $\alpha = 47.51°$, respectively. This is particularly important for the misaligned case. Indeed, $\alpha = 47.51°$ would correspond to essentially zero sensitivity to stochastic backgrounds, while we see from figure 27 that, for $\alpha = 45°$, we already have an interesting sensitivity to stochastic backgrounds, so a small offset from the perfectly misaligned configuration is already very useful for recovering a part of the sensitivity to stochastic searches (without basically affecting the searches for compact binary coalescences, as discussed in section 2). See appendix B for more details.

JCAP07(2023)068

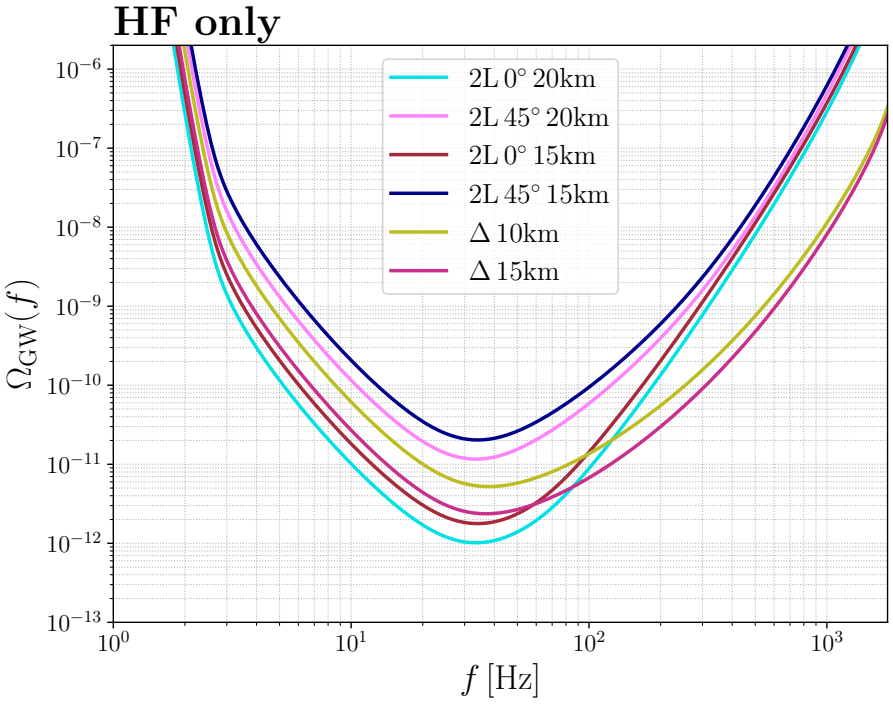

Figure 28. As in figure 27, for the HF-only configurations.

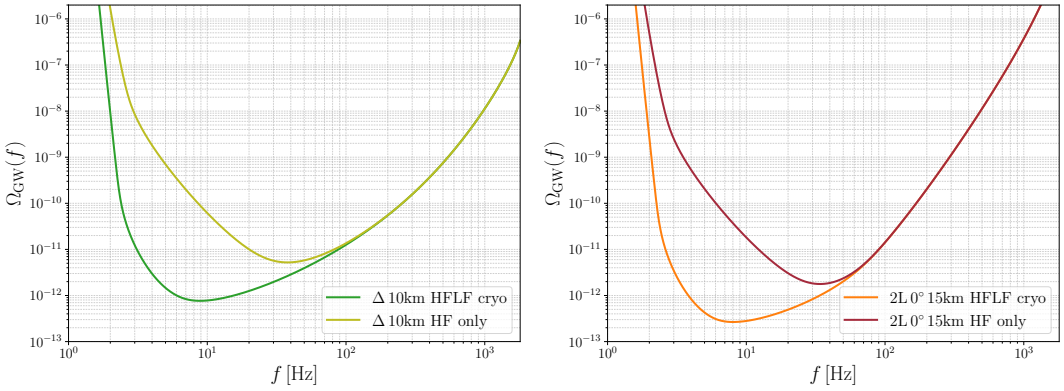

Figure 29. Left: ET power-law integrated sensitivity for the triangle configuration for the full HFLF-cryo configuration and the HF-only configuration, assuming $\mathrm{SNR}_{th} = 1$ and $T_{\rm obs} = 1$yr and including only cross-correlations between detectors. Right: the same for the 2L-15km-0° configuration.

We observe that the triangular configurations perform better at high frequency since the overlap reduction function remains constant at high frequencies for co-located detectors rather than falling to zero. The 2L configurations do better at low frequencies, up to several tens of Hz, but only for co-aligned detectors (since this maximises the coherence for the stochastic search). The case of 45 deg 2L configurations are universally the worst.

JCAP07(2023)068

Figure 29 compares the power-law sensitivities obtained from the HFLF-cryo and the HF-only ASDs for the 2L 15km with parallel arms (left panel) and for the 10 km triangle (right). Since $\Omega_{\rm gw}(f)$ is quadratic in the strain, the loss of the low-frequency sensitivity has a huge impact on the sensitivity to stochastic backgrounds at low frequencies. For instance, for the 2L 15km with parallel arms, the HF-only configuration is worse than the HFLF-cryo by a factor $\sim 10^2$ at 10 Hz, and $\sim 10^3$ at 3 Hz. In contrast, the sensitivity above about 60 Hz is unaffected.

5.2 Angular sensitivity

In this section we study the angular resolution of different ET configurations in the context of an SGWB. We follow the formalism in [117], whom we refer the reader for details and derivations (see also [118, 119] for recent forecasts about the ET sensitivity to angular anisotropies). The sensitivity with which we can measure a given multipole of the background intensity is characterized by a quantity, N_ℓ, such that the signal-to-noise ratio of an angular power spectrum is given by

$$\mathrm{SNR}^2 \equiv \sum_\ell (2\ell+1)\frac{C_\ell}{N_\ell}\,, \tag{5.5}$$

where the C_ℓ have been defined in eq. (5.4). The N_ℓ can be computed from

$$N_\ell^{-1} \equiv \frac{1}{2}\sum_{ABCD}\int df \int dt\, G_\ell^{AB,CD}(t,f)\,, \tag{5.6}$$

where

$$G_\ell^{AB,CD}(t,f) \equiv \left(\frac{2\mathcal{E}(f)}{5}\right)^2 \left(\mathsf{N}_f^{-1}\right)^{AB}\left(\mathsf{N}_f^{-1}\right)^{CD} \frac{\sum_m \mathrm{Re}\left(\mathcal{A}_{BC,\ell m}(t,f)\mathcal{A}^*_{DA,\ell m}(t,f)\right)}{2\ell+1}\,, \tag{5.7}$$

and

$$\mathcal{A}_{AB,\ell m}(t,f) \equiv \int d^2\hat{\mathbf{n}}\, Y^*_{\ell m}(\hat{\mathbf{n}})\,\mathcal{A}_{AB}(t,f,\hat{\mathbf{n}})\,, \tag{5.8}$$

is the angular multipole of the antenna pattern; we explicitly indicated its time dependence. These expressions allow one to predict the angular power spectrum of a given experiment and scan strategy. A key assumption made in obtaining this result is that the time-integrated response of the instrument can be compressed into an angular power spectrum. In practice, this will not be the case, since the scan strategy cannot be designed to average the noise over the m-modes and the resulting estimator will be sub-optimal. This is a necessary assumption for any analytical estimate; however, in practice, optimal estimators will have to account for inhomogeneous noise in m-modes.

Eq. (5.6) involves a two-dimensional integral over t and f, where the integrand involves at least one computationally expensive spherical harmonic transform of the antenna pattern $\mathcal{A}$. This can be simplified further for experiments with a constant configuration (e.g. constant arm lengths, angular separations between arms, relative detector positions). As explained in [117], in this limit the network changes as a function of time as a rotating solid. Hence the antenna patterns at different times are related to each other through simple three-dimensional rotations (i.e. $\mathcal{A}(t,f,\hat{\mathbf{n}}) = \mathcal{A}(f,\mathsf{R}_t\hat{\mathbf{n}})$, where R_t is a time-dependent rotation matrix). Recalling that a rotation only mixes the m-modes for each fixed ℓ in $\mathcal{A}_{\ell m}$,

JCAP07(2023)068

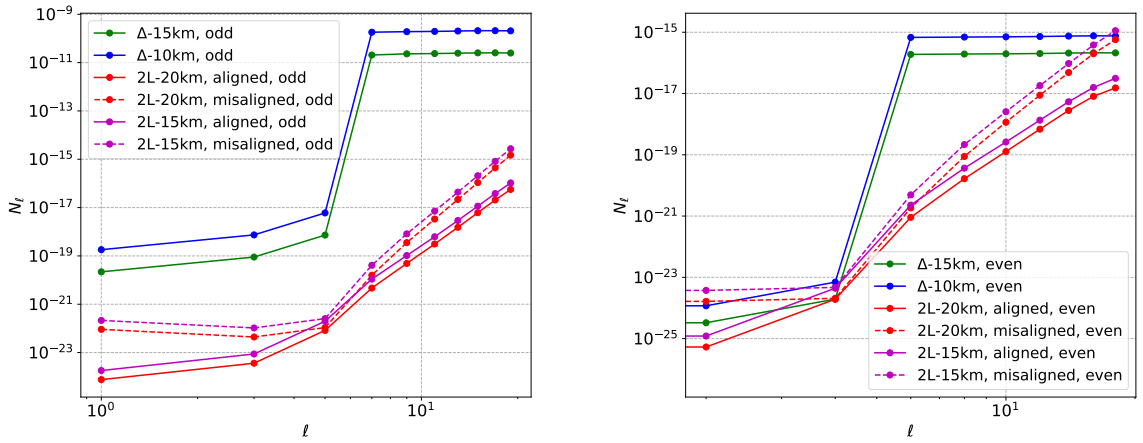

Figure 30. Noise per angular multipole at a reference frequency of 100 Hz for the four configurations under study. In the left and right panel we show the sensitivity to odd and even multipoles, respectively. All figures are obtained using the `schNell` package https://github.com/damonge/schNell.

the function G_ℓ in (5.7) does not depend on t (assuming detector noise to be stationary). In this case one gets the compact expression

$$N_\ell^{-1} = \frac{T_{\rm obs}}{2} \sum_{ABCD} \int df\, G_\ell^{AB,CD}(f)\,, \tag{5.9}$$

where $T_{\rm obs}$ is the total observing time.

In figure 30 we plot the noise per multipole N_ℓ at a reference frequency $f_{\rm ref} = 100$ Hz for different detector configurations. *When looking at odd multipoles, we see that the 2L configurations are much more sensitive than triangular configurations.* This is due to the fact that the three nested interferometers composing a triangular detector are separated by a baseline whose size is one arm length, while the two L-shaped detectors of the network have a much larger baseline. As a consequence, the antenna pattern function of triangular configuration is almost completely even under parity, hence the instrument has a very bad sensitivity to odd multipoles, see [117]. Furthermore, as expected, aligned detectors have better sensitivity than misaligned detectors. *We observe that, with the most favourable configurations, i.e.* 2L *aligned with 15km or 20 km length, we are potentially able to detect a dipole anisotropy at the level of* $\sim 10^{-12}$ *(hence* $N_{\ell=1} \sim 10^{-24}$*), which is the size of the kinematic dipole expected from a background component on the edge of being detected by LVC at O5 sensitivity*, see also [114].[20]

5.3 Astrophysical backgrounds

Binary mergers nowadays detected by LIGO-Virgo-KAGRA are only the tip of the iceberg. In fact, a large fraction of the events at larger distances are not resolved by the detectors and are expected to constitute the dominating contribution of the astrophysical background. For compact binary coalescences (CBCs), eq. (5.1) can be rewritten in term of energy density flux as [120]

$$\Omega_{\rm gw}(f) = \frac{1}{c\rho_c} f\mathcal{F}(f), \tag{5.10}$$

[20] We observe that the plateau at high-ℓ values is symptomatic of the fact that we have lost sensitivity to those multipoles, see [117].

JCAP07(2023)068

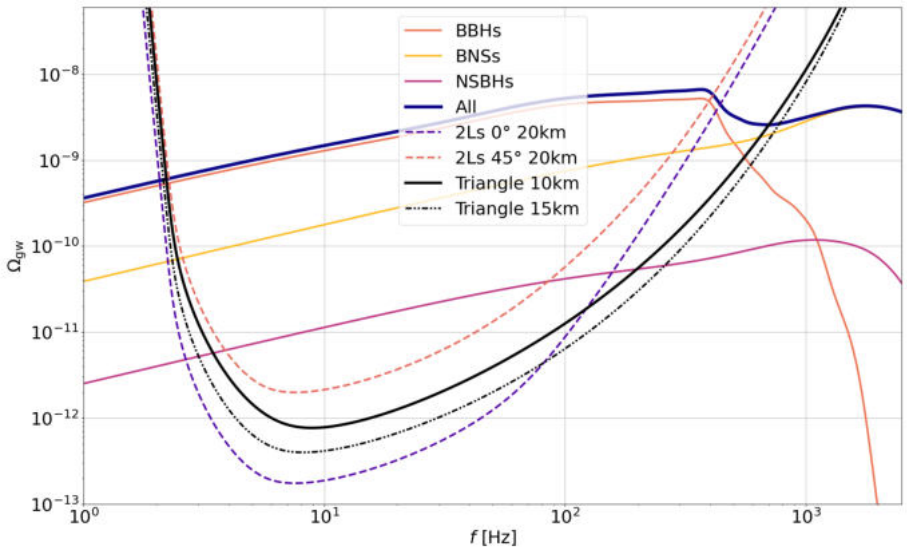

Figure 31. Background prediction for the current state-of-the-art astrophysical models, assuming a metallicity spread $\sigma_Z = 0.3$.

where $\mathcal{F}(f)$ is defined as

$$\mathcal{F}(f) = T^{-1} \sum_{k=1}^{N} \frac{1}{4\pi r^2} \frac{dE_{\rm gw}^k}{df}(f)\,, \tag{5.11}$$

and the sum is over the N individual merger contributions arriving on the detector during an observation time T. Rewriting the energy density, one can express the spectrum $\Omega_{\rm gw}(f)$ in terms of frequency domain waveforms:

$$\Omega_{\rm gw}(f) = \frac{\pi\, c^2}{2\, G\, \rho_c} f\, T^{-1} \sum_{k=1}^{N} f^2\, \tilde{h}_k^2(f), \tag{5.12}$$

with $\tilde{h}_k^2(f)$ the sum of the squared Fourier domain GW amplitudes for the two polarization $+/\times$:

$$\tilde{h}_k^2(f) = \tilde{h}_{+,k}^2(f) + \tilde{h}_{\times,k}^2(f). \tag{5.13}$$

Figure 31 shows predictions for the background, derived from the current state-of-the-art of population synthesis models [43, 44, 47, 48, 50, 52, 54] with a metallicity spread $\sigma_Z = 0.3$ for the three types of binary: binary neutron stars (BNSs), binary black holes (BBHs), and neutrons star-black hole systems (NSBHs). The BNS and BBH population are the ones described in section 3 and used through this paper to evaluate general metrics and several specific science cases. On these plots are also shown the PLS for the main configurations of this study, already shown in figure 27.[21] The low-frequency part of the spectrum is predicted to have an evolution proportional to $f^{2/3}$, typical for the inspiral phase of compact objects binaries. This shape is common to all CBCs, therefore a sign of a specific population on the background is given by deviations from the $f^{2/3}$ behavior. For example, in figure 31 the deviation of the total background ('All', dark blue curve) from the $f^{2/3}$ shape between

[21] Here, and in figure 32, the PLS are computed including only cross-correlation between detectors, and setting $\mathrm{SNR}_{th} = 1$ and $T_{\rm obs} = 1$ yr, as in the plots of section 5.1.

JCAP07(2023)068

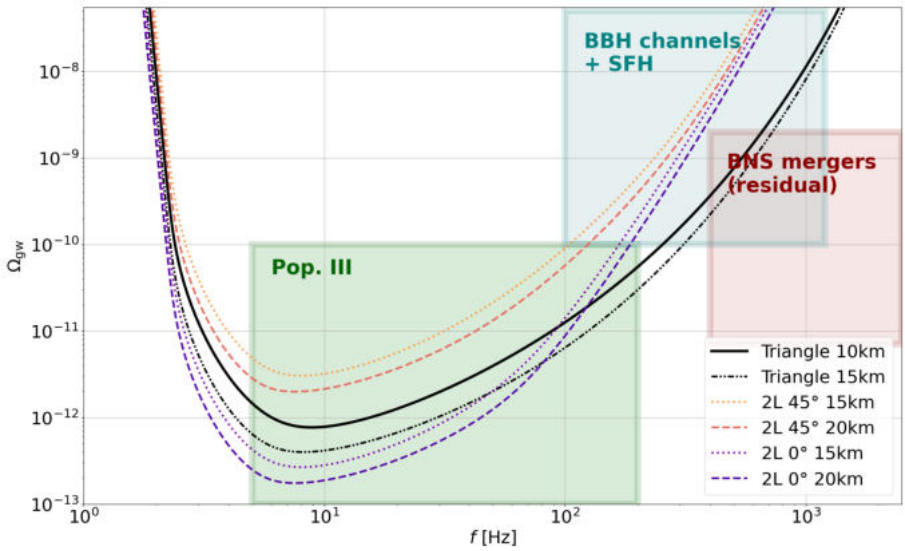

Figure 32. Location of the predicted signatures for the three main challenges for the CBC background.

90-500Hz is due to the inclusion of BBHs from the cluster, while the deviation above 1000Hz is coming from the BNSs. Consequently, the background will be a new observation channel for population studies of compact objects.

Stellar CBC background challenges in ET can be divided into three main categories: the search of Population III stars, the study of BBH formation channels combined with the star formation history (SFH), and the residual BNSs background. All these categories are represented on figure 32 at the location of predicted background signatures, together with the ET PLS for the different geometries considered (all taken with their best ASD, see section 2).

BBHs channels + SFH. This part of the spectrum is where (depending on their masses and spins) individual BBHs stop emitting gravitational waves, so that the overall spectrum drops. Two main factors can imprint some signature in the range [100-1200] Hz: (1) the SFH, which is a combination of metallicity/redshift, and star formation rate/redshift relations; and (2) the formation and evolution channel of the binary (i.e. the environment of the binary formation/evolution). The detection of these signatures will be a new channel of observation for the stellar formation and evolution [121, 122]. *For this specific signature the triangle configuration is preferable to any of the four* 2L *configurations that we have considered (15 or 20 km arm-length, aligned or at* 45°*), because its sensitivity to stochastic backgrounds will be better for frequencies above 200 Hz.*

Population III. Population III stars are the first, metal-free stars that formed in the Universe [123]. The peak of the merger rate density of compact remnants left by Population III stars is expected to be at high redshift, $z \sim 8 - 16$ [124–128]. All of the unresolved population III merger events then combine to an SGWB in the $[5 - 200]$ Hz frequency range that may deviate from the usual $f^{2/3}$ power-law behaviour [129–133]. This is due to the fact that, while population I/II stars produce an SGWB in the LIGO/Virgo frequency band during their inspiral phase, population III stars would instead show up at the merger and ringdown phases. *In the frequency range where population III stars could leave their imprint, the* 2L *configurations with parallel arms are the best ones.*

JCAP07(2023)068

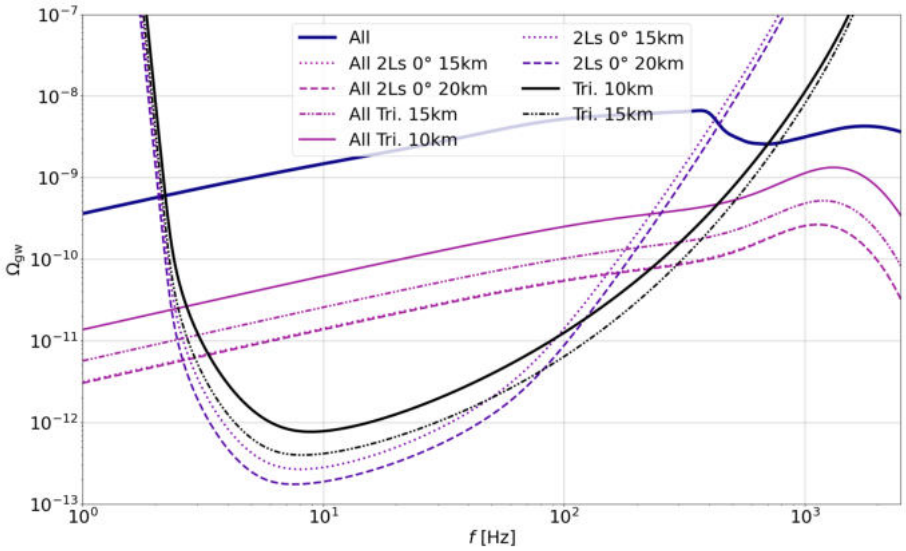

Figure 33. Backgrounds from all types of binaries (BBHs+BNSs+NSBHs), compared to the sensitivity of various detector configurations. The blue thick line corresponds to the total background, while the violet ones to the residuals (i.e. the background obtained after the subtraction of resolved sources) for the different configurations.

BNS residual mergers. The background, as it is defined, contains only non-resolved gravitational waves. In that sense, the residual background (background obtained after subtraction of all resolved sources[22]) will reveal the BNSs contributions to the background. Figure 33 shows the residual backgrounds for each type of binary and some of the configurations. As for BNSs, they are more difficult to be resolved due to their low masses, and their gravitational waves will mostly remain in the background and dominate it [121, 129].

5.4 Impact of correlated magnetic, seismic and Newtonian noise

Since searches for a stochastic gravitational-wave background (SGWB) [134] typically rely on cross-correlating data from two or more detectors, they are also susceptible to correlated noise. In this section we will discuss the impact of different noise sources on the ET and how they affect the different configurations, that is triangular versus 2L configuration. In section 5.4.1 we will discuss the effect of correlations in the seismic and accompanying Newtonian noise (NN), whereas section 5.4.2 focuses on correlations in magnetic field fluctuations.

In the following sections, we have used the ET-D design sensitivity in a triangular design with arm lengths of 10 km. However, the discussion depends minimally on this assumption and is a good representation for the comparison of the triangular versus 2L configurations regardless of the exact arm length and sensitivity.

At the end of the section, in table 12 the frequency regions of searches for an SGWB affected by correlated noise are summarized. We want to point out that here we only discuss the effect of fundamental noise sources, which implies that infrastructural noise sources will have to be reduced to a similar or lower level than the fundamental noise sources. This is, to some extent, discussed for magnetic noise in section 5.4.2; for all noise sources, i.e magnetic, seismic and Newtonian noise, this should be investigated further. Furthermore, we stress

[22]We assumed an SNR threshold of 12 to define a source as resolved. The resolved sources are then subtracted to obtain the residual background.

JCAP07(2023)068

that most of these correlated noise investigations focus on the effects of the search for an isotropic SGWB. However, as shown in a recent study on the effect of magnetic glitches due to lightning strikes [135], some correlated transient events might also affect other searches, which should be further investigated for seismic and Newtonian noise.

5.4.1 Seismic and Newtonian Noise

During the last decade, much research has focused on understanding the effect of seismic and Newtonian noise on the sensitivity of ET [136–140]. In a recent study the possibility of correlated seismic and Newtonian noise is investigated for the ET triangular configuration [141]. Searches for a SGWB using data from the second-generation gravitational-wave interferometric detectors, LIGO and Virgo, are considered to have no correlations in the seismic ambient field due to their large separation and the damping of seismic waves. However, in the triangular design of the ET the input and output mirrors of two interferometers are proposed to be separated by distances of only several hundred of meters. As illustrated in figure 11 of [141], there are five coupling locations between two ET interferometers, of which two are between aligned mirrors and the remaining three between mirrors rotated by 60°. Based on the ET design report [142] the horizontal separation between those mirrors is about 300–500 m for the aligned mirrors and 330–560 m for the other pairs [141].

To investigate correlations between seismic measurements over a scale of several hundreds of meters, ref. [141] analyzed data at the Earth's surface from geophones deployed near Terziet (NL) [143] and underground data from seismometers in the former Homestake mine (South Dakota, U.S.A.) [144]. The study concludes that at the surface at Terziet significant (above Gaussian noise background) seismic correlations exist between sensors with a separation of several hundreds of meters. The 50th percentile coherence is significant up to about 10 Hz, whereas the 90% coherence is significant up to 50 Hz, which is the highest recorded frequency. For 90% of the time at Homestake there is significant coherence up to 20 Hz and more than 50% even up to 40 Hz; that is the highest frequency before the response of the sensors decreases drastically. Neither the coherence nor the cross-power spectral density (CSD) were observed to have a dependence on distance (between 200m and 800m). At both locations night times are observed to be quieter, with lower CSDs. At night there are more periods when there is significant correlated noise. These studies indicate that there is a non-negligible amount of coherence during a significant amount of time (night and day), up to frequencies of 50 Hz. This leads to the conclusion that the effect of these correlated noise sources should be understood, particularly for searches for an SGWB.

Note that in [141] it is emphasized that some correlations are considered to be of anthropogenic origin. Furthermore, some of the power spectral densities (PSDs) observed at the candidate sites are lower than the CSD observed in the Homestake mine, and therefore site-specific studies should be envisioned in the future. However, the results discussed in [141] are expected to give a good indication of the order of magnitude of the possible levels of correlated seismic and Newtonian noise which might be expected in an underground environment. Homestake represents an underground environment where both ambient and anthropogenic noise sources are present. This may also be expected for ET, since its infrastructures could be expected to introduce additional anthropogenic noise, regardless of various attempts to reduce and shield them.

It is possible, based on the measurements of correlations of the seismic noise, to estimate the correlated Newtonian Noise (NN). The NN is a disturbance produced in the gravitational-wave detector by local fluctuations of the gravitational field. Two types of seismic waves

JCAP07(2023)068

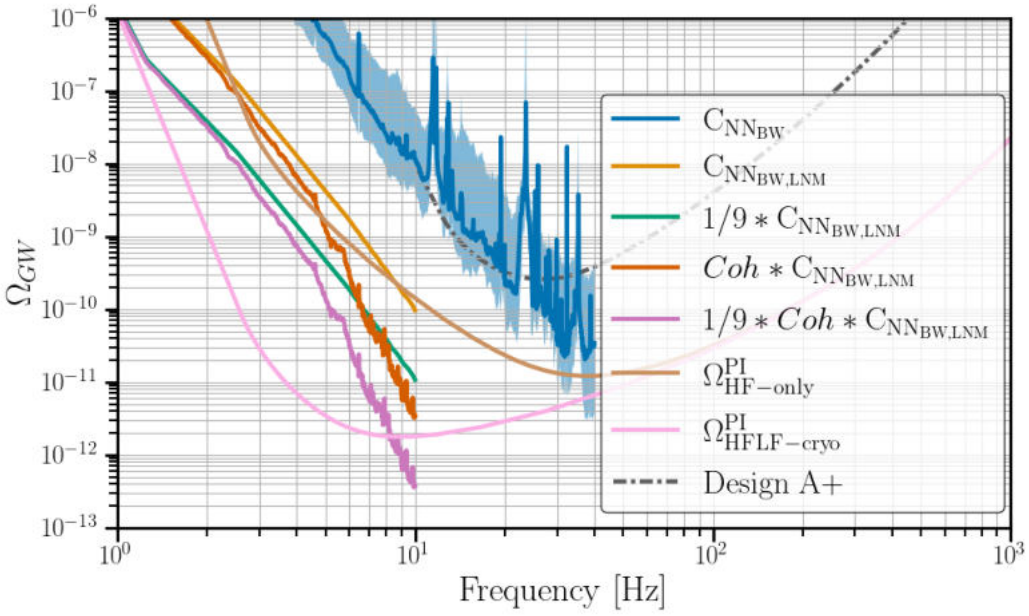

Figure 34. The projected impact from correlated NN from body-waves $C_{NN_{BW}}$, as calculated in section III of [141], is shown in blue. The blue line represents the median value, and the associated surface is delimited by the 10% and 90% percentiles. Also curves with more optimistic assumptions (see the text) are shown. Based on figure 16 of [141]. Adapted with permission from [141], copyright (2022) by the American Physical Society.

produce NN: the first are Rayleigh waves which propagate at the surface of the Earth, and the second are body waves present in the Earth's mantle. The NN from Rayleigh waves decreases significantly with depth, so their effect on ET will be limited if one assumes an underground facility at 300 m. As shown in figure 15 of [141], the NN from Rayleigh waves significantly impacts the power-law integrated sensitivity of ET only up to about 5 Hz.[23] At higher frequencies, no effect is expected.

The median contribution from correlated body waves, however, is expected to be three to five times higher than the ET sensitivity, in the range of 2 Hz to 10 Hz. While it is important to investigate the impact of noise on the sensitivity curve, correlated noise can more drastically affect some searches. The search for a SGWB typically relies on the cross-correlation of data from two detectors to decrease the Gaussian detector noise and improve the search sensitivity.

Figure 34 presents the expected impact on the search for a SGWB due to NN produced by body waves.[24] It shows that the budget calculated in [141] affects the SGWB search up to at least 40 Hz (blue band), which is the highest frequency in the analysis. Near 3 Hz, this gives an effect which is larger than the 1 yr ET sensitivity curve for the SGWB (light brown line in figure 34) by a factor $\sim 8 \times 10^6$ (90% percentile), or $\sim 6 \times 10^5$ (50% percentile).

[23] The power-law integrated sensitivity is defined as in [145], see also appendix A. We use an SNR of 1 after one year of data at a 100% duty cycle.

[24] To produce this figure, for the broadband ($\Omega^{PLS}_{HF-only}$, $\Omega^{PLS}_{HFLF-cryo}$) sensitivity to an SGWB we assumed one year of observation time (100% duty cycle). The one-year PLS curve of the A+ design for the LIGO Hanford, LIGO Livingston detectors and AdV+ design for the Virgo detector is represented by the dot-dashed curve. LIGO's A+ and Virgo's AdV+ design are the interferometer designs which are aimed to be reached during O5 [23]. This curve was obtained using the open data provided by the LVK collaborations [146] and was first presented in [147]. Note that in this figure we present the 1σ PLS, whereas in [147] the 2σ PLS-curve is shown.

JCAP07(2023)068

According to the noise estimate shown in blue in figure 34, with the triangular configuration the sensitivity of ET to an SGWB, at least below $\mathcal{O}(50-100)$ Hz, would be of the same order of magnitude as LIGO's A+ and Virgo's AdV+ design. Even assuming that an optimistic factor of 10 NN cancellation [136] could be applied to each interferometer, i.e. a factor of 100 for the SGWB budget, the search for an SGWB would still be impacted up to ∼ 30 Hz. When considering the night-time data with fewer anthropogenic activities, the impact decreases but stays at the same order of magnitude, i.e. a factor $\sim 10^5 - 10^6$ at 3 Hz [141].

In figure 34 we also provide the result from a more optimistic scenario (pink curve). The construction of this scenario is broken down as follows. We start from the yellow curve, which displays the affect of NN from body waves assuming a seismic spectrum identical to the Peterson low noise model [148] and 100% coherence. We then assume a NN cancellation by a factor of 3 (i.e. a factor of 9 on the stochastic budget), which is considered as a realistic target (green curve). The dark orange curve is generated from the assumption that the coherence equals to the median coherence observed in Homestake, as reported in [141]. Finally the pink curve represents the Peterson low noise model multiplied by the coherence observed at Homestake, as well as a factor of 3 NN cancellations for each detector. *This pink curve represents the most optimistic scenario that one can achieve. In this case, SGWB searches will still be affected by correlated NN up to ∼10Hz.*

The effect of correlated noise presented above, as well as possible additional effects from infrastructural noise, would only affect the search for an SGWB in the case of the triangular design leading to closely located interferometers. The problem of co-located correlations (of order a few hundred meters) of the seismic field should represent no problem for very distant L-shaped interferometers. However, for a triangle one can take advantage of the "null-channel" to estimate the power spectrum [149, 150], see the discussion in section 7. In the future, site-specific studies could give more detailed information. Furthermore, it would be important to estimate the order of magnitude of correlated noise expected by infrastructural noise sources caused by the 'typical equipment' needed for an underground, cryogenic gravitational-wave interferometer.

Finally, the effects of seismic transients such as (micro-)earthquakes should be understood. The latter would not only affect the search for an SGWB but could also be expected to affect searches for other GW signals such as CBCs, bursts or continuous waves if the noise sources are too loud. Further studies on the possible effect of correlated seismic transients would also be advisable. Such a study could be envisioned to investigate the possibility of lock-loss, similar to an earlier study for LIGO [151], or the impact on the sensitivity, similar to a study of the effect from earthquakes as part of the O3 environment investigations done at Virgo [152]. In the studies for ET one should also look into the possibility of correlations, as well as the 'transient Newtonian Noise', linked to the transient seismic fields and how these might introduce additional effects on the different signal searches.

5.4.2 Magnetic noise

One noise source commonly investigated with respect to the search for an SGWB is the Schumann resonances [153, 154]. These are standing electromagnetic waves in the cavity formed by the Earth's surface and the ionosphere, and are driven by lightning strikes all across the globe. The fundamental mode has an amplitude between $\sim$ 0.5 pT and $\sim$ 1 pT depending on the location and time of the day and year. The resonances are several Hz wide and have frequencies ∼7.8Hz, ∼14Hz, ∼21Hz, ...

JCAP07(2023)068

To explain how magnetic fields couple to the interferometer, it is instructive to understand how the coupling is measured. On a regular basis, strong magnetic fields are generated in the experimental buildings of the current generation of interferometric detectors. By injecting fields many times stronger than the ambient magnetic field one tries to measure their effect on the strain ASD. We define Y and X to be the ASD of the strain and witness channel (magnetometer) respectively. We use the subscript 'inj' and 'bck' refer to times during the injection, respectively a quiet background time just before/after the injection. Then we can measure the magnetic coupling function κ as follows [155],

$$\kappa_{\text{measured}}(f) = \sqrt{\frac{Y^2_{\text{inj}}(f) - Y^2_{\text{bck}}(f)}{X^2_{\text{inj}}(f) - X^2_{\text{bck}}(f)}} \,. \tag{5.14}$$

The coupling function describes how strong the strain data will be affected given ambient magnetic fields.

In recent work, the effect of the Schumann resonances and other forms of correlated magnetic noise on ET was investigated [156]. At low frequencies (< 30 Hz) it was shown that the magnetic coupling function has to be improved by two to four orders of magnitude compared to the second-generation detectors Advanced LIGO and Advanced Virgo in order to prevent significant coupling. Note that compared to the Advanced Virgo coupling function, a factor of 5 improvement could be expected due to the larger mirror mass of the ET [157, 158]. However, this assumes that the same actuator magnets as with Advanced Virgo will be used, which will make the control of the test mass more difficult. Furthermore, at low frequencies, the Advanced LIGO magnetic coupling is lower compared to the Advanced Virgo magnetic coupling. Therefore the electrostatic actuator design used by Advanced LIGO should be considered for ET. If ET will rather have a magnetic coupling similar to that of Advanced Virgo, the impact of correlated magnetic noise is predicted to be larger and will impact searches at a wider frequency band, up to $f \lesssim 50$ Hz. One must also stress the danger that induced eddy currents close-by to sensitive detector parts pose, so these should be minimized as much as possible.

The effect of magnetic noise is shown in figure 35, based on figure 6 of [156]. It presents the ratio of $\kappa^{\text{SGWB}}_{\text{HF-only}}$ and the magnetic coupling measured at LIGO and Virgo. The same reatio is also whon for $\kappa^{\text{SGWB}}_{\text{HFLF-cryo}}$. Here $\kappa^{\text{SGWB}}_{\text{HF-only}}$ and $\kappa^{\text{SGWB}}_{\text{HFLF-cryo}}$ are the magnetic coupling for each ET interferometer such that no effect of correlated magnetic noise is present in the search for an isotropic SGWB using one year of data with 100% duty cycle at the HF-only, respectively HFLF-cryo design sensitivity. For more details on the computation, we refer the reader to [156]. The needed improvement of the magnetic coupling such that magnetic noise is not larger than 1/10 of the ASD,[25] is roughly a factor 10 less stringent than the SGWB constraint. For more information see figure 6 and the accompanying discussion of [156]. Note that in [156] was not taken into account a factor of 5 of reduction obtained by increasing the mirror mass. In the top left panel of figure 35 we applied this additional factor-of-5 reduction for Virgo's magnetic coupling below 100 Hz. At higher frequencies, the coupling function is dominated by different mechanisms. We note that in the recent LIGO-Virgo third observing run (O3), for which we use the magnetic coupling function, an additional coupling was observed [155] compared to the earlier work describing the inverse proportionality with mirror mass [158]. Therefore it is not guaranteed that this reduction could be achieved if the other coupling mechanisms are not properly understood and mitigated.

[25] This is a typical requirement for noise sources which are considered not to be a 'fundamental' noise source, i.e. part of the calculation of the optimal sensitivity curve.

JCAP07(2023)068

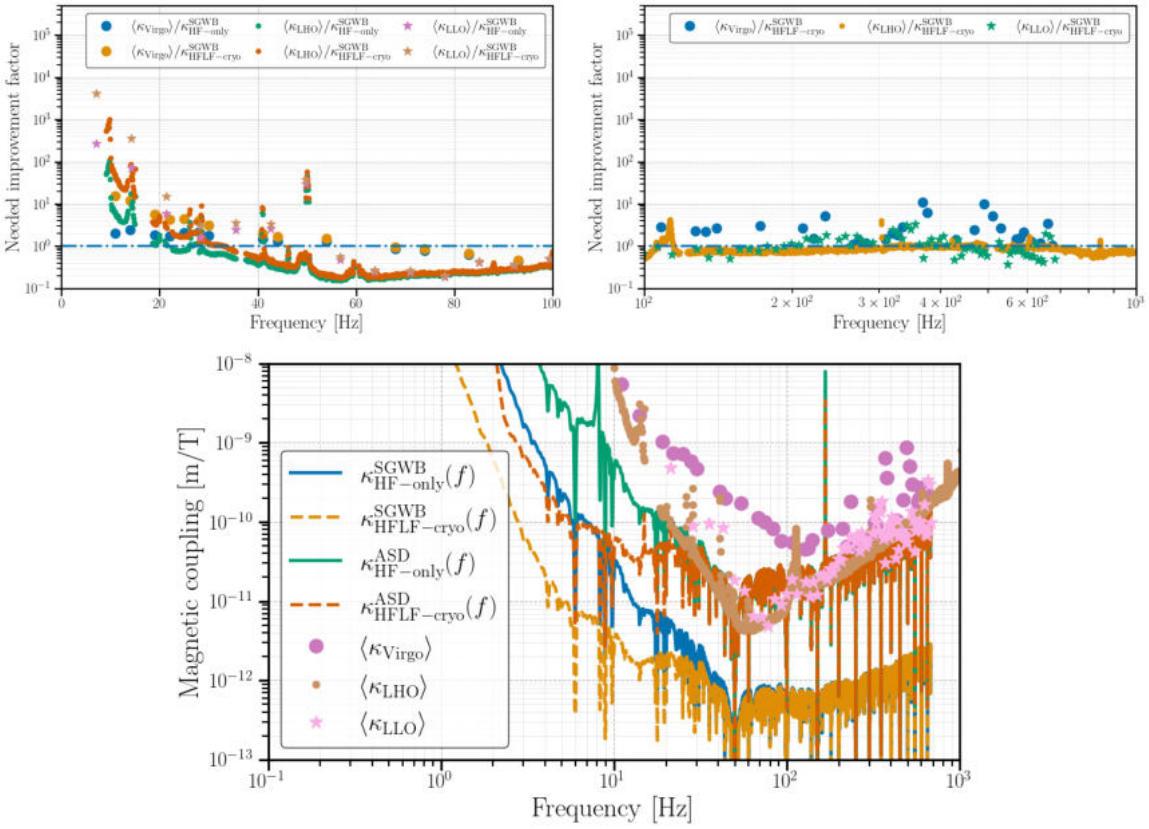

Figure 35. Top panels: needed improvement factor as a function of frequency for the upper limits on the ET magnetic coupling function, such that the isotropic SGWB search is unaffected. LHO and LLO refer respectively to the LIGO Hanford and LIGO Livingston observatories. The low-frequency (left panel) magnetic coupling poses a greater challenge for the operation of ET compared to the high-frequency (right panel) magnetic coupling. In both panels, the dash-dotted blue line indicates the line where no improvement is necessary. This figure is based on the two right panels of figure 6 of [156], however, we have used an additional factor of 5 in the reduction due to the larger mirror mass when going from Virgo to ET, in line with earlier work [157, 158]. This only applies to the left panel, since at high frequencies the coupling is dominated by other mechanisms. We report the upper limits for both the HF-only and HFLF-cryo sensitivity for SGWB searches (in [156] they used ET-B and ET-D). Note that, for $f > 100$ Hz, HF-only and HFLF-cryo have the same sensitivity to a SGWB, so we only present the HFLF results in the top left panel. Bottom panel: the upper limits on the maximal allowed magnetic coupling to prevent impact on the ASD and/or SGWB searches in the pessimistic scenario where magnetic infrastructural noise, as measured in the central building at Virgo, will be fully correlated between interferometers. The upper limits are provided for both HF-only and HFLF-cryo. The upper limits are compared with the mean observed magnetic coupling at the LIGO and Virgo detectors. Based on figure 7 of [156]. Adapted with permission from [156], copyright (2021) by the American Physical Society.

Up to ~ 20 Hz, the observed amplitude of the magnetic CSD is similar, regardless of the separation between the detectors [135]. At higher frequencies, the magnetic CSD decreases due to stronger attenuation of electromagnetic fields travelling long distances. Therefore the effect of correlations in magnetic field fluctuations up to ~ 30 Hz on ET is (mainly) independent of the detector configuration. Both the triangular and 2L designs will be impacted at the same order of magnitude. However, it is important to understand the distance between

JCAP07(2023)068

the detectors and large thunderstorm regions. Regions with large thunderstorm activity are the Americas, sub-Saharan Africa and southeast Asia [159], but more research is needed to investigate the 'local' activity in Europe and the possible impact on gravitational-wave interferometric detectors.

To summarize the effect of fundamental magnetic noise on HFLF-cryo ET, we can state that at low frequencies (<30 Hz) an effect of up to $\mathcal{O}(10^3)$ *will be present on the ASD and up to* $\mathcal{O}(10^4)$ *on the sensitivity for the SGWB. This is (mainly) independent of the triangular versus 2L configuration, due to the low attenuation of electromagnetic fields at these frequencies. Despite the dramatic effects of correlated magnetic noise, one can consider several approaches to reduce the magnetic coupling, as will be further discussed at the end of this section.*

At higher frequencies, minimal effects are expected [156], however, these are more dependent on the configuration. The co-located triangular design will be more susceptible compared to two spatially separated Ls. Even more important is the location of the detector with respect to active thunderstorm regions.

The effect from individual lightning strikes is also predicted to impact the ET sensitivity [135], in case of similar magnetic coupling as at LIGO and Virgo. A glitch rate of $\mathcal{O}(10^5)$ *for correlated magnetic transients per week could be expected, with the potential to affect ET's detector sensitivity <50 Hz [135]. It might also impact background estimation for CBC and burst searches. The 2L configuration is less prone to effects coming from coherent lightning strikes compared to the triangular design.*

Depending on which coupling function is used, the magnetic contamination at low frequencies ($\lesssim$50 Hz) is roughly at the same level (or worse) than the NN from body waves as projected in figure 34. However, there is a crucial difference between the two scenarios: the effect of the NN can only be mitigated by noise cancellation methods. For the magnetic noise, noise cancellation is also an option [160], however one can also directly attempt to improve the magnetic coupling function. An earlier study investigated the possibility of additional magnetic shielding and considered several configurations of Helmholtz coils or a spherical shell made out of chain-link metal [161]. This study showed that a factor-of-10 reduction in the magnetic coupling function should be feasible by several different shielding approaches. These results are promising, given the 'simple' methods proposed. One can consider doing better by using mu metal or superconducting coils, however, this will come at a significantly larger cost. Furthermore one can seek to reduce the number of magnets (or metallic parts) attached to the lower stages of your suspensions and test masses [162]. Even better would be to move magnets and metallic structures higher up in the suspension chain, leading to the dampening of the magnetic fields by the respective pendulum stages. Finally, the induction of currents in cables of e.g. the actuator system [162] might be mitigated by using optical fibres where possible, definitely in sensitive locations. More research is needed to obtain reductions in magnetic coupling by different methods. Nevertheless, one could envision substantially decreasing the effect of magnetic fields by using a combination of the proposed methods, which might however come at a non-negligible investment cost. We would also like to point out that the study [156] showed that ET's sensitivity curve might be affected up to $\sim$ 15Hz-20Hz (top left panel of figure 6 of [156]), and some additional shielding and/or redesign of the suspensions is needed to prevent any limitations on ETs sensitivity curve.

The previous discussion assumes all effects from infrastructural noise are overcome. This infrastructural magnetic noise is typically about two orders of magnitude louder than the fundamental magnetic noise; for example, note the effects in second-generation detectors such as Virgo's central building [156]. In the case of a very pessimistic assumption, where the

JCAP07(2023)068

	SGWB searches	
Noise type	Triangle	2L
Seismic ambient	Yes, $\lesssim$ 4 Hz[26]	No
NN ambient — Rayleigh waves	Yes, $\lesssim$ 5 Hz[27]	No
NN ambient — Body waves	Yes, $\lesssim$ 40 Hz	No
Magnetic ambient	Yes, $\lesssim$ 30Hz, possibly $\gtrsim$ 100Hz[28]	Yes, $\lesssim$ 30Hz

Table 12. Frequency regions over which searches for an isotropic SGWB would be affected, considering different types of correlated noise and assuming no improvements in the magnetic coupling function with respect to Advanced LIGO and Advanced Virgo. Furthermore, in this table, we only mention fundamental noise sources and we neglect the potential effects of local (infrastructural) noise. Whereas more research is needed to address these noise sources in the case of seismic and Newtonian noise, for magnetic noise an initial study [156] showed that the correlated noise might affect the entire frequency band for which measurements of the magnetic coupling exist, i.e. between $\sim$ 10 Hz and $\sim$ 675 Hz. This would only affect the search for an SGWB in the case of the triangular configuration.

magnetic noise in ET is the same as in the Virgo central building and it is fully correlated between two ET interferometers, an additional one to two orders of magnitude improvement of the magnetic coupling function will be required. This would only apply to the co-located interferometers, such as the ET triangular configuration. Furthermore, this would imply that the entire frequency range over which measurements of the magnetic coupling exist ($\sim 10 - 675$) Hz, would be affected if no improvement in the magnetic coupling is achieved with respect to Advanced LIGO and Advanced Virgo. In that scenario, the magnetic noise has the potential to limit the ET sensitivity, as shown in the bottom panel of figure 35 [156].

This would imply that even greater investments might be needed to sufficiently reduce the magnetic coupling in the case of the triangular configuration, as compared to the 2L configuration. Further research is needed to understand to which level these infrastructural noise sources could be produced and correlated between the ET interferometers.

6 Impacts of detector designs on specific science cases

We now discuss how different geometries, or different ASDs, affect specific aspects of the Science Case, examining a broad set of particularly significant questions in fundamental physics, cosmology, and astrophysics.

6.1 Physics near the BH horizon

A cornerstone of fundamental physics is testing the nature of compact objects and the gravitational interaction in the relativistic, highly-dynamical regime at the scale of the BH horizon. In vacuum GR, the Kerr geometry [163] is the unique physically acceptable equilibrium, asymptotically flat BH solution [164–166]. Therefore, deviations from the Kerr metric require either modified gravity or specific matter fields within GR.

[26] Assuming a horizontal-to-vertical and vertical-to-horizontal coupling $\lesssim 10^{-12}$ above 4Hz. Tilt measurements and coupling was not taken into account. For details see [141].

[27] Assuming an underground facility located at a depth of 300m. For details see [141].

[28] This assumes a magnetic coupling function similar to LIGO Hanford. For a coupling similar to Virgo magnetic contamination is possible $\lesssim$ 50Hz and $\gtrsim$ 100Hz. Furthermore, additional research is needed with respect to lightning activity in Europe and the effect might be site-dependent. For more details see [156] and [135].

JCAP07(2023)068

$SNR_{GW150914}$	HFLF-cryo	HF-only
Δ-10 km	141	141
Δ-15 km	190	190
2L-15 km-0°	196	196
2L-15 km-45°	192	192
2L-20 km-0°	240	240
2L-20 km-45°	235	235

Table 13. Projected ringdown SNR of GW150914 as detected by ET with different detector geometries (left column headers) and PSDs (top row headers). As explained in the main text, we do not observe differences between different PSDs because the signal is dominated by a monochromatic component at a frequency insensitive to the LF part of the PSD.

In the following, we discuss the impact of detector designs on specific tests of the nature of compact objects and the physics at the BH horizon.

6.1.1 Testing the GR predictions for space-time dynamics near the horizon

The ringdown waveform originates from the perturbed remnant object, and can be approximated as a superposition of damped sinusoids characterized by the complex quasinormal modes (QNMs) of the remnant. The frequencies, damping times, amplitudes, and phases of QNMs depend on the binary progenitors and on the underlying theory of gravity.

There are countably infinite QNMs indexed by (l, m, n), where (l, m) denote the angular dependence of the mode and $n = 0, 1, 2$ is the overtone index (with $n = 0$ labelling the fundamental tone). The $(l, m, n) = (2, 2, 0)$ is the dominant mode in a binary BH ringdown signal and the excitation of the subdominant modes depends on the initial configuration of the progenitor binary [167–173].

If the remnant is a Kerr BH and the underlying theory is GR, the entire QNM spectrum is fully characterized by its mass M_f and dimensionless spin χ_f. The *BH spectroscopy* program [169, 174–178] aims at detecting more than one QNM, providing us with multiple independent null-hypothesis tests of GR. In addition, even if the remnant is described by the Kerr solution but the underlying theory is not GR or the progenitors are not BHs (for example NSs or more exotic objects), then the QNM amplitudes and phases would be different from the GR prediction [173]. Thus, measuring the ringdown modes in the post-merger signal of a binary coalescence provides a clean and robust way to test GR and the nature of the remnant.

The fundamental QNM frequency and damping time have been measured by the LVK Collaboration only for a few events, providing an independent measurement of the mass and spin of the remnant which is in agreement with what inferred from the inspiral-merger phase [8]. The first GW event, GW150914, stands out among those with the highest accuracy.

If measured with ET, GW150914 would have had a ringdown signal-to-noise ratio between 141 and 240 depending on the detector configuration, see table 13. It would therefore constitute a golden event with exquisite precision in the measurability of the QNM spectrum. We can quantify the measurability of a GW150914-like event with ET using a Fisher matrix formalism [176, 179]. We include the first three subdominant modes $(3, 3, 0)$, $(2, 1, 0)$ and $(4, 4, 0)$, modeling their amplitudes through the numerical fits in [169, 173], and assuming a start time for the ringdown at $t \approx 10M$ after the peak of the waveform. The relative uncertainties on the dominant frequencies f_{220} and damping times τ_{220} are prospected to scale

JCAP07(2023)068

with the ringdown SNR as

$$\frac{\Delta f_{220}}{f_{220}} \sim 0.2\% \left(\frac{100}{\mathrm{SNR}}\right) , \qquad \frac{\Delta \tau_{220}}{\tau_{220}} \sim 2\% \left(\frac{100}{\mathrm{SNR}}\right) , \tag{6.1}$$

which propagate similar relative errors on the mass and spin of the remnant (assuming the latter to be a Kerr BH) thus giving an estimate of the performance of consistency tests informed by the inspiral part of the signal [8]. On the other hand, the subdominant frequencies scale as

$$\frac{\Delta f_{330}}{f_{330}} \sim 2\% \left(\frac{100}{\mathrm{SNR}}\right) , \quad \frac{\Delta f_{210}}{f_{210}} \sim 4\% \left(\frac{100}{\mathrm{SNR}}\right) , \quad \frac{\Delta f_{440}}{f_{440}} \sim 3\% \left(\frac{100}{\mathrm{SNR}}\right) . \tag{6.2}$$

This shows that, by detecting high-SNR events, and in particular golden events with SNR $\geq$ 100, ET will be able to measure the QNM spectrum at the percent level for individual events. Moreover, by stacking together multiple events (see table 14 below), it will be possible to test deviations from the GR predictions at the sub-percent level.

Next, using the BBH population catalog generated with the FASTCLUSTER code [53, 54] as described in section 3, we estimate the event rates for BH spectroscopy with different ET designs. Figure 36 shows the distributions of source-frame mass $M_f^z = (1+z)M_f$ and χ_f for the final BH, as predicted from the simulated BBH merger events in the catalog, and computed from the analytical fits in [180, 181].[29] The spin χ_f clusters around 0.7 as a consequence of the fact that the majority of the BBH events in the catalog have progenitor mass ratio close to unity (with only a small portion having mass ratio $q \equiv m_1/m_2 \gtrsim 5$) and moderate progenitor spins. Furthermore, we see that the distribution of the QNM fundamental frequency peaks at around 100 Hz, which sets the typical scale of the (almost monochromatic) ringdown signal.

In order to assess the feasibility of BH spectroscopy with different ET configurations, we compute the number of ringdown detections per year. Here a detection corresponds to SNR $\geq$ 12 in the ringdown-only portion of the signal. Moreover, we compute the number of ringdown detections per year with ringdonwn signal-to-noise ratio SNR $\geq$ 50 and with SNR $\geq$ 100, the latter representing golden events for BH spectroscopy. All detector designs are assumed in the HFLF-cryo configuration. *We did not find any significant difference when the LF instrument is absent. This is due to the fact that the ringdown signal is almost monochromatic and, as shown in figure 36, there is a negligible portion of events for frequencies $f_{220} \lesssim 20$ Hz, where the contribution of the LF instrument impacts on the ET sensitivity curve.* Results are reported in table 14 for the particular realization of the catalog considered here, where the rates are subjected to the statistical Poisson counting uncertainty $\sigma(N_{\rm det}) \approx \sqrt{N_{\rm det}}$.

In conclusion, for BH spectroscopy, the baseline 10 km triangle configuration allows for ~ 34 *high-SNR events and 3 golden events per year. While these numbers are already extremely interesting, both the 15 km triangle design and the 15 km 2L design allow to increase by a factor* $\sim 3-4$ *the detection rate w.r.t. the baseline, with* 90+ *high-SNR events and* 9+ *golden events per year and a slight preference for the 15-km triangle. The 20 km 2L configurations show the best performances in terms of detected events, with* ~ 240 *high-SNR events*[30] *and* ~ 20 *golden events per year.* Table 14 also reports the event rates as measured

[29] We also benchmarked them against `surfinBH` [182], which is a machine learning predictor trained on numerical simulations, finding excellent agreement within the common regimes of validity.

[30] A back-of-the-envelope estimate, assuming that by stacking $N_{\rm det}$ signals the errors shown in eq. (6.2) are reduced by a factor $\approx \sqrt{N_{\rm det}}$, suggests that by stacking multiple ringdown detections with SNR > 50, the 2L-15 km-45° configuration can reach $\approx 0.1\%$ accuracy for the subdominant QNMs.

JCAP07(2023)068

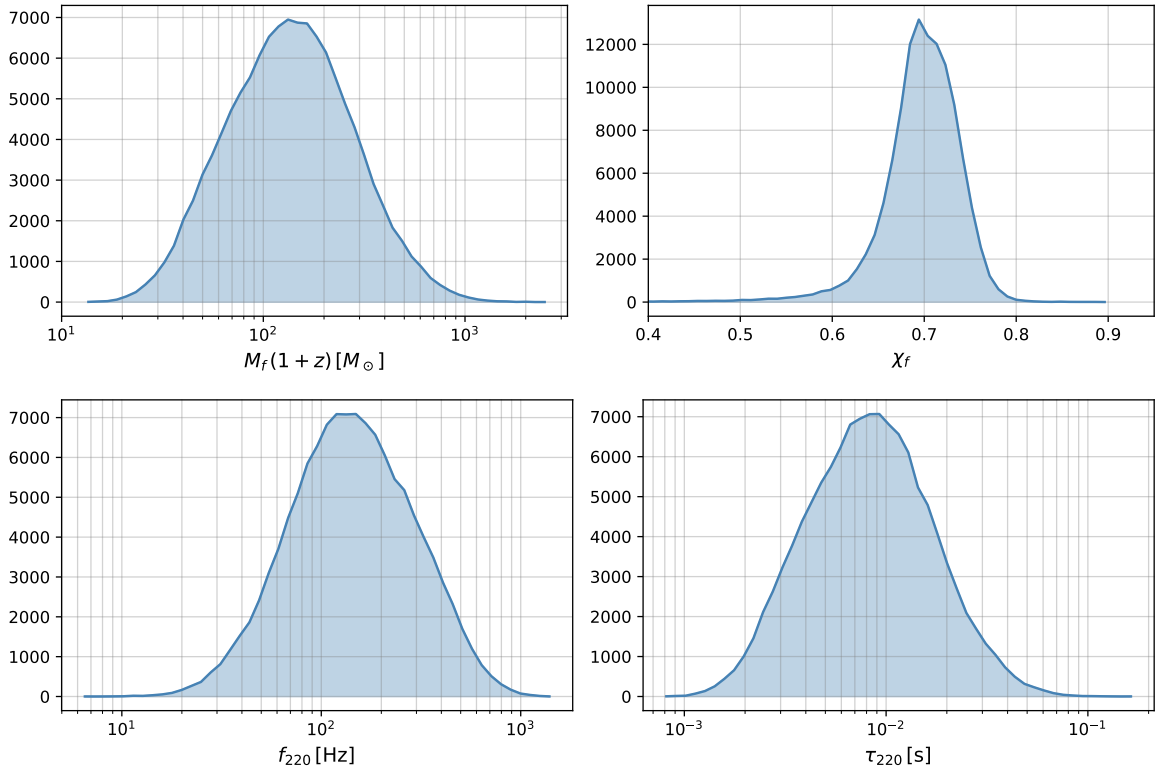

Figure 36. Top: distribution of the redshifted final masses and dimensionless final spins from the simulated BBH events as detailed in section 3. Bottom: corresponding distribution of the ringdown frequency and damping time of the dominant $(2, 2, 0)$ mode.

	$N_{\rm det}(\mathrm{SNR} \geq 12)$	$N_{\rm det}(\mathrm{SNR} \geq 50)$	$N_{\rm det}(\mathrm{SNR} \geq 100)$	max(SNR)
LVKI-O5	15	0	0	38
ET				
Δ-10 km	4665	34	3	262
Δ-15 km	11692	117	13	317
2L-15 km-0°	11627	110	11	281
2L-15 km-45°	10175	97	9	330
2L-20 km-0°	18972	255	21	327
2L-20 km-45°	17185	228	18	384

Table 14. Number of ringdown events per year above the detection threshold (SNR $\geq$ 12), with high signal-to-noise ratio (SNR $\geq$ 50), and golden events (SNR $\geq$ 100) for different proposed detector designs (all taken in the HFLF-cryo configuration) and compared to the most optmistic prospect for LVKI in O5. The last column displays the SNR of the loudest event in the catalogue. Here SNR refers to the ringdown part of the signal only.

by the LVKI network in O5. *We see that ET will constitute a game changer for probing near-horizon physics.*

Next, we investigate the redshift reach of BH spectroscopy for the two representative cases of a 10-km triangle and a 15km-45°-2L configuration. Figure 37 (left) shows the event rate per year as a function of the redshift: while ET is capable of detecting ringdown events up to redshift $z \lesssim 14$, high-SNR are limited to $z \lesssim 4$ and golden events are limited to

JCAP07(2023)068

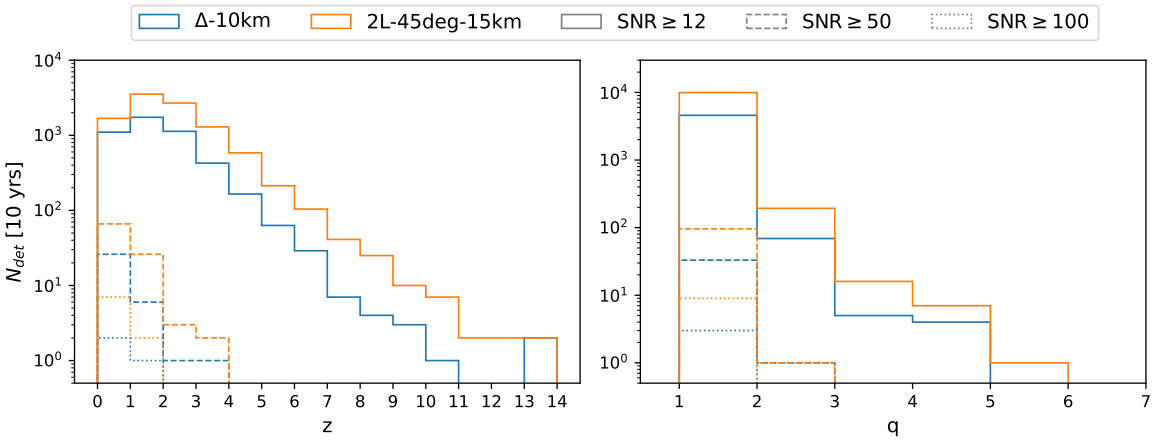

Figure 37. Ringdown event rates as a function of redshift (left) and mass ratio (right) for the baseline 10km triangle and the 15km-45°-2L configuration. Different colors indicate detectors configurations; continuous, dashed, and dotted contours indicate different ringdown SNR thresholds.

$z \lesssim 2$. Figure 37 (right) displays the complementary information of the event rate as a function of the mass ratio: we see that the loud ringdown events are limited to small mass ratios $q \lesssim 3$ while high mass-ratio events are detected with moderate or small SNR. Since different mass ratios excite different modes in the ringdown spectrum, high mass-ratio events offer valuable complementary information and it is, therefore, desirable to develop efficient stacking techniques [183–185] to take advantage from them.

Finally, in table 15 we also computed the event rates when ET operates in synergy with a single 40 km CE detector and with a network of one 40 km CE and one 20 km CE. The results show that joint detections by ET in its baseline configuration and CE produce ringdown rates comparable with ET alone in its 2L-20 km configurations, and that a 15 km or 20 km ET in synergy with CE will constitute a major improvement for BH spectroscopy as it will result in between 30 to 50 golden events per year. We also observe that the differences among the results, induced by different choices of the ET geometry, remain quite significant even when ET is in a network with 1CE or with 2CE.

6.1.2 Searching for echoes and near-horizon structures

Exotic compact objects (ECOs) are horizonless objects predicted in certain quantum-gravity extensions of GR and in the presence of exotic matter fields [186–188]. Some broad motivations for ECOs are (see [187] for a review): i) resolving the singularities inevitably present inside BHs within GR; ii) evading deep conceptual conundrums associated with the presence of a horizon (most notably, the information loss paradox); or iii) simply providing effective models for new species of compact objects that might co-exist in the universe along with BHs and NSs.

Several models of ECOs have been conceived, including BH "fuzzball" microstates in string theories [189, 190] and boson stars as self-gravitating objects made of massive bosonic fields minimally coupled to GR [191, 192]. One can devise a model-independent framework [193] in which the ECO properties are parametrized in terms of their effective radius $r_0 = r_+(1+\epsilon)$ (where r_+ is the would-be location of the Kerr BH horizon and ϵ is a dimensionless closeness parameter), and the reflectivity $\mathcal{R}$ at the effective radius with a generic phase $\phi(\mathcal{R})$. The BH case is described by a null reflectivity at the horizon for any frequency,

JCAP07(2023)068

ET (+1CE)	$N_{\rm det}(\mathrm{SNR} \geq 12)$	$N_{\rm det}(\mathrm{SNR} \geq 50)$	$N_{\rm det}(\mathrm{SNR} \geq 100)$	max(SNR)
Δ-10 km	17268	188	18	298
Δ-15 km	23634	311	29	350
2L-15 km-0°	23342	311	29	317
2L-15 km-45°	22262	290	27	362
2L-20 km-0°	29307	504	41	359
2L-20 km-45°	28126	439	38	412
ET (+2CE)				
Δ-10 km	20990	268	25	308
Δ-15 km	27065	383	38	359
2L-15 km-0°	26691	384	37	327
2L-15 km-45°	25749	357	37	370
2L-20 km-0°	32266	597	49	368
2L-20 km-45°	31197	531	45	420

Table 15. Same as table 14 but with a single 40 km CE detector (top) or with one 40 km CE detector and one 20 km CE detector (bottom) added to the network.

whereas an ECO reflects part of the incoming radiation, i.e. $\mathcal{R} \neq 0$ (the reflectivity is generically complex and frequency dependent). Because of this reflectivity, ECOs emit a different GW signal relative to the BH case. One of their smoking guns is the emission of a modulated train of GW echoes in the late-time ringdown stage of a compact binary coalescence, associated to signals reflected off the object interior [194, 195]. When an ECO remnant with $\epsilon \ll 1$ forms, a ringdown analogous to the BH one is emitted at early times, followed by a new signal in the form of late-time echoes. Several searches for GW echoes in LVK data have been performed, claiming no evidence for their observation [8, 196–199] (although some results are controversial, see [188]).

Here, we assess the detectability of GW echoes with different ET configurations. We focus on a GW150914-like system (final mass $M_f = 70M_\odot$ and final spin $\chi_f = 0.68$) placed at a fiducial distance $d_L = 1$ Gpc. We use the frequency-domain echo template developed in ref. [200] for a representative choice $\epsilon = 10^{-5}$ where we vary the reflectivity in the range $\mathcal{R} \in [0.01, 0.99]$ and set $\phi(\mathcal{R}) = 0$. Figure 38 shows the fractional percentage errors (obtained with a Fisher matrix analysis) on the reflectivity of an ECO for different ET configurations. The fractional error is a proxy for the detectability of ECOs, since the BH case corresponds to $\mathcal{R} = 0$ and therefore any putative measurement of $\mathcal{R}$ should exclude $\mathcal{R} = 0$ with the highest confidence level. We report the values of $\sigma_{\mathcal{R}}/\mathcal{R}$ after averaging over the sky position and the inclination angle. We take the detectors in the cryogenic HFLF configuration but, *as in the ringdown analysis reported in section 6.1.1, we do not find significant deviations when the LF instrument is not operating.*

JCAP07(2023)068

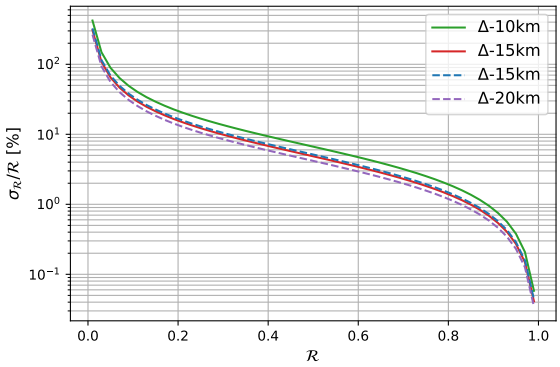

Figure 38. Fractional percentage errors on the ECO reflectivity $\mathcal{R}$ for a GW150914-like event placed at $d_L = 1$ Gpc with final mass $M_f = 70M_\odot$ and final spin $\chi_f = 0.68$. The detector is taken in the cryogenic HFLF configuration and errors are averaged over the sky position and the inclination angle. There are no significant deviations in the figure for the HF-only configuration. The Fisher-matrix parameters are $\{M_f, \chi_f, \mathcal{R}, \phi(\mathcal{R}), \epsilon\}$, where $\mathcal{R}$ is generically a complex number, and the amplitude and phases $\{\mathcal{A}_{lmn}, \phi_{lmn}\}$ of the excited modes.

	$\sigma_{\mathcal{R}}/\mathcal{R}$ [%]		
	$\mathcal{R} = 0.01$	$\mathcal{R} = 0.5$	$\mathcal{R} = 0.99$
Δ-10 km	422	7	0.06
Δ-15 km	308	5	0.04
2L-15 km	326	5	0.04
2L-20 km	265	4	0.03

Table 16. Fractional percentage errors on the measurability of the ECO reflectivity $\mathcal{R}$ for small ($\mathcal{R} = 0.01$), medium ($\mathcal{R} = 0.5$) and large ($\mathcal{R} = 0.99$) reflectivity for the same system and detector configuration of figure 38.

The main result is that the detector configuration affects the accuracy on the reflectivity of compact objects by a factor of ~ 2 *between the 10 km designs and the 20 km designs, with the 15 km designs representing the best compromise.*

This is further quantified in table 16 for three values of the reflectivity (small, medium and large, respectively). We can ascribe these differences to the larger SNR of longer arm length configurations. The distribution of the SNR follows the same statistics of the ringdown SNR as reported in table 14 and figure 37 and therefore the same considerations apply about the advantage of a 15-km design relative to the baseline 10-km design.

6.1.3 Constraining tidal effects and multipolar structure

The multipolar structure of a Kerr BH can be elegantly written as [201],

$$M_\ell^{\rm BH} + iS_\ell^{\rm BH} = M^{\ell+1}\,(i\chi)^\ell\,, \tag{6.3}$$

where $\chi := J/M^2$ is the dimensionless spin, $M = M_{00}$, $J = S_{10}$, $M_\ell = M_{\ell 0}$, $S_\ell = S_{\ell 0}$, with M_{lm} and S_{lm} being the mass and current multipole-moment tensors, respectively. For a Kerr BH, the only nonvanishing multipole moments have $m = 0$ and the mass (current) multipole

JCAP07(2023)068

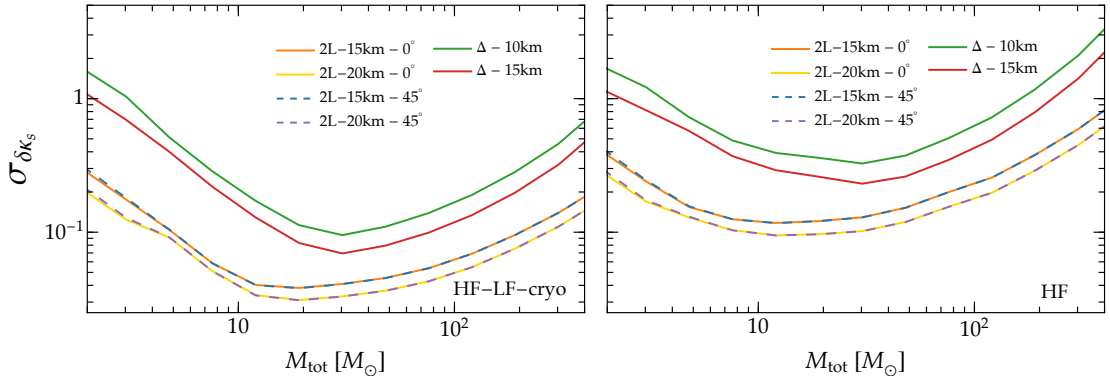

Figure 39. 1-σ uncertainty on the parameter controlling deviations on the symmetric combination of the spin-induced ECO quadrupole moment, $\kappa_s = 1 + \delta\kappa_s$, with $\kappa_s = 1$ corresponding to binaries with Kerr BHs. We assume the Kerr case ($\delta\kappa_s = 0$) and optimally-oriented sources with mass ratio $q = 2$, non-precessing spins $\chi_1 = 0.9$, $\chi_2 = 0.7$ at a luminosity distance of $d_L = 100\,$Mpc. The optimal orientation depends on the detector location and configuration. The Fisher-matrix parameters are $\{\mathcal{M}_c, \eta, d_L, \theta, \phi, \iota, \psi, t_c, \Phi_c, \chi_{1,z}, \chi_{2,z}, \delta\kappa_s\}$.

moments vanish when ℓ is odd (even). These properties are a consequence of the *axial* and *equatorial symmetry* of the Kerr solution.

In general, objects other than BHs violate these symmetries and the unique relation (6.3) between all multipole moments and the BH mass and spin. Their multipolar structure can be schematically written as

$$M_{\ell m} = M_\ell^{\rm BH} + \delta M_{\ell m}\,, \qquad S_{\ell m} = S_\ell^{\rm BH} + \delta S_{\ell m}\,, \tag{6.4}$$

where $\delta M_{\ell m}$ and $\delta S_{\ell m}$ are some model-dependent corrections to the mass and current multipole moments.

Generically, the mass quadrupole moment M_{2m} is the dominant multipolar contribution, entering the inspiral GW signal at second PN order [202]. When $m \neq 0$, this term can induce binary precession even in the absence of progenitor spins [203]. Deviations from standard BH predictions can be parameterized by defining $M_{20} = -\kappa M^3 \chi^2$, where $\kappa = 1$ corresponds to the Kerr case, while $\kappa(\chi)$ in all other cases. At the 2PN order, contributions from the quadrupole moments of the binary components enter the waveform through symmetric and antisymmetric combinations given by $\kappa_s = (\kappa_1 + \kappa_2)/2$ and $\kappa_a = (\kappa_1 - \kappa_2)/2$, respectively. The latter can be recast in terms of deviations from the Kerr baseline as $\kappa_s = 1 + \delta\kappa_s$, and $\kappa_a = \delta\kappa_a$. Figure 39 shows the absolute errors on the parameter $\delta\kappa_s$ as a function of the binary total mass, for representative systems with mass ratio $q = 2$ and spins $(\chi_1, \chi_2) = (0.9, 0.7)$ aligned to the orbital angular momentum (and therefore nonprecessing). We use a TaylorF2 waveform model, truncating the inspiral phase at the ISCO of the Kerr remnant, also including corrections induced by the self-force and the spin of the less massive object [204].

We find that the differences on the uncertainties obtained assuming the triangle and the L-shaped configurations are typically of a factor two in favor of the triangle, across the range of masses we considered.

Another smoking-gun deviation from the standard Kerr BH in GR is given by the tidal deformability, considered in section 3.2 for BNSs. A remarkable result in GR is that the tidal

JCAP07(2023)068

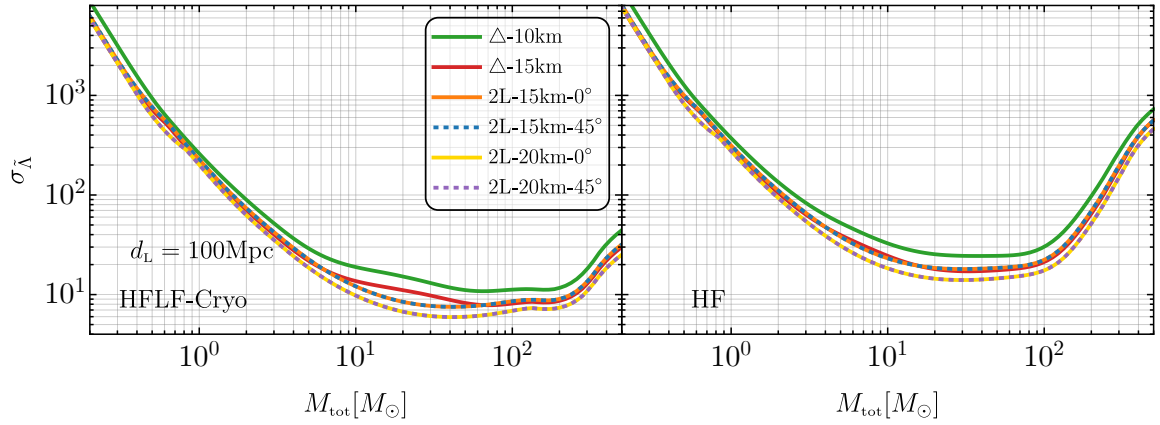

Figure 40. Absolute (1-σ) uncertainty on the tidal deformability $\tilde{\Lambda}$ as a function of total mass $M_{\rm tot}$ in the source frame for the various configurations. We assume negligible deformability of the source, nonspinning equal-mass binaries, and an optimally oriented source at a distance $d_L = 100\,$Mpc. The optimal orientation depends on the detector location and configuration. The Fisher-matrix parameters are $\{\mathcal{M}_c, \eta, d_L, \theta, \phi, \iota, \psi, t_c, \Phi_c, \chi_{1,z}, \chi_{2,z}, \tilde{\Lambda}, \delta\tilde{\Lambda}\}$. These results complement what presented in section 3.2 for BNSs to the case of ECOs or subsolar BHs (i.e. PBHs) potentially observable with ET, see more details in section 6.3.3.

deformability of BHs is precisely zero [205–207], at variance with any other object in GR or with BHs in modified gravity [208–213].

Figure 40 shows the absolute error on the binary tidal parameter $\tilde{\Lambda}$ as a function of the source frame total mass, for non-spinning, equal-mass, optimally oriented binaries, at luminosity distance $d_L = 100\,$Mpc. We assume the TaylorF2 waveform,[31] cutting the inspiral phase at the ISCO frequency of a remnant Schwarzschild BH with mass $\approx M_{\rm tot}$. Extending the Fisher analysis to higher frequencies would significantly improve measurement errors but would require specific ECO models.

We conclude that different ET configurations do not impact significantly on the accuracy in the measurement of the tidal deformability for $M_{\rm tot} \lesssim \mathcal{O}(M_\odot)$, while differences are slightly larger, within typically a factor of order 2, for heavier binaries (with the 2L configurations performing again better than the triangle ones).

6.2 Nuclear physics

One of the longstanding open challenges in nuclear physics is to determine the properties of matter at supranuclear densities. Given the extremely high central densities in neutron stars and the possibility to form merger remnants that not only probe the highest densities in our Universe before black hole formation but also matter at nonzero temperature, the Einstein Telescope will provide important nuclear-physics insights, see e.g., refs. [15, 214–222]. In particular, it will be possible to probe the cold EoS from the inspiral phase with unprecedented accuracy and furthermore, in contrast to existing gravitational-wave detectors, there is a high chance of detecting gravitational-wave emission from the merger and its

[31] We checked that, at the level of the comparison between different configurations, assuming the IMRPhenomD_NRTidalv2 waveform approximant gives analogous results. However, in the range of masses of its validity, the latter provides a smaller uncertainty on $\tilde{\Lambda}$ due to the fact that the waveform (calibrated on BNS coalescences) is valid up to higher frequencies, as well as to a dependence of the amplitude on the deformability (which is only included in the phase of TaylorF2).

JCAP07(2023)068

remnant which not only probes the cold EoS but would also allow us to place constraints at the EoS at temperatures up to ~ 50MeV; cf. e.g. [223] and references therein. For these reasons, it is essential to understand to which extent the different detector configurations impact possible nuclear-physics constraints.

6.2.1 Radius estimation from Fisher-matrix computation

We start by assessing the accuracy of constraining the EoS by providing estimates for the uncertainty in the inferred radius based on the Fisher matrix approach. The results used here differ from those in section 3.2 due to the assumption of a common EoS for the NSs when producing the events catalog. In particular, we adopt the DD-LZ1 model[32] [224–226] and compute the adimensional tidal deformability parameters of the objects from their source-frame masses m, using the $\Lambda(m)$ relation predicted by this EoS. The choice of DD-LZ1 is dictated by its high allowed maximum mass (of $2.56\,\mathrm{M}_\odot$); this makes it consistent with the BNS population model used throughout this work which, as mentioned in section 3, assumes a source-frame mass distribution of the component objects uniform between $1.1\,\mathrm{M}_\odot$ and $2.5\,\mathrm{M}_\odot$. Moreover, the behavior of DD-LZ1 complies with all the present constraints from low energy nuclear physics [227]. As in section 3.2, the results are produced using the `GWFAST` package [17, 32] and adopting the IMRPhenomD_NRTidalv2 waveform model. A detailed study of the effect of the injection EoS and waveform model is ongoing.

We use two ways to transform the error of the tidal deformability $\tilde{\Lambda}$ [defined in eq. (3.1)] into the error on the measurement of the NS radius R. The first approach assumes that $\tilde{\Lambda} \propto R^6$, which leads to

$$\frac{\Delta R}{R} = \frac{1}{6}\frac{\Delta\tilde{\Lambda}}{\tilde{\Lambda}}, \tag{6.5}$$

and arises from relations derived in ref. [228]. This allows us directly to compute the individual radius uncertainty $\Delta R/R$ for all detections. We summarize these results in figure 41. *Comparing different configurations (left panel), we find that the main limiting factor is the arm-length of the gravitational-wave detectors, so the 10 km triangle performs less well than a 15 km 2L.* Consistently with a number of other results in section 3, the right panel of figure 41 shows that the 2L with 15 km arms at 45° in the HF-only configuration performs at a level comparable to the 10 km triangle in the full HFLF cryo configuration.

An important consequence of the large number of BNS detections with ET is that we can noticeably improve the EoS constraints by stacking information from multiple detections at different masses, which enables constraining the EoS at different densities. To quantify this, we perform a simple analysis in which we assume a common radius of 12km radius for all neutron stars. While this assumption is a priori unrealistic, it nevertheless captures the feature that different neutron star measurements will probe the same underlying hyper-parameters characterizing the EoS. To obtain a combined ansatz, we compute the average $\overline{(\Delta\tilde{\Lambda}/\tilde{\Lambda})}$ and use

$$\Delta R_{\rm all} = \frac{1}{6\sqrt{N_{\rm det}}}\overline{\left(\frac{\Delta\tilde{\Lambda}}{\tilde{\Lambda}}\right)}\ 12\mathrm{km}. \tag{6.6}$$

[32] We point out that the EoSs employed here do not contain phase transitions, however, we expect that the presence of a strong phase transition will likely influence the accuracy to which we can measure the neutron star radius.

JCAP07(2023)068

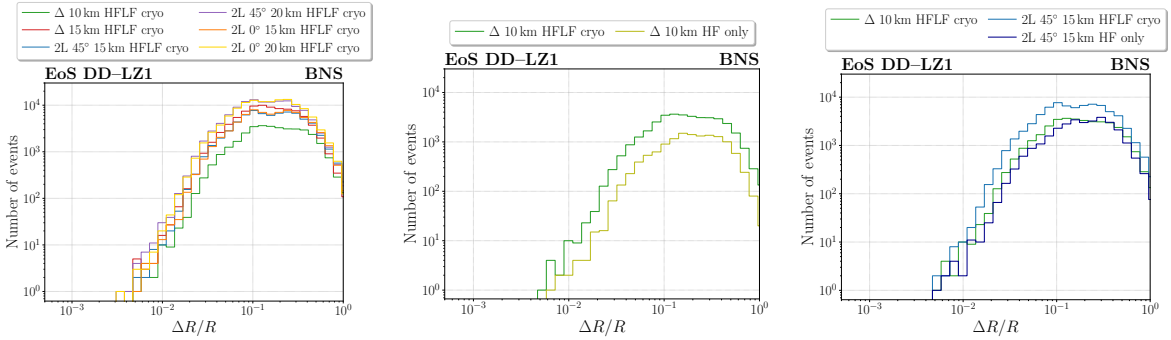

Figure 41. Distribution of the relative errors on the NS radius attainable from the adimensional tidal deformability combination $\tilde{\Lambda}$, as measured by different detector configurations and sensitivity curves. In particular, the left panel shows the results for the six geometries considered, all with their best sensitivity, the central panel for the 10 km triangle with the two different ASDs, and the right panel for the 2L with 15 km arms at 45° and the two ASDs considered.

We present results for $R_{\rm all}$ in table 17 for all ET configurations, from which we see that *loosing the LF instrument, the constraints gets worse by about a factor of 2, irrespectively of the geometry.*

In table 18, complementing the results in section 3.3, we also report the results for some ET geometries, all with their full HFLF cryogenic ASD, working in a network with 1 or 2 CE detectors. To improve the reliability of the Fisher matrix approach, we restrict the analysis to events with a relative error on the adimensional tidal deformability of $\Delta\tilde{\Lambda}/\tilde{\Lambda} \leq 50\%$. This threshold is chosen to have a large number of events in each configuration and with each ASD, and also reflects the fact that the loudest events — with smaller errors — will be the ones providing most of the information. We emphasize that this error represents only the statistical uncertainty; however, systematic uncertainties, e.g., due to modeling errors in the gravitational waveform will also be important [229]. Moreover, we stress that the results shown in figure 41 and in tables 17 and 18 depend on the choice of the EoS. From the dependence of the tidal deformability on the star's compactness, it is evident that, with increasing mass, the tidal deformability decreases. Thus EoS models predicting large maximum masses in general also predict very low values of Λ close to the maximum mass, which is difficult to constrain. Indeed, DD-LZ1 predicts tidal deformability as small as $\Lambda \sim 5$ for $m \simeq 2.56\,\mathrm{M}_\odot$. Assuming a different EoS [which might require a lowering of the maximum mass in the mass distribution to accommodate the maximum mass allowed by the EoS] could result in tighter or broader constraints. This will be discussed in further details in section 6.2.2. Furthermore, the uniform distribution adopted in section 3.2 predicts smaller values for the error on the radius, but using an EoS enables including the physical effect of the tidal deformability parameter decreasing with increasing mass. The results presented here should be taken only as indicative, however, they still provide a relevant benchmark for comparing different detector configurations.

Our second approach is based on first generating a prior distribution of EoS by Monte-Carlo sampling of a large parameter set of 10 independent, uniformly distributed empirical parameters. These parameters characterize the density dependence of the energy in the symmetric matter (i.e. equal number of protons and neutrons) and of the symmetry energy (i.e. the variation of binding energy as a function of the neutron-to-proton ratio). They are given by the successive derivatives with respect to the density of the symmetric matter and symmetry energy functionals, calculated at the equilibrium density of symmetric matter.

JCAP07(2023)068

Geometry \ ASD	HFLF cryo		HF only	
	$N_{\rm det}^{\Delta\tilde{\Lambda}/\tilde{\Lambda}\leq 0.5}$	$\Delta R_{\rm all}$ [m]	$N_{\rm det}^{\Delta\tilde{\Lambda}/\tilde{\Lambda}\leq 0.5}$	$\Delta R_{\rm all}$ [m]
Δ 10 km	4878	10.0	1412	19.2
Δ 15 km	15285	5.7	4047	11.3
2L 15 km 45°	12013	6.4	3194	12.4
2L 20 km 45°	25489	4.4	7387	8.2
2L 15 km 0°	11884	6.5	3357	12.1
2L 20 km 0°	23988	4.5	7081	8.3
1L 20 km	5464	9.4	1493	19.1

Table 17. Number of detections, $N_{\rm det}$ with $\Delta\tilde{\Lambda}/\tilde{\Lambda} \leq 50\%$, and statistical error on the NS radius obtained combining all of them according to (6.6), $\Delta R_{\rm all}$ (in meters), for various geometries and ASDs.

Geometry \ ASD	HFLF cryo + 1CE		HFLF cryo + 2CE	
	$N_{\rm det}^{\Delta\tilde{\Lambda}/\tilde{\Lambda}\leq 0.5}$	$\Delta R_{\rm all}$ [m]	$N_{\rm det}^{\Delta\tilde{\Lambda}/\tilde{\Lambda}\leq 0.5}$	$\Delta R_{\rm all}$ [m]
Δ 10 km	24129	4.6	35694	3.8
2L 15 km 45°	35172	3.8	47791	3.2
2L 15 km 0°	35217	3.8	48581	3.2

Table 18. Same as in table 17 with some selected geometries, all with the full HFLF cryogenic ASD, in combination with 1 CE detector with a length of 40 km and 2 CE detectors, one with a length of 40 km and the other of 20 km.

Their prior distribution is consistent with the present empirical knowledge for a large set of nuclear data [227]. The use of the same functional to describe the core and the inhomogeneous crust [230] guarantees a consistent estimation of the crust-core transition inside the neutron star and thus consistent predictions for its radius. This approach enables incorporating priors from nuclear physics on the EoS and including the uncertainties at high densities. The only limiting assumption is that matter is composed of charged leptons, nucleons and nuclei only, and in particular that no first-order phase transition occurs. There might also be some dependence on the different approximations applied to treat inhomogeneous matter, e.g. assuming vanishing temperature, which could slightly modify the crust properties (see e.g. [231]). However, this should not affect the comparison of different configurations. The assumed nuclear prior complies with the chiral EFT energy per particle band for symmetric and pure neutron matter as given by [232] for baryon number densities $0.02 \leq n_B \leq 0.18\text{fm}^{-3}$, see [233] for details of the current implementation.

In figure 42 we show the mass-radius distribution for the nuclear prior described above along with the posteriors at 68% and 95% confidence intervals assuming 5970 simulated "observations" obtained from a Fisher matrix calculation. We also indicated the DD-LZ1 EoS used as input EoS in the calculation. The full compatibility of the DD-LZ1 model with nuclear physics constraints is shown by the fact that the injected mass-radius relation sits in the middle of the nuclear informed prior. This particular simulation was performed with geometry 2L -20 km with aligned arms (cryogenic), but we have checked that different configurations do not make any significant difference in the outcome, provided that the number of detections exceeds $N_{det} \sim 6000$.

JCAP07(2023)068

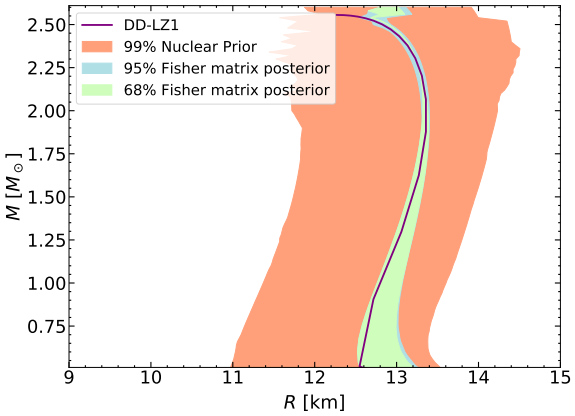

Figure 42. Posterior distribution for NS mass-radius relation obtained assuming 5970 detections with geometry 2L -20 km with aligned arms. For comparison, the results obtained from the nuclear prior as well the underlying DD-LZ1 EoS model used in the Fisher matrix calculations are displayed.

N_{det}	$R_{1.4M_\odot}{}^{+\Delta R_+}_{-\Delta R_-}$ [km]	$R_{2.0M_\odot}{}^{+\Delta R_+}_{-\Delta R_-}$ [km]
Prior	$12.983^{+0.420}_{-0.420}$	$13.156^{+0.447}_{-0.454}$
54	$13.163^{+0.221}_{-0.227}$	$13.358^{+0.234}_{-0.242}$
592	$13.146^{+0.122}_{-0.136}$	$13.355^{+0.099}_{-0.083}$
5970	$13.107^{+0.148}_{-0.037}$	$13.332^{+0.050}_{-0.013}$

Table 19. Number of detections, N_{det} along with 1σ uncertainty on radii for 1.4 and 2.0 solar mass NSs obtained for geometry 2L-20km-0° using nuclear prior.

To understand the impact of different number of detections using the same geometry as above, we summarize the 1σ uncertainty on radii for 1.4 and 2.0 solar mass NSs with 54, 592 and 5970 detections in table 19. We can observe that the uncertainty on the radii only roughly follows the Poissonian law as described in eq. (6.6). The reason is probably that the radius is not a direct observable but, rather, is obtained in a convoluted way from the TOV equation and the underlying hypothesis on the EoS formalism. As a general statement, we can see that the Poisson hypothesis tends to underestimate the radius uncertainty from the Fisher matrix analysis, unless the number of detections is extremely large (more than $N_{det} \sim 6000$). Moreover, we should also stress that the uncertainty estimations of table 19 might be underestimated themselves, because of the restrictive hypothesis of a continuous equation of state at any density. Nevertheless, these results give us an indicative impact of ET measurements on the radii uncertainties using a fairly general EoS, within the hypothesis of purely nucleonic degrees of freedom.

6.2.2 Full parameter estimation results

In addition to our estimates based on the Fisher matrix computations, we also perform full parameter estimation studies.

For this analysis, we consider three different physical systems (A,B,C) corresponding to different input equations of state (APR4 and H4), mass ratios (symmetric or asymmetric), and spins (zero or non-zero). The values of those injection parameters can be seen on the

JCAP07(2023)068

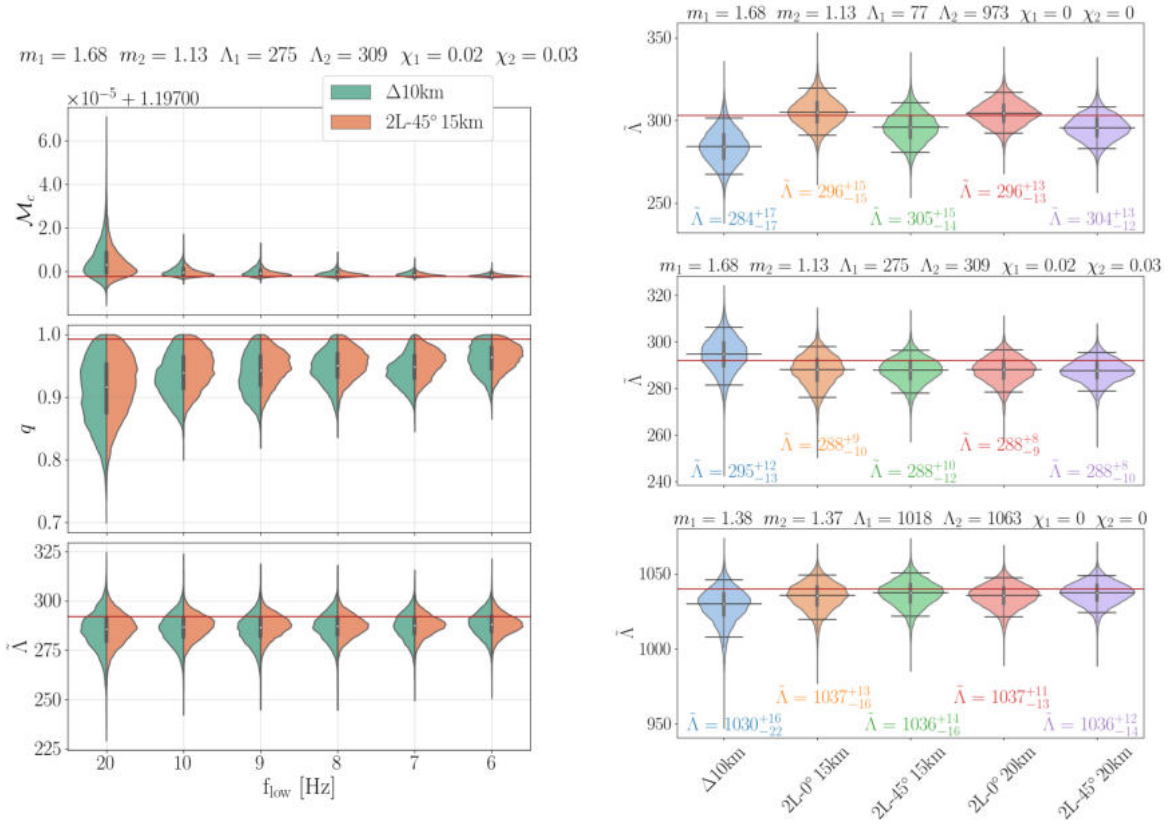

Figure 43. Left: constraints on the chirp mass $\mathcal{M}_c$, mass ratio q, and tidal deformability $\tilde{\Lambda}$ for a binary neutron star system with parameters listed at the top of the panel. A decreasing minimum frequency noticeably increases the accuracy of measuring the chirp mass and also has an important effect on determining the mass ratio but has a smaller effect on the measurement of the tidal deformability. Right: constraints on the tidal deformability for three different physical systems and different detector designs using an initial frequency of 6Hz.

Name	Injection model	m_1, m_2 [$M_\odot$]	$\mathcal{M}_c$ [$M_\odot$]	Λ_1, Λ_2	$\tilde{\Lambda}$	χ_1, χ_2
Source A	APR4	1.68, 1.13	1.19479	77, 973	303	0,0
Source B	APR4	1.38, 1.37	1.19700	275, 309	292	0.02, 0.03
Source C	H4	1.38, 1.37	1.19700	1018, 1063	1040	0, 0

Table 20. Source properties used for the full PE injections in section 6.2.2.

different panels of figure 43, and on table 20. The choice of the particular systems follows the injection study of [234] done by the LVK.

For these studies, we use the relative binning technique [235–237] to reduce the computational cost of our analysis. Figure 43 shows some of our main findings, and we refer to [238] for more details. We analyze signals injected in zero noise, to avoid the impact of fluctuations from noise when analyzing different starting frequencies. The left panel shows the impact of varying the initial frequency on the recovery of the chirp mass, the mass ratio, and the

JCAP07(2023)068

source	Geometry	$n_{\rm sat}$	$E_{\rm sat}$	$K_{\rm sat}$	$E_{\rm sym}$	$L_{\rm sym}$	$K_{\rm sym}$
source-A	2L 20km 0°	$0.164^{+0.005}_{-0.004}$	$-16.18^{+0.41}_{-0.40}$	228^{+34}_{-24}	$31.65^{+2.85}_{-2.15}$	$40.9^{+9.1}_{-13.9}$	-262^{+61}_{-70}
	Δ 10km	0.164^{+005}_{-007}	$-16.14^{+0.44}_{-0.42}$	229^{+27}_{-25}	$31.59^{+3.41}_{-2.99}$	$40.1^{+14.8}_{-15.1}$	-269^{+83}_{-70}
source-B	2L 20km 0°	$0.162^{+0.007}_{-0.007}$	$-16.06^{+0.54}_{-0.47}$	227^{+29}_{-27}	$30.91^{+2.69}_{-2.81}$	$42.0^{+21.9}_{-19.0}$	-197^{+155}_{-141}
	Δ 10km	$0.163^{+0.006}_{-0.007}$	$-16.05^{+0.53}_{-0.49}$	227^{+27}_{-26}	$30.86^{+3.34}_{-2.86}$	$40.9^{+17.1}_{-18.9}$	-208^{+165}_{-137}
source-C	2L 20km 0°	$0.155^{+0.005}_{-0.004}$	$-15.94^{+0.44}_{-0.56}$	236^{+21}_{-17}	$30.96^{+1.54}_{-2.06}$	$70.3^{+11.7}_{-10.3}$	74^{+78}_{-87}
	Δ 10km	$0.156^{+0.004}_{-0.005}$	$-15.92^{+0.47}_{-0.49}$	236^{+23}_{-19}	$30.92^{+1.58}_{-2.02}$	$70.8^{+11.2}_{-11.8}$	74^{+78}_{-87}

Table 21. Values for the nuclear-matter parameters up to second order in units of MeV except for $n_{\rm sat}$, which is in units of fm^{-3}. For ET, the two configurations leading to the smallest and largest uncertainties have been chosen; all other configurations give uncertainties in-between these.

source	Geometry	$R_{1.4M_\odot}$ [km]
source-A	2L 20km 0°	$11.44^{+0.13}_{-0.13}$
	Δ 10km	$11.34^{+0.15}_{-0.15}$
source-B	2L 20km 0°	$11.30^{+0.19}_{-0.21}$
	Δ 10km	$11.32^{+0.20}_{-0.20}$
source-C	2L 20km 0°	$13.69^{+0.07}_{-0.06}$
	Δ 10 km	$13.68^{+0.06}_{-0.07}$

Table 22. Radii (km) for $1.4M_\odot$ neutron stars as obtained for different geometries and different sources from the full parameter estimation runs under the nucleonic hypothesis. Again, as in table 21, only the geometries leading to the smallest and largest uncertainties, respectively, are shown here.

tidal deformability. Overall the width of the 90% confidence interval for the recovery of the chirp mass reduces by more than an order of magnitude when going from 20 to 6Hz, and also the size of the 90% confidence interval for the mass ratio shrinks by a factor of 2. However, the constraint on the tidal deformability reduces only by about 25%. *Comparing the* Δ10km *and the 2L* 15km *setup, we find that the 2L configuration is overall better for measuring tidal deformability by about 25%, where this difference is more or less independent of the initial frequency. As shown in [238], this is due mainly to the different arm lengths.* In the right panel of figure 43, we compare the $\tilde{\Lambda}$ posteriors for three different physical systems, and five different detector configurations. In this case, we use an initial frequency $f_{\rm low} = 10$ Hz for all the runs, and a noise simulated with the HFLF cryogenic sensitivity. We find that in general, the aligned or misaligned 2L detector configurations lead to similar results. The 2L configurations result in tighter bounds on $\tilde{\Lambda}$ than the Δ10km one; as above, these improvements arise mainly from the different arm lengths. It is also worth pointing out that the error on $\tilde{\Lambda}$ for the three selected sources, as reported in the right panel of figure 43, is consistent with that found by Fisher matrix calculations within a few percent, for the various detector configurations considered.

6.2.3 Connected uncertainty of nuclear-physics parameters

An immediate question is to what extent the different proposed configurations of the instrument can improve on our knowledge of nuclear matter and NS properties. In section 6.2.1 we have already discussed estimates for the uncertainties on the NS radius resulting from the different detector configurations. Here we will continue the discussion by analysing the full

JCAP07(2023)068

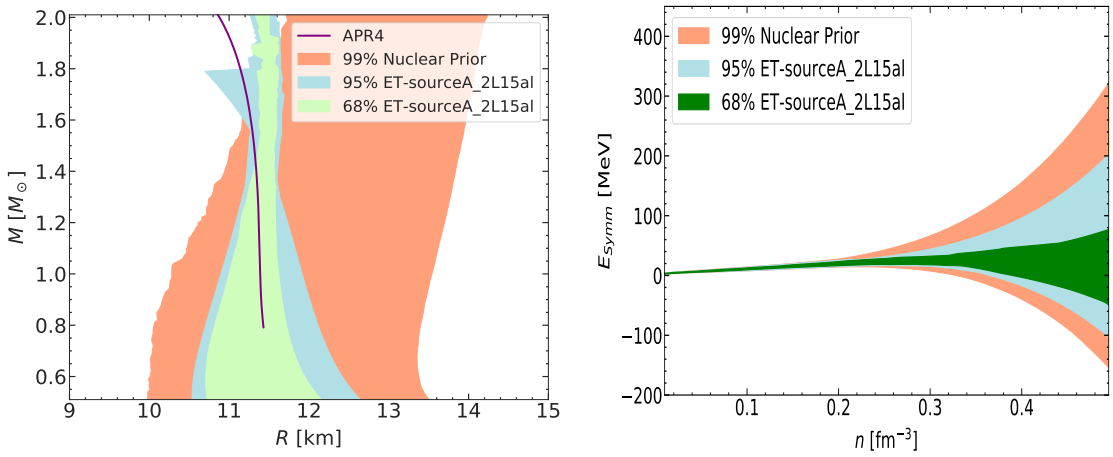

Figure 44. Posterior distribution for NS mass-radius relation (left) and the nuclear symmetry energy as function of baryon number density (right) for source A with geometry 2L -15 km with aligned arms. For comparison, the results obtained from the nuclear prior are also shown.

parameter estimation results for the three sources discussed above. As above, we employ the prior on the EoS from present-day nuclear physics knowledge [233] as a baseline. Because of the nuclear physics constraints, a number of popular equations of state might be only marginally compatible with our nuclear physics informed prior. This is particularly the case of the APR4 model, that was never confronted to nuclear physics data. This can be seen from the NS mass-radius relation shown in figure 44 (left panel) for source A and the 2L geometry with 15 km arm length. In this figure, we can see that the APR model predicts too small radii for the heaviest neutron stars, with respect to our nuclear prior.[33] This explains why the injection value is not precisely recovered in the posterior distribution. For this reason, the radius uncertainty estimation will not be reliable for the higher masses and is not analyzed in the following. In table 21 we summarise the posterior results for the different nuclear-matter parameters up to second order at saturation density with the three sources for the two configurations of the instrument leading to the smallest and largest uncertainty, respectively. These parameters represent the equilibrium density ($n_{\rm sat}$) and energy ($E_{\rm sat}$), the symmetry energy at saturation ($E_{\rm sym}$) and its slope ($L_{\rm sym}$), and the nuclear matter compressibility in the isoscalar ($K_{\rm sat}$) and isovector sector ($K_{\rm sym}$). For the symmetry energy, the posterior as a function of density is shown in figure 44 (right panel) for source A and the 2L geometry with 15 km arm length. The results indicate first of all that the injected properties are reasonably well recovered, even if the input model is only marginally compatible with our nuclear physics informed prior. On the scale of this figure, the differences between the proposed configurations of the instrument are insignificant and the 2L geometry is only slightly favored concerning the constraints on the nuclear-matter parameters.

In table 22 we summarise the posterior results for the NS radius at the fiducial mass 1.4 $M_\odot$. with the three sources for the two configurations of the instrument leading to the smallest and largest uncertainty, respectively. We can see that the uncertainties depend stronger on the injection model than on the configuration of the instrument. The absolute values are different from those obtained with the Fisher matrix approach, and reported in table 17 and 19. This is essentially due to the fact that the results in table 22 are

[33] In this figure, in order to allow for slightly smaller radii, we have relaxed the 2 solar mass constraint for the nuclear prior which is applied in figure 42 above.

JCAP07(2023)068

obtained on single events with very high SNR, which thus result in tight constraints on the source parameters, while the ones in section 6.2.1 are produced from runs on a full realistic population of sources, the vast majority of which have much higher statistical uncertainties, resulting in looser constraints on the EoS parameters. Also, we again stress that the results presented in table 17 are obtained through the extremely simplified metric in eq. (6.6), and should thus only be considered as indicative for the comparison of the various detector configurations.

To conclude, even if the quantitative uncertainties depend on many not fully controlled factors, from the NS mass-radius posterior shown in figure 44 (left panel), *the improvement with respect to current knowledge by Einstein Telescope is clearly seen.* In addition, the present analysis assumes at each time one detected source, i.e., an inspiral with two given masses, whereas the Einstein Telescope will detect tens of thousands of different BNS merger events with a distribution of NS mass. This staggering will considerably reduce the uncertainty on the density dependence of the dense matter EoS and hence the nuclear-matter parameters and the information on the NS radius; see also the discussion in section 6.2.1. *The impact of the instrument geometry on these conclusions is only marginal; as above, the results indicate that the 2L geometry is favored, but the difference with the other geometries is not significant.*

6.2.4 Postmerger detectability

A BNS system typically merges at a frequency of $\sim$ 1 kHz. After the merger, there are a number of physical processes, such as thermal effects, turbulences, phase transitions, magnetohydrodynamical instabilities, dissipative processes etc. [215, 239–244], which drive the postmerger physics leading to different remnants, depending on the masses of the neutron stars and EOS of the system. The merger remnant can be either a black hole, a hypermassive NS (HMNS), a supramassive NS (SMNS) or a massive NS. If the mass of the merger remnant is above a threshold mass it will collapse to a BH [245–247]. Otherwise, there is a post-merger gravitational-wave signal that can last over a time scale of about 10ms up to several 100ms [248] emitted at frequencies of $\sim 2-4$ kHz. While the postmerger signal from a BNS merger is not expected to be detectable for 2G detectors due to their insufficient sensitivity at high frequencies, it will be accessible to 3G detectors. Due to the complicated physical effects involved, postmerger signals are most accurately represented by numerical relativity (NR) simulations. For this study we will use NR waveforms [222, 249–252].

To determine the detectability of the postmerger signal with different detector configurations, we will compute and compare the SNR from the postmerger signal for a set of NR BNS waveforms as seen by the various configurations considered in this study. The postmerger SNR is defined as the SNR of the signal from the merger frequency [253] of the BNS system, up to 8192 Hz. We use a set of 6 BNS-NR waveforms from the SACRA catalogue [254], the masses and tidal deformabilities of which are given in table 23. For each detector geometry and PSD configuration, and each NR waveform, we use the same random set of 60 (ra, dec, ψ) values and quote the averaged postmerger SNR ($\rho_{\rm pm}^{\rm Avg}$) for each of the NR waveforms.

The left panel of figure 45 shows $\rho_{\rm pm}^{\rm Avg}$ for all the detector geometry — PSD combinations. for the system 15H_135_135_00155. As the high-frequency sensitivity of the HFLF cryo and HF-only PSDs are quite similar, the postmerger SNRs for these two PSDs are almost equal. We see the majority of variation occurring with varying arm-length for a given detector shape and changing detector shapes (triangular vs. 2L configurations). The maximum $\rho_{\rm pm}^{\rm Avg}$

JCAP07(2023)068

Configuration name	mass1	mass2	Λ_1	Λ_2
15H_135_135_00155	1.35	1.35	1211	1211
125H_107_146_0015	1.07	1.46	3196	535
H_117_156_00155	1.17	1.56	1415	238
H_135_135_00155	1.35	1.35	607	607
125H_121_151_00155	1.21	1.51	1621	435
H_118_155_00155	1.18	1.55	1354	249

Table 23. Table of the BNS-NR waveforms and their physical parameters used to compute the postmerger SNR.

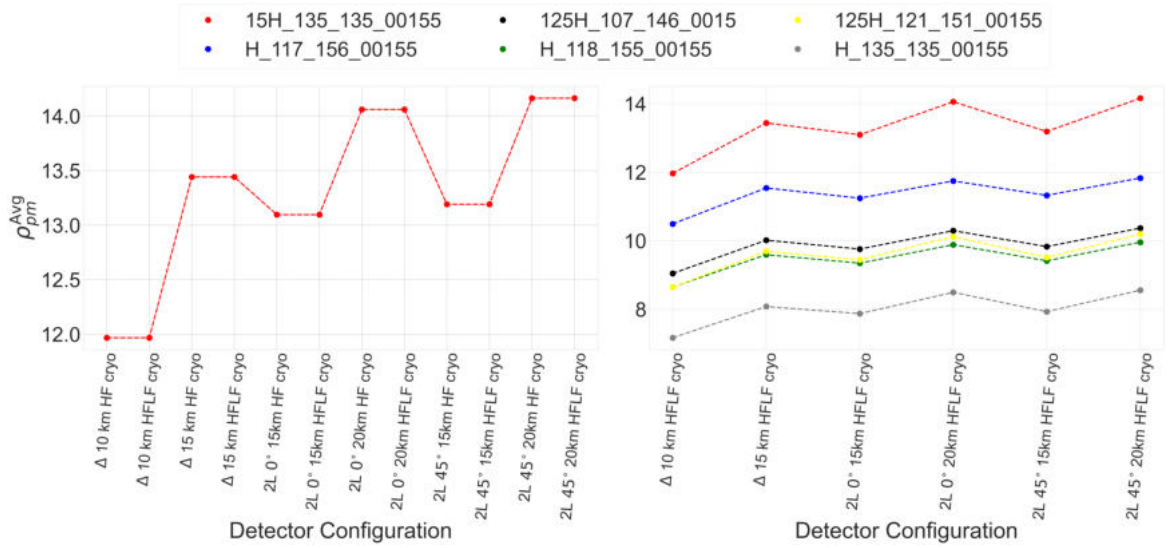

Figure 45. Left: averaged postmerger SNR for the 15H_135_135_00155 system for different detector configuration and PSD combinations. Right: averaged postmerger SNR for all the BNS-NR systems as given in table 23 for different detector configuration and HLFL cryo PSD. Each BNS-NR system is plotted with a different color with the detector configuration given on the x-axis.

for this system is seen by the 2L 45° 20km HLFL configuration which is $\sim 20\%$ larger than the minimum value, which corresponds the Δ 10km HF configuration.

The right panel of figure 45 shows $\rho^{\rm Avg}_{\rm pm}$ for all the BNS-NR systems for the different detector configurations and only the HFLF cryo PSD. For all the BNS-NR systems, 2L 20km 45° gives the highest postmerger SNR. For $\rho^{\rm Avg}_{\rm pm}$, there is not much difference between the SNR for 2L 0° and 45° (~ 0.7 %) irrespective of the arm length. Going from 15km 2L to 20km 2L gives a $\sim 6\%$ increase in $\rho^{\rm Avg}_{\rm pm}$. Between Δ 10 km and Δ 15 km, we see $\sim 11\%$ increase.

These results show that the performances of the different geometries are relatively similar within a $10-20\%$ *level, with 2L* 45° *20km detector configuration being the best for detecting postmerger signals.*

6.2.5 Conclusions: nuclear physics with ET

The Einstein Telescope will significantly advance our ability to constrain fundamental nuclear-physics properties, going well beyond the capabilities with any existing observatory

JCAP07(2023)068

or experiment, and providing complementary constraints to explore large domains of the QCD phase diagram. For example, the upgrade of the FAIR at the GSI Helmholtz Centre for Heavy Ion Research will probe matter which is only slightly neutron-rich and at lower baryon densities and higher temperatures than what is expected for ET, which can reach the most extreme densities. Furthermore, the X-ray observatory NICER and proposed future instruments, such as eXTP, Strobe-X or ATHENA will be able to improve on current knowledge of cold dense matter by observing more pulsars and increasing the length of the observational data period and thus obtain NS radii with a precision of a few percent, similar to the anticipated improvements with the existing advanced LIGO and advanced Virgo detectors (even in combination with KAGRA and LIGO India) or proposed upgrades such as LIGO A# and Virgo_next. ET, in addition to being able to determine NS radii with a statistical precision of sub-percent order due to the immense statistics with 10^5 mergers expected per year, will also be the only instrument able to add to the zero temperature β-equilibrated NS matter the information on the hot ultra-dense matter from the postmerger phase. *With regards to the payoffs for nuclear physics, there is no significant difference between the different detector configurations, with longer arm-lengths leading to slightly better results.*

6.3 Population studies

6.3.1 Merger rate reconstruction

Since ET will have a long distance range, it will see binary coalescences out to cosmological distances. Therefore, it will probe the merger rate up to high redshifts. Knowing how the BBHs are distributed in the Universe would help constrain their various formation channels, leading to a better understanding of how such binaries form [54, 255–258]. Different models exist, often assuming that the merger rate follows the star formation rate with some additional contribution coming from primordial black holes. Models differ in the details but most of them agree on the general shape of the distribution: the merger rate increases up to a redshift between 1 and 2 before decaying for higher redshifts (see [255, 258] for examples). The merger rate as a function of the redshift is written as [259]

$$\frac{dR}{dz}(z) = \rho(z)\frac{dV}{dz}\,, \tag{6.7}$$

where $V(z)$ is the comoving volume up to redshift z and

$$\rho(z) \propto \int_{t_d^{\min}}^{+\infty} \frac{\rho_*(z_f(z,t_d))}{1+z_f(z,t_d)} P(t_d) dt_d \tag{6.8}$$

is the binary formation rate, where ρ_* is the star formation rate, z is the redshift of interest, z_f is the redshift at which the binary is formed, t_d is the time delay between the formation of the binary and its merger, and $P(t_d)$ is the probability to have a given time delay.

To evaluate how well different configurations for ET would be able to identify the merger rate density, we follow a procedure similar to [260], with a theoretical population made of 10 years of BBHs as given by [258], and discussed in section 3. Then, we start by assigning a random sky location to the binaries. We compute their (network) SNRs and keep only the events with an SNR higher than 9 for a given configuration. The others are considered non-detectable. These events are then used to estimate the detector's efficiency as a function of the redshift. For each event, we perform a Fisher matrix analysis to obtain a multivariate Gaussian likelihood and sample from it to have an approximation for the

JCAP07(2023)068

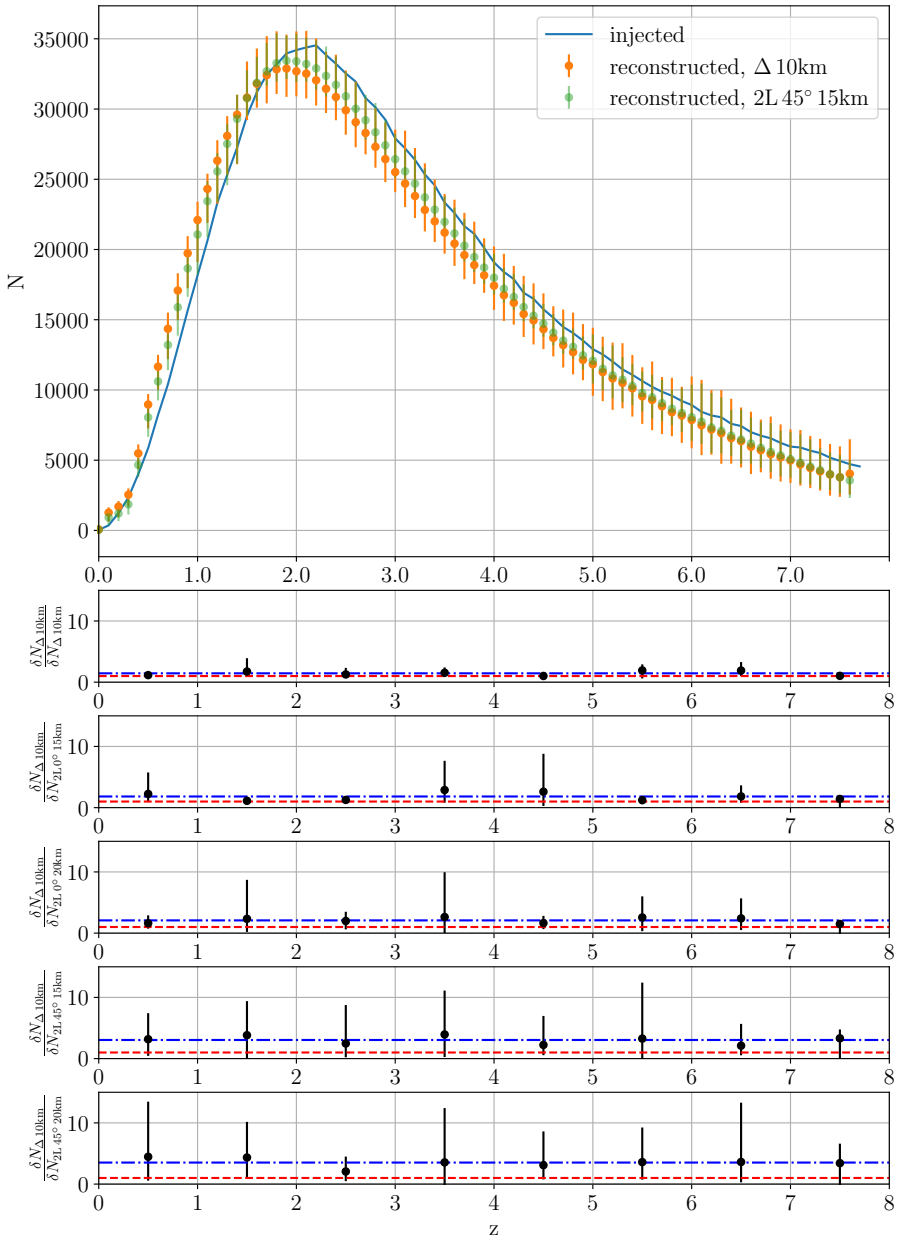

Figure 46. *Top:* representation of the reconstructed merger rate with the 90% confidence interval for 10 years of observation of ET in a triangular shape with 10km arms (orange) and ET with 2 L-shaped detectors with 15km arms at 45° (green). The blue line represents the true merger rate distribution. The two configurations enable one to reconstruct the merger rate but the accuracy is better for the 2 L-shaped detectors. *Bottom:* ratio of the width of the 90% confidence interval for the triangular 10km configuration with the other possible configuration. The red line corresponds to the case where the two detectors are equivalent, while the blue line is the average ratio. The hierarchy to be seen in this figure is that the 2-L aligned detectors are better than the triangular ones, and the 2L with arms at 45° are more accurate than the 2 L's with arms at 0°. For a given configuration, the increase in arm length gives a small improvement, mainly due to the increase in SNR.

JCAP07(2023)068

Other configuration	Ratio width 90% confidence interval
Δ 15 km	1.2
2 L 0° 15 km	1.8
2 L 0° 20km	2.0
2 L 45° 15 km	2.9
2 L 45° 20 km	3.3

Table 24. Mean values for the ratios of the 90% confidence intervals in the merger rate reconstruction between ET triangle with 10 km arm-lengths and the other possible configuration envisaged in this work. 2 L's are more accurate than one triangle, with L's rotated by 45° the one with respect to the other being better. This happens because of the reduced error on the sky location. For a given configuration, increasing the arm length by 5km does not strongly increase the accuracy since the only source of improvement is the increased SNR for the observed events.

JCAP07(2023)068

measurements [219]. For each detectable BBH, we make a Gaussian centered on the mean value of the recovered posterior (which corresponds roughly to the injected value since the result of a Fisher matrix is centered on the true value), with a width equal to the standard deviation of the luminosity distance posterior obtained from sampling the Fisher likelihood. We then draw a *measured* luminosity distance. This is done for all the detectable BBHs. Then, we convert the luminosity distances to redshifts and count the number of events that we have in the redshift bins. This gives an observed merger rate, which is then corrected by the efficiency to account for the number of mergers we theoretically expect to miss for each redshift bin. We repeat the drawing of measurements 250 times to get error bars on the observed merger rate.

The top panel of figure 46 shows the reconstructed merger rate for 10 years of detections with ET seen as a single triangle with 10 km arms versus ET as 2 L's with 15km arms and a 45° rotation between the two detectors. The other panels show the ratio in accuracy between the single triangle with 10 km arms and the other configurations considered in this work. *Although the two configurations lead to a correct reconstruction of the merger rate, one sees that the configuration made of 2* L*-shaped detectors leads to a more accurate reconstruction* as it has smaller error bars and closer central values. The increase in the ratio is such that a hierarchy can be established between the different configurations. 2 L's are better than a single triangle and L's rotated by 45° are better than aligned ones. Table 24 shows the mean ratio found between the detectors. The improvement from one detector configuration to the other is driven by a reduction in error on the luminosity distance. On the other hand, for a given configuration, 5 km longer arms are slightly better, which can be understood by the increased SNR of events. *Nevertheless, it is still possible to have a good grasp of the merger rate density for all the configurations within 10 years of observation.* This should be quite helpful in the quest to reveal the formation channels for BBH mergers.

6.3.2 Constraints on PBHs from high-redshift mergers

Primordial black holes (PBHs) may form in the early universe and represent a dark matter (DM) candidate (see e.g. ref. [261] for a review). Many constraints were set on their abundance in a wide range of masses [262] and recent GW detections suggest that, within standard scenarios, PBHs can only account for a subdominant DM component in the stellar mass range [122, 263–286]. Nonetheless, a discovery of a sub-population of PBHs would have fundamental consequences for our understanding of cosmology and particle physics (see e.g. [287–291]).

One "smoking-gun" signature of the primordial scenario is the production of high redshift mergers, which are unique targets of 3G detectors. The PBH model predicts a merger rate density that grows monotonically with redshift [267, 269, 271, 292, 293], with a power-law scaling of the form $R_{\rm PBH}(z) \propto [t(z)/t(z=0)]^{-34/37}$, where $t(z)$ indicates the age of the universe at redshift z. This rate evolution extends up to redshifts $z \gtrsim \mathcal{O}(10^3)$. On the contrary, even though large uncertainties are still present, astrophysical-origin mergers are generically not expected to occur at $z \gtrsim 30$ in standard cosmologies [294] (see also [124–127, 295–308]).

Recently, it was shown that a PBH population which may be compatible with a subset of the recent LVK observations would also lead to a large number of high-redshift detections at 3G experiments [280]. Observations of such distant events may be characterised by large measurement uncertainties on the inferred luminosity distance due to the low SNR [309–312]. However, focusing on constraining the merger rate evolution at redshift larger than $\mathcal{O}(10)$ may allow probing PBH populations up to abundances as low as $f_{\rm PBH} \approx 10^{-5}$ [313] in the solar mass range (even including the contamination of a population of Pop-III binaries), which would improve current capabilities by orders of magnitude. Therefore, the search for high-redshift primordial mergers is one of the scientific targets of the ET experiment.

In order to test the performance of different configurations to search and constrain a PBH population, we consider the benchmark PBH model resulting from the analysis in ref. [282]. The PBH model hyper-parameters are: $[M_c, \sigma]$ determining the PBH mass distribution, modeled as a lognormal function with mean M_c and width σ; the abundance $f_{\rm PBH}$ normalised with respect to the dark matter; the redshift $z_{\text{cut-off}}$ characterising PBH accretion [314]. These are assumed to be given by the population inference result of ref. [282], constraining the potential contribution from a PBH subpopulation to the GWTC-2 catalog and representing an upper bound on the PBH abundance in this mass range. In particular, we adopt $M_c = 34.54 M_\odot$, $\sigma = 0.41$, $f_{\rm PBH} = 10^{-3.64}$ and $z_{\text{cut-off}} = 23.90$, such that the PBH channel may be adequate in explaining around $(1-21)\%$ of the detections in the O1/O2/O3a run of LVC, and given the associated astrophysical models considered, the mass gap event GW190521.

We compute the number of detectable PBH events, $N_{\rm det}$, by estimating the detector network selection bias based on an injection of $N = 10^6$ events at redshift $z \geq 10$. We randomise event directions and orientations, and we assume negligible PBH spins (compatible with the prediction of the standard scenario at high redshift [271, 314, 315]). The computation is performed using the IMRPhenomHM waveform model. We set a detection threshold SNR ≥ 9. The minimum testable abundance is conservatively estimated by requiring at least one detectable event per year with $z \geq 30$ [280, 316]. This simplified approach provides an estimate of the ET capabilities which is consistent with actual population analyses, as performed in ref. [313].

We report the result of the analysis for the various configurations in tables 25, 26 and 27, detailing how the detection prospects change as a function of the configuration geometry, the inclusion of a single 40 km CE detector in the network, and removal of the low-frequency instrument, respectively. In each table, we indicate the number of detectable events above redshift $z > 10$ and $z > 30$, alongside the estimated minimum testable abundance. *The comparison of tables 25 and 27 shows the important of the LF instrument for the observation of PBH at large redshifts. In particular, without the LF instrument, there are no detection at $z \geq 30$, for all the geometries considered.*

The importance of the LF instrument when searching high redshift mergers can be intuitively understood by looking at figure 47, where we compare the signal amplitude for a

JCAP07(2023)068

Configuration	$N_{\rm det}(z>10)$ [1/yr]	$N_{\rm det}(z>30)$ [1/yr]	$f_{\rm PBH}^{\rm constrained}$ [$\times 10^{-5}$]
Δ-10km	**1140**	**77**	**2.61**
Δ-15km	1764	261	1.42
2L-15km-0°	1597	238	1.48
2L-15km-45°	1651	221	1.54
2L-20km-0°	1984	434	1.10
2L-20km-45°	2080	416	1.12

Table 25. Capabilities for constraining high-redshift PBH mergers of the various ET geometries (all taken with their HFLFcryo ASD). From left to right, columns report the number of detectable events per year at redshift larger than 10 or 30 assuming the PBH population from ref. [282]. The rightmost column reports the minimum testable PBH abundance, see more details in the main text. In bold we indicate the reference configuration.

Configuration	$N_{\rm det}(z>10)$ [1/yr]	$N_{\rm det}(z>30)$ [1/yr]	$f_{\rm PBH}^{\rm constrained}$ [$\times 10^{-5}$]
CE40km	1373	47	3.34
Δ-10km + CE40km	1940	180	1.71
Δ-15km + CE40km	2276	372	1.19
2L-15km-45° + CE40km	2210	333	1.26
2L-20km-45° + CE40km	2476	522	1.00

Table 26. Same as table 25 for four ET geometries in a network configurations including one 40km Cosmic Explorer. ET is only taken here in its HFLFcryo configuration.

Configuration	$N_{\rm det}(z>10)$ [1/yr]	$N_{\rm det}(z>30)$ [1/yr]	$f_{\rm PBH}^{\rm constrained}$ [$\times 10^{-5}$]
Δ-10km-HF	15	0.00	—
Δ-15km-HF	85	0.00	—
2L-15km-0°-HF	75	0.00	—
2L-15km-45°-HF	69	0.00	—
2L-20km-0°-HF	178	0.00	—
2L-20km-45°-HF	170	0.00	—

Table 27. Same as table 25 for configurations with the HF-only ASD.

merger with source frame mass $M_{\rm src}^{\rm tot} = 20 M_\odot$ located close to the horizon (i.e. having SNR = 9 in the Δ-10km-HFLF-Cryo configuration). Due to the large source redshift, the detector frame mass is redshifted by a large factor, and the majority of SNR can only accumulate in the LF portion of the sensitivity curve.

In order to fully exploit the high redshift smoking-gun signature of a PBH population of mergers, sufficient precision on the source distance is also necessary, to distinguish PBHs from potential Pop-III contaminants. The performance of ET on single-event-identification was studied in details ref. [309, 312] adopting a Bayesian parameter estimation. A limited precision on the source redshift may also impact the ability to reconstruct the merger rate

JCAP07(2023)068

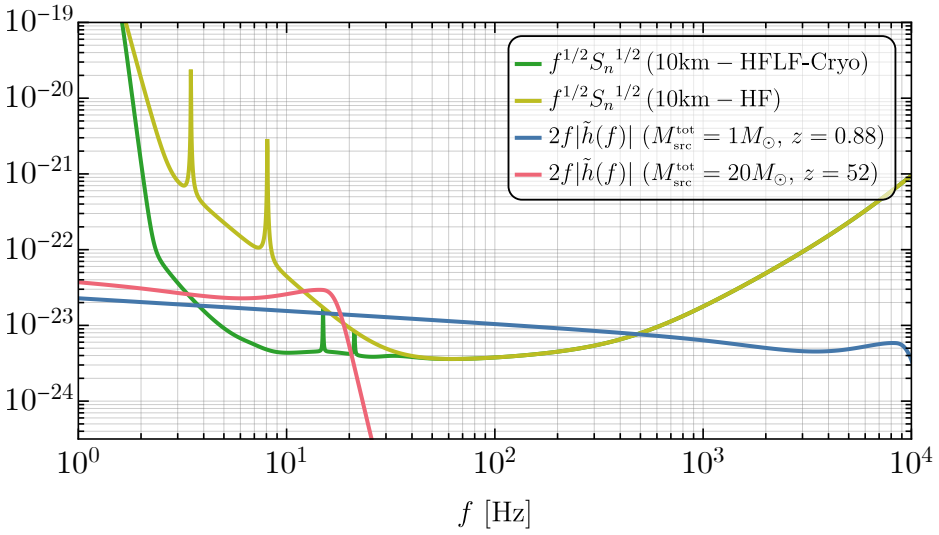

Figure 47. Comparison between the amplitude of a PBH binary signal $2f|\tilde{h}(f)|$ and the ET detector sensitivity curves $(fS_n)^{1/2}$ shown in green (10km-HFLF-Cryo) or yellow (10km-HF). We consider a distant merger with source frame mass $M_{\rm src}^{\rm tot} = 20M_\odot$ at $z = 52$. Also, we show a subsolar merger with $M_{\rm src}^{\rm tot} = 1M_\odot$ at $z = 0.88$. In both cases, we assume $q = 1$, optimal orientation of the binary and the redshift is fixed in order to have SNR=9 in the Δ-10km-HFLF-Cryo configuration.

evolution at high redshift within a population analysis, as shown in refs. [311, 313]. Based on a Fisher Matrix analysis, we compare the performance of different configurations in figure 48, which reports the maximum source redshift above which a relative precision on d_L better than 10% and 1% cannot be achieved. The relative error σ_{d_L}/d_L is highly impacted by the performance of the detector configurations at low frequencies and follows the general trend observed in the behaviour of the horizon (see figure 3) and number of detectable high redshift PBH events (i.e. tables 25, 26 and 27). We refer to [317] for further details on the analysis.

As far as the comparison of the performance of the various configurations is concerned, the results can be summarised as follows.

i) The 10 km triangle is the one that performs less well. In its full HFLF-cryo configuration, for the assumed PBH population, the 2L-15km-45° configuration would detect about three times more events with $z > 30$ than the 10 km triangle.

ii) A dramatic reduction in the number of high-redshift event is observed in the absence of the LF instrument, to the extent that no events are detected at redshifts $z > 30$, where a detection is identified as a PBH. This is also reflected in the behaviour of the uncertainties on the luminosity distance.

This is due to the reduced capabilities at small frequencies, where most of the high-z events are expected, as they are characterised by a large detector frame total mass.

6.3.3 Other PBH signatures

In this section, we analyse some other observables which may be crucial to discover/constrain the population of PBHs (see ref. [310] for a systematic overview and [317] for further details on the present analysis).

JCAP07(2023)068

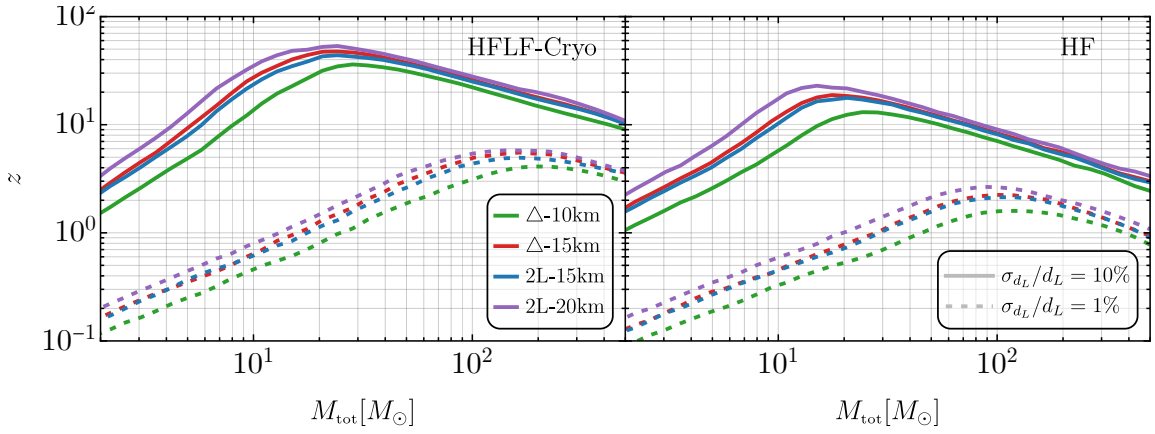

Figure 48. Contour lines of constant relative error on d_L as a function of source frame total mass $M_{\rm tot}$ and source redshift z. Different colors indicate different configurations while each panel (from left to right) assume HFLF-Cryo and HF, respectively. The solid (dashed) lines corresponds to $\sigma_{d_L}/d_L = 10\%$ (1%). We assume equal masses $m_1 = m_2$ and optimal orientation of the binary. As a consequence of setting $\iota = 0$, aligned and misaligned 2L configurations result in the same performance for this kind of estimation.

∘ **Subsolar mass range.** The distribution of PBH masses $m_{\rm PBH}$ is determined by the characteristic size and statistical properties of the density perturbations, corresponding to curvature perturbations generated during the inflationary epoch. Within this standard formation scenario, $m_{\rm PBH}$ is related to the mass contained in the cosmological horizon at the time of the collapse, and a wider range of masses is accessible compared to astrophysical BHs [318]. PBHs, in particular, can have subsolar masses, which are not expected from standard stellar evolution, while they can also populate the astrophysical mass gaps [291, 319, 320]. For masses $m_i \gtrsim 3M_\odot$ PBHs should be distinguished from stellar-origin BHs by mass-spin measurements [310, 314, 321]. The range $M_\odot \lesssim m_i \lesssim 3M_\odot$ can be distinguished from NS thanks to tidal deformability measurements (see section 6.1.3). Finally, the subsolar range represents a smoking-gun signature of the non-standard, i.e. potentially primordial, origin of a binary.[34,35]

The Einstein Telescope will dramatically extend the reach of current technology when searching for mergers with at least one component below the Chandrasekhar limit [316, 324]. In figure 49 we show the detection horizon in the subsolar mass range, extending figure 3 in the range of masses where only PBHs, white dwarfs, brown dwarfs, or exotic compact objects [187] (e.g. boson stars [325]) can appear. *As a large portion of the SNR is built up in the HF range of the sensitivity curve, the horizons are only slightly dependent on the LF instrument.* This feature is shown in figure 47, where we compare the signal amplitude for a subsolar merger with source frame mass $M^{\rm tot}_{\rm src} = 1M_\odot$ located close to the horizon (i.e. having SNR = 9 in the Δ-10km-HFLF-Cryo configuration).

[34] See, however, ref. [322] for models in which subsolar BHs are born out of dark sector interactions. Also, in this case, the detection of subsolar mergers would indicate new physics.

[35] While in the main text we focus on nearly equal mass mergers with $q \approx 1$, other potentially interesting systems for the detection of subsolar objects are intermediate mass ratio inspirals, given the high precision in measuring the mass of the light object at subpercent level [323]. Due to the relevance of the low-frequency range for these observations, the implementation of the LF interferometer could in principle enhance the capability of detecting these systems.

JCAP07(2023)068

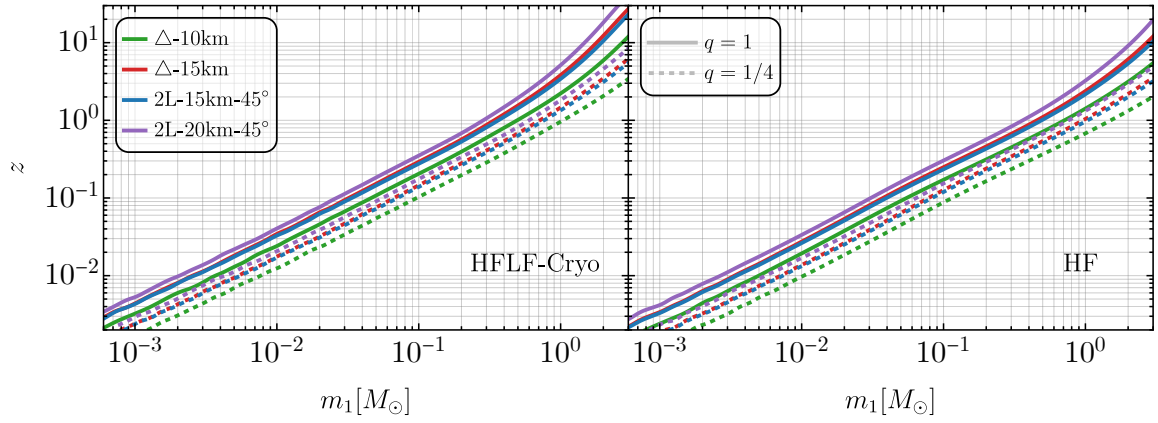

Figure 49. Detection horizons for non-spinning PBH binaries assuming a mass ratio $q = 1$ or $q = 1/4$, for the various detector configurations considered. This plot extends figure 3 in the sub-solar mass range, of interest for PBHs.

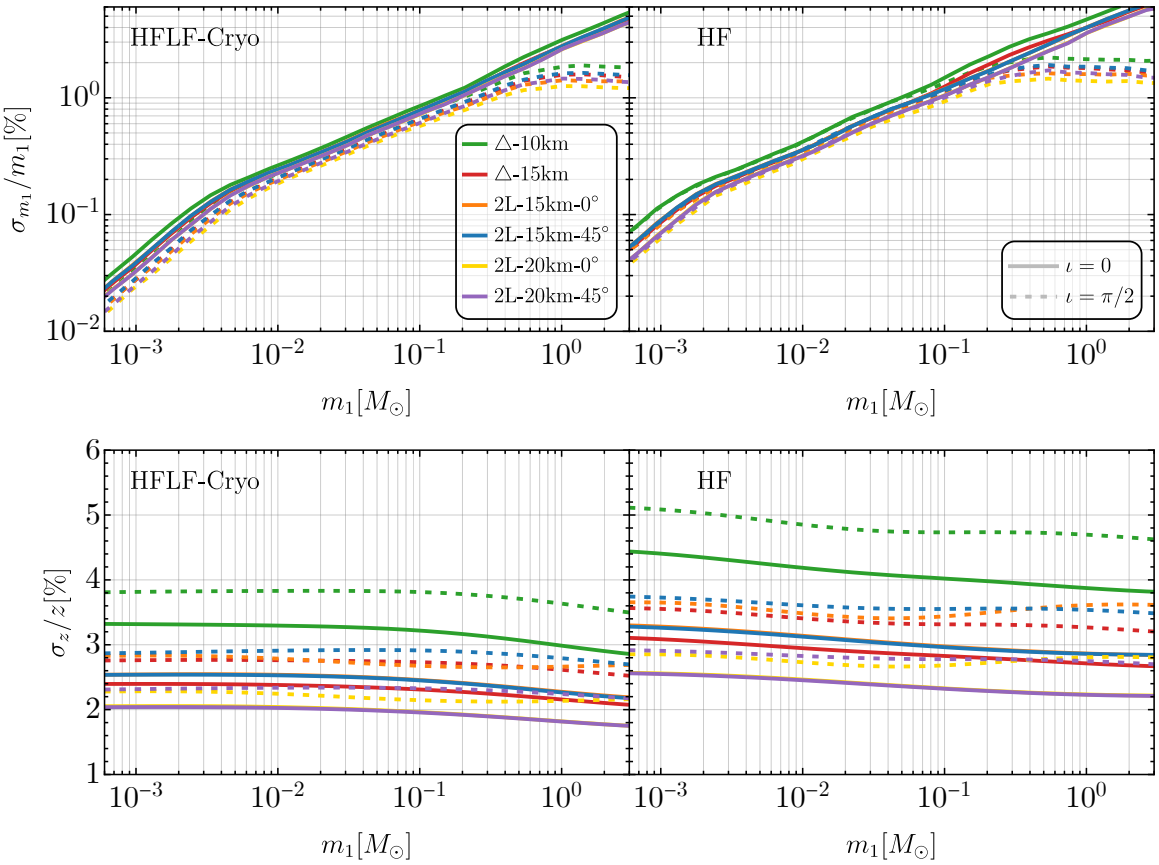

Figure 50. Relative error on the primary source frame mass (top) and source redshift (bottom) as a function of m_1 in the subsolar range. We consider a source located at a distance such that the SNR = 30 in the Δ-10km HFLF-Cryo configuration.

JCAP07(2023)068

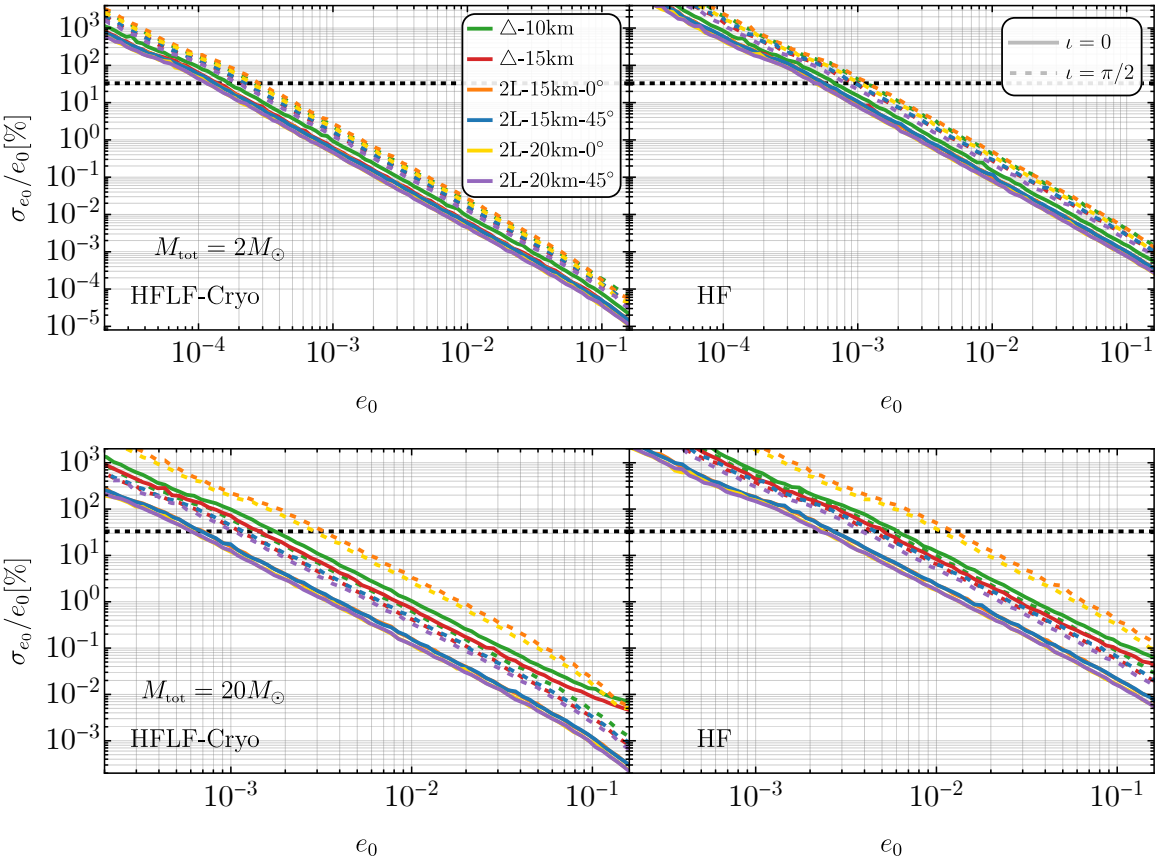

Figure 51. Relative error on the eccentricity e_0 at $f_0 = 10$Hz as a function of its injected value for a binary with a total source frame mass of $M_{\rm tot} = 2M_\odot$ and $d_L = 100$ Mpc in the upper panel, while $M_{\rm tot} = 20M_\odot$ and $d_L = 500$ Mpc in the lower panel. For the range of eccentricities in the horizontal axis (that are too large for PBH binaries), one is able to exclude (at 3σ level) a PBH origin for events that fall below the horizontal black dashed line.

In figure 50 we compare the performance of different ET configurations when measuring the source frame mass and distance of subsolar PBH mergers. In order to perform a proper comparison between different designs, for each mass m_1, we arbitrarily assume a source located at a distance fixed in order to have SNR= 30 in the Δ-10km HFLF-cryo configuration. We adopt the IMRPhenomHM waveform model and test both face-on ($\iota = 0$) and edge-on ($\iota = \pi/2$) binaries. *In this case we conclude that the loss of the LF sensitivity results only in a minor reduction of the uncertainty on m_1 and z. The length of the arms, which leads to a larger SNR, is the main factor responsible for the different performance of the various designs.*

∘ **Eccentricity measurements.** Another key prediction of the PBH model involves the eccentricity e. While formed with large eccentricity at high redshift [326, 327], PBH binaries then have enough time to circularize before the GW signal can enter the observation band of current and future detectors [310]. Therefore, PBH binary candidates must have small eccentricities. Let us mention here that, on a more general scope, the measurement of eccentricity may also inform us about the possible astrophysical formation pathway of a binary. While isolated formation channels predict small values of e in the observable range of

JCAP07(2023)068

frequencies of 3G detectors, dynamical channels predicts a fraction $\mathcal{O}(10\%)$ with $e > 0.1$ [54, 328–333]. This can be used to distinguish the origin of compact objects (see e.g. [334–337]).

To test the sensitivity of the various configurations to the measurement of a possible orbital eccentricity, we use the TaylorF2 inspiral-only waveform model [338–340] with the extension presented in [341] to account for a small eccentricity in the orbit. Using as reference values for the total source-frame mass $M_{\rm tot} = 2M_\odot$ and $20M_\odot$, for each detector configuration, we compute the relative error that can be attained on equal mass, non spinning systems, as a function of the eccentricity e_0 defined at $f_{0,\rm ecc} = 10$Hz. The distance to the source is fixed to $d_L = 100$ Mpc for the case $M_{\rm tot} = 2M_\odot$ and to $d_L = 500$ Mpc for the other. The results for the relative errors attainable on e_0 are reported in figure 51. *We notice, in particular, the great relevance of the LF instrument to perform eccentricity measurements.* This can be traced to the fact that eccentricity gives larger effects during the inspiral (i.e. at low frequencies) since when going closer to a merger, a binary system tends to circularize, with $e_0 \propto f_{\rm GW}^{-19/18}$. The range of values of e_0 shown on the horizontal axis of figure 51 corresponds to eccentricities that are too large for a PBH binary, that are expected to have $e_0 \sim 10^{-6}$ when they reach $f = 10$ Hz [310]. Therefore, in this range, if at the same time the relative error on e_0 for a given detection is sufficiently small, e.g. below the horizontal dashed line in the figure (which corresponds to $\Delta e_0/e_0 = 0.33$), one would be able to exclude that this event has a primordial origin.

The information in figures 49, 50 and 51 can be summarised as follows:

i) among the considered geometries, the triangle is the less performing giving e.g., uncertainties on the estimates of redshift about 1.4 times larger as compared to the 2L configurations, with both the considered ASDs.

ii) the LF instrument turns out to be of great relevance for the reconstruction of the eccentricity (with a gain in relative error that can be larger than one order of magnitude) and to a lesser extent also in the reconstruction of the masses and distances of sub-solar objects that, thanks to the LF sensitivity, can stay in the band for more cycles.

6.4 Cosmology

6.4.1 Hubble parameter and dark energy from joint GW/EM detections

In the context of cosmological studies, a key property of compact binary coalescences is that, from their GW signal, one can reconstruct the luminosity distance to the source [342]. Compact binary coalescences are then typically called 'standard sirens', by analogy with the 'standard candles' that provide absolute cosmological distance measurements from electromagnetic observations. Since the GW signal does not provide a direct measurement of the redshift, the ideal situation to constrain cosmological parameters is to measure the redshift of the host galaxy of the gravitational-wave source. Due to the poor localization capability of the gravitational-wave detectors, the host galaxy is typically identified only if we detect an electromagnetic counterpart (with some possible exceptions, see section 6.4.3). There are, however, a variety of statistical methods, based either on spatial correlations with galaxies or large-scale structures, or on features in the mass distribution of the sources, that can be used to extract cosmological information even in the absence of an electromagnetic counterpart [9, 343–371]. Standard sirens, either with counterpart or combined to statistical methods, allow us to measure the Hubble parameter H_0 at small redshifts while, at the larger redshifts that become accessible to a 3G detector, we can also explore the dark energy (DE) sector, through the study of the DE equation of state and of modified GW propagation. In

JCAP07(2023)068

this section we explore the relative potential of different ET configurations for cosmology, limiting ourselves to the study of GW sources with an electromagnetic counterpart, while in sections 6.4.2 and 6.4.3 we will discuss alternative possibilities. For this purpose, among the instruments discussed in section 4.2, the most useful are those which enable to obtain precise (spectroscopic) measurement of the host galaxy redshift. In particular, following the analysis in [372], we consider joint GW/EM detections between ET and THESEUS. We consider this instrument, for the detection of the associated short GRB, since the localisation capabilities ($\sim$ arcmin/arcsec) of both the XGIS and SXI instruments of THESEUS facilitate the follow-up by ground-based telescopes, guaranteeing a high chance of obtaining the redshift determination (see the discussion in section 4.2). We consider only the prompt emission (see tables 6 and 7 for the number of joint detection per year). We further consider the joint detections between ET and VRO, which is able to observe the kilonova emission produced by BNS mergers in the optical band and give a precise localization for accurate redshift measurements. As discussed in section 4, this allows us to study multi-messenger prospects for ET both at the high redhsifts probed by GRB observations and at $z \lesssim (0.3-0.4)$, where it will be possible to detect kilonova emission using wide field telescopes.

We stress that the absolute estimates for the accuracy that we will obtain below for H_0, as well as for the parameters describing the DE equation of state and modified GW propagation introduced in the following, should not be understood as forecasts for the overall capability of ET for measuring these cosmological parameters. We are focusing here only on standard sirens observed from two specific instruments (in this case, THESEUS and VRO). Apart from the fact that the results also rely on assumptions on their performances and specific observational strategies, other EM observatories are expected to operate together with ET, increasing the sample of detections and/or adding further complementary information. On top of this, 'dark sirens', i.e. coalescing binaries without an observed electromagnetic counterpart, can provide very significant information through various statistical techniques, as mentioned above. In particular, the correlation with galaxy catalogs already provides valuable cosmological information at the level of current LVC data: the statistical method has been applied to extract H_0 from the recent LIGO/Virgo detections in a number of papers [9, 359, 364, 373–376], and to studies of the DE sector in [359, 365, 377, 378]. These studies in the ET era will greatly benefit from Euclid and the Large Synoptic Survey Telescope (LSST) surveys by the VRO which will map billion of galaxies giving more precise photometric redshifts, and spectroscopic surveys by multi-object survey spectrographs such as WAVE or 4MOST. Furthermore, several other ideas have been put forward to extract cosmological information from ET, see e.g. [348–350, 355, 356, 362, 363, 377, 379]. Therefore, an assessment of the full capabilities of ET for estimating cosmological parameters must take into account all these opportunities. Here, we focus on two examples, the joint GW/EM detections by ET+THESEUS and by ET+VRO, with the purpose of evaluating the relative performances of different configurations of ET in these specific situations, rather than the absolute precision to which cosmological parameters can be reconstructed at ET.

For the ET+THESEUS analysis, the population of BNSs and the associated EM signal at high energies are generated following the approach in ref. [18]. Following the same approach adopted in section 4, we fix the EM signal for each BNS of the population, for the entire set of simulations corresponding to the different ET configurations and geometries. As a reference, we consider 5 years of observations, and we select from our simulation a sample of events, such that among them there are 75 joint detections with the configuration 2L 20 km HFLF cryo (see table 6). Considering the same BNS sample, we then compute the

JCAP07(2023)068

number of joint detections for all the other configurations. With this method, we are correctly evaluating the capabilities of the ET configurations considering all of them to have the same total observational time, the same BNS sample and the same EM signal. In this derivation, the duty cycle of each ET configuration is taken into account.

We have performed parameter estimation using both `GWFISH` [31] and `GWFAST` [17, 32], finding full agreement. A delicate point of the parameter estimation procedure is that the events that give a detectable GRB are close to face-on, where the degeneracy between the luminosity distance d_L and the inclination angle ι results in large errors on d_L, and often unreliable inversion of the Fisher matrices. This can be cured by imposing a prior on ι, which reflects the information that, if a jet was observed from cosmological distances, the binary was close to face-on. A full analysis of the corresponding selection effects is quite non-trivial, and is in progress. For this study, we observe that all the GRBs of our catalog have $|\iota| < (5-10)\,\mathrm{deg}$.[36] We also keep fixed the position of the source in the sky, having assumed that the host galaxy has been identified. We then use the simple (and common) prescription of setting $\Delta d_L/d_L = 2/\mathrm{SNR}$. This expression, with a factor of two included to be conservative, corresponds to the large SNR limit of the Fisher-matrix analysis when all other parameters are fixed. Since ι and the position in the sky are the parameters that are most degenerate with d_L, once these are kept fixed or strongly constrained by priors, this limiting value can become a reasonable approximation. A more detailed study on this is in progress. We then add in quadrature an error $\Delta d_L/d_L = 0.05z$ due to lensing, as in [380, 381] (see also [382] for more recent justification). From the value of z of a joint GW+EM event of our catalog, we then compute the nominal value of its luminosity distance using a fiducial ΛCDM model (we use the fiducial values $H_0 = 67.66\,\mathrm{km\,s^{-1}\,Mpc^{-1}}$ and $\Omega_M = 0.31$, from *Planck-2018* [383]), and the error Δd_L from the above procedure and then, in order to simulate the realistic setting of an experiment, we scatter the 'observed' value of d_L using a Gaussian distribution with the given Δd_L.

In a similar way, we study the capabilities of the synergy between ET and VRO. The population of sources and their respective KN emission are generated through the procedure described in section 4. In this case, the number of events considered corresponds to one year of observations, rather than 5, due to the larger number of potential joint detections (see section 4 and table 10 for details). We consider the observational strategy consisting on following-up all the events localized with $\Delta\Omega_{90\%} < 40\ \mathrm{deg}^2$, two filter ($g$ and i) observations repeated the first and second night after the merger and an exposure time for each pointing of 600 s. In particular, for each configuration we consider a number of sources matching the ones reported in column 3 of table 10. Note that, thanks to its isotropic nature, the KN emission can be observed irrespectively of the binary inclination, resulting in a sample of events with better conditioning for the Fisher matrix analysis, thanks to a milder degeneracy between ι and d_L.

We now present the results obtained for $(H_0, \Omega_{m,0})$, for the DE equation of state, and for modified GW propagation.

Hubble constant. In a flat ΛCDM model, the relation between the luminosity distance d_L and the redshift is

$$d_L(z) = \frac{c}{H_0}\,(1+z)\int_0^z \frac{d\tilde{z}}{\sqrt{\Omega_M(1+\tilde{z})^3+\Omega_\Lambda}}\,, \tag{6.9}$$

[36] More precisely, to take into account the periodicity of ι, they have $\min(\iota, 180^\circ - \iota) < (5-10)\,\mathrm{deg}$.

JCAP07(2023)068

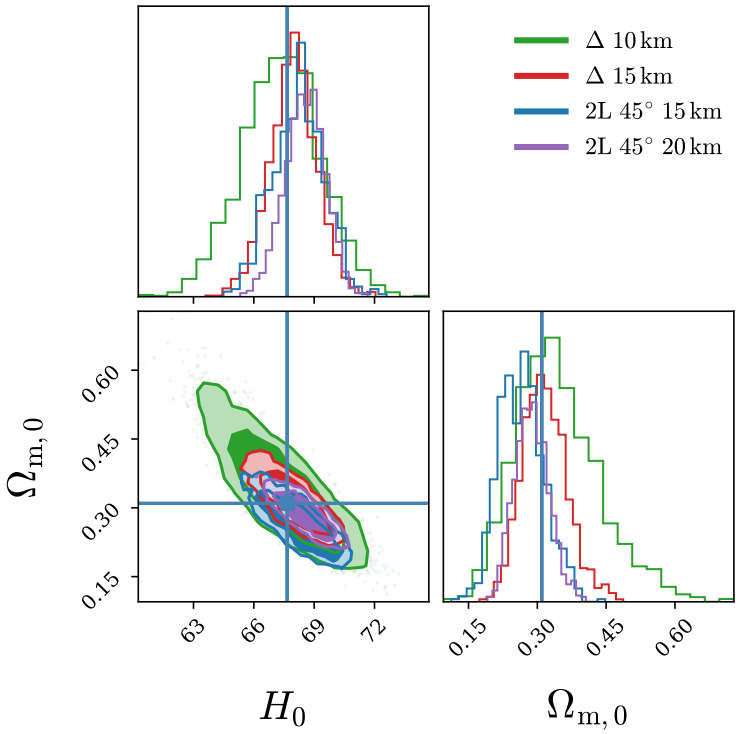

Figure 52. Reconstruction of the parameters H_0 and Ω_M in ΛCDM, from the joint GW+EM events obtained with ET+THESEUS in 5 yr of observations, for the different geometries of ET shown, all with their HFLF-cryo sensitivity.

Configuration	$\Delta H_0/H_0$	$\Delta\Omega_M/\Omega_M$
Δ-10km	0.057	0.546
Δ-15km	0.035	0.290
2L-15km-45°	0.040	0.370
2L-20km-45°	0.029	0.276

Table 28. Relative errors on H_0 and Ω_M in ΛCDM (median and symmetric 68% CI), from the joint GW+EM events obtained with ET+THESEUS, for the different geometries of ET shown, all with their HFLF-cryo sensitivity. We stress that no prior from electromagnetic observations, such as CMB+BAO+SNe, is used here; with such priors, the accuracy on H_0 becomes sub-percent.

where Ω_M is the present matter fraction and Ω_Λ is the energy density fraction associated with the cosmological constant (we neglect the contribution from radiation, which is completely negligible at the redshifts relevant for standard sirens. In this approximation $\Omega_\Lambda = 1 - \Omega_M$ for a flat ΛCDM cosmology). At low redshift this reduces to Hubble's law $d_L(z) \simeq (c/H_0)z$, so standard sirens at low redshift can allow us to measure H_0.

The first measurement of H_0 from a standard siren with counterpart has been obtained from GW170817 [384]. However, the error from this single detection is still too large to discriminate between the value of H_0 obtained from late-Universe probes [385, 386], and that inferred from early-Universe probes assuming ΛCDM [387, 388], which are currently in disagreement at 5.3σ level.

JCAP07(2023)068

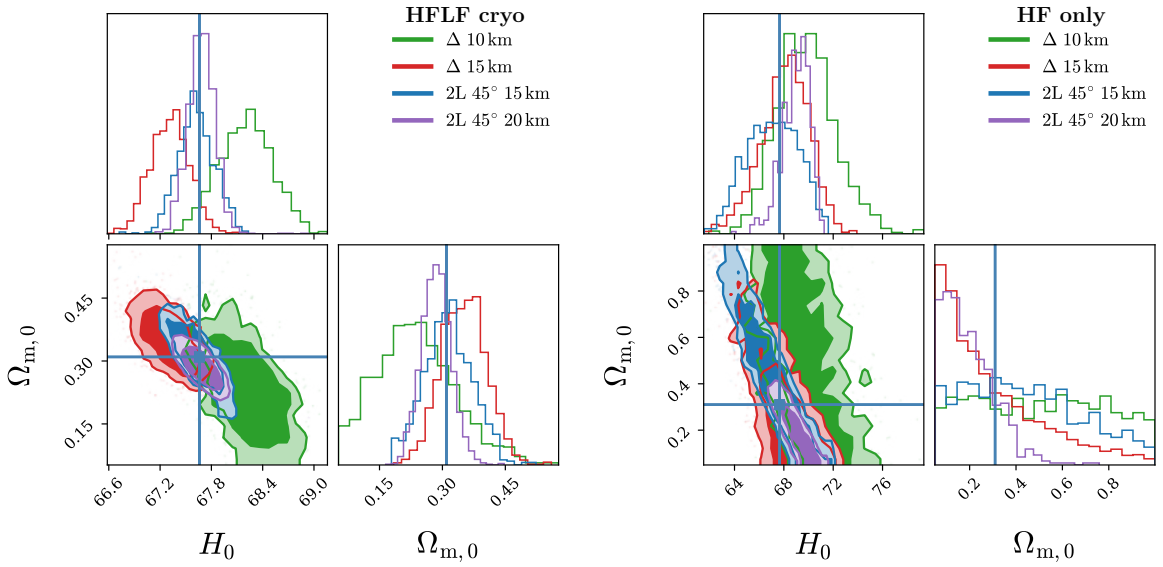

Figure 53. Reconstruction of the parameters H_0 and Ω_M in ΛCDM, from the joint GW+EM events obtained with ET+VRO in 1 yr of observations, for the different geometries of ET shown, in the left panel with their HFLF-cryo sensitivity and in the right panel with the HF instrument only.

HFLF cryogenic		
Configuration	$\Delta H_0/H_0$	$\Delta\Omega_M/\Omega_M$
Δ-10km	0.009	0.832
Δ-15km	0.007	0.303
2L-15km-45°	0.006	0.370
2L-20km-45°	0.004	0.243

HF only		
Configuration	$\Delta H_0/H_0$	$\Delta\Omega_M/\Omega_M$
Δ-10km	0.065	1.23
Δ-15km	0.057	1.86
2L-15km-45°	0.066	1.31
2L-20km-45°	0.031	1.22

Table 29. Relative errors on H_0 and Ω_M in ΛCDM (median and symmetric 68% CI), from the joint GW+EM events obtained with ET+VRO in 1 yr of observations, for the different geometries of ET shown, in the left table with their HFLF-cryo sensitivity and in the right table with the HF instrument only.

Our results for H_0 and Ω_M are shown in figure 52 and table 28 for ET+THESEUS (that shows the result of a typical realization of the catalog of joint detections, among several that we have generated), and in figure 53 and table 29 for ET+VRO. We should stress that these are the results obtained from standard sirens only, without any prior from cosmological electromagnetic probes. Of course, CMB, BAO, SNe, structure formation, and other electromagnetic probes provide much stronger constraints on Ω_M; assuming ΛCDM, *Planck-2018* fixes $\Omega_M = 0.315 \pm 0.007$ [383], i.e. $\Delta\Omega_M/\Omega_M \simeq 0.022$, much smaller than what can be obtained from standard sirens alone. In principle, one could then combine cosmological and standard sirens data, as in [372], reducing significantly the error on H_0.[37] In any case, for our present

[37]The limits on H_0 reported here, obtained from GWs+GRB only, are consistent with the results in [372], after taking into account that we are considering 5 years of data (which is more consistent with updated estimates for the expected duration of the THESEUS mission), while the data in [372] were relative to a 10 yr period, and that we use a model for short GRBs normalized to the observations (which takes into account the fact that not all BNS merger produce a GRB), resulting in a smaller number of joint GW+GRB detections. As shown in [372], if one further combines the constraints from joint GW+EM detection with purely

JCAP07(2023)068

purpose of comparing the different geometries, figures 52 and 53 and tables 28 and 29 contain the information that we need, on the relative performances of the different ET configurations.

We see that the best results for H_0 are obtained by ET+VRO, whose detections are potentially more numerous and at small redshift, where the impact of H_0 is bigger. However, we notice that the results obtained for THESEUS are very solid and conservative: they are based on the current observations of short GRBs and consider only the prompt emission (including the afterglow detections by XGIS and SXI will increase the detections per year by a factor of about 3). In contrast, the VRO estimates strongly depend on the BNS merger rate normalization (which, on the basis of the GW observations by the LIGO and Virgo detectors, can be one order of magnitude smaller or larger).

Concerning the comparison of configurations we find that *the triangle-15km and the* 2L-*15km-45° have quite similar accuracy on* H_0 *for this test, and improve by a factor* $\sim (1.3-1.6)$ *the result of the 10 km triangle, for* ET+THESEUS *and* ET+VRO *(with* ET *taken in both cases in the* HFLF-cryo *configuration). From the* ET+VRO *results, we also see the huge impact of the* LF *instrument, which allows us to observe a larger number of sources with good localization and results in constraints more than a factor of 7 tighter on* H_0 *and more than a factor of 2 tighter on* $\Omega_{m,0}$.

Observe that the reduction of joint ET+VRO detections is dramatic if we lose the low-frequency: only 6% of the events detected by the triangle-10 km HFLF-cryo, and only 11% of those detected by the 2L-15km HFLF-cryo, are observed by the corresponding HF-only configurations, see columns 4 of table 11 and table 10. In contrast, for the joint ET+THESEUS detections the reduction is much smaller: 60% of the events detected by the triangle-10 km HFLF-cryo and 70% of those detected by the 2L-15km HFLF-cryo are observed by the corresponding HF-only configurations, see columns 4 of table 11 and table 10. Taking into account that the detections are distributed in the same redshift range (see for example figure 24), the observations of THESEUS together with ET-HF become comparable to those obtained by THESEUS together with ET at full HFLF-cryo sensitivity, in a observation time longer by a factor ~ 1.5 (which could also be partly compensated if the duty cycle of the HF-only instrument will be larger than that of the full HFLF-cryo configuration).

Dark energy equation of state. An accurate measurement of the Hubble parameter with GWs would be of course very interesting a priori. However, it is in principle possible (although by no means guaranteed) that, by the time that 3G detectors will be operative, the discrepancy on H_0 between late-Universe and early-Universe probes might have already found a resolution. More specific to 3G detectors is the possibility of testing the cosmological model with GWs up to moderate and large redshifts, where signatures of a dynamical dark energy could be found.

In general, on cosmological scales, one performs a separation between the homogeneous Friedmann-Robertson-Walker (FRW) background, and scalar, vector and tensor perturbations over it; tensor perturbations, when they are well inside the cosmological horizon, are just GWs propagating on the FRW background. Whenever gravity is modified on cosmological scales, both the background evolution and the dynamics in the sectors of scalar and tensor perturbations are modified (vector perturbations usually decay and are irrelevant). Here we discuss the effect of dark energy on the background evolution, which, as we will recall, can be described by an effective dark energy (DE) equation of state, while below we will discuss the modification of the tensor sector related to modified GW propagation.

electromagnetic observations from CMB, BAO, SNe, etc, the accuracy on H_0 reaches the subpercent level.

JCAP07(2023)068

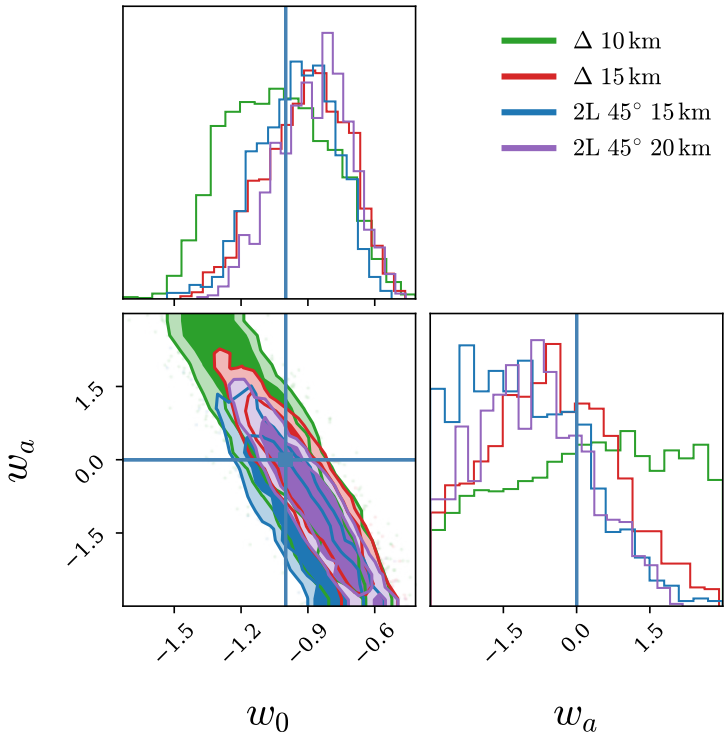

Figure 54. Reconstruction of the DE equation of state parameters w_0 and w_a, from the joint GW+EM events obtained with ET+THESEUS in 5 yr of observations, for the different geometries of ET shown, all with their HFLF-cryo sensitivity.

Configuration	Δw_0	Δw_a
Δ-10km	0.49	3.81
Δ-15km	0.40	2.65
2L-15km-45°	0.35	2.55
2L-20km-45°	0.34	2.40

Table 30. Absolute errors on the DE equation of state parameters w_0 and w_a (symmetric 68% CI), from the joint GW+EM events obtained with ET+THESEUS, for the different geometries of ET shown, all with their HFLF-cryo sensitivity.

At the background level, the effect of a dynamical dark energy component is described by the DE density $\rho_{\rm DE}(z)$ and by its pressure $p_{\rm DE}(z)$. Equivalently, one can introduce the DE equation of state $w_{\rm DE}(z)$, defined by $p_{\rm DE}(z) = w_{\rm DE}(z)\rho_{\rm DE}(z)$. The standard ΛCDM model is recovered for $w_{\rm DE}(z) = -1$. Using the conservation of the DE energy-momentum tensor, one finds that the DE density is given as a function of redshift by

$$\rho_{\rm DE}(z) = \rho_0 \Omega_{\rm DE} \exp\left\{3\int_0^z \frac{d\tilde{z}}{1+\tilde{z}}\left[1+w_{\rm DE}(\tilde{z})\right]\right\}, \tag{6.10}$$

where $\Omega_{\rm DE} = \rho_{\rm DE}(0)/\rho_0$ is the DE density fraction and $\rho_0 = 3H_0^2/(8\pi G)$ is the critical density. At the background level, the properties of DE are therefore encoded just in one function $w_{\rm DE}(z)$. The corresponding expression for the luminosity distance (neglecting again

JCAP07(2023)068

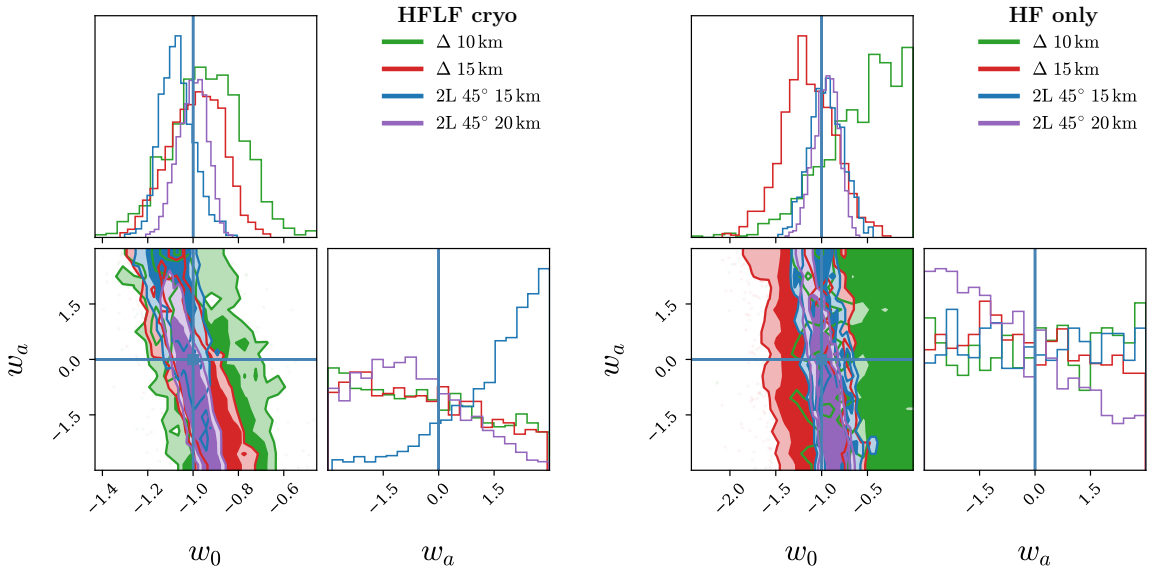

Figure 55. Reconstruction of the DE equation of state parameters w_0 and w_a, from the joint GW+EM events obtained with ET+VRO in 1 yr of observations, for the different geometries of ET shown, in the left panel with their HFLF-cryo sensitivity and in the right panel with the HF instrument only.

HFLF cryogenic		
Configuration	Δw_0	Δw_a
Δ-10km	0.31	3.92
Δ-15km	0.23	3.69
2L-15km-45°	0.14	2.49
2L-20km-45°	0.13	2.89

HF only		
Configuration	Δw_0	Δw_a
Δ-10km	0.85	4.26
Δ-15km	0.56	3.84
2L-15km-45°	0.37	4.13
2L-20km-45°	0.27	3.52

Table 31. Absolute errors on the DE equation of state parameters w_0 and w_a (symmetric 68% CI), from the joint GW+EM events obtained with ET+VRO, for the different geometries of ET shown, in the left table with their HFLF-cryo sensitivity and in the right table with the HF instrument only.

radiation) is

$$d_L(z) = \frac{c}{H_0}(1+z)\int_0^z \frac{d\tilde{z}}{\sqrt{\Omega_M(1+\tilde{z})^3 + \rho_{\rm DE}(\tilde{z})/\rho_0}}\,, \tag{6.11}$$

and reduces to eq. (6.9) when $\rho_{\rm DE}(\tilde{z})$ is a constant, i.e. when $w_{\rm DE}(z) = -1$. Any redshift dependence of $\rho_{\rm DE}$, i.e. any deviation of the DE equation of state from the ΛCDM value $w_{\rm DE} = -1$, would provide evidence for a dynamical dark energy.

In general, it is difficult to extract from the data a full function of redshift, such as $w_{\rm DE}(z)$, and a parametrization in terms of a small number of parameters is useful. For the DE equation of state a standard choice is the (w_0, w_a) parametrization [389, 390],

$$w_{\rm DE}(z) = w_0 + \frac{z}{1+z} w_a\,. \tag{6.12}$$

Combining eq. (6.11) with eqs. (6.10) and (6.12), from the measurements of the luminosity distance and redshift of an ensemble of sources we can perform the inference on the cosmolog-

JCAP07(2023)068

ical parameters H_0, Ω_M, w_0, w_a. The constraining power of GWs alone is too weak to provide useful information on all these parameters (as we already saw just for (H_0, Ω_M) in table 28), so one is obliged to combine standard sirens with other cosmological probes. In this context, it is then common to assume that H_0, Ω_M are simply fixed, or strongly constrained by priors obtained from electromagnetic probes, and keep only (w_0, w_a) in the inference. Several forecasts of (w_0, w_a) for ET already exist in the literature [372, 380, 381, 391]. Here we present updated results using our catalog of joint ET+THESEUS detections, for the various ET geometries considered, as well as ET+VRO for the various geometries and the two ASDs (as we saw above, in the case of ET+THESEUS, the loss of the LF instrument is much less dramatic, and basically can be compensated by increasing by a factor ~ 1.5 the observation time, which does not affect the relative performances of the geometries). The results are shown in figure 54 and table 30 for ET+THESEUS and in figure 55 and table 31 for ET+VRO.[38]

For ET+THESEUS*, we see that the differences in performances are not large between the various geometries: the* 2L *15km* 45° *and the* 2L *20km* 45° *are quite comparable and slightly better than the 15-km triangle, while the 10 km triangle performs less well (e.g. by a factor 1.4 on* w_0*, with respect to the* 2L *15km* 45°*). For* ET+VRO *the situation is similar, with slightly larger differences (the 10 km triangle performs less well, with respect to the* 2L *15km* 45°*, by a factor 2.2 on* w_0*). We also notice again the improvement brought by the LF instrument for the VRO+ET case, with results tighter on* w_0 *by a factor* $\sim (2.4 - 2.7)$*, depending on the geometry.*

Modified GW propagation. As we have discussed, the DE equation of state characterizes the impact of dark energy on the background evolution and, as such, can also be studied with purely electromagnetic probes. Current *Planck-2018* analysis from CMB, combined with SNe and BAO, including both w_0 and w_a in the inference, find $w_0 = -0.961 \pm 0.077$ and $w_a = -0.28^{+0.31}_{-0.27}$ (68% c.l.) [383]. While GW observation can provide an independent probe of these quantities, it is not evident that even 3G detectors will be able to improve quantitatively on these accuracies. As we see from tables 30 and 31, this is certainly not the case for the specific example of joint ET+THESEUS or ET+VRO observations that we are considering, where we are well above the $\sim 7\%$ accuracy on w_0 that we already have from CMB+BAO+SNe. For instance (recalling that in ΛCDM $w_0 = -1$, so the absolute errors on w_0 reported in tables 31 and 30 are the same as the relative errors), for ET+VRO the configuration 2L-15km-45° reaches an accuracy on w_0 of 14%, while the 10 km triangle of 31%.

As emphasized in [391, 392], in the tensor sector the situation is different, and potentially much more interesting, for two reasons: (1) Modified GW propagation can only be tested from GW observations at large redshift, and therefore current limits (see below) are much broader. (2) There exist phenomenologically viable and theoretically motivated modified gravity models [393] that comply with all observational bounds at the background level and in the scalar perturbation sector (where, therefore, they differ from ΛCDM by at most a few percent level) and, nevertheless, in the tensor sector predict deviations from GR and ΛCDM that could be as large as 80% [394, 395].

The effect is due to a modification of the equation that governs the propagation of tensor perturbations over FRW. In GR, this is given by

$$\tilde{h}_A'' + 2\mathcal{H}\tilde{h}_A' + c^2 k^2 \tilde{h}_A = 0\,, \tag{6.13}$$

[38] The results for ET+THESEUS, obtained with `GWFAST`, have been double-checked using `TiDoFM`, finding broad agreement.

JCAP07(2023)068

Configuration	$\Delta\Xi_0/\Xi_0$	Δn
Δ-10km	0.071	2.87
Δ-15km	0.040	3.01
2L-15km-45°	0.049	2.91
2L-20km-45°	0.030	3.12

Table 32. Errors on the parameters Ξ_0 and n that describe modified GW propagation (median and symmetric 68% CI), from the joint GW+EM events obtained with ET+THESEUS, for the different geometries of ET shown, all with their HFLF-cryo sensitivity.

where $\tilde{h}_A(\eta, \mathbf{k})$ is the Fourier-transformed GW amplitude, $A = +, \times$ labels the two GW polarizations, the prime denotes the derivative with respect to cosmic time η [which is defined by $d\eta = dt/a(t)$], $a(\eta)$ is the FRW scale factor, and $\mathcal{H} = a'/a$. Whenever gravity is modified on cosmological scales, unavoidably this propagation equation is also modified, as has been seen on many explicit examples [394–402]. A change in the coefficient of the $k^2\tilde{h}_A$ term induces a speed of GWs, $c_{\rm gw}$, different from that of light. After the observation of GW170817, this is now excluded at a level $|c_{\rm gw} - c|/c < \mathcal{O}(10^{-15})$ [3]. However, the modified gravity models that pass this constraint still, in general, induce a change in the 'friction term', so the propagation equation for tensor modes becomes,

$$\tilde{h}_A'' + 2\mathcal{H}[1 - \delta(\eta)]\tilde{h}_A' + c^2k^2\tilde{h}_A = 0\,, \tag{6.14}$$

for some function $\delta(\eta)$ that encodes the modifications from GR. In GR, using eq. (6.13), one finds that the GW amplitude decreases over cosmological distances as the inverse of the FRW scale factor. From this one can show that, after propagation from the source to the observer, the amplitude of the GW from a compact binary coalescence is proportional to the inverse of the luminosity distance to the source (see, e.g. section 4.1.4 of [403]). This is at the origin of the fact that compact binaries are standard sirens, i.e. that the luminosity distance of the source can be extracted from their gravitational signal. However, when the GW propagation is rather governed by eq. (6.14), this result is affected. It can then be shown that the quantity extracted from GW observations is no longer the standard luminosity distance $d_L(z)$ of the source [that, in this context, we will denote by $d_L^{\rm em}(z)$, since this is the quantity that would be measured, for instance, using the electromagnetic signal from a counterpart]. Rather, the quantity extracted from GW observation is a 'GW luminosity distance' $d_L^{\rm gw}(z)$ [392], related to $d_L^{\rm em}(z)$ by [391, 392]

$$d_L^{\rm gw}(z) = d_L^{\rm em}(z)\exp\left\{-\int_0^z \frac{dz'}{1+z'}\,\delta(z')\right\}\,, \tag{6.15}$$

where the function δ that appears in eq. (6.14) has now been written as a function of redshift.

Similarly to what we have discussed for the DE equation of state, inference on a full function of redshift such as $\delta(z)$ is difficult (although it can be performed, to some extent, with the technique of Gaussian process reconstruction [404]), and it is convenient to introduce a parametrization. A very convenient choice, in terms of two parameters (Ξ_0, n), has been proposed in [391]. Rather than parametrizing $\delta(z)$, it is simpler to parametrize directly the ratio $d_L^{\rm gw}(z)/d_L^{\rm em}(z)$ (which is also the directly observed quantity), in the form

$$\frac{d_L^{\rm gw}(z)}{d_L^{\rm em}(z)} = \Xi_0 + \frac{1-\Xi_0}{(1+z)^n}\,. \tag{6.16}$$

JCAP07(2023)068

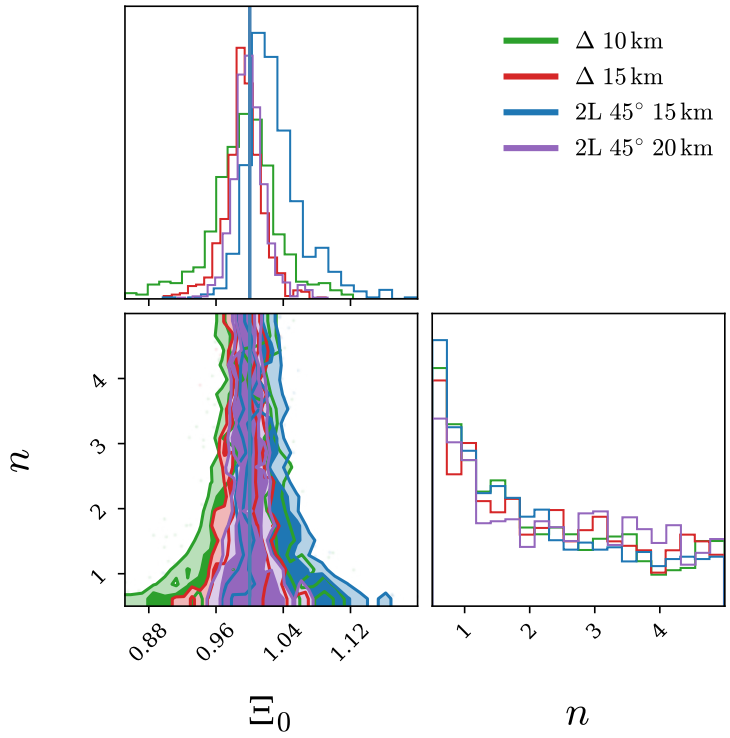

Figure 56. Reconstruction of the parameters Ξ_0 and n in modified gravity, from the joint GW+EM events obtained with ET+THESEUS in 5 yr of observations, for the different geometries of ET shown, all with their HFLF-cryo sensitivity.

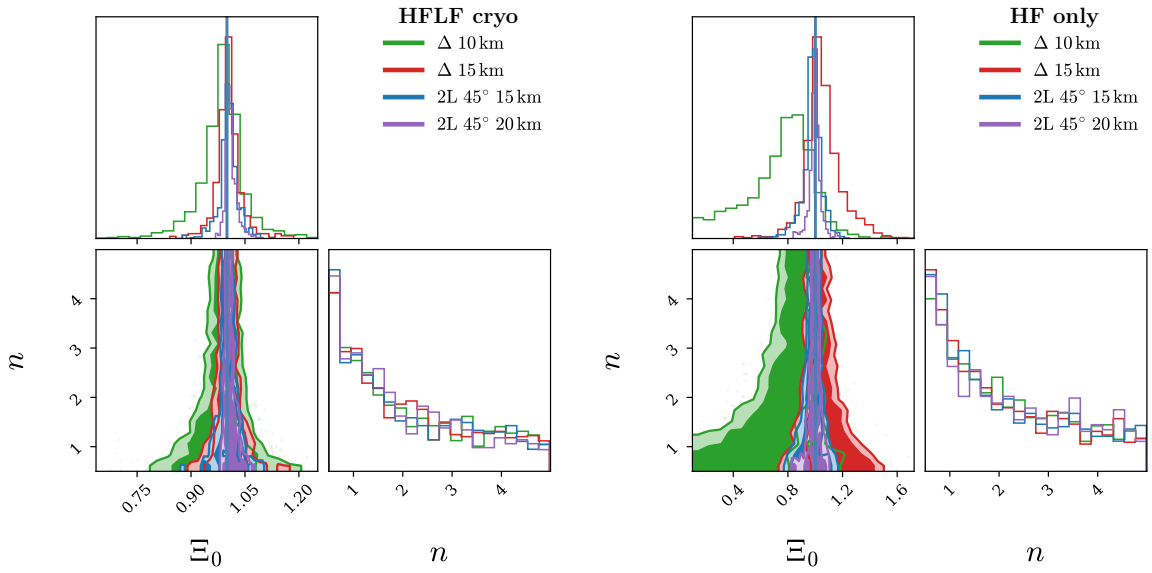

Figure 57. Reconstruction of the parameters Ξ_0 and n in modified gravity, from the joint GW+EM events obtained with ET+VRO in 1 yr of observations, for the different geometries of ET shown, in the left panel with their HFLF-cryo sensitivity and in the right panel with the HF instrument only.

JCAP07(2023)068

HFLF cryogenic		
Configuration	$\Delta\Xi_0/\Xi_0$	Δn
Δ-10km	0.097	3.04
Δ-15km	0.051	2.95
2L-15km-45°	0.038	2.95
2L-20km-45°	0.027	2.59

HF only		
Configuration	$\Delta\Xi_0/\Xi_0$	Δn
Δ-10km	0.617	2.80
Δ-15km	0.207	2.87
2L-15km-45°	0.108	2.88
2L-20km-45°	0.063	3.00

Table 33. Errors on the parameters Ξ_0 and n that describe modified GW propagation (median and symmetric 68% CI), from the joint GW+EM events obtained with ET+VRO, for the different geometries of ET shown, in the left table with their HFLF-cryo sensitivity and in the right table with the HF instrument only.

This parametrization reproduces the fact that, at $z = 0$, $d_L^{\rm gw}/d_L^{\rm em} = 1$ since, as the distance to the source goes to zero, there can be no effect from modified propagation. In the opposite limit of large redshifts, in contrast, eq. (6.16) predicts that $d_L^{\rm gw}/d_L^{\rm em}$ approaches a constant value Ξ_0. This is motivated by the fact that, in typical modified gravity models, the deviations from GR only appear in the recent cosmological epoch, so $\delta(z)$ goes to zero at large redshift, and the integral in eq. (6.15) saturates to a constant. The parametrization (6.16), interpolates between these two limiting behaviors, with a power-law determined by n, and GR corresponds to $\Xi_0 = 1$ (for any n). This simple parametrization has been shown to work remarkably well for practically all best-studied modified gravity models [402]. A particularly interesting example is given by the model proposed in [393] (see [395, 405] for reviews) that, while complying with all current cosmological constraints, predicts modified GW propagation with a value of Ξ_0 that (depending on a single parameter related to the initial conditions of the cosmological evolution) can differ from the GR value $\Xi_0 = 1$ by an amount between a few percent up to a value $\Xi_0 \simeq 1.8$ [394, 395], that would correspond to a 80% deviation from GR. Limits on Ξ_0 have already been obtained from the current set of LVC detections, either from GW170817 as a standard siren with counterpart [391], or using BBH dark sirens from the O1, O2 and O3a LIGO/Virgo run, and performing a correlation with galaxy catalogs. This results in the value $\Xi_0 = 2.1^{+3.2}_{-1.2}$ [359].[39] Using instead a joint cosmology-population analysis that exploits the mass scales in the BBH mass function [355, 377] and the GWTC-3 catalog of detections [6] one finds the constraints $\Xi_0 = 1.2 \pm 0.7$ [365].

Here we show the constraint on Ξ_0 that can be obtained from the joint set of GW and electromagnetic observations obtained from ET+THESEUS and ET+VRO. As we have stressed at the beginning of this section, the absolute estimates for the accuracy that we will present should not be understood as the forecast for the overall capability of ET for measuring these cosmological parameters, since we are studying the information that could be obtained from two examples, namely the joint detections of ET+THESEUS and ET+VRO, and, as discussed at the beginning of this section, there are other ways of obtaining information on Ξ_0 from the ET data. Again, here we are mainly interested in the relative performances of the different ET configurations on some concrete examples.

Figure 56 and table 32 show the results for the parameters Ξ_0 and n that characterize modified GW propagation from the ET+THESEUS joint detections, while figure 57, and ta-

[39] An even more stringent result is obtained if one accepts the tentative identification of the flare ZTF19abanrhr as the electromagnetic counterpart of the BBH coalescence GW190521. Then, the analysis in [359] gives $\Xi_0 = 1.8^{+0.9}_{-0.6}$. (68% c.l.). This is consistent with similar results obtained in [406].

JCAP07(2023)068

ble 33 show the results for ET+VRO. *The hierarchy of performances is similar to that for H_0, with the 2L 20 km providing the best results, followed by the 15 km triangle and the 2L 15 km with similar performances (with 2L-15 km better than triangle-15km for ET+VRO), and the 10 km triangle providing the less good performances. For ET+VRO, the huge improvement as a consequence of the inclusion of the LF instrument is also apparent.*

Observe that, in view of the discussion above, the accuracy that can be obtained from Ξ_0 even from these two specific examples, which ranges between 3% and 10% depending on the geometry with the full sensitivity curve, is already very interesting in absolute terms, since current 1σ limits are at the $60\% - 100\%$ level, and furthermore there are models that predicts a potentially much higher signal.

6.4.2 Hubble parameter and dark energy from BNS tidal deformability

BNS have an intrinsic mass scale and can only exist in a narrow range of masses. This mass scale is imprinted in the tidal interaction between the component NSs. Therefore, if the nuclear EoS is known, one can determine the source-frame masses by a measurement of the tidal deformability. This, in turn, would allow the measurement of the redshift directly from a GW observation because it is the redshifted mass that is inferred from the point-particle approximation of the waveform. Such a method was first proposed in [348] and further explored in [407, 408]. A measurement of the Hubble constant using a known relationship between the tidal parameter and source-frame mass was explored in [351, 361, 369] while [368] showed that one can simultaneously estimate both the nuclear EoS and the Hubble constant using future observatories. A measurement of the dark energy EoS was explored in [357, 366].

In this section, we explore the potential of different ET configurations to constrain the expansion history of the Universe assuming that the nuclear EoS is known. It is found in [361] that up to a 15% uncertainty in the knowledge of the EoS does not affect the measurement of the Hubble constant in a meaningful manner. We use the TaylorF2 waveform model augmented with the 5PN and 6PN tidal terms in the phase, terminating the signal at the ISCO frequency corresponding to the total mass of the binary. In section. 6.1.3, it was found that the results using this model versus an inspiral-merger-ringdown (IMR) waveform gives similar results. Since the analysis in this section is along similar lines, we expect the same to hold here too. Additionally, we assume the DD-LZ1 EoS for the NS for reasons elucidated in section 6.2.1. We fit the logarithm (base 10) of the tidal deformability as a function of the mass of the NS using a fourth-order polynomial given by

$$\log_{10}\Lambda(m) = -0.3550\,m^4 + 2.162\,m^3 - 4.652\,m^2 + 2.514\,m + 3.892\,, \tag{6.17}$$

where m is in units of $M_\odot$. We verify that the fit reproduces the slope of the curve accurately with maximum errors at a few percent. This is crucial because it is the slope of the curve that contributes to the Fisher errors on the redshift.

The Fisher errors from the d_L-z space are then propagated to the space of cosmological parameters, $\vec{\phi}$, via another Fisher matrix given by [409]

$$\mathcal{G}_{ij} = \sum_{k=1}^{N} \frac{1}{\sigma^2_{d_L,k}} \frac{\partial d^k_L(z)}{\partial \phi^i} \frac{\partial d^k_L(z)}{\partial \phi^j}\,, \tag{6.18}$$

where N is the total number of observations in the catalog and $\sigma^2_{d_L,k}$ is the total luminosity distance error for the k-th event given by

$$(\sigma_{d_L})^2 = (\sigma^h_{d_L})^2 + (\sigma^z_{d_L})^2. \tag{6.19}$$

JCAP07(2023)068

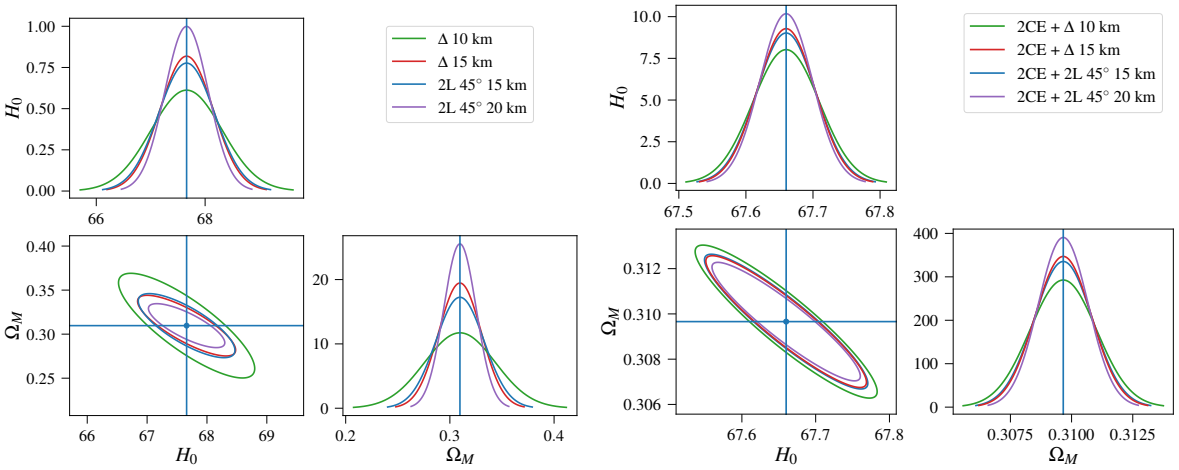

Figure 58. Constraints on the parameters H_0 and Ω_M in ΛCDM model using one year GW observations from BNS alone for different ET geometries. The covariance for a standalone ET is shown in the left panel while ET in a network with 2CE is shown in the right panel. H_0 is measured in $\mathrm{km\,s^{-1}\,Mpc^{-1}}$.

Configuration	$\Delta H_0/H_0$	$\Delta\Omega_M/\Omega_M$
Δ-10km	9.63×10^{-3}	1.10×10^{-1}
Δ-15km	7.20×10^{-3}	6.62×10^{-2}
2L-15km-45°	7.59×10^{-3}	7.47×10^{-2}
2L-20km-45°	5.90×10^{-3}	5.04×10^{-2}

Configuration	$\Delta H_0/H_0$	$\Delta\Omega_M/\Omega_M$
Δ-10km +2CE	7.35×10^{-4}	4.40×10^{-3}
Δ-15km +2CE	6.35×10^{-4}	3.71×10^{-3}
2L-15km-45° +2CE	6.54×10^{-4}	3.84×10^{-3}
2L-20km-45° +2CE	5.79×10^{-4}	3.30×10^{-3}

Table 34. Standard deviation on the parameters H_0 and Ω_M in ΛCDM using one year of GW observations from BNS alone for different geometries of ET alone (left) and ET in a network with 2CE (right). ET is always taken with the full HFLF-cryo sensitivity.

Here, $\sigma^h_{d_L}$ is the contribution to the luminosity distance error due to the error in the GW amplitude while $\sigma^z_{d_L}$ is that due to the error in the redshift measurement, given by

$$\sigma^z_{D_L} = \left|\frac{\partial D_L}{\partial z}\right|\sigma_z. \tag{6.20}$$

In writing eq. (6.18), we have neglected the correlations in the d_L-z space for simplicity.

Hubble constant. The results for H_0 and Ω_M are shown in figure 58 and table 34. A description of ΛCDM cosmology is given in section 6.4.1. We see that a single year of observing run can achieve sub-percent errors on H_0 with ET alone, albeit the errors improve by an order of magnitude when ET operates in a network with 2CE. The ET configuration with two 20km L-shaped detectors at 45° gives the best constraints. Similar trends follow for the dark matter energy density parameter, Ω_M, which can be constrained at percent level precision, except for the case of a standalone 10km triangular ET which can only achieve an accuracy of $\sim 10\%$.

Dark energy equation of state. The results for the dark energy equation of state parameters are shown in figure 59 and the 1σ errors tabulated in table 35. A description of the dark energy model considered here is in section 6.4.1. We see that the 2L 20km at 45° obtains

JCAP07(2023)068

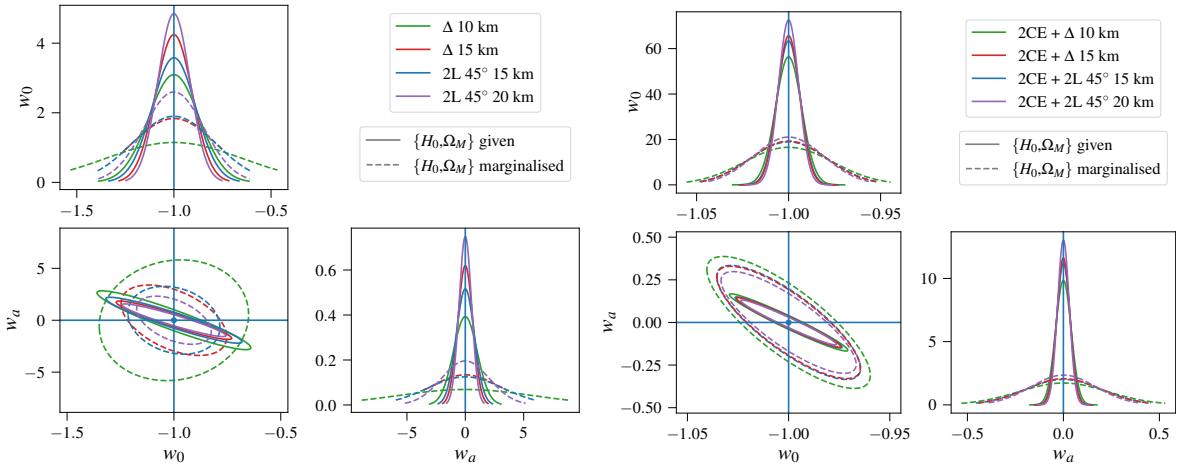

Figure 59. Constraints on the w_0-w_a plane in a dynamical dark energy model using one year GW observations from BNS alone for different ET geometries. The covariance for a standalone ET is shown in the left panel while ET in a network with 2CE is shown in the right panel.

Configuration	Δw_0	Δw_a
Δ-10km	0.348	5.79
Δ-15km	0.217	2.98
2L-15km-45°	0.210	3.19
2L-20km-45°	0.153	2.04

Configuration	Δw_0	Δw_a
Δ-10km +2CE	0.0241	0.231
Δ-15km +2CE	0.0207	0.193
2L-15km-45° +2CE	0.0211	0.198
2L-20km-45° +2CE	0.0189	0.169

Configuration	Δw_0	Δw_a
Δ-10km	0.129	1.02
Δ-15km	0.0940	0.644
2L-15km-45°	0.111	0.773
2L-20km-45°	0.0823	0.532

Configuration	Δw_0	Δw_a
Δ-10km +2CE	7.07×10^{-3}	0.0405
Δ-15km +2CE	6.08×10^{-3}	0.0343
2L-15km-45° +2CE	6.29×10^{-3}	0.0356
2L-20km-45° +2CE	5.50×10^{-3}	0.0306

Table 35. Errors on the parameters w_0 and w_a (68% c.l.) in a dynamical dark energy model using one year of GW observations from BNS alone for different geometries of ET alone (left) and ET in a network with 2CE (right), all with their HFLF-cryo sensitivity. The top panel shows the constraints marginalised over the parameters H_0 and Ω_M whereas, in the bottom panel, the ΛCDM parameters are assumed to be known a priori.

the best constraints on the parameters, albeit the EoS parameter w_a is not constrained by a standalone ET if one marginalises over the ΛCDM parameters. In such a scenario, it is common to fix the ΛCDM parameters to that measured with EM probes and measure only the dark energy parameters using GWs. In this case, except for the single 10km triangular ET configuration, the EoS parameters can be constrained.

Modified GW propagation. We next consider modified gravitational wave propagation, using the parametrization (6.16). The bounds on the corresponding parameters Ξ_0 and n are shown in figure 60 and the corresponding error (at 68% c.l.) are tabulated in table 36. A difference from the analysis of the previous section using EM counterparts is that we assume fiducial values of $\Xi_0 = 1.1$ and $n = 2.5$. As described in section 6.4.1, these values are consis-

JCAP07(2023)068

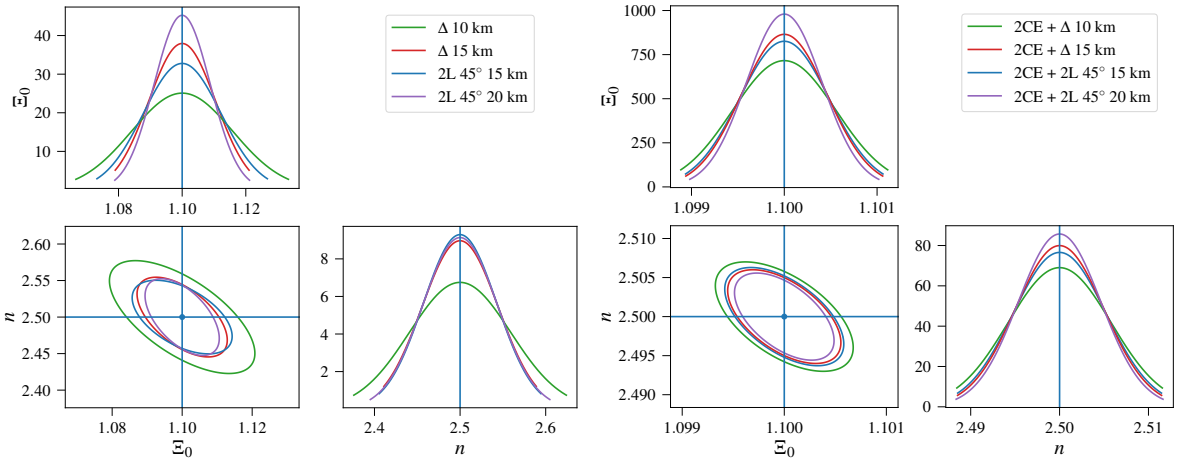

Figure 60. Constraints on the Ξ_0-n plane in a modified gravity model with modified tensor perturbations using one year GW observations from BNS alone for different ET geometries. The covariance for a standalone ET is shown in the left panel while ET in a network with 2CE is shown in the right panel. The ΛCDM parameters are assumed to be known a priori.

Configuration	$\Delta\Xi_0/\Xi_0$	Δn
Δ-10km	1.06×10^{-2}	5.91×10^{-2}
Δ-15km	7.01×10^{-3}	4.45×10^{-2}
2L-15km-45°	8.11×10^{-3}	4.29×10^{-2}
2L-20km-45°	5.88×10^{-3}	4.37×10^{-2}

Configuration	$\Delta\Xi_0/\Xi_0$	Δn
Δ-10km +2CE	3.71×10^{-4}	5.78×10^{-3}
Δ-15km +2CE	3.07×10^{-4}	4.99×10^{-3}
2L-15km-45° +2CE	3.22×10^{-4}	5.21×10^{-3}
2L-20km-45° +2CE	2.71×10^{-4}	4.99×10^{-3}

Table 36. Errors (at 68% c.l.) on the parameters Ξ_0 and n that describe modified GW propagation, using one year of GW observations from BNS alone for different geometries of ET alone (left) and ET in a network with 2CE (right), all with their HFLF-cryo sensitivity. The ΛCDM parameters are assumed to be known a priori.

tent with all current observations. We do this because the form of the parameterization (6.16) renders the Fisher matrix (6.18) singular for GR value of $\Xi_0 = 1$ and for $n = 0$. Any value of n away from $n = 0$ is sufficient to make the Fisher matrix well-defined. We choose $n = 2.5$ for reasons outlined in [372]. We see that the hierarchy among the configurations is analogous to that found in table 32, with the 2L 20km with arms at 45° providing the best results, followed by 2L 15km with arms at 45° and triangle 15km, that gives quite similar results, while the triangular 10km ET gives the largest errors.

6.4.3 Hubble parameter from high-mass ratio events

A main limitation for the reconstruction of the luminosity distance d_L is the fact that it is highly correlated with the angle ι between the binary's orbital angular momentum and the observer's line-of-sight.[40] Purely based on the signal-to-noise ratio of an event, for large SNR we should expect that the luminosity distance d_L of a source is measured to an accuracy of $\Delta d_L/d_L = 1/\mathrm{SNR}$. However, this limit is never reached since this correlation (as well as, to lesser extent, the correlation with sky location) degrades the accuracy, typically leading

[40] For precessing binaries ι would be a function of time since the orbital angular momentum precesses about the total angular momentum, which includes the companions' spin angular momenta. For such systems, ι should be defined at some fixed, but arbitrary, instant of time.

JCAP07(2023)068

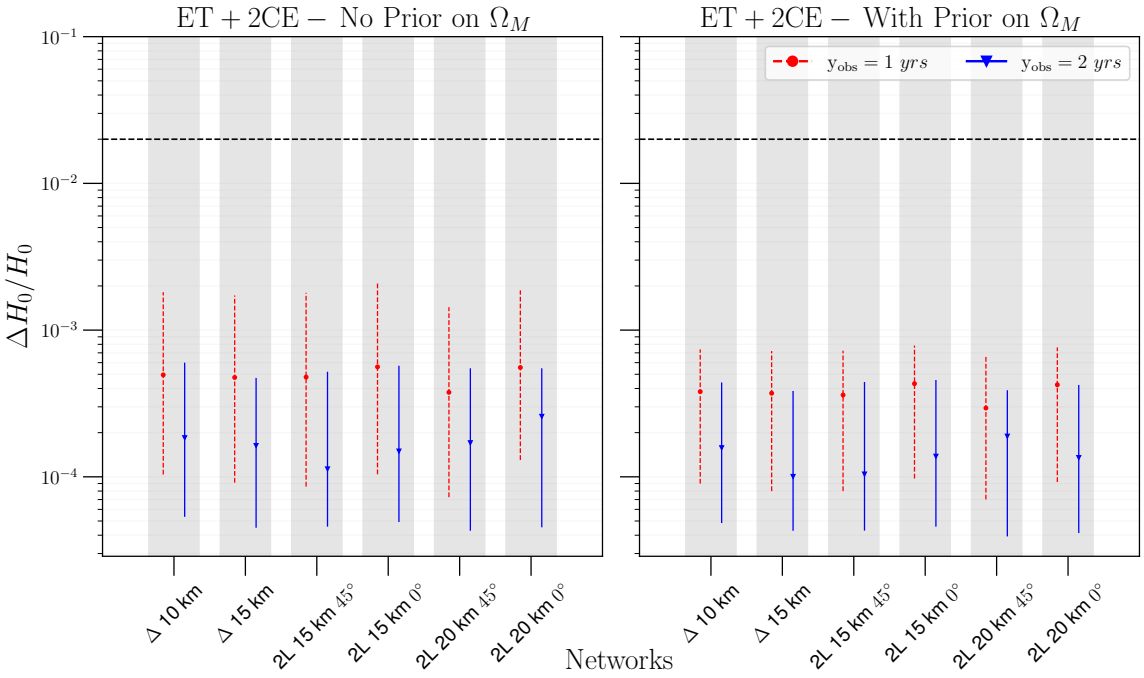

Figure 61. The accuracy with which the Hubble constant can be measured by different detector networks by high-mass ratio binary black holes, with events corresponding to 1 and 2 yrs of observation time picked randomly from the 10-year catalog of BBH events located within $z = 0.1$. In the left plot, H_0 is measured with no prior imposed on the dark matter energy density Ω_M, while for the right plot we assume a gaussian prior with a width of 0.017. The markers show the median value of the fractional error in H_0 and the error bars denote the 68% confidence region.

to error in the distance measurement an order of magnitude larger [410] (unless the angle ι and the sky location of the source can be fixed by the observation of an associated GRB, see the discussion on page 96). For instance, when the inclination angle changes from 0 to $\pi/6$ radians, the relative amplitudes of the h_+ and $h_\times$ polarizations of the dominant quadrupole mode change by no more than 1%, while the overall amplitude reduces by 12%. This change in amplitude can be entirely compensated by moving the binary 12% closer to the observer without an appreciable change in the polarization content of the observed signal.

This scenario changes dramatically for high-mass ratio events from either neutron star-black hole or double black hole binaries. Significant energy in the higher-order modes can break the distance-inclination angle degeneracy since the polarization modes have a different dependence on the inclination angle. In a recent paper [411] it has been shown that high-mass ratio events with large SNR would not only break the d_L-ι degeneracy, but a small population of such events would also localize the source to a region small enough to contain, on average, just one L_* galaxy. This helps in obtaining the redshift of the source from the galaxy, although the source itself may not have an EM afterglow. As already mentioned, these events are called *dark sirens* and can measure the Hubble constant without the need for an extra distance calibrator. Some of these events, albeit very rare, could measure the Hubble constant to an accuracy of better than 2% with a single event with no known systematics and are called *golden H_0 events.* This method could be one of the most *precise* and *accurate* way of measuring the Hubble constant.

JCAP07(2023)068

Since BBHs are not likely to be associated with an EM counterpart, the only way to identify the true host is to localize the source to a single galaxy. For NSBH events, however, we expect EM afterglows if the mass ratio is not too small (say, greater than about 1:4). While asymmetric masses in a NSBH binary could help break the distance-inclination degeneracy, the host galaxy could be identified from the kilonova. Additionally, for NSBH binaries with large mass asymmetry, it is also possible to identify the host within the sky localization from gravitational wave observations. In this sense, NSBH binaries could be used as both bright and dark sirens or *gray* sirens.

For BBH systems, we restrict our population to events within the redshift $z = 0.1$, or 476 Mpc. This leaves us with 86 BBH mergers in a span of 10 years. Among these, we choose those events for which the sky area is constrained to better than 0.04 deg^2, as we expect only one L_* galaxy to lie in this sky patch up to a redshift of 0.1 [412]. For the events that qualify, we obtain the measurement errors in luminosity distance by calculating the Fisher information matrix. Assuming the ΛCDM cosmology, the errors in d_L can be converted to measurement uncertainty in H_0 after accounting for the measurement errors in the matter density, Ω_M. We present the bounds on H_0 for two cases: without taking a prior on Ω_M, and with a gaussian prior on Ω_M. The width of the gaussian prior is fixed to the sum of the squares of the bounds placed on Ω_M by Planck [383] and SH0ES [413], which is equal to 0.017. Using binary black holes as dark sirens, the accuracy with which H_0 would be measured by different detector configurations in a network of ET and two CE detectors, one of which is a 40 km arm length detector and the other 20 km, is shown in figure 61.

For NSBH systems, the Hubble constant can be measured with gravitational waves both without (dark sirens) and with (bright sirens) electromagnetic counterpart. From the 10 year population, we choose events that qualify as dark or bright sirens (and make sure to not double-count events that qualify as both). The NSBH events that qualify as dark sirens are chosen in the same way as was done for BBH systems. For bright sirens, we only consider events that lie within a redshift of $z = 0.5$, as we do not expect to detect the kilonovae from events that lie farther. In addition, only those events are selected for which the sky position is measured better than 9.6 deg^2, i.e. the field of view of the Rubin observatory. For these events, we generate the kilonova light curves with DD2 as the neutron star equation of state using the numerical recipes from [414, 415]. We claim that a particular kilonova is detected with the Rubin observatory by using the same criteria that were used in section 4.3, i.e. the luminosity of the kilonova should be brighter than the limiting magnitude (corresponding to 600s of exposure) of the g and the i filters on two consecutive nights. We also assume a 50% duty cycle for the Rubin observatory. The events for which the corresponding kilonova is detected qualify as bright sirens and are considered for the measurement of the Hubble constant. The luminosity distance errors for both dark and bright siren events are combined and the measurement errors for Ω_M are accounted for in the same way as was done for BBH dark siren events. The accuracy in measurement of H_0 using this gray siren approach with NSBH systems is shown in figure 62.

Among the events that contribute to the measurement of the Hubble constant, there are certain *golden* events for which the accuracy in the measurement of the luminosity distance is better than 2%. Such events can individually measure H_0 with a precision better than 2% and resolve the Hubble tension. The number of such golden binaries is given in table 37, both for the dark siren case with BBHs, and for the gray siren case with NSBH systems, and an observation span of 10 years. *We see that, when in a network with 2CE detectors, the performances of all the ET geometries considered are comparable in the measurement of the Hubble*

JCAP07(2023)068

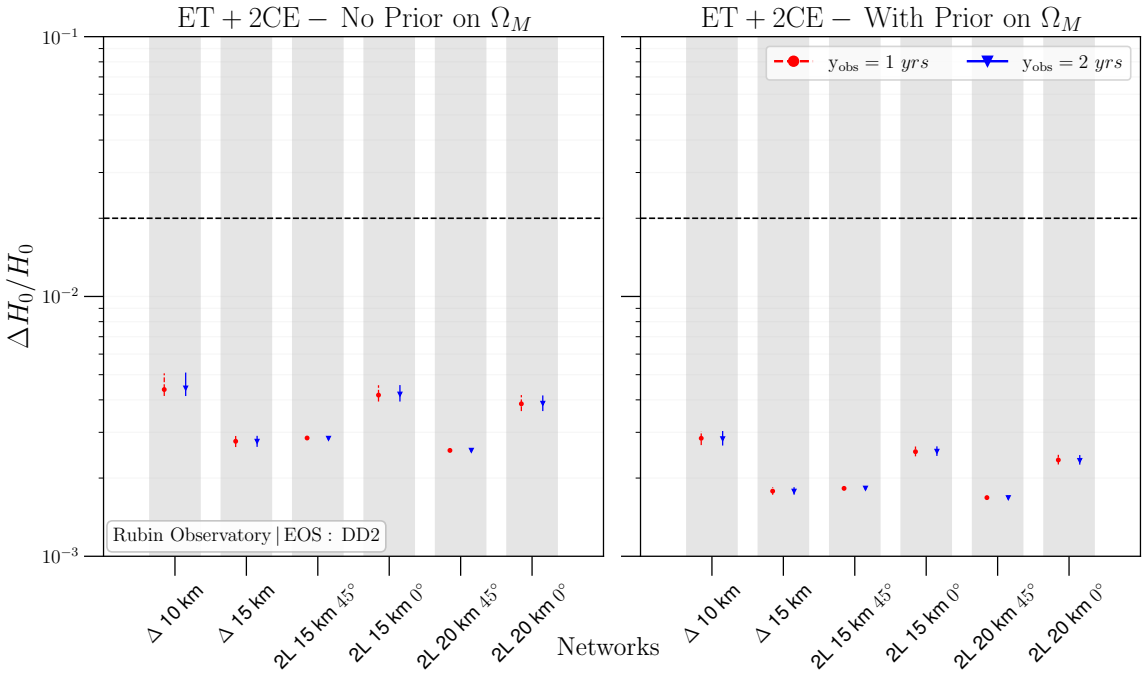

Figure 62. Same as figure 61 except the results are obtained for the NSBH population instead of the BBH population. Moreover, the results were obtained by combining measurement accuracies from systems that produce kilonovae in addition to those that identify a unique host within the localization error box.

Configuration	BBH		NSBH	
	With 2CE	Without 2CE	With 2CE	Without 2CE
Δ 10 km	68	5	21	0
Δ 15 km	74	7	30	0
2L 15 km 45°	73	4	25	1
2L 15 km 0°	69	0	21	0
2L 20 km 45°	77	8	37	1
2L 20 km 0°	70	0	22	0

Table 37. The number of dark siren BBH golden events and gray siren NSBH golden events for different ET detector configurations in an observation time of 10 years.

constant using the dark and gray siren approaches. In contrast, for ET alone, the L-shaped configurations with parallel arms perform significantly worse compared to the other configurations, as they are unable to detect a single golden event in an observing time of 10 years.

6.5 Cosmological stochastic backgrounds

In this section we consider the performances of the various ET geometries for the detection of specific examples of stochastic backgrounds of cosmological origin. In section 6.5.1 we compare the ET sensitivities with the predictions from models of cosmic strings, while in section 6.5.2 we consider the stochastic background produced by a phase transition in

JCAP07(2023)068

the early Universe. Finally, in section 6.5.3, we study the prospects for separating these cosmological backgrounds from the astrophysical stochastic background.

6.5.1 Cosmic strings

Phase transitions followed by spontaneously broken symmetries may lead to the production of topological defects as relics of the previous more symmetric phase of the Universe. Within Grand Unified Theories, it has been shown [416] that cosmic strings (line-like defects) are generically formed. At the energy scales relevant to cosmology, the width of a string is negligible relative to its characteristic size. Such strings (Nambu-Goto strings) are parameterised by a single dimensionless quantity, the string tension $G\mu$ related to the energy scale η at which cosmic strings are formed through $G\mu \sim 10^{-6}[\eta/(10^{16}\text{GeV})]^2$ (we set the speed of light $c = 1$).

Cosmic strings emit bursts of beamed gravitational radiation. The main sources of bursts are kinks, cusps or kink-kink collisions. Kinks are discontinuities in the tangent vector of the string that propagate at the speed of light and appear in pairs. Cusps are points on the string that briefly travel at the speed of light. The incoherent superposition of these bursts through the history of the Universe produces a strongly non-Gaussian stochastic gravitational wave background [417]. Occasionally there may also be sharp and high-amplitude bursts of GWs above this stochastic background. The production of gravitational waves by cosmic strings offers a tool to probe particle physics beyond the Standard Model at energy scales much above the ones reached by accelerators. A non-detection of a stochastic background of gravitational waves imposes bounds on the cosmic string tension and therefore on particle physics models beyond the Standard Model. ET will be able to considerably improve on current 2G bounds [418].

In figures 63 and 64 we show the prediction for $\Omega_{\text{GW}}(f)$ for two different models of the loop distribution of cosmic strings, denoted as models A [419] and model B [420], and different values of the string tension $G\mu$. In model A the loop production function can be determined from Nambu-Goto simulations of cosmic string networks. In model B the distribution of non-self-intersecting scaling loops is the extracted quantity from different simulations. Within the latter model, loops are formed at all sizes following a power-law while the scaling loop distribution is cut-off on small scales by the gravitational back-reaction. In model B are produced many more tiny loops than in the model A. These two models for the loop distributions have been used by the LVK collaboration to put constraints on cosmic strings from O1, O2 and O3 data [418].

The various curves define the power-law integrated sensitivity for each ET configuration, assuming SNR=1 and $T_{\text{obs}} = 1$ yr. As already remarked in section 5.1, *the triangular configurations perform better at high frequency, because the overlap reduction function remains constant at high frequencies for co-located detectors, while it falls to zero for widely separated detectors. The 2L shape configuration does better around a frequency of 10 Hz, but only for co-aligned detectors (this maximises the coherence for the stochastic search). The case of 45 deg 2L configurations is universally the worst.* We conclude that, for the considered loop distributions (models A and B), the best stochastic constraints on the string tension are $\sim 10^{-19}$, corresponding to an energy scale between 10^8 GeV and 3×10^{10} GeV, 6 to 8 orders of magnitude above the electroweak scale.

6.5.2 First-order phase transition

As the Universe cooled down, it may have undergone a first-order phase transition (FOPT) with bubbles of true vacuum forming, expanding and colliding [421–423]. This in turn leads

JCAP07(2023)068

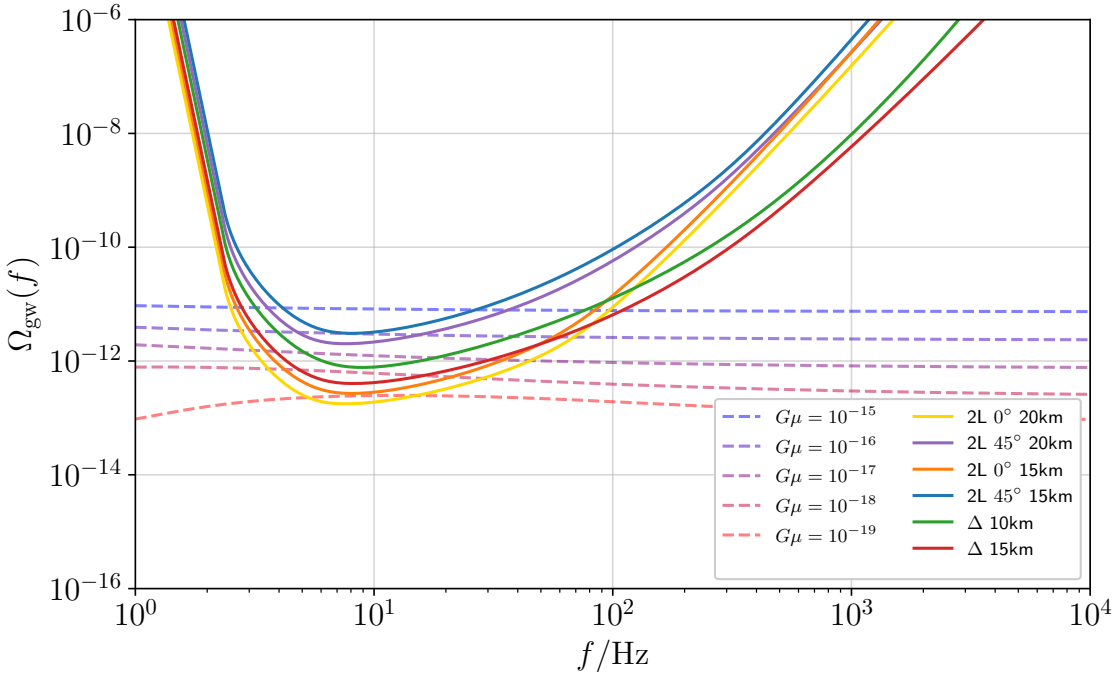

Figure 63. Energy density of gravitational waves emitted from cosmic string loops with loop distribution given by model A [419]. The various curves define the power-law integrated sensitivity for each ET configuration, assuming $\mathrm{SNR}_{th} = 1$ and $T_{\rm obs} = 1$ yr.

to gravitational waves generated from the collision of bubbles, and from the sound waves and turbulence in the surrounding plasma (see e.g. [85, 424] for reviews). The frequency of gravitational radiation emitted depends on the temperature. For a temperature of the order $(10^5 - 10^{10})$ GeV, energy scales inaccessible to particle colliders, we find a SGWB that peaks in the ET frequency range. Here we briefly discuss ET detection prospects of supercooled FOPTs, a special class of FOPTs which is expected to create the "loudest" gravitational waves [425, 426].

The gravitational wave spectrum from a supercooled FOPT depends only on two parameters, namely the reheating temperature $T_{\rm RH}$ and inverse duration $\beta/H_{\rm RH}$, where we denote $H_{\rm RH} \equiv H(T_{\rm RH})$.[41] Note that the strength of transition α that affects the SGWB for the more general FOPTs, does not impact the supercooled spectrum. In figure 65 we simulate a SGWB containing the residual from unresolved CBCs and an FOPT signal for a range of $T_{\rm RH}$ and $\beta/H_{\rm RH}$ values. The left panel includes a FOPT signal that is dominated by bubble collisions, while the right panel is for a FOPT signal dominated by sound waves. Turbulence is expected to be subdominant to both bubble collisions and sound waves, so we exclude it from our study. It is clear that we will be able to exclude a large part of the parameter space with the next generation of GW detectors.

6.5.3 Source separation

The unresolved astrophysical mergers are expected to be the dominant contribution to the background observed by ET. It is therefore important to subtract the individual sources, as discussed in the previous section, in the hope to reveal the cosmological background. Note

[41] For simplicity, we assume wall velocity to be equal to the speed of light.

JCAP07(2023)068

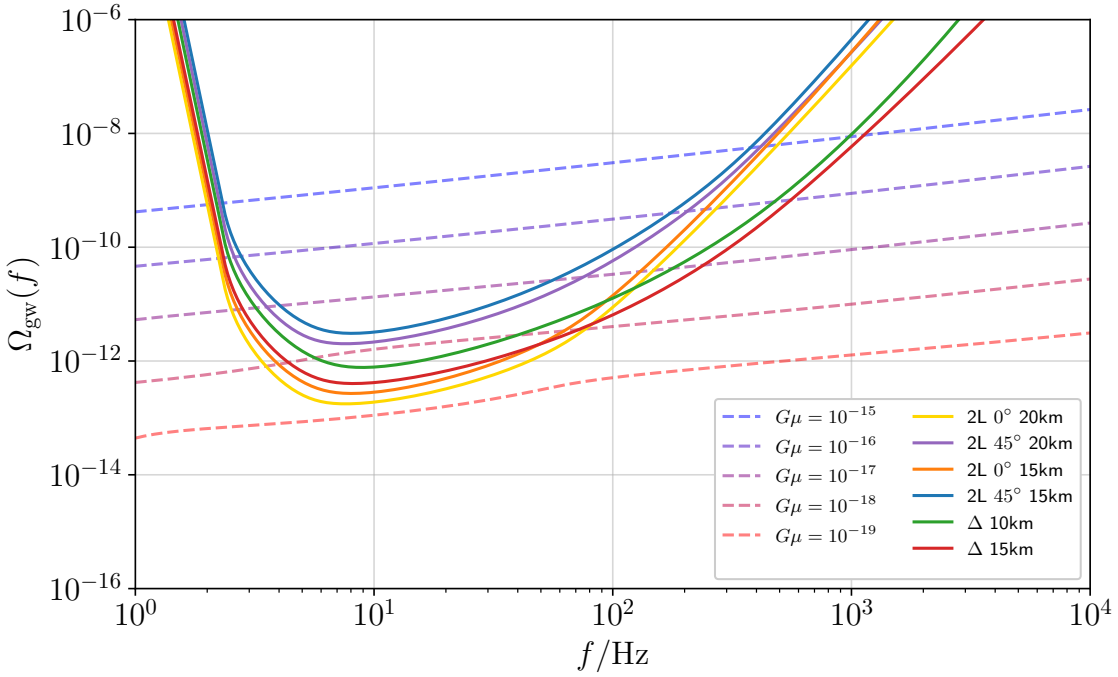

Figure 64. Energy density of gravitational waves emitted from cosmic string loops with loop distribution given by model B [420]. The various curves define the power-law integrated sensitivity for each ET configuration, assuming $\mathrm{SNR}_{th} = 1$ and $T_{\rm obs} = 1$ yr.

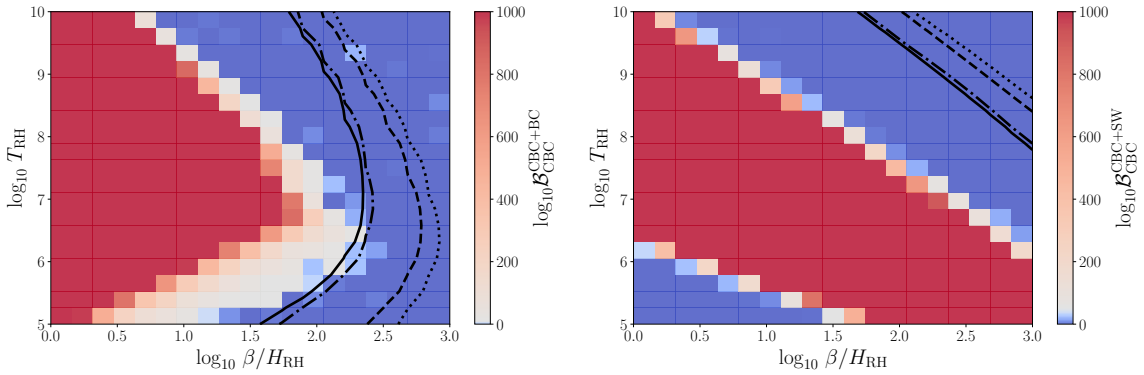

Figure 65. Detectability of bubble collisions (left) and sound wave (right) dominated supercooled FOPT with next-generation ET detector. The dashed line is the detection threshold using 10 km triangular ET configuration, the dotted line is 15 km triangular configuration, while the solid and dot-dashed contours are for two L-shaped detectors with 15 km and 20 km arms, respectively.

that the imperfect subtraction of CBC sources may pose a serious threat to digging out a cosmological background, and extensive research must be done to improve the subtraction methods [427, 428]. Here we take as an example two cosmological sources: cosmic strings and an early-Universe first-order phase transition.

By limiting the study to the frequency range $f \in [10, 100]$ Hz, we can assume the CBC background to follow $f^{2/3}$ and the cosmic strings background to be frequency-independent, i.e. $\Omega_{\rm CS} = \text{const}$. The first-order phase transition is modeled as a broken power-law (with

JCAP07(2023)068

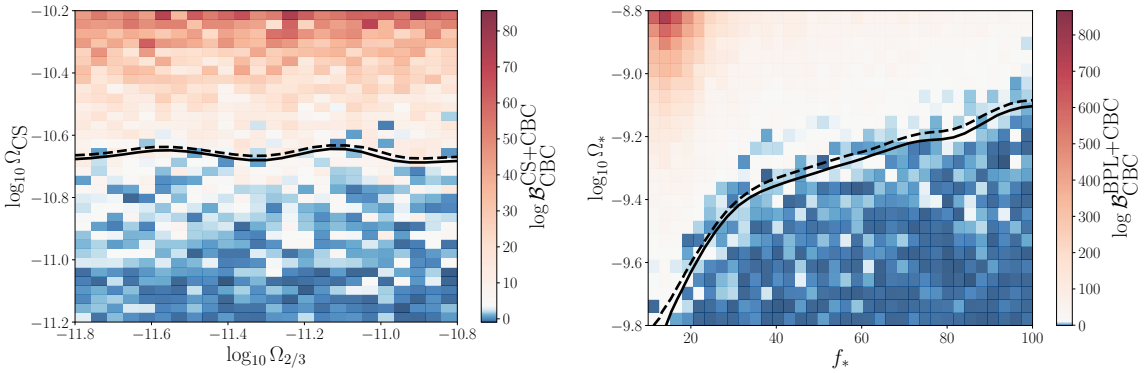

Figure 66. Upper limits we can place on the amplitude of the background from cosmic strings (left panel) and a first-order phase transition (right panel) with ET's triangular 10 km configuration (dashed line) and 2L 20 km configuration (solid line). We assume a strong preference for a signal that contains an astrophysical and a cosmological contribution, relative to a signal containing only unresolved astrophysical objects for log Bayes factors greater than 8.

Ω_* amplitude and f_* break frequency), with the assumption that the sound-wave component is the dominant contribution to the cosmological SGWB. We simulate astrophysical and cosmological SGWB and perform a model selection study of the signal. For details on the parameter estimation Bayesian tools, see [429]. We compute Bayes factors for a CBC signal to noise, and for a combination of cosmological and CBC signal to noise. Comparing the two Bayes factors demonstrates if one model is preferred over the other, i.e. if we can detect the presence of a cosmological signal. From figure 66 we conclude that a cosmic strings background of amplitude 2.2×10^{-11} and a first-order phase transition background of amplitude up to 4.0×10^{-10} (at 25 Hz) will be probed with this 3G detector.

Note that the various ET configuration makes little quantitative difference to the results, but including next-generation Cosmic Explorer can lead to great improvement in SGWB source separation.

6.6 Continuous waves

Broadly speaking, the class of *continuous waves* (CW) comprises all deterministic[42] GW signals that last much longer than typical transient signals, whose durations vary from a fraction of a second to tens or hundreds seconds at the most. No CW has been detected so far, although interesting upper limits have been established, see e.g. [430–432] for recent reviews. The prototypical source of CWs is a spinning neutron star, asymmetric with respect to the rotation axis, that emits a quasi-monochromatic gravitational wave whose frequency changes extremely slowly over time. For such sources, the expected signal duration is much longer than one day, meaning that the frequency modulation due to the Doppler effect, caused by the motion of the Earth, and the phase and amplitude modulations due to the detector radiation pattern functions, play relevant roles.

Actually, other sources of CW-like signals have been investigated. In particular, *transient CW* signals (tCW) have been considered, such as those expected to be emitted by a newborn magnetar, in the early stages of its evolution [433–436]. In this case, the frequency secular variation is caused by a combination of the electromagnetic emission, due to the

[42] In contrast to GW backgrounds, which are described by means of stochastic processes.

JCAP07(2023)068

super-strong magnetic field, and the gravitational-wave emission, due to the strong asymmetry induced by the electromagnetic field itself. As a consequence, the resulting source spin-down is orders of magnitudes faster than for standard neutron stars, producing a signal that stays in the sensitivity band of detectors for hours or days.

Recently, several theoretical works have shown that GW detectors can also be used to probe dark matter, see e.g. [437] for a comprehensive review. In many of the proposed mechanisms, the resulting signal has a CW-like nature. This is, for instance, the case for depleting scalar or vector ultra-light boson clouds that could form around Kerr black holes through superradiance [438], the interaction of dark matter particles with detector components [439],[43] or the early inspiral of sub-solar mass primordial black holes [440].

The typical duration of CW signals has some important consequences. First, once detected, a CW source can be monitored for long periods of time, becoming a true laboratory for fundamental physics and astrophysics, and potentially allowing observations of tiny deviations from the assumed models (for instance, a deviation from GR, in the form of non-standard polarizations [441]). At the same time, signal persistence allows us to reduce the false alarm probability of any candidate virtually to zero, because if a signal is present in a given dataset — even with low significance — it will also appear in new datasets, and its significance will increase until a detection can be claimed (of course, this is not necessarily true for tCWs). Moreover, CW source parameters can be measured with very high accuracy, as their uncertainties decrease with the observation time. On the other hand, CW signals are predicted to have small amplitudes, compared to e.g. typical CBC signals, and to search for them can require a huge computational cost. For this reason, the development of increasingly sensitive, robust, and computationally efficient algorithms is a very active field that grows in parallel to current detector upgrades and R&D for future detectors, such as ET. In the following, we give more details on different sources of CW-like signals, focusing attention on the impact that different ET configurations have on the chance of detection.

6.6.1 CWs from spinning neutron stars

Spinning neutron stars (NS), isolated or in a binary system, asymmetric with respect to the rotation axis, emit a persistent gravitational wave signal with frequency in a given ratio to the rotation frequency of the star.

The typical amplitude of CWs signals is difficult to estimate, as it depends on poorly known quantities, especially the star's ellipticity, which is a measure of its degree of asymmetry. In the case of a CW emitted by a non-accreting, spinning NS, assuming it is asymmetric with respect to its rotation axis, the signal amplitude is given by

$$h_0 = \frac{4\pi^2 G}{c^4}\frac{\epsilon I_{zz} f^2}{d} \approx 1.06\times10^{-26}\left(\frac{\epsilon}{10^{-6}}\right)\times\left(\frac{I_{zz}}{10^{38}\,\mathrm{kg\ m^2}}\right)\left(\frac{f}{100\,\mathrm{Hz}}\right)^2\left(\frac{1\,\mathrm{kpc}}{d}\right), \quad (6.21)$$

where d is the source distance, f is the GW frequency (equal to two times the star's spin frequency in the prototypical case of a NS rotating around one of its principal axes of inertia), $\epsilon \equiv (I_{xx} - I_{yy})/I_{zz}$ is the ellipticity of the star, and I_{zz} is the moment of inertia of the star with respect to the principal axis aligned with the rotation axis.

The search for CWs from spinning NSs depends on the amount of information we have or we assume to have on the sources. For *targeted* searches, we use accurate measurements

[43] In this case the effect of the interaction is not a true GW signal, but is such to induce a relative motion of the optical components which can be searched as if it was a standard gravitational wave.

JCAP07(2023)068

of the main NS parameters, namely the position, spin frequency and its derivative(s), and Keplerian parameters for NSs in binary systems, obtained from electromagnetic (EM) observations (typically radio, gamma, or X-rays) to perform very sensitive searches based on matched filtering. Data from the detector network can be coherently combined in order to increase the sensitivity; see [442] for the most recent O3 results obtained by the LIGO and Virgo Collaborations for targeted searches. On the other hand, there are *all-sky* searches for NSs without an EM counterpart, in which a portion of the parameter space as large as possible is explored. Due to computational load constraints, such searches are based on hierarchical semi-coherent methods which sacrifice some sensitivity in order to make them computationally feasible. See [443] for the latest LVK all-sky search results. Searches covering "intermediate" cases are also routinely carried out. For instance, *narrow-band* searches slightly extend the parameter space around the EM-inferred parameters of known pulsars, in order to account for possible small — fraction of a Hz — mismatches between the EM and GW emission [444]. *Directed searches* assume the source position is known, while the star's rotational parameters are unknown, as in the case of the supernova remnants or the galactic center [445, 446]. All-sky and directed searches typically use data from different detectors (or runs of the same detector) in order to make coincidences among outliers, with the aim of suppressing the false alarm probability. Although no detection of CWs has been made so far, interesting upper limits on the star's ellipticity have been placed, see references above. These can be interpreted in terms of constraints on the residual initial star's deformation frozen after crust solidification or as due to an inner magnetic field misaligned with the rotation axis, using a given ratio with the external poloidal one.

Although the range of CW searches for spinning NSs is very wide, in the following we provide some figures of merit about detection perspectives by ET focusing on two relevant cases, targeted and all-sky searches, that bracket the span of typical searches in terms of dimension of the explored parameters space, sensitivity and computational cost.

For targeted searches, we provide some summary results in table 38 where, for different ET configurations, the number of potentially detectable sources (among those contained in the ATNF catalogue[44]) is given, under three different assumptions of the source ellipticity. We consider a total observation time $T_{\rm obs} = 1$ year, a duty cycle of 85% and assume to make a fully-coherent search based on matched filtering. In the case of 2L-shaped network, results do not depend on the relative orientation of the two detectors. Columns 2 indicates the number of detectable pulsars under the assumption that they emit at their spin-down limit, i.e. that all their spin-down is due to the emission of GWs. This provides a theoretical upper limit to the emitted strain, given by

$$h_{0,\rm sd} = \frac{1}{d}\left(\frac{5GI_{zz}}{2c^3}\frac{|\dot{f}|}{f}\right)^{1/2}, \tag{6.22}$$

where $\dot{f}$ is the signal frequency first time derivative. The corresponding limit on the star ellipticity is

$$\epsilon_{\rm sd} = \frac{h_{0,\rm sd}}{I_{zz}}\left(\frac{c^4 d}{4\pi^2 G f^2}\right) \approx 9.46\times10^{-6}\left(\frac{h_{0,\rm sd}}{10^{-25}}\right)\times\left(\frac{10^{38}\,\mathrm{kg\,m^2}}{I_{zz}}\right)\left(\frac{100\,\mathrm{Hz}}{f}\right)^2\left(\frac{d}{1\,\mathrm{kpc}}\right). \tag{6.23}$$

[44] https://www.atnf.csiro.au/research/pulsar/psrcat/.

JCAP07(2023)068

Configuration	n_1	n_2	n_3
Δ 10km	866 (2.5×10^{-10}, 1.3×10^{-4})	180 (2.5×10^{-10}, 4.4×10^{-9})	19 (2.5×10^{-10}, 7.5×10^{-10})
Δ 10km HF-only	398 (2.5×10^{-10}, 6.2×10^{-6})	178 (2.5×10^{-10}, 4.4×10^{-9})	19 (2.5×10^{-10}, 7.5×10^{-10})
Δ 15km	983 (2.1×10^{-10}, 1.1×10^{-4})	214 (2.1×10^{-10}, 4.4×10^{-9})	33 (2.1×10^{-10}, 7.9×10^{-10})
2L 15km	959 (2.0×10^{-10}, 1.2×10^{-4})	206 (2.0×10^{-10}, 4.2×10^{-9})	29 (2.0×10^{-10}, 8.1×10^{-10})
2L 15km HF-only	451 (2.0×10^{-10}, 5.6×10^{-6})	203 (2.0×10^{-10}, 4.0×10^{-9})	29 (2.0×10^{-10}, 8.1×10^{-10})
2L 20km	1035 (1.8×10^{-10}, 1.1×10^{-4})	227 (1.8×10^{-10}, 4.3×10^{-9})	33 (1.8×10^{-10}, 7.3×10^{-10})

Table 38. Expected number of detectable sources, assuming three different conditions for the ellipticity: $\epsilon = \epsilon_{sd}$ (n_1), $\epsilon = min(\epsilon_{sd},\ 10^{-6})$ (n_2), $\epsilon = min(\epsilon_{sd},\ 10^{-9})$ (n_3), assuming a total observation time $T_{\rm obs} = 1$ year and a duty cycle of 85%. For each case, we give in parentheses the minimum and median value of ellipticity for detectable signals.

The number of pulsars given in column 3 is computed by assuming that every star's ellipticity is the minimum of the spin-down limited value ϵ_{sd} and 10^{-6}, which is of the order of the maximum theoretical ellipticity a NS with a standard EOS could have [447]. In column 4, the number of detectable pulsars is computed assuming the minimum ellipticity between ϵ_{sd} and 10^{-9}, which is considered as a plausible value for millisecond pulsars [448, 449]. For each case, we also report the minimum and median value of the ellipticity for the potentially detectable sources.

From this table, we can draw some considerations. *The main factor affecting the number of detectable sources is the arm length, rather then the network geometry.* Indeed, by coherently combining individual detector data streams, the triangle configuration would provide a sensitivity gain of $\sqrt{3/2}$, with respect to the 2L network, which is nearly fully balanced by the shape factor, so that at the end what mostly contributes to the sensitivity is the arm length. *We also note that, for the more realistic choices on star's ellipticities, corresponding to columns n_2 and n_3, most of the potentially detectable sources are millisecond or young fast pulsars, spinning at frequencies larger than a few tens of Hertz, for which the low frequency sensitivity of the detectors is not particularly relevant.* The corresponding typical values of the ellipticity are of about 2×10^{-10}, corresponding to "mountains" extending from the star's surface not higher than about $1\mu m$. Lastly, focusing on the most conservative condition, given by column n_3, we find that *the number of potential detections increases by 50-70% going from 10km-arm detectors to 15 or 20km-arm detectors.*

Wide-parameter searches are based on semi-coherent methods in which data segments of given duration are incoherently combined. In principle, they are less sensitive than targeted ones, but can cover a huge parameter space and are intrinsically more robust against non-predicted deviations from the assumed signal model. Concerning, in particular, all-sky searches, figure 67 shows, for different detector configurations, the minimum detectable ellipticity as a function of the signal frequency, assuming source rotational evolution is dominated by the emission of GWs and a fixed source distance of 8 kpc. These results have been obtained considering an analysis done by means of the FrequencyHough pipeline [450], a semi-coherent procedure routinely used in current CW searches, whose sensitivity can be estimated (under the assumption the noise is Gaussian) as

$$h_{\rm min,95\%} \approx \frac{4.97}{N^{1/4}}\sqrt{\frac{S_n(f)}{T_{\rm FFT}}}\sqrt{{\rm CR}_{\rm thr}+1.6449}, \tag{6.24}$$

where $N = T_{\rm obs}/T_{\rm FFT}$ is the ratio between the total observation time and the duration of the data segments to be incoherently combined, $S_n(f)$ is the detector average noise power

JCAP07(2023)068

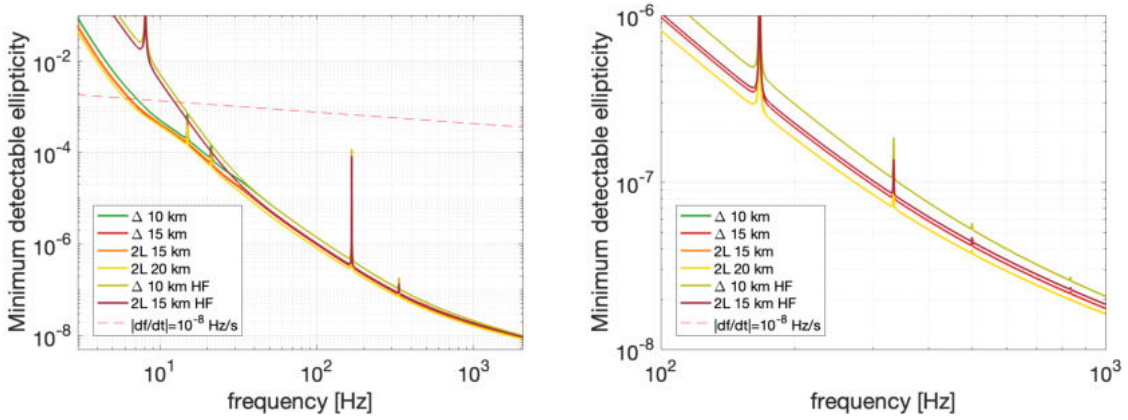

Figure 67. ET sensitivity reach to all-sky searches of CWs (95% C.L.). The various continuous curves are the minimum detectable ellipticity as a function of frequency for different detector configurations, assuming a source distance of 8 kpc, an observation time $T_{\rm obs}$=1 yr, a duty cycle D=85% and data segments duration $T_{\rm FFT}$=10 days. The dashed curve indicates a constant spin-down of 10^{-8} Hz/s. Right plot is a zoom of the left plot in the high frequency region. On the scale of the right plot, the curves corresponding to Δ 10 km HF and Δ 10 km coincides, and similarly for those corresponding to the 2L 15 km HF and 2L 15 km configurations.

spectrum and $\mathrm{CR_{thr}}$ is the threshold Critical Ratio to select outliers. In the plot, we used $T_{\rm obs}$=1 year, $T_{\rm FFT}$=10 days and $\mathrm{CR_{thr}} = 3.4$ for triangular configurations and $\mathrm{CR_{thr}} = 4$ for L-shape configurations. The presence of more that one detector is exploited in such kind of searches to strongly reduce the false alarm probability. For the standard search parameters considered here, the number of points in the parameter space (sky position, frequency and frequency derivatives) is of the order of 10^{23}. Assuming that for each detector of the order of 10^{12} outliers are selected,[45] it is possible to show that double coincidences are enough to reduce the number of candidates to O(10), and that triple coincidences would allow — in principle — to shrink this number to a negligible level, assuming ideal Gaussian noise [450]. As a matter of fact, in practice we expect a significant number of candidates to survive the coincidence step, due to non-Gaussian instrumental artefacts which, inevitably, pollute the data. Having triple coincidences, as for the triangle configuration, allows to better reduce false candidates with respect to the 2L configuration. This implies that in the former case we can use a slightly lower threshold for outliers selection, with the aim of having a similar number of candidates after the coincidences. A lower threshold, according to eq. (6.24), corresponds to a better sensitivity. Of course the exact value of the threshold would depend on the non-Gaussian, non-stationary features of the actual dataset, which are difficult to predict in advance. As a rule of thumb, we decide to reduce the threshold on the CR from 4 to 3.4 in the case of the triangular configuration. This choice would correspond to a reduction of one order of magnitude in the false alarm probability in presence of Gaussian noise.

As for targeted search, the relative orientation of the two triangular detector in the 2L-shaped configuration does not impact on the analysis outcome. *A clear feature of these results is that different configurations do not produce very different results, especially in the high frequency range, which corresponds to smaller ellipticities. In general, however, longer-*

[45] Currently, the typical number of selected outliers is O(10^{10}), but we devise an increase of two orders of magnitude as reasonable in the ET era.

JCAP07(2023)068

arm detectors perform better than shorter ones, with differences up to a few tens percent. For instance, a source located at 8 kpc, and emitting a signal at about 500 Hz, would be detected if its ellipticity is at least $\sim (4-5) \times 10^{-8}$. At a given frequency, the ellipticity scales linearly with the distance. Nearby sources, located within $\sim$ 1 kpc, would produce detectable signals with an ellipticity as small as few times per 10^{-9}, if spinning at around 500 Hz. Although current searches typically use a shorter data segment duration, values as large as 10 days are reasonable, and likely conservative, for the ET era, given the algorithmic developments and the increase in available computing power. It is interesting to stress, however, that while the sensitivity of semi-coherent searches scales as the fourth root of the segment duration, the dimension of the parameter space scales at least as the duration to the fifth power. This means, for instance, that using segments of 30 days, instead of 10, would provide a theoretical sensitivity gain of about 30%, in front of a computing cost at least 3^5 times bigger. Moreover, and probably even more importantly, the use of very long segment durations reduces the search robustness with respect to unmodeled signal features, which can translate into a sensitivity loss. As an example, a source may have a significant intrinsic transversal velocity with respect to the line of sight. If not taken into account, it may determine a sub-optimal Doppler correction as a consequence of the change of sky position during the observation time. Another possibility is that a signal may be characterized by some level of frequency wandering due to some unpredicted mechanism, involving the interaction with other objects, or due to intrinsic processes in the source (see e.g. [451, 452] for analysis methods that tackle this issue). It is then important to note that a reasoned balancing among theoretical sensitivity, available computing power and algorithm robustness must be always taken into account when new algorithms for wide-parameter searches are developed.

6.6.2 Transient CWs

Newly-born neutron stars could be extremely deformed and emit very strong GWs immediately after they have formed from a binary neutron star merger or supernova explosion. See [453, 454] and references therein for recent observational evidences.

Such systems are astrophysically very interesting: detecting a remnant of a neutron star merger would help to improve constraints on the equation of state [455–458] compared to only considering the inspiral of the system alone [234, 459, 460] in the case of binary neutron star mergers or only electromagnetic observations of the supernova. Furthermore, detecting such a system would be a huge step in multi-messenger astronomy, and would allow us to determine the nature of the remnant, something at which electromagnetic observations can only hint. As we saw from GW170817, astronomers were able to see the remnant in multiple ways — UV, IR, visible — and each way seemed to imply a different expected remnant. Some studies report the formation of a hypermassive neutron star lasting for $\mathcal{O}$(s) [461–465], while others saw continued energy emission from a long-lived remnant [466–469]. In the latter case, the signal emitted would last longer than the canonical $\mathcal{O}$(s) expected from mergers, but shorter than the durations $\mathcal{O}$(years) expected from much older, asymmetrically rotating neutron stars. This "intermediate" regime of signal durations would contain very interesting physics, and yet until recently, not much effort had been made to search for these kinds of sources.

Such searches for a remnant of GW170817 were performed on O2 data, analyzing data in segments of $\mathcal{O}$(seconds) for burst-like signals and $\mathcal{O}$(hours-days) for tCWs, and set the first-ever upper limits on GW emission from a remnant [470, 471]. In contrast to ordinary CWs, tCWs last for a much shorter time, have very large spin-downs, and have frequencies that evolve non-linearly over time. Thus, new analysis methods had to be designed to search

JCAP07(2023)068

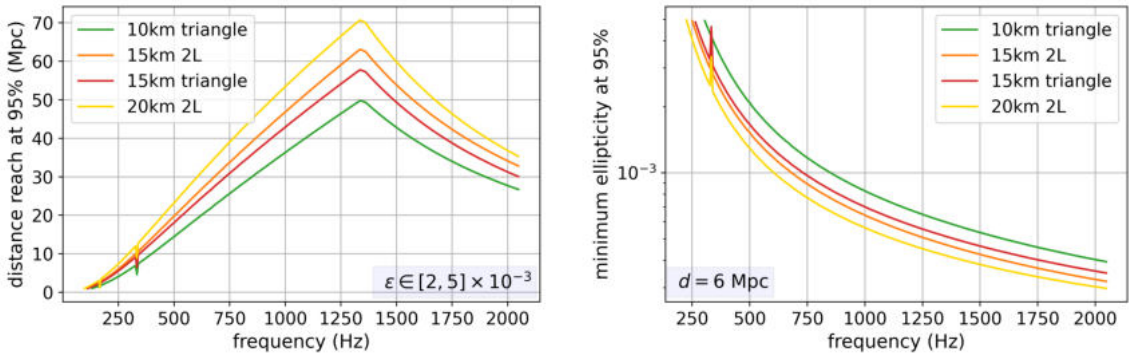

Figure 68. Left: ET distance reach to transient CW signals emitted by remnants of binary neutron star mergers or supernovae for various arm lengths and shapes, fixing the configuration to allow both high and low-frequency enhancements. The ellipticites used to construct these curves are the maximum allowed by energy conservation, assuming that all rotational energy is emitted in GWs, and imposing $\epsilon \leq 5 \times 10^{-3}$, the largest expected degree of deformation. At frequencies for which the ellipticity given by energy conservation exceeds 5×10^3, we impose $\epsilon = 5 \times 10^{-3}$. Right: ET minimum detectable ellipticity for different configurations for newborn neutron stars 6 Mpc away. Both plots use $\dot{f}_0 \leq -1 \times 10^{-4}$ Hz/s, $T_{\rm FFT} \sim 70$ s, $T_{\rm obs} = 1$ day, and $I_{zz} = 10^{38}$ kg· m^2.

for these signals [472–477]. The sensitivity of the O2 search allowed us to reach distances $\mathcal{O}(1)$ Mpc; however, with ET, we will be able to reach distances of $\mathcal{O}(10 - 100)$ Mpc, depending on the degree of deformation of the neutron star. To compute this sensitivity, we use an equation similar to eq. (6.24), that has been generalized for power-law signals and gives the maximum distance reach at a given confidence level:

$$d_{\rm max} = 4.63 \cdot 10^{-9}\ {\rm m} \left(\frac{I_{zz}}{10^{38}\ {\rm kg{\cdot}m^2}}\right) \left(\frac{\epsilon}{10^{-3}}\right) \frac{1}{N^{1/4}} \frac{T_{\rm FFT}}{\sqrt{T_{\rm obs}}} \left(\sum_i \frac{\mathcal{F}_i^2}{S_n(f_i)}\right)^{1/2} ({\rm CR_{thr}} + 1.6449)^{-1/2}. \tag{6.25}$$

Here, $\mathcal{F}_i = f_i^2$ is short-hand for the ith frequency, and the sum goes over all frequencies during $T_{\rm obs}$.

In the left-hand panel of figure 68, we plot the expected distance reach for different ET configurations, for a braking index $n = 5$, i.e. pure GW emission. The ellipticity at each frequency is the maximum allowed by energy conservation, and we restrict to ellipticities less than 5×10^{-3}, the largest expected for newborn neutron stars [478]. However, at frequencies below ~ 1200 Hz, the ellipticity given by energy conservation is much larger than that allowed theoretically; hence, we impose $\epsilon = 5 \times 10^{-3}$ up to 1200 Hz. In this regime, we see that the distance reach steadily increases with frequency at a fixed $\epsilon = 5 \times 10^{-3}$, which is consistent with eq. (6.25). For frequencies greater than 1200 Hz, the distance reach decreases slightly, since at this point, the ellipticity allowed by energy conservation is in fact less than 5×10^{-3}. Magnetars formed in core collapse supernovae look more promising, in terms of event rate, with respect to those following the merger of NS binary systems. The overall core collpase supernova rate is of the order of one event per year within 10 Mpc (4 events/yr within 20 Mpc) [479]. The fraction of core collapses leading to the formation of a magnetar is uncertain and, while past estimations pointed to the $(1 - 10)\%$ range [480], more recent results, based on observations and a more proper consideration of selection effects, typically provide higher values, even of the order of 40%, see e.g. [481]. This would correspond to a magnetar

JCAP07(2023)068

formation rate of ~ 2 per year within 20 Mpc, which is well within the search distance reach for a wide range of initial spin frequencies, for the optimistic deformation rate discussed above.

In the right-hand panel of figure 68 we plot the minimum detectable ellipticity at a fixed distance of 6 Mpc, at which we expect to detect magnetars forming at a rate of one per 5-10 years. At such a distance, the only low-frequency ($\lesssim 20$ Hz) sources that could produce a detectable gravitational-wave signal are those with unphysical ellipticities, i.e. $\epsilon > 1$, so we omit those on the plot. We only consider frequencies at which the minimum detectable ellipticity is less than 5×10^{-3}, which is consistent with the left-hand panel. In fact, at such distance, we would be able to detect the tCW from newborn magnetars with ellipticity of the order $10^{-3} - 10^{-4}$, much lower than the maximum predicted value.

We see that the differences among configurations are mostly driven by the arm-length, and there is little difference between the 2L-15km and 15km triangle. As in the CW case, we have applied $\mathrm{CR_{thr}} = 4$ for the 2L case, and $\mathrm{CR_{thr}} = 3.4$ in the triangle case to capture the anticipated improvements in both computational power in the 3G era and improved coincidences resulting from a triangle-shaped detector. Furthermore, these plots are created with the full HFLF xylophone configuration. *If we were to remove the low-frequency instrument in the left-hand panel, the distance at low frequencies* $\lesssim 100$ *Hz (not shown) decreases from* $\mathcal{O}(1-10)$ *kpc to* $\mathcal{O}(0.1-1)$ *kpc. This could be relevant, since the enhancements due to the LF instrument allow us to reach the galactic center at low frequencies.* However, in the right-hand panel, the results do not vary at all, since the ellipticities are already unphysical at frequencies below 30 Hz (not shown).

6.6.3 Search for dark matter with CWs

GW detectors could probe the existence of some kinds of dark matter (DM) [482]. In many cases, DM has been predicted to produce CW-like signals, so that data analysis methods used for the search of "standard" CW or tCW have been extended, see e.g. [483], and applied to the search for DM signatures. Ultralight bosons are interesting DM candidates, including dark photons and Quantum ChromoDynamics axions [438, 484–486]. Potential detectable systems might be boson clouds formed around spinning BHs or vector bosons in form of dark photons. Detectable continuous signals can arise also from compact dark objects or primordial black holes.

Boson clouds around black holes. Ultra-light bosons fields present in the nearby regions of a Kerr black hole can clump around it through a superradiant mechanism, forming a BH-boson "cloud" system at the expense of the BH angular momentum [438, 486, 487]. This formation channel is maximally efficient when the particles's Compton wavelength is comparable to the size of the BH, $\hbar/(m_b c) \simeq GM_{\mathrm{BH}}/c^2$, where m_b is the boson mass, M_{BH} is the black hole mass, $\hbar$ is the reduced Planck's constant, and c is the speed of light. Once formed, the cloud starts to dissipate via particle annihilation to gravitons, emitting a quasi-monochromatic and long-duration signal with a frequency dependent mainly on the boson mass,

$$f_{\mathrm{gw}} \approx 483\,\mathrm{Hz}\left(\frac{m_{\mathrm{b}}c^2}{10^{-12}\ \mathrm{eV}}\right) . \tag{6.26}$$

Earth-bound detectors are mostly sensitive to boson masses in the $10^{-14} - 10^{-11}$ eV$/c^2$ range [452]. The BH-boson cloud system is often referred to as a gravitational atom. The emitted signal is characterized by a spin-up due to the cloud mass decrease, which reduces

JCAP07(2023)068

its binding energy [488, 489], as well as to boson self-interaction [490]. The GW signal amplitude is

$$h(t) = h_0 \left(1 + t/\tau_{\rm gw}\right)^{-1} , \tag{6.27}$$

where h_0 is mainly determined by the BH and boson masses, the BH initial spin and the distance, through

$$h_0 \simeq 3 \times 10^{-24} \left(\frac{\alpha}{0.1}\right)^7 \left(\frac{\chi_i - \chi_c}{0.5}\right) \left(\frac{M_{\rm BH}}{10\ {\rm M}_\odot}\right) \left(\frac{1\ {\rm kpc}}{d}\right) , \tag{6.28}$$

where α is the fine-structure constant of the gravitational atom, given by

$$\alpha = \frac{G M_{\rm BH}}{c^3} \frac{m_b c^2}{\hbar} . \tag{6.29}$$

The gravitational-wave timescale $\tau_{\rm gw}$ is also dependent on the BH mass, the boson mass and the BH initial spin [438, 452, 489]. The detection of CW signals from boson clouds would allow to establish a fascinating connection among particle physics and black holes. Null results, as those obtained so far, see e.g. [452, 491, 492], brings anyway valuable constraints on the permitted boson masses.

Dark-matter particles interacting with GW detectors. Another interesting scientific scenario for ET are ultralight particles behaving as a classical field interacting coherently with the atoms of the test masses. For instance, dark photons coupled to the baryon or baryons minus leptons number $\mathrm{U}(1)_B/\mathrm{U}(1)_{B-L}$ have been considered in literature. These particles can produce an oscillating force on dark charged objects [439, 493, 494]. The same type of behavior is expected for tensor particles [495]. Different production mechanisms have been proposed for the dark photon production, such as misalignment mechanism associated with the inflationary epoch, light scalar decay or cosmic strings [496, 497]. The dark photon DM field oscillations impinge a time-dependent Equivalence Principle-violating force acting on the test masses. This will produce a change in the relative length of the detector's arms, causing a signal strain at the detector output. The time-dependent force acting on the test masses produces a strain oscillating at the same frequency and phase as the dark photon field [439, 498–500]. It should be noted that a similar signal may be produced in the case of scalar dark matter particles directly interacting with the mirrors. In particular, as described by [501], the interaction of the scalar bosons with the detector beam-splitter will induce oscillations in the thickness of the mirror due to the oscillations of the fundamental constants [502–504]. They could also interact with the particles in the reference cavity in the detector, resulting in a similar measurable oscillation of fundamental constants [505]. The signal frequency is determined by the dark photon mass, $f_0 = m_A c^2/(2\pi\hbar)$, corresponding for Earth-based detectors to dark photon masses in the range $10^{-14} - 10^{-11}$ eV/c^2. In fact, the signal is not exactly monochromatic due to the fact dark photon particles follows a Maxwell-Boltzmann velocity distribution.

Taking into account the physics of dark-matter signals, different CW methods based on cross correlation and excess power have been applied to look for these types of signals [439, 498, 506, 507], and have resulted in competitive constraints on $\mathrm{U}(1)_B$ coupling using data from the most recent observing run of advanced LIGO/Virgo/KAGRA [499, 508], and on scalar dilaton dark-matter coupling to electrons and photons using GEO600 data [501]. Furthermore, projected constraints for axions altering the polarization of light shining down the interferometer arms have been produced [509, 510].

JCAP07(2023)068

When considering the different configurations and geometries, we note that the 2L geometry would experience a larger strain due to dark photons by a factor of $2/\sqrt{3} \sim 1.15$ compared to a triangle-shaped detector, independent of the arm-length [439]. Since any frequency (or mass) for the dark photon or other dark matter particle is possible, both the low- and the high-frequency instruments of the ET xylophone configuration are important. Furthermore, increased arm length is also the primary way to improve sensitivity to these particles, since they behave just as traditional CWs, though T_{FFT} could not be as long as 10 days because of the frequency modulation induced by the Maxwell-Boltzmann distributed velocities. Finally, the triangle-shaped detector would allow triple coincidences, but since the dark-photon signal would show up looking like "correlated noise" between the detectors, having a single triangle-shaped detector in one place may increase the number of correlated noise disturbances, reducing the sensitivity to dark-matter particles.

Inspiraling compact dark objects and PBHs. Dark matter can be present in our universe in form of macroscopic objects, we generically refer to as compact dark objects (CDOs). The actual formation channel and the origin of CDOs is still widely debated. CDOs can form pairs and emit an almost monochromatic signal while being far from the coalescence phase. Primordial BHs (PBHs), that we have discussed in detail in sections 6.3.2 and 6.3.3, are an example of CDOs. In the context of CW signals, binary systems made of sub-solar mass PBHs as well as more generic CDOs, represent potential targets. Indeed, the GW signals emitted by these systems, when the two compact objects are far away from the coalescence and their masses are small enough, say $< 10^{-2}\ M_{\odot}$, i.e below the mass range considered in section 6.3.3, can be modeled as CW or tCW signals with a spin-up described by a power law, see e.g. [440, 511].

If the chirp mass is small enough, the frequency can be modeled exactly as the linear frequency Taylor expansion used for standard CW searches. This means that, for instance, a pair of inspiralling PBHs with chirp masses below $10^{-5}\ M_{\odot}$ would emit a GW signal indistinguishable from those arising from non-axisymmetric rotating NSs spinning up, and upper limits have already been placed on the fraction of dark matter that PBHs could compose (f_{PBH}) using CW results from the O3a and O3 observing runs [443, 512].

These upper limits on f_{PBH} derived from CW searches are of particular importance, since they lie within the "asteroid-mass" PBH mass regime. In this mass range, there are almost no existing constraints on f_{PBH} [261]. ET will allow us to probe realistic f_{PBH} in the asteroid-mass regime (currently upper limits on $f_{\mathrm{PBH}} > 1$ from these searches), and will result in an improvement of 1-2 orders of magnitude, regardless of the detector configuration or geometry [440]. The same comparison of different detector designs discussed in section 6.6.1 for all-sky searches would be applicable here, since the constraints on f_{PBH} are derived from all-sky search results.

6.6.4 Conclusions

We have considered here the impact of different ET geometries and configurations on the detectability of persistent GW signals. In the case of CWs from slowly spinning down asymmetricaly rotating neutron stars, we find that the number of detectable sources in targeted searches is mostly sensitive to the arm length while, for realistic degrees of deformation to high-frequency enchancements, the shape of the detector does not have a relevant role. Furthermore, in all-sky searches, we expect to be able to use a value of T_{FFT} that is ~ 100 times longer than used in analyses today, and thus find that we can constrain the ellipticity

JCAP07(2023)068

of unknown neutron stars to be less than 1×10^{-7} at frequencies above 300 Hz from the galactic center. This sensitivity is also mostly a function of the arm-length, and does not vary significantly between design choice.

For transient CWs, the arm length is also the most important factor that determines the relativity sensitivity of the different configurations considered, with the low-frequency sensitivity only helping to reach the galactic center at signal frequencies below $\sim$ 30 Hz. However, we considered sources with initial spin-downs one to three orders of magnitude smaller than those searched for in [471], determined by the maximum allowed ellipticity predicted theoretically. This limited our distance reach by a couple of orders of magnitude compared to the ellipticities $10^{-2} - 10^{-1}$ considered in [471].

We have hinted at the possibility of constraining exotic physics with CW and tCW searches, and note that the results presented here can be recast in terms of constraints on, e.g. the fraction of dark matter that PBHs could compose, the maximum coupling strength to baryons that dark-matter particle could have, or boson/black hole mass pairs that could be excluded from existing.

All these results must be interpreted carefully, since they assume Gaussian noise and a lack of detector artifacts. In practice, glitches and noise lines will affect the sensitivity to all of these sources. Noise lines will inhibit dark-matter and CW searches the most, since they focus on persistent, long-lived GWs, while glitches are more problematic for the transient CW searches. We have tried to capture the impact of improved coincidences by lowering $\mathrm{CR}_{\mathrm{thr}}$ for the triangle-shaped detector compared to the 2L one; however, these thresholds are subject to change in practice based on available computing power and the characteristics of the noise. We do not consider explicitly how the so-called "null stream" would impact the detectability of these sources, though we expect that our methods, already designed to be robust against noise disturbances and glitches, can achieve comparable sensitivities as those obtained in Gaussian noise, based on current GW searches.

7 The role of the null stream in the triangle-2L comparison

The null stream is a signal-free linear combination of the interferometer strain data, and it plays an important role in the comparison of 2L and triangle (Δ) configurations of ET. A null stream can be formed for an arbitrary GW detector network with at least three detectors, but generally only for one GW signal at a time [513]. However, the Δ configuration allows one to form a null stream that cancels out all gravitational-wave signals simultaneously [120], because of its closed geometry of component arms and almost negligible light travel times between components. The null stream in the Δ configuration (from now on just "null stream") has the unique ability to provide access to a signal-free channel, and therefore access to the properties of (incoherent) instrumental noise without contamination from gravitational-wave signals [149].

It should be stressed that inference from data with the null stream noise discarded is identical to coherent inference from the full set of data so that access to the null stream does not directly improve inference [514]. Moreover, a 2L configuration without access to the null stream may still achieve good noise mitigation but requires more complex methods that introduce uncertainty into the process. Access to the null stream provides a more straightforward way (compared to the 2L configuration) to extract the power-spectral density (PSD) of the detector noise and enables unique data-analysis techniques for improved science

JCAP07(2023)068

extraction. In the following, we will describe some of these techniques and their impact on science extraction.

Estimation of unbiased noise power spectrum. Within the Δ configuration of ET, the null stream $d_{\rm null}$ can be straightforwardly formed by

$$d_{\rm null} = d_1 + d_2 + d_3, \tag{7.1}$$

where d_i are the strain data for the individual detectors in the triangle. If the noise properties are homogeneous and incoherent among these detectors, then the noise PSD of each detector S_n^i can be estimated by

$$S_n^i = \frac{1}{3} S_n^{\rm null}, \tag{7.2}$$

where $S_n^{\rm null}$ is the PSD of the null stream. In the absence of a null stream, it is non-trivial to disentangle the detector noise from the unresolvable GW signals, which is also referred to as "confusion noise".

Assuming uncorrelated noise, another method to estimate the instrument-noise PSD is by calculating the cross power-spectral density (CSD) of the null stream with the data streams [149]:

$$\langle d_{\rm null} d_i^* \rangle = S_n^i, \tag{7.3}$$

where S_n^i is the PSD of detector i. This method does not require the PSD of different interferometers to be the same.

Noise can be produced identically in two interferometers, which would therefore not appear in the null stream and bias PSD estimates that use the null stream. Technically, the bias in PSD estimates is produced by the real part of the complex-valued instrument-noise CSDs between interferometers. The natural magnetic background is a possible source of such noise. Also seismic gravity fluctuations are considered a possible source of identical noise. However, over the $> 400\,$m distances between any two test masses of two LF interferometers, this so-called Newtonian noise is most likely weakly correlated [515], which means that one should only expect a mild suppression in the null stream. See section 5.4 for a more in-depth discussion of these noise sources. Ref. [150] shows that, given knowledge of the correlated/non-identical noise sources (e.g. through witness sensors), unbiased instrument-noise PSD estimates can in principle be obtained even in the presence of correlated noise.

Impact on science extraction. The most direct impact of an unbiased estimate of the noise power spectrum is on the measurement of the stochastic gravitational-wave background. By subtracting the null stream PSD from the individual detector PSD, one obtains the PSD of the GW signals S_h present in the data

$$S_h \simeq S_n^i - \frac{1}{3} S_n^{\rm null}, \tag{7.4}$$

where the equality holds when the noise is identical amongst individual detectors (see e.g. refs. [149] and [150] for discussion on deviations from this assumption). S_h can be directly related to the SGWB if the data contains no resolvable signals. Otherwise, one has to first subtract the loud sources from the data (see e.g. refs. [516, 517]).

The inability to disentangle detector noise from confusion noise also has the effect of raising the overall perceived noise level. In a templated GW search, the effect manifests as a loss

JCAP07(2023)068

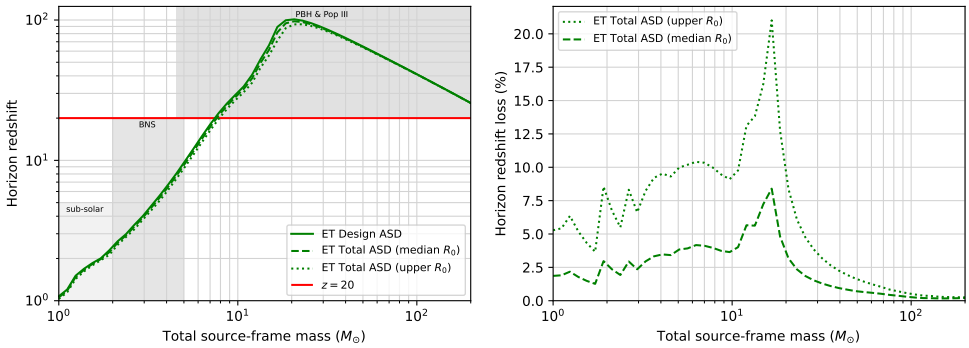

Figure 69. The loss in the ET detection horizon, as estimated in [516], due to the confusion of instrumental noise and compact binary inspirals. Dashed lines show the effect of the median local merger rate and dotted lines represent the upper merger rate. A higher merger rate introduces a stronger confusion noise and hence the higher horizon redshift loss. This effect can be mitigated by the ET null stream available in the Δ configuration.

of matched filtering SNR, and it is demonstrated in figure 69. Figure 69 shows the CBC horizon redshift (left) and its percentage loss (right) as a function of the total source-frame mass and for different merger rates. The loss in the redshift reach of ET increases with a higher merger rate of compact binaries, and for BBHs it may appear between $\approx 2.5\%$ and $\approx 20\%$, depending also on the mass of the CBC. For the Δ configuration, the efficiency for mitigating this effect approaches 100% as the sensitivity of all ET components approaches the same level.

Furthermore, the confusion noise impacts a calculation of the false alarm rate (FAR), the probability of incorrectly rejecting the noise hypothesis. The FAR is calculated by comparing the noise-induced (background) distribution of a detection statistic (e.g. SNR for matched filtering) with the one measured from a signal candidate. For example, one could perform matched filtering on time shifted data (between the individual detectors) to estimate the background distribution (see e.g. ref. [518]). FAR calculations typically assume that the number of genuine GW detectable signals is low enough not to impact the estimate, which will not be the case for ET anymore. By estimating the noise background distribution directly from the null stream (e.g. time shifting the null stream with respect to itself), one could mitigate the contamination from confusion noise and thereby improving the detection sensitivity and accuracy.

Mitigation of transient detector glitches. A number of known instrumental noise artefacts such as glitches invalidate the standard assumption that the data is described by a superposition of the Gaussian instrumental noise and GW signals. If unmodeled, they will appear as false positives, whereas modeling glitches introduces additional uncertainties. Unlike GWs, these artefacts will appear as non-Gaussian outliers in the null stream, which provides an opportunity to remove them. Ref. [149] outlines two methods for eliminating glitches with the null stream. First, one can identify glitches by match-filtering them in the null stream. Second, one can identify null stream data segments that are inconsistent with Gaussian noise. The authors show that it is possible to end up with a clean Gaussian background in the Δ configuration in the limit where ET components approach the same sensitivity.

JCAP07(2023)068

Impact on science extraction. The non-Gaussian part of the background causes extended tails in the noise background and therefore limits the FAR. The exact extent to which this happens will only be known when ET is operational. Current gravitational wave observatories not only discover more GWs while achieving a better sensitivity but also retract more spurious signals [519]. This increasing trend might continue down to the design sensitivity of the ET. The null stream will reduce the uncertainty associated with modeling glitches, and allow us to mitigate the effects of non-Gaussian noise. The most prominent benefit of the null stream is expected for high-mass distant BBHs that mimic glitches as well as for signals that are only described by phenomenological models.

Control of known and unknown systematic errors. Any errors in the detector calibration can propagate into the null stream to cause incomplete cancellations of gravitational wave amplitudes [520]. If the signal waveform is a-priori well understood, and if its parameters are well-measured by the network of detectors, then the residual signal in the null stream will be the product (in the frequency domain) of the calibration error and known weighted amounts of signal [521]. One can detect this residual by performing matched filtering on the null stream. The calibration error can be obtained by fitting with a family of specific functions supplemented by the SNR output of the matched filters over a number of detected events. The ET null stream in the triangle configuration reduces the uncertainty in calibration parameters, which may propagate to GW signal parameters. However, the level of systematic errors in detector calibration in ET is not known, and even for current detectors it is only known to be less than 2% [522]. Therefore, it is not clear how many signals in ET will be affected by these systematic errors. Further studies are also necessary to demonstrate the performance of ET null stream calibration compared to other techniques, as well as the impact on the gravitational wave parameter estimation. In the worst case scenario, in 2L detectors calibration uncertainties will have to be estimated simultaneously with gravitational-wave source parameters, which would increase the computational cost of the analyses and introduce additional uncertainty. Note also that ref. [521] estimates that, in a network of at least three L-shaped 3G detectors, the calibration error can be inferred at the percent level if supplemented with $O(100)$ relatively loud (SNR=20) events.

8 Summary

In this work we have performed a detailed study of the Science Case of ET, significantly expanding the study in ref. [15]. We have considered both ET in its reference design (a 10 km triangle in a xylophone configuration, with an HF instrument and a cryogenic LF instrument), as well as variations on the reference design, both in the geometry (triangle vs 2L, with different arm lengths) and in the ASD (full sensitivity vs HF instrument only).

First of all, the significantly more detailed study of the Science Case performed here confirms and provides more detail and evidence for the picture summarized in ref. [15]: *ET, in its reference configuration, is a superb detector, with an extraordinary discovery potential in the domains of astrophysics, cosmology and fundamental physics.* With order $10^4 - 10^5$ BBH, BNS and NSBH detections per year, it will address and provide answers to an extremely rich and varied set of scientific questions; at the same time, it will penetrate deeply into unknown territories, where revolutionary discoveries could await for us.

Starting from the extraordinary potential of the reference design, it is, however, still mandatory to study what happens under variations of this baseline. At the very least, this allows us to understand how the different elements of the design, such as its geometry or

JCAP07(2023)068

the relative roles of the HF and LF instruments, concur to produce the scientific output of ET, and what could be reached in intermediate stages of the commissioning of the detector. Furthermore, this study can suggest directions where changes of the baseline design could results in improvements of the science output. The original structure of the ET design was first laid down 10-15 years ago [10–12], well before the first detections of GWs. At that time, one was not even sure that there was, out there, a population of BBHs that coalesced within a Hubble time. Now we have a statistically significant catalog of detections, and building on the understanding that has accumulated thanks to these discoveries and the studies that they have stimulated, we are now able to present in this paper a study based on astrophysically-motivated populations.[46]

8.1 Comparison of different geometries

In this paper we have examined several different geometries, comparing two L-shaped detectors on widely separated sites to a single-site triangle, and with different choices of arm-length (and relative orientations for the two L-shaped detectors), to provide a broad set of options. We will begin by summarizing the main results from the comparison of the 15 km 2L configuration with the 10 km triangle, in section 8.1.1. In section 8.1.2 we will instead summarize the results of the comparison between the 15 km 2L and the 15 km triangle. In section 8.1.3 we also summarize the results for a single third-generation L-shaped detector. Further elements of the comparison between geometries, including correlated noise, the null stream, etc., are summarized in section 8.1.5.

8.1.1 Comparison between 15 km 2L and 10 km triangle

Focusing first on the comparison of the 15 km 2L with the 10 km triangle, the main results can be summarized as follows.

- **Binary Black Holes.** The results of section 3.1 show that, for BBHs, the 2L configuration with 15 km arms, oriented at 45°, is superior to a 10 km triangle for the estimation of all parameters, and especially luminosity distance, see figure 5 in the main text and tables 39–42 in appendix C. To put things into perspective, for all parameters (except luminosity distance) the differences are at the level of factors of 2-3, while both configurations outperform LVKI-O5 by orders of magnitudes on all parameters (with less large, but still significant differences for angular localization), see figures 8 and 9. For instance, while all ET configurations detect basically the whole BBH population with SNR $\geq$ 12, if we restrict to 'golden events' with SNR $\geq$ 100 the 2L-15km-45° configuration detects (in our sample realization) 4933 BBH/yr, while the 10 km triangle 2298, and LVKI-O5 only 4. For SNR $\geq$ 200 these figures becomes 644, 282 and 2, respectively; see table 39 in appendix C. For most parameters, as mentioned above, the differences between the 15 km 2L at 45° and the 10 km triangle are at the level of factors 2-3, in favor of the 2L; however, they are significantly larger for the accuracy on luminosity distance: in the 2L-15km-45° configuration there are 202 BBH/yr with error on d_L smaller than 1%, to be compared with 28 for the 10 km triangle (and, in our sample realization, just 1 for LVKI-O5). For angular localization, focusing on the events with $\Delta\Omega_{90\%} \leq 50\,\mathrm{deg}^2$, we find 10304 BBH/yr for 2L-15km-45°, 6064 for

[46] Last but not least, the setting up and the development of the ET Observational Science Board allowed the formation of a coherent scientific community focused on ET, with the necessary expertise across the rather broad range of subjects needed for such a study.

JCAP07(2023)068

the 10 km triangle and 1607 for LVKI-O5, while for $\Delta\Omega_{90\%} \leq 10\,\mathrm{deg}^2$ these numbers become 2124, 914 and 599, respectively; see table 40.[47] The corresponding difference in the joint accuracies on d_L and angular resolution shows that, also for this metric, the 2L-15km-45° is clearly superior to the 10 km triangle, see figure 6.

In contrast, the 2L configurations with parallel arms are disfavored, because of their worse angular resolution; e.g., for 2L-15km-0° there are 3030 BBH/yr with $\Delta\Omega_{90\%} \leq 50\,\mathrm{deg}^2$), to be compared with 10304 BBH/yr for 2L-15km-45°; for $\Delta\Omega_{90\%} \leq 10\,\mathrm{deg}^2$ the difference is even larger, with 374 BBH/yr for 2L-15km-0° (so, almost a factor of two less than LVKI-O5), compared to 2124 for 2L-15km-45°.

- **Binary Neutron Stars.** Similar conclusions follow from the study of parameter estimation for BNSs in section 3.2, see figure 11 and tables 42–44. Again the 2L with 15 km arms at 45° improves on the already remarkable performances of the 10 km triangle, typically by factors of order 2-3, while both outperform LVKI-O5. For instance, if we restrict to 'golden events' with SNR ≥ 50, the 2L-15km-45° configuration detects 1052 events per year, while the 10 km triangle 458 and LVKI-O5 only 3 (for SNR ≥ 100 these figures becomes 134, 57 and 0, respectively). If we consider, instead, events with error on luminosity distance smaller than 10%, there is almost a factor of 10 between 2L-15km-45° and the 10 km triangle, with 479 events/yr for 2L-15km-45° and 52 for the 10 km triangle (and only 1 for LVKI-O5; as always, in particular for small numbers, these are the numbers for our specific sample realization). For angular localization, focusing on the events with $\Delta\Omega_{90\%} \leq 100\,\mathrm{deg}^2$, we find 559 events/yr for 2L-15km-45°, 184 for the 10 km triangle and 51 for LVKI-O5, see table 43 (however, for a handful of very close events, localizable to better than 10 deg^2, the five-detector network LVKI-O5 does better, and we get 25, 8 and 31 events, respectively). The left panel of figure 12 shows that, also for BNS, the 2L-15km-45° is clearly superior to the 10 km triangle for the joint accuracy on d_L and angular resolution, that determine the localization volume.

  The 2L configurations with parallel arms has again an angular localization capability worse than that of the 2L configuration at 45°, but the effect is less strong compared to BBHs (see the panel for $\Delta\Omega_{90\%}$ in figure 11).[48] On the other hand, the accuracy on the inclination angle ι for the parallel configurations is, comparatively, quite poor. Since ι is degenerate with the luminosity distance d_L, also for d_L the parallel 2L configuration has significantly lower performance compared to the configuration at 45°. For instance, for the 2L-15km-0° we get 48 BNS/yr with error on d_L better than 10%, a factor of 10 lower than the 479 BNS/yr for 2L-15km-45°. As for angular localization, for 2L-15km-0° we get 293 BNS/yr localized better than $100\,\mathrm{deg}^2$, so slightly better than the 10 km triangle, but about a factor of 2 worse than the 559 BNS/yr for 2L-15km-45°; see again table 43.

  For the parameter $\tilde{\Lambda}$ that encodes the tidal deformability of the neutron stars, we see from figure 11 and table 44 that, again, the 2L with 15 km arms improves by a factor ~ 2 the already remarkable performances of the 10 km triangle, and both outperform LVKI-O5 by orders of magnitudes. For instance, considering the events with an error

[47] Here the difference with LVKI-O5 becomes smaller: the events with very accurate angular localization are in general the closest, so they are accessible also to LVKI-O5, which can have good localization thanks to its network of five widely separated detectors.

[48] This is due to the long duration of BNS signals, which allow using the rotation of the Earth to localize the signal, also for the parallel setting.

JCAP07(2023)068

on $\tilde{\Lambda}$ smaller than 10%, we get 2463 BNS/yr for 2L-15km-45°, 1040 for the 10-km triangle, and 2 for LVKI-O5. For events with an error on $\tilde{\Lambda}$ smaller than 5% these numbers become 200, 96 and 0, respectively.

- **ET in a network with CE.** When ET is inserted in a network with Cosmic Explorer (either a single CE 40 km detector or two 2 CE detectors, one with 40 km and one with 20 km arms) the performance of the whole ET+CE network is, naturally, somewhat less sensitive to the choice of geometry for ET. However, the differences are still significant, particularly for the ET+1CE network. For instance, for ET+1CE, the number of BBHs with SNR > 200 is 1.8×10^3 when ET is in the 10 km triangle configuration, and raises to 2.4×10^3 for 2L-15km-45°, while the number of BBHs localized better than $10\,\mathrm{deg}^2$ raises from 3.0×10^4 to 3.6×10^4, and the number of BBHs with luminosity distance measured better than 1% raises from 2.9×10^3 to 4.3×10^3 (or from 5.3×10^3 to 7.0×10^3, for ET+2CE); see figure 18 and tables 39, 40.

  For BNSs, at ET+1CE, the number of detections/yr with SNR > 100 is 312 when ET is in the 10 km triangle configuration, and raises to 418 for 2L-15km-45°; the number of BNS/yr localized to better than $10\,\mathrm{deg}^2$ raises from 2.4×10^3 to 3.8×10^3; the number of BNS/yr with luminosity distance measured better than 1% raises from 4.1×10^3 to 7.9×10^3 (or from 1.4×10^4 to 1.9×10^4, for ET+2CE); and the number of BNS/yr with tidal deformability measured better than 5% raises from 243 to 400 (or from 337 to 535 for ET+2CE); see figure 19 and tables 42–44.

  In general, we see that the choice of geometry still has significant consequences also when ET is in a 3G network with one or two CE.

- **Multi-messenger astrophysics.** For multi-messenger astrophysics, the results of section 4 show that, again, the 2L-15km-45° allows us to obtain a further improvement on the already remarkable performances of the 10 km triangle (and is comparable to the 15 km triangle), enabling the observation of a larger number of well-localized events, up to a larger redshift. The number of short GRBs with an associated GW signal increases by about 30% making possible a joint detection at larger redshifts, and the number of expected kilonovae counterparts increases by a factor of 2. The better volumetric localization of 2L-15km-45° with respect to 10 km triangle, as shown in figure 6, facilitates the search of the EM counterpart giving the possibility to use galaxy-targeting strategy and enables a more efficient removal of contaminants. For pre-merger alerts with sky-localization smaller than 100 deg^2, the 15 km triangle is performing better than the 10 km triangle and the 15 km 2L configuration, reaching almost the capability of the 2L configuration with 20 km arms, see table 3.

- **Stochastic backgrounds.** For stochastic backgrounds, the best configurations are either 2L with parallel arms or the triangles, with the 2L parallel being the best below about 100 Hz and the triangle above 100 Hz. The 2L with arms at 45° is worse than the 2L with parallel arms[49] below about $200 - 300$ Hz, while the two become comparable above $200 - 300$ Hz (where, however, both are less good than the triangle); see figure 27. However, to exploit the better sensitivity (below 200-300 Hz) of 2L-parallel with respect to 2L-45° for studies of cosmology, the subtraction of

[49] See section 2 for the definition that we use for the relative angle between the L-shaped detectors, which differs by about 2.51° from the more standard one using the great circle connecting the two detectors.

JCAP07(2023)068

the astrophysical background is necessary, see section 6.5.3. An imperfect subtraction of CBC sources would pose a serious threat to reaching the nominal sensitivity to a cosmological background (see [427, 428, 523] for recent discussions), possibly even wiping out any advantage of the 2L-parallel with respect to the 2L-45° configuration.

The ability to resolve the angular distribution of stochastic backgrounds, through their lowest multipoles, is significantly better for the 2L configurations (both aligned and misaligned) compared to the triangle, see figure 30.

The analysis in section 6 shows that (as could be expected) the performance of the various geometries, with respect to the specific science cases studied, broadly follows the indications obtained from the more general metrics studied in sections 3–5. The 10 km triangle is a game-changer with respect to LVKI-O5, allowing a jump of orders of magnitudes, accessing physics that it is well beyond reach for 2G detectors. The 15 km 2L with arms at 45° provides a further gain with respect to the 10 km triangle, typically by factors of order 2-3, depending on the specific scientific question. Some examples, from the various studies presented in this paper, are as follows.

- Concerning tests of GR based on BH quasinormal modes, we see from table 13 that the ringdown SNR of GW150914 would have had a remarkable value of 141 in the 10 km triangle, which would further raise to 192 in 2L-15km-45°, inducing a corresponding difference in the reconstruction of ringdown frequencies and damping times, according to eq. (6.1). Furthermore, we see from table 14 that the 10 km triangle would detect 41 events/yr with a ringdown SNR higher than 50, that raise to 110 events/yr for the 2L-15km-45° (for a ringdown SNR higher than 100, these numbers become 4 and 10, respectively), resulting in a further difference in performance when stacking different events.

- For nuclear physics studies, we see from table 17 that the 10 km triangle can reach a remarkable accuracy of 10.0 m on the radius of neutron stars (taken the same for all NS, just as a proxy for the actual hyper-parameters determining the NS equation of state); the 2L-15km-45° further brings it down to 6.4 m, thanks to a more accurate reconstruction of tidal deformability for individual events, and the stacking of a larger number of events. For the postmerger SNR, instead, we see from figure 45 that the differences between different geometries do not exceed the $(10-20)\%$ level, with the hierarchy fixed by the arm length.

- For the reconstruction of the merger rate, figure 46 and table 24 show that both the 2L-15km-45° configurations and the 10-km triangle lead to a correct reconstruction of the merger rate, although the 2L-15km-45° configuration leads to a more accurate reconstruction, by an average factor ~ 3 in the central values.

- For primordial BHs, assuming the PBH population model mentioned in the text, the 10 km triangle would detect 77 events/yr at $z > 30$ (a smoking-gun signature for a primordial origin), which is already quite remarkable. The 2L-15km-45° configuration would further rise this by a factor ~ 3, with 238 events/yr, resulting in a limit on the PBH abundance stronger by a factor about 1.8; see table 25.

- In cosmology, we see from tables 28–34 that, for the tests that we have performed, the results for the accuracy on H_0, on the dark energy equation of state and on modified GW propagation from the various geometries analyzed are quite similar.[50] In general,

[50]Here we restricted to the 10 and 15 km triangles and the 15 and 20 km 2L at 45°.

JCAP07(2023)068

the 2L-15km-45° can improve the results of the 10 km triangle on the accuracy of H_0, w_0 or Ξ_0 by factors ranging between $\sim (1.3 - 2.5)$, depending on the test.[51]

To sum up, the first overall conclusion that emerges is that:

> *1. All the triangular and 2L geometries that we have investigated can be the baseline for a superb 3G detector, that will allow us to improve by orders of magnitudes compared to 2G detectors, and allow us to penetrate deeply into unknown territories.*

How far we will penetrate into such territories, however, depends to some extent on the configuration chosen. From the above discussion, it follows that

> *2a. The 2L-15km-45° configuration in general offers better scientific return with respect to the 10 km triangle, improving on most figures of merits and scientific cases, by factors typically of order 2-3 on the errors of the relevant parameters.*

8.1.2 Comparison between 15 km 2L and 15 km triangle

We next summarize the main results of the comparison between the 15 km triangle and the 2L-15km-45° configuration, so in this case we change the geometry while keeping the arm-length fixed. The main results of this comparison are as follows:

- For parameter estimation of BBHs, the 2L-15km-45° is clearly superior to the 15 km triangle for the estimate of luminosity distance (with 202 events/yr with d_L measured better than 1%, against 77 for the 15 km triangle), and quite similar for all other parameters, see figure 5 and the first row of figure 10, and tables 40 and 41 in appendix C. Correspondingly, also the number of sources with good overall volume localization (say, error less than 1% on d_L and angular resolution better than 50 deg^2), is clearly better for the 2L-15km-45°, see the right panel in figure 6.

- The same holds for parameter estimation of BNSs, see figure 11 and the first row of figure 16, and tables 43 and 44 in appendix C. In particular, the 2L-15km-45° has 479 events with d_L measured better than 10%, to be compared with 153 for the 15 km triangle (which become 4328 to be compared with 1756, requiring an error smaller than 30%); see table 43. Instead, for angular resolution, the 15 km 2L with arms at 45° and the 15 km triangle are quite comparable (e.g., for the BNS localized better than 100 deg^2, with a threshold SNR > 12 we find 559 events/yr for 2L-15km-45° and 479 for the 15km triangle, see table 43, which become 644 and 764, respectively, with SNR > 8, see table 1. At this level, the comparison is of course affected also by sample variance). The respective joint distribution of events with respect to distance and angular localization is shown in the right panel of figure 12, which again shows an overall preference for 2L-15km-45°. For all other parameters the performances are quite similar.

- This reflects also on several aspects of the science case, where we see that the 2L-15km-45° and the 15 km triangle have similar performances; this can be seen, e.g.,

[51] Larger differences, in favor of the 15km-2L-45° with respect to the 10km triangle (and, to some extent, also with respect to the 15km triangle), are expected when extracting cosmological information by correlating dark sirens with galaxy catalogs, because of the much better volume localization of the 2L-15km-45° configuration, see figure 6 for BBHs, and figure 12 for BNSs. A quantitative assessment, however, also depends on the completeness of the galaxy catalogs that will be available when ET will be in operation. Work on this is in progress.

JCAP07(2023)068

in tables 1, 6 and 10 for multi-messenger astrophysics (except for the pre-merger alerts for which the 15 km triangle results are better, as shown in table 3); tables 13 and 14 for physics near the BH horizon; figure 40 for tidal deformability of exotic compact objects; table 17 for the measurement of the NS radii; figure 45 for the post-merger signal of BNS coalescences; table 24 for the merger rate reconstruction (where the 2L-15km-45° is a factor of 2-3 better than the 15 km triangle); table 25 and figure 48 for primordial BHs; or tables 28–36 for cosmology.

The overall conclusion, in this comparison, is that:

2b. The 2L-15km-45° configuration and the 15 km triangle have very similar performances on all parameters both for BBHs and BNSs, except for luminosity distance, where the 2L-15km-45° configuration is better by a factor ~ 3 *in the number events with accurately measured distance.*

8.1.3 A single L-shaped detector

Finally, we have considered the performance of a single L-shaped detector with 20 km arms, still with the ET characteristics in terms of ASD. The conclusion is that such a detector, taken as a single detector not inserted into a network with other 3G detectors, is not capable of delivering the science expected from the next generation of detectors. Its capability of angular localization of the source, and of reconstruction of the luminosity distance, would even be very much inferior to what the LVK network is expected to reach by the end of the O5 run, see the corresponding panels in figures 7 and 13 (actually, the number of well-localized sources detected per year would not even really improve on the results already obtained with the current GWTC-3 catalog of detections). This would result in a complete loss of all the science case aspects of 3G detectors related to multi-messenger astrophysics and to cosmology. Stochastic backgrounds of GWs, that in the frequency band of ground-based detectors can only be detected by correlating the output of two or more detectors, would also not be accessible to a single 3G detector, giving up again the corresponding aspects of the science case related to early Universe cosmology and to astrophysics. Furthermore, with a single detector, unmodeled burst signals and short signals due to massive BBH coalescences would be hard to distinguish from instrumental glitches, rendering problematic any confident detection of transient sources.

Therefore, a single L-shaped detector does not have a valid science case, even with 20 km arms (or longer). If inserted in an international network with 2CE, such as detector could be a useful addition to the network. However, given the scale of the investment, ET must have a solid science case, independently of the decisions that will be taken by other funding agencies, unrelated to a European project. Therefore:

3. A single L-shaped detector is not a viable alternative, independently of arm length. If a single-site solution should be preferred for ET, the detector must necessarily have the triangular geometry.

8.1.4 The null stream

The triangle has the advantage of having a null stream, where the GW signal cancels. This will certainly be beneficial. However, while the mathematics of the null stream is elegant, when one is confronted to its use in the concrete setting of the experiment several issues arise, that make it difficult to quantify reliably its impact.

JCAP07(2023)068

First of all, the triangle null stream is only operative when the interferometers in all three arms are on, so it is quite sensitive to the duty cycle. In this work we have assumed an uncorrelated 85% duty cycle in each L-shaped detector, and in each of the three detectors composing the triangle, see section 3; in this case the null stream will be available for $(0.85)^3 = 61\%$ of the run time. Assuming instead an independent duty cycle of 80% for each arm (the best duty cycle for the O3b LVK run is 79% [524]), implies that the null stream will only be available for 51% of the run time. However, the triangle design is considerably more complex than that of 2G detectors, with two interferometers in each detector (an HF interferometer, and a LF interferometer working at cryogenic temperatures), and it is difficult to reliably estimate what the duty cycle will be. In a (hopefully very pessimistic) scenario where each of the six interferometers has an independent duty cycle of 80%, the null stream would only be available for 26% of the run time.

An advantage of the null stream is that it provides a direct estimate of the instrument-noise PSD, see eq. (7.3). Here, however, enters the assumption that noise in different arms are uncorrelated. Noise produced identically in two interferometers (as could be the case for the natural magnetic background or seismic gravity fluctuations) would not appear in the null stream, and would therefore bias the PSD estimates that use the null stream (unless these noise can be identified and characterized, e.g. with witness sensors).

Assuming to have obtained an unbiased estimate of the PSD, the most direct impact would be on the measurement of the stochastic gravitational-wave background. An unbiased estimate of the PSD would also be beneficial for compact binary coalescences, to avoid a reduction of the detection horizon from the confusion noise of the unresolved BNS (that, being long-lasting, can produce a continuous backgrounds, contrary to BBHs that rather produce a 'popcorn noise, see section 5). However, here the advantage of the null stream should be weighted against the possibility of making longer arms. Figure 69 shows that, assuming a value of the local rate R_0 of BNS mergers equal to the median of the currently allowed range, the reduction in the horizon range for the 2L detectors, due to this confusion noise, would be between 2% and 7.5% for CBCs with masses below $20M_\odot$, and negligible above. With extreme assumptions on the rate R_0, taken at the upper limit of the currently allowed range, the reduction would be between 5% and 20% for CBCs with masses below $20M_\odot$, and again negligible above. The triangle null stream would be able to mitigate this reduction, possibly eliminating it completely, which is certainly very beneficial. On the other hand, we see from figure 4, left panel, that, in the same range of masses, the 2L 15km at 45° configuration has an horizon distance larger than the 10 km triangle by a factor $\sim (1.4-1.8)$, i.e. $(140-180)\%$.

The confusion noise also impacts the calculation of the false alarm rate. The null stream would allow estimating the noise background distribution directly (e.g. time shifting the null stream with respect to itself). In this way one could obtain more accurate estimates of the false alarm rate.

The null stream can be very effective at subtracting glitches, that would appear as non-Gaussian outliers in the null stream. The most prominent benefit in this case is expected for high-mass distant BBHs, that mimic glitches, as well as for signals that are only described by phenomenological models. In a 2L configuration, one would have to rely only on coincidences between detectors, and environmental sensing.

Another potential virtue of the null stream is that is reduces the uncertainty in the calibration (although it only provides relative calibration errors). However, the level of systematic errors in detector calibration in ET is not known. As discussed in section 7, further studies are needed to demonstrate the performance of the ET null stream calibration, com-

JCAP07(2023)068

pared to other calibration techniques. In the worst case scenario, in 2L detectors calibration uncertainties will have to be estimated simultaneously with gravitational-wave source parameters, which would increase the computational cost of the analyses and introduce additional uncertainty.

In summary, while in the triangle configuration the null stream would certainly be beneficial, its concrete application is subject to several uncertainties that are difficult/impossible to model before building and commissioning the detector, such as the duty cycle, the level of correlated or identical noise in different arms, the level of non-gaussianity in the noise or, as for instance in the case of detector calibration, the state of advancement of other alternative techniques.

8.1.5 Further aspects of the triangle-2L comparison

In this section we summarize our discussions of further aspects that are relevant to the comparison between the triangle and the 2L configurations.

- **Correlated noise.** For the triangle vs. 2L comparison an important aspect, that needs further studies, is that the triangle configurations suffer from a potential threat from correlated Newtonian, seismic and magnetic noise, or lightening strikes; while significant uncertainties exist in their estimate, these correlated noise might spoil the sensitivity to stochastic backgrounds below some frequency and, possibly, even to unmodeled bursts. A network of two widely spaced L-shaped detectors is significantly less sensitive to these problems.

  More in detail, an important potential danger, for all triangle configurations, is due to the fact that some mirrors of different nested interferometers are apart by a few hundred meters and, on this scale, correlated seismic and Newtonian noise can be important. This has been studied in detail only recently [141]. According to that analysis, such correlated noise would swamp the sensitivity to stochastic backgrounds of ET, in its 10 km triangle configuration, up to frequencies of order $(50 - 100)$ Hz (blue curve in figure 34), to the extent that the actual sensitivity of ET to stochastic backgrounds, up to these frequencies, would not improve on LIGO's A+ and Virgo's AdV+ design. Different assumptions could result in a lower level of noise, also shown in figure 34. With the most optimistic assumptions, the search for a stochastic background would still be impacted up to ~ 10 Hz (pink curve in figure 34). Such problems arise from correlations on the scale of hundreds of meters, and therefore do not concern a 2L configuration with widely spaced detectors.

  Magnetic noise will also pose difficulties to the triangle configuration: in the case of a very pessimistic assumption, where the magnetic noise in ET is the same as in the Virgo central building and it is fully correlated between two ET interferometers, it will affect the ASD sensitivity over the entire frequency band, by several orders of magnitudes at low frequencies, $f \lesssim \mathcal{O}(30)\,\text{Hz}$, and by a factor 1-10 at higher frequencies, see the lower panel in figure 35. Again, this would only apply for the co-located interferometers in the triangular configuration. However, further research is needed to understand to which level these infrastructural noise sources would be correlated.

  Compared to the triangular design, the 2L configuration is also less prone to effects coming from coherent lightning strikes, which could affect not only stochastic background searches, but, potentially, also the search for unmodeled bursts.

JCAP07(2023)068

- **Site optimization for 2L.** Finally, it should be observed that, in this work, no effort was made to optimize the distance between the two L-shaped detectors, even just within Europe, and we simply used the locations of the two current candidate sites. A longer baseline would improve in particular the localization accuracy, as well as the estimation of the parameters more strongly correlated with angular localization.[52]

8.2 The role of the low-frequency sensitivity

We now draw our conclusions from the comparison between the two different choices of the amplitude spectral density (ASD) that we have studied, namely the full xylophone design, consisting of a high-frequency instrument together with a low-frequency instrument working at cryogenic temperature ('HFLF-cryo'), and the situation in which there is only the high-frequency instrument ('HF-only'). The main messages that emerge from our analysis are the following:

> *4. The low-frequency sensitivity is crucial for exploiting the full scientific potential of ET. In the HF-only configuration, independently of the geometry chosen, several crucial scientific targets of the science case would be lost or significantly diminished.*

For instance:

- For all geometries, in the HF-only configuration the number of BNS sources localized to better than $10^2\,\mathrm{deg}^2$ (which are the sources relevant for multi-messenger studies) degrades catastrophically; with the threshold SNR ≥ 8 that we use for multi-messenger studies, we see from tables 1 and 2 that, for the 10 km triangle, the number of detections with $\Delta\Omega_{90\%} < 10^2\,\mathrm{deg}^2$ (and all orbit inclinations) decreases from 280 to 14 BNS/yr, i.e. by a factor of 20 (and from 26 to 7 for events with viewing angle less than 15°), while for the 2L 15km-45° it decreases from 644 to 76 (for all orbit inclinations), or from 68 to 35 (for viewing angle less than 15°). Note that the reduction is more severe for the 10 km triangle than for the 2L 15km-45° configuration. Increasing the SNR threshold the effect is even stronger: for SNR ≥ 12, the number of events localized to better than $10^2\,\mathrm{deg}^2$ decreases from 184 to 4 BNS/yr for the 10 km triangle while, for the 2L 15km-45°, it decreases from 559 to 11; see table 43.

  Indeed, the decrease is so severe that the number of BNS/yr localized to better than $10^2\,\mathrm{deg}^2$ would even become much lower than what will be obtained already by LVKI during the O5 run, see the panel on $\Delta\Omega_{90\%}$ in figures 14 and 15, and table 43: as we mentioned, the number of BNS/yr with SNR ≥ 12 and $\Delta\Omega_{90\%} < 10^2\,\mathrm{deg}^2$ would be 11 for the 2L 15km-45° HF-only, and 4 for the 10 km triangle HF-only; by comparison, for LVKI-O5 we find 51 BNS/yr with SNR ≥ 12 and $\Delta\Omega_{90\%} < 10^2\,\mathrm{deg}^2$.

  The accuracy on the measurement of the luminosity distance also degrades dramatically. For instance, for the 2L with 15 km arms at 45°, the number of BNS/yr with d_L measured to better than 10% degrades from 479 in the HFLF-cryo configuration, to 12 in the HF configuration, while for the 10 km triangle it degrades from 52 to 1; for

[52] A third possible candidate site, depending on the outcome of the geological studies, could emerge near Kamenz, in the Lusatia region, Saxony (Germany). The great circle chord distance between the Sardinia site and the site in the Meuse-Rhine is 1165.0 km, while that between the Sardinia site and Kamenz is 1247.3 km, so the two distances are quite comparable, with the Sardinia-Kamenz distance larger by about 7%. In contrast, the great circle chord distance between Kamenz and the site in Meuse-Rhine is 575.4 km, significantly smaller.

JCAP07(2023)068

2L-15km-45°, the number of events/yr with d_L measured to better than 5% degrades from $\mathcal{O}(100)$ in the HFLF-cryo configuration, to about 1. The same trend is observed for BNS 'golden events', see figure 16. The accuracy on many other parameters would also degrade significantly, see again figures 14 and 15. These results are due to the fact that, with the low-frequency sensitivity ensured by the LF instrument, BNSs stay in the bandwidth for a long time, with a corresponding crucial benefit for parameter estimation and, particularly, localization and the partial disentangling of the polarizations, that allows us to alleviate the degeneracy between d_L and $\cos\iota$.

- For the same reason, for BNS, pre-merger alerts for localized events would become impossible without the low-frequency instrument, compare table 3 with table 4. For instance, for the 10 km triangle the total number of BNS/yr detected 30 min before merger would go from 905 (of which 10 localized, 30 min before merger, to better than $10^2\,\mathrm{deg}^2$ and 85 better than $10^3\,\mathrm{deg}^2$) to zero; for the 2L 15km-45° it would go from 2172 (of which 20 localized, 30 min before merger, to better than $10^2\,\mathrm{deg}^2$ and 194 better than $10^3\,\mathrm{deg}^2$) again to zero. As an example, an event such as GW170817 would enter the ET bandwidth about 1 day before the merger with the full HFLF-cryo sensitivity, but only $\mathcal{O}(10)$ minutes before the merger with an ASD such that it entered the detector bandwidth only at 10 Hz.

  This would have a dramatic impact on the possibility to detect precursors, and to probe the prompt/early counterparts, which provide rich information on the physics acting in the GRB engine and jet launch and kilonova ejecta. Of particular interest are prompt/early detection in the very high-energy gamma rays and ultraviolet.

- For the multi-messenger studies, losing the low frequencies reduces the detection of short GRBs with associated gravitational-wave signals; the number of joint detection decreases by about 40% for the 10 km triangle, by about 30% for the 15 km triangle and 2L with 15 km arms at 45°, and 20% for the 2L with 20 km arms at 45°, see tables 6 and 7. The reduction is more severe for kilonova counterparts: the triangle HF configurations detect less than 6% of the kilonovae detected by triangle HFLF-cryo, while the 2L HF-only configurations detect less than 15% of the KNe detected by the 2L HFLF-cryo configuration, see tables 10 and 11. Note that, once again, the triangle geometry is more heavily affected than the 2L by the loss of the low frequency instrument. The reduction of short GRBs with an associated GW signal might impact our understanding of the physics of the GRB engine and relativistic jets, by requiring more years of joint observations to achieve the same science goals. However for cosmology, nuclear physics, and studies of the heavy-elements nucleosynthesis which rely on kilonova detections, loosing the LF has a major impact on achieving the goals themselves.

  It is worth noting that, for short GRBs, the HF-only 2L-15km-45° and the HF-only 15km triangle enable the detection of the GW signal for a number of GRBs comparable to the full HFLF-cryo triangle with 10 km arms. On the other hand, for the kilonovae counterparts, no HF-only configuration (even HF-only 2L with 20 km arms at 45°) is comparable to 10 km triangle HFLF-cryo. This is due to a different type of search: while to observe short GRBs, wide FoV satellites in survey mode are used and the temporal coincidence of the GW/GRB signals are used to identify a joint detection, to search for kilonovae the telescopes FoV is typically much smaller than the GW localization uncertainty and thus requires selecting better-localized events to be

JCAP07(2023)068

followed up. The much-improved localization obtained by accessing low-frequencies then becomes a key parameter for the search.

- The HF-only configuration has a significantly smaller reach in distance, compared to the HFLF-cryo configuration, in the whole mass range relevant to 3G detectors, as can be seen from the right panels in figures 3 and 4.

  This has several significant consequences. In the range of masses relevant to BNS, for the 10 km triangle, the redshift to which a BNS with optimal orientation and sky location can be detected would decrease from $z \simeq 4$ down to $z \simeq 2$ (or, for the 2L-15km-45° , from $z \simeq 6$ to $z \simeq 3$). This is particularly significant since the peak of the star formation rate is around $z \simeq 2-3$, so studies of demography and population of BNS would be strongly impacted.

  The lowest reach in redshift would also make it impossible to identify primordial BHs on the basis of the criterion that BBHs at $z \gtrsim 30$ cannot be of astrophysical origin. For instance, for the 10 km triangle, the maximum redshift at which a compact binary coalescence could be seen, for optimal values of the total mass and optimal orientation and sky location, reduces from $z \simeq 100$ in the HFLF-cryo configuration to $z \simeq 20$ in the HF configuration, see figure 3.

  Intermediate mass BHs, with masses in the range $(10^3 - 10^4) M_\odot$, would also be visible to significantly smaller distances, see again figure 3, reducing significantly the chances of discovery. As an example, a BBH with total mass $5 \times 10^3\, M_\odot$ would be visible up to $z \simeq 1.1$ in the HFLF-cryo configurations (almost independently of geometry), but only up to $z \simeq 0.6$ in the HF only configurations, corresponding to a reduction by a factor ~ 5 in the comoving volume explored and in the corresponding chances of detection.

- The measurement of the eccentricity of subsolar mass compact objects, an important criterion for assessing or excluding the primordial origin of a BBH, would degrade by more than one order of magnitude, see figure 51.

- The degradation of the accuracy in luminosity distance and angular localization would basically render impossible all studies of cosmology, such as accurate measurements of H_0 and especially studies of the dark energy equation of state and of modified GW propagation, which crucially rely on accuracy in sky localization and luminosity distance for events at large z. Similarly, the exquisite localization accuracy on some high-mass ratio events, needed to extract the Hubble parameter from them, see section 6.4.3, would be impossible without the LF instrument.

- For a number of other aspects of the science case the loss of the LF instrument would not be as disruptive, but would still results in a loss of accuracy on the relevant parameters, by factors of order 2-3. This is the case, for instance, for the possibility of distinguishing BHs from Exotic Compact Objects on the basis of the spin-induced quadrupole moment or of a non-vanishing tidal deformability (figures 39 and 40), or for the accuracy on the reconstruction of NS radii, see table 17.

On the other hand, not all aspects of the Science Case depend on the LF instrument, and another important conclusion that follows from our study is:

> *5. There are some important targets of the Science Case that depend only on the HF sensitivity, and that could be fully reached with an HF-only instrument.*

JCAP07(2023)068

In particular:

- For multi-messenger astronomy, the number of joint detections of GWs from a BNS merger and the associated X-ray afterglow, as could be detected by an instrument such as THESEUS in survey mode, is basically independent of the LF instrument; see table 8.

- Tests of physics near the BH horizon based on the ringdown signal of the final BH are completely independent of the LF instrument, see table 13 and the discussion in section 6.1.1. The same holds for the search of echoes and near-horizon structures, see section 6.1.2.

- The post-merger signal of BNS coalescences, that contains the information of the NS equation of state, is concentrated in the high-frequency region, and is completely insensitive to the presence of the LF instrument, see the left panel in figure 45.

- The detectability of sub-solar mass primordial BHs is another example of a metric that is not affected by the loss of the LF instrument; see figure 50.

- Stochastic backgrounds of cosmological origin are in general expected to have a smooth power-like behavior, $\Omega_{\rm gw}(f) \propto f^{\alpha}$, over the bandwidth of ground based or space-borne detectors (with the exception of backgrounds from cosmological phase transitions, that will be broadly peaked around a characteristic frequency). At the very low frequencies, say $f \sim 10^{-18}\,$Hz, tested by CMB, there are extremely stringent limits $\Omega_{\rm gw} \lesssim 10^{-15}$ (see, e.g. chapter 22 of [85]). Therefore, at the frequencies of ground based detectors, a stochastic background, relic of the early Universe, could only be detectable if it grows with frequency, $\Omega_{\rm gw}(f) \propto f^{\alpha}$ with $\alpha > 0$, at least until a frequency where it saturates, followed by a cutoff. For this reason, the stochastic background predicted by standard single-field slow-roll inflation is not detectable, since it is basically flat (in fact, slightly red, i.e. $\alpha < 0$). However, there are alternative cosmological models that predict spectra with $\alpha > 0$, such as the pre-big-bang model [525, 526] or axion inflation (see [527], or figure 12 of [15]). In these cases, a significant part of the SNR could accumulate in the high-frequency part of the detector bandwidth, where the LF instrument does not contribute to the sensitivity to stochastic backgrounds, see figure 29. A similar behavior takes place, in the ET bandwidth, in the model for cosmic strings whose predictions are shown in figure 64.

A final important conclusion that emerges from our study is that:

> *6. For some important aspects of the Science Case, the 2L with 15 km arms at 45°, already in the HF-only configuration, is comparable the 10 km triangle in a full HFLF-cryo configuration.*

In particular:

- For parameter estimation of BBHs, the 2L with 15 km arms at 45° in the HF-only configuration is comparable to the 10 km triangle at full HFLF-cryo sensitivity, with better performance of luminosity distance, less good performance on mass reconstruction, and equivalent performances on all other parameters and in SNR distribution, see figure 9. The performance of the 2L-15km-45° configuration is also equivalent to that of the 10 km triangle for what concerns 'golden BBH events', see the lower row of figure 10.

JCAP07(2023)068

- From the right panel of figure 41 we see that, for the measurement of the neutron star radii and the consequences for nuclear physics that we can derive from it, the 2L with 15 km arms at 45° already in the HF-only configuration has performances very similar to that of the full 10 km triangle HFLF-cryo.

- For all the items discussed above, where the LF instrument does not contribute (joint GW+X-ray afterglow and, to some extent, GRB detections, tests of physics near the BH horizon, post-merger signal of BNS coalescences, sub-solar mass BHs, stochastic backgrounds growing as f^α with $\alpha > 0$), the 2L-15km-45° in the HF only configuration will be superior to the 10 km triangle with the full HFLF-cryo sensitivity.

8.3 Conclusions

The decisions on the ideal design of a detector such as the Einstein Telescope, which is meant to have a leading role in the field of gravitational waves for decades, are part of a complex process. In this study we have considered alternatives to the geometry (a single-site triangle against two widely separated L-shaped interferometers, with different options for the arm-lengths) and to other aspects of the design (considering the baseline design given by a full xylophone configuration with a high frequency instrument together with a cryogenic low-frequency instrument, and comparing it to a high-frequency only instrument).

The first conclusion of this work, which extends the study presented in [15], is that, whatever geometry is decided between the triangle and 2L configurations considered, ET will clearly be a game-changer. It will over-perform the network of 2G observatories at their best expected O5 sensitivities by several orders of magnitudes in all relevant metrics, accessing physics that it is well beyond reach for 2G detectors. Note, however, that this is only true for the triangle and for the 2L configurations. A single L-shaped detector, not inserted in a global 3G network, even with a very long arm length, does not have a viable Science Case, at the level expected from a 3G detector.

The comparison between the 10 km triangle and a 15 km 2L shows that, from the scientific point of view, the 15 km 2L with arms at 45° is superior on basically all the metrics that we have considered, with the exception of the nominal sensitivity to stochastic backgrounds. However, in this case we have seen that the triangle suffers from a potentially very significant treat from correlated noise, particularly at low frequencies.[53] For compact binary coalescences, the better performances of the 15 km 2L with arms at 45° allow us to gain typically further factors of order 2-3 on the number of events which pass given cuts on SNR, or on the accuracy of reconstruction of various parameters and physical quantities. In fact, we have found that the 15 km 2L with arms at 45° is quite comparable to the 15 km triangle: the two have very similar performances for the reconstruction of all parameters of compact binary coalescences, except for luminosity distance, for which the 15 km 2L with arms at 45° is significantly better.

Another interesting element that emerged from our study is that the configuration 2L 15km at 45° gives a better possibility of proceeding in steps, compared to the 10 km triangle. Both for the triangle and 2L configurations, the full scientific outcome expected from a 3G detector will only be reached in the full configuration with the HF and the cryogenic LF instrument. However, the 2L 15km at 45°, already in the HF-only configuration,

[53] Furthermore, more work is needed to asses the effect of an imperfect subtraction of the astrophysical backgrounds, which could limit the sensitivity to cosmological backgrounds to a level fixed in all cases by the accuracy of the subtraction.

JCAP07(2023)068

would be sufficient to obtain some important results (which is true only to a lesser extent for the 10 km triangle). It is therefore natural to investigate whether a staging procedure will be advantageous, where the HF interferometer, which is the simpler to commission, is put into operation first, until the full HFLF-cryo configuration is reached, possibly going through intermediate steps such as, for instance, an LF instrument working, at first, at room temperatures. These issues, however, are beyond the scope of this study, and should be examined within the context of the ET Instrument Science Board.

Finally, the triangle configuration is prone to the effect of correlated Newtonian, seismic and magnetic noise on the scale of hundreds of meters. While more work is needed to fully understand them, these effects might pose a risk/challenge to obtaining the target sensitivity of the triangle, particularly in the low-frequency region.

Acknowledgments

The research leading to these results has been conceived and developed within the ET Observational Science Board (OSB). We are particularly grateful to Giancarlo Cella, Gianluca Guidi and Frank Ohme for their extremely careful and very useful internal refereeing of the manuscript. We thank Marie-Anne Bizouard, Nelson Christensen, Fernando Ferroni, Harald Lück, Mario Martinez, Ed Porter, Michele Punturo, Tania Regimbau, David Shoemaker, Achim Stahl and Patrice Verdier for very useful discussions and feedback. We express special thanks to Jameson G. Rollins for his consultations about the use of PyGWINC.

The work of Michele Maggiore, Stefano Foffa, Francesco Iacovelli, Michele Mancarella and Niccolò Muttoni is supported by the Swiss National Science Foundation, grant 200020_191957, and by the SwissMap National Center for Competence in Research, and made use of the Yggdrasil cluster at the University of Geneva. M. Branchesi acknowledges financial support from the Italian Ministry of University and Research (MUR) for the PRIN grant METE under contract no. 2020KB33TP. B. Banerjee acknowledge financial support from MUR (PRIN 2017 grant 20179ZF5KS). M. Branchesi and G. Oganesyan acknowledge financial support from the AHEAD2020 project (grant agreement n. 871158). The Gran Sasso Science Institute group acknowledges Stefano Bagnasco, Federica Legger, Sara Vallero, and the INFN Computing Center of Turin for providing support and computational resources. V. De Luca is supported by funds provided by the Center for Particle Cosmology at the University of Pennsylvania. Elisa Maggio acknowledges funding from the Deutsche Forschungsgemeinschaft (DFG) — project number: 386119226. G.Franciolini acknowledges financial support provided under the European Union's H2020 ERC, Starting Grant agreement no. DarkGRA-757480 and under the MIUR PRIN programme, and support from the Amaldi Research Center funded by the MIUR program "Dipartimento di Eccellenza" (CUP: B81I18001170001). This work was partly enabled by the UCL Cosmoparticle Initiative. Katarina Martinovic is supported by King's College London through a Postgraduate International Scholarship. M. Mapelli, C. Périgois and F. Santoliquido acknowledge financial support from the European Research Council for the ERC Consolidator grant DEMOBLACK, under contract no. 770017. M. Mancarella and C. Pacilio are supported by European Union's H2020 ERC Starting Grant No. 945155-GWmining and Cariplo Foundation Grant No. 2021-0555. Numerical calculations by C. Pacilio have been made possible through a CINECA-INFN agreement, providing access to resources on MARCONI at CINECA. Anuradha Samajdar thanks the Alexander von Humboldt foundation in Germany for a Humboldt fellowship for postdoctoral researchers. Paolo

JCAP07(2023)068

Pani acknowledges financial support provided under the European Union's H2020 ERC, Starting Grant agreement no. DarkGRA-757480 and under the MIUR PRIN and FARE programmes (GW-NEXT, CUP: B84I20000100001). BG is supported by the Italian Ministry of Education, University and Research within the PRIN 2017 Research Program Framework, n. 2017SYRTCN. Mairi Sakellariadou is supported in part by the Science and Technology Facility Council (STFC), United Kingdom, under the research grant ST/P000258/1. ACJ was supported by the Science and Technology Facilities Council through the UKRI Quantum Technologies for Fundamental Physics Programme [grant number ST/T005904/1]. Swetha Bhagwat is supported by the UKRI Stephen Hawking Fellowship with grant ref. no EP/W005727. Angelo Ricciardone acknowledges financial support from the Supporting TAlent in ReSearch@University of Padova (STARS@UNIPD) for the project "Constraining Cosmology and Astrophysics with Gravitational Waves, Cosmic Microwave Background and Large-Scale Structure cross-correlations". Kamiel Janssens is supported by FWO-Vlaanderen via grant number 11C5720N. F.Gulminelli and C.Mondal acknowledge partial support from the In2p3 Master Project NewMAC. D. Alonso is supported by the Science and Technology Facilities Council through an Ernest Rutherford Fellowship, grant reference ST/P004474. Ssohrab Borhanian acknowledges support from the Deutsche Forschungsgemeinschaft, DFG, project MEMI number BE 6301/2-1. Arnab Dhani, Ish Gupta and B.S. Sathyaprakash were supported by NSF grant numbers PHY-2012083, AST-2006384 and PHY-2207638. G. Cusin is supported by CNRS and by Swiss National Science Fundation (Ambizione grant — *Gravitational wave propagation in the clustered universe).*

JCAP07(2023)068

A Basic formalism for stochastic backgrounds

In this appendix we review several basic concepts relevant for the characterization of stochastic GW backgrounds. At the frequencies of ground-based detectors, to obtain an interesting sensitivity one needs to cross-correlate the output of at least two detectors in a network, see e.g. [83, 528] for reviews: as a consequence the observable quantity is not a strain, but rather quantities quadratic in the strain. One usually introduces a polarisation tensor defined (in frequency space) as

$$\tilde{\mathcal{P}}_{ab} = \tilde{h}^*_a \tilde{h}_b \,, \tag{A.1}$$

with $a, b = +, \times$ and we defined the superposition of signals in a given direction $\hat{\mathbf{n}}$ and at a given frequency f as

$$\tilde{h}_{ij}(\hat{\mathbf{n}}, f) = \tilde{h}_+(\hat{\mathbf{n}}, f) e^+_{ij}(\hat{\mathbf{n}}) + \tilde{h}_\times(\hat{\mathbf{n}}, f) e^\times_{ij}(\hat{\mathbf{n}}) \,. \tag{A.2}$$

In full generality the polarisation tensor, being a complex 2×2 tensor, can be decomposed in a basis of the identity and Pauli matrices as

$$\tilde{\mathcal{P}}_{ab}(\hat{\mathbf{n}}, f) = \frac{1}{2} \left[I(\hat{\mathbf{n}}, f) 1_{ab} + U(\hat{\mathbf{n}}, f) \sigma^{(1)}_{ab} + V(\hat{\mathbf{n}}, f) \sigma^{(2)}_{ab} + Q(\hat{\mathbf{n}}, f) \sigma^{(3)}_{ab} \right] , \tag{A.3}$$

where the coefficients I, U, V, Q are Stokes parameters describing intensity and polarisation, respectively. Polarisation is expected to be very small if we consider a homogeneous and isotropic AGWB and a CGWB: the amount of polarisation generated via classical diffusion is very small for both background components, see [105]. However, there is a non-negligible amount of circular polarization in the AGWB, generated by Poisson fluctuations in the number of unresolved sources, which can be detected by third-generation interferometers

with SNR> 1 (see [529]). Measuring a highly polarised background component would therefore be interesting both for shedding light on some cosmological parity-violating generation mechanisms (see e.g. [530, 531]) or to estimate whether the SGWB comes from a handful of sources or a relatively large population of binaries. Here we focus on the study of intensity and of its spectrum. It is common in the literature to introduce a dimensionless quantity related to intensity via

$$\begin{aligned}\Omega_{\rm gw}(\hat{\mathbf{n}}, f) &\equiv \frac{4\pi^2 f^3}{G\rho_c} I(\hat{\mathbf{n}}, f) \\ &= \frac{1}{\rho_c}\frac{d\rho_{\rm gw}(\hat{\mathbf{n}}, f)}{d\ln f\, d^2\hat{\mathbf{n}}}\,,\end{aligned} \tag{A.4}$$

where the second equality clarifies the physical meaning of this observable: it corresponds to the background energy density, $\rho_{\rm gw}(\hat{\mathbf{n}}, f)$, per unit of logarithmic frequency and unit solid angle (normalised to the critical density of the Universe today, ρ_c), that reaches the observed from a direction $\hat{\mathbf{n}}$.

To characterize the detector sensitivity to stochastic backgrounds, we use the Power-Law integrated Sensitivity curve (PLS), introduced for the first time in [145] for a network of L-shaped detectors, and we extend it to the case of triangular detectors, following [117]. When dealing with triangular detectors (three nested detectors), one has to keep in mind that the noise between two detectors with an arm in common is not uncorrelated, hence the correlation has to be accounted for when computing the PLS. Here we assume that the noise in ET is 20% correlated between detectors with an arm in common. As we discuss in section 5.4, see in particular figure 34, this is a value intermediate between the extremes of modeled noise correlations; we chose here a frequency-independent correlation for simplicity.

Let us assume to have a network of N detectors. The normalized overlap reduction function (see [21, 145, 403]) for a detector pair $\{A, B\}$ in the network is defined as

$$\gamma_{AB}(f) = \frac{5}{8\pi}\int \mathrm{d}^2\hat{\mathbf{n}}\left[F_A^+(\hat{\mathbf{n}})\,F_B^+(\hat{\mathbf{n}}) + F_A^\times(\hat{\mathbf{n}})\,F_B^\times(\hat{\mathbf{n}})\right] e^{i2\pi\frac{f}{c}\hat{\mathbf{n}}\cdot\boldsymbol{\Delta}\mathbf{x}_{AB}}\,, \tag{A.5}$$

where $\boldsymbol{\Delta}\mathbf{x}_{AB} = \mathbf{x}_B - \mathbf{x}_A$ is the separation between the two detectors A and B.

The normalization factor $5/(8\pi)$ in eq. (A.5) is conventionally introduced so that $\gamma_{AB}(f) = 1$ for two co-located and perfectly aligned detectors with orthogonal arms. The quantities $F_A^+(\hat{\mathbf{n}})$ and $F_A^\times(\hat{\mathbf{n}})$ are the detector A pattern functions (and similarly for B). They are determined by the detector A response tensor $\mathbf{D}_A$ and the polarisation tensors $\mathbf{e}^{+,\times}$ as $F_A^+(\hat{\mathbf{n}}) = \mathrm{Tr}\left[\mathbf{D}_A\,\mathbf{e}^+(\hat{\mathbf{n}})\right]$ and $F_A^\times(\hat{\mathbf{n}}) = \mathrm{Tr}\left[\mathbf{D}_A\,\mathbf{e}^\times(\hat{\mathbf{n}})\right]$.

For a Michelson interferometer with arms pointing along the directions $\mathbf{u}_A$ and $\mathbf{v}_A$, the detector A response tensor has components D_A^{ij} given by (see e.g. [21])

$$D_A^{ij} = (u_A^i u_A^j - v_A^i v_A^j)/2\,. \tag{A.6}$$

We start with the effective noise power spectral density. In full generality, this is given by

$$S_{\rm eff}(f) = \left[\sum_{A,B,C>B,D>A} (N_f^{-1})^{AB}\,\gamma_{BC}(f)\,(N_f^{-1})^{CD}\,\gamma_{DA}(f)\right]^{-1/2}\,, \tag{A.7}$$

where N_f^{-1} is the inverse of the noise covariance matrix of the network at each frequency f. The restrictions on the sum in eq. (A.7) ensure that only a cross-correlation search at

JCAP07(2023)068

unordered pairs of distinct detectors is considered, thus excluding auto-correlations (and without double counting).

Notice that in the case of uncorrelated detector noises, the noise matrix is diagonal

$$(N_f^{-1})^{AB} = \frac{\delta^{AB}}{N_f^{AA}}\,, \tag{A.8}$$

where N_f^{AA} is the noise power spectral density (PSD) of the detector A. In this case eq. (A.7) can be simplified to:

$$S_{\rm eff}(f) = \left[\sum_{A=1}^{N}\sum_{C>A}^{N}\frac{\gamma_{AC}^2(f)}{N_f^{AA}N_f^{CC}}\right]^{-1/2}\,. \tag{A.9}$$

However, for triangular detectors, we need to know both the noise variance (diagonal terms) and the cross-detector noise covariance (off-diagonal).

We define an effective dimensionless noise energy spectrum for $S_{\rm eff}(f)$ in eq. (A.7) as

$$\Omega_{\rm eff}(f) = \frac{10\pi^2}{3H_0^2}f^3 S_{\rm eff}(f) \tag{A.10}$$

and consider an isotropic and unpolarized stochastic GW background with fractional energy density contribution $\Omega_{\rm gw}(f)$ with respect to the critical energy density ρ_c of the Universe today. With the definition (A.10), the integrated signal-to-noise ratio ρ for a cross-correlation search at the network in a frequency range from $f_{\rm min}$ to $f_{\rm max}$, for a coincident observation time T, is [403]

$$\rho = \left[2T\int_{f_{\rm min}}^{f_{\rm max}}{\rm d}f\,\frac{\Omega_{\rm gw}^2(f)}{\Omega_{\rm eff}^2(f)}\right]^{1/2}\,. \tag{A.11}$$

For a set of power-law indices β, we write

$$\Omega_{\rm gw}(f) = \Omega_\beta(f/f_{\rm ref})^\beta \tag{A.12}$$

where $f_{\rm ref}$ is a reference frequency such that, at $f = f_{\rm ref}$, $\Omega_{\rm gw}(f)$ has the value Ω_β, and we compute the value of the amplitude Ω_β such that the integrated signal-to-noise ratio ρ has some fixed value. Using eq. (A.11), this is given by

$$\Omega_\beta = \frac{\rho}{\sqrt{2T}}\left[\int_{f_{\rm min}}^{f_{\rm max}}{\rm d}f\,\frac{(f/f_{\rm ref})^{2\beta}}{\Omega_{\rm eff}^2(f)}\right]^{-1/2}\,. \tag{A.13}$$

In the following we will set $\rho = 1$. For each pair of values (β, Ω_β), we compute $\Omega_{\rm GW} = \Omega_\beta(f/f_{\rm ref})^\beta$. The envelope is the power-law integrated sensitivity curve. Formally it is given by

$$\Omega_{\rm PLS}(f) = \max_\beta\left[\Omega_\beta\left(\frac{f}{f_{\rm ref}}\right)^\beta\right]\,. \tag{A.14}$$

Any line (on a log-log plot) that is tangent to the power-law integrated sensitivity curve corresponds to a gravitational-wave background power-law spectrum with an integrated signal-to-noise ratio $\rho = 1$. This implies that, if the curve for a predicted background lies everywhere below the sensitivity curve, then $\rho < 1$ for such a background. Note that, from the definition (A.12) of Ω_β and $f_{\rm ref}$, a change in the choice of $f_{\rm ref}$ is compensated by a corresponding change of Ω_β, such that $\Omega_\beta f_{\rm ref}^{-\beta}$ remains constant. Therefore, the value of Ω_β obtained from eq. (A.13) depends on the arbitrary choice of $f_{\rm ref}$, but $\Omega_{\rm PLS}(f)$, given by eq. (A.14), does not.

JCAP07(2023)068

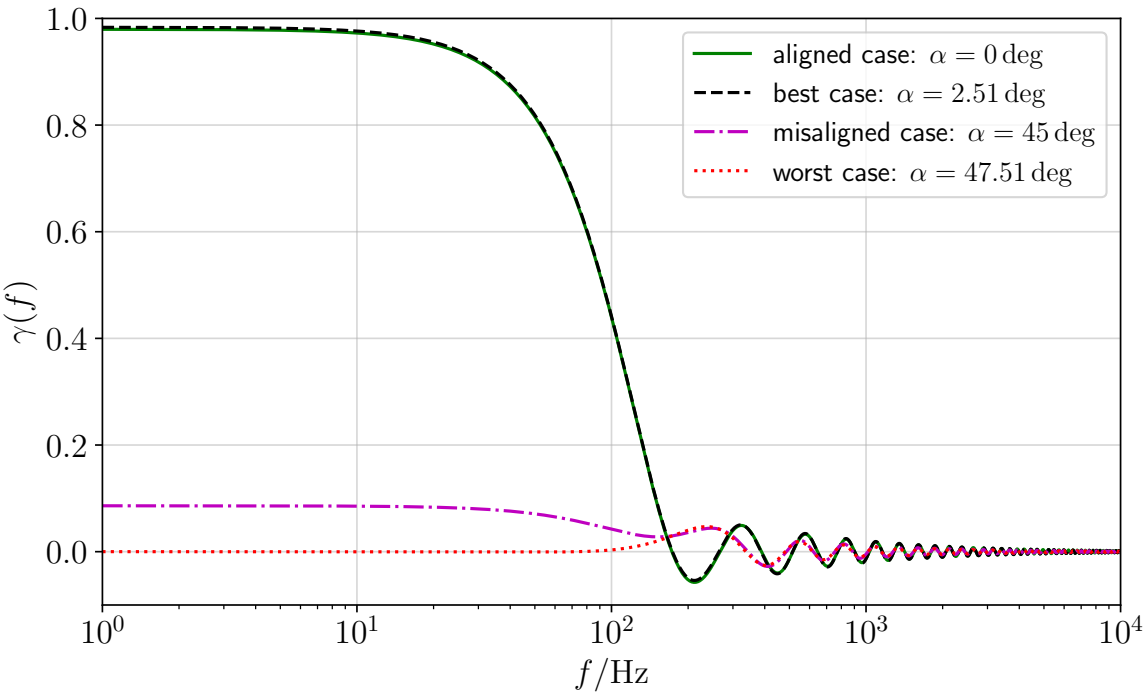

Figure 70. Normalized overlap reduction function (ORF) $\gamma(f)$ for different values of the angle α.

B Sensitivity to stochastic backgrounds of misaligned 2L configurations

Focusing on the stochastic gravitational-wave background, we highlight below the effect of the orientation of the two L-shaped interferometers on the peak sensitivity. As discussed in section 2, in this paper we have fixed the arms of the Sardinia interferometer so that they point locally East and North, and rotate anti-clockwise the arms of the Netherlands interferometer by an angle α with respect to the local East-North directions. The angle $\alpha = 0$ differs from the usual definition of the alignment of two interferometers with respect to the great circle [21, 22] by 2.51 degrees and is clearly not the maximum possible alignment, due to the curvature of the Earth between the two sites.

In figure 70 we show the normalized overlap reduction function (ORF) defined in eq. (A.5) as a function of frequency, for the $\alpha = 0$ deg and $\alpha = 45$ deg cases, which are the examples considered in the main text. However, the best and worst cases for a stochastic search are the values $\alpha = 2.51$ deg and $\alpha = 47.51$ deg, respectively. Clearly, while varying the angle α near the 0 deg case has very little impact, the consequences of varying α just a few degrees around the 45 deg are very important. These results reflects into a significant dependence on α of the peak sensitivity to the stochastic gravitational-wave background.

Figure 71 illustrates the peak sensitivity to the stochastic gravitational-wave background (minimum value of the power-law integrated curve) as a function of the angle α. The choices $\alpha = 0$ deg and 45 deg, considered in the main text of this document, are not respectively the best and worst cases for stochastic searches. Varying the angle α near the 0 deg case has very little impact, but varying α just a few degrees around the 45 deg case varies the peak sensitivity to the stochastic gravitational-wave background by orders of magnitude. As one can clearly see, the best and worst cases for stochastic searches, are when $\alpha = 2.51$ deg and 47.51 deg, respectively.

JCAP07(2023)068

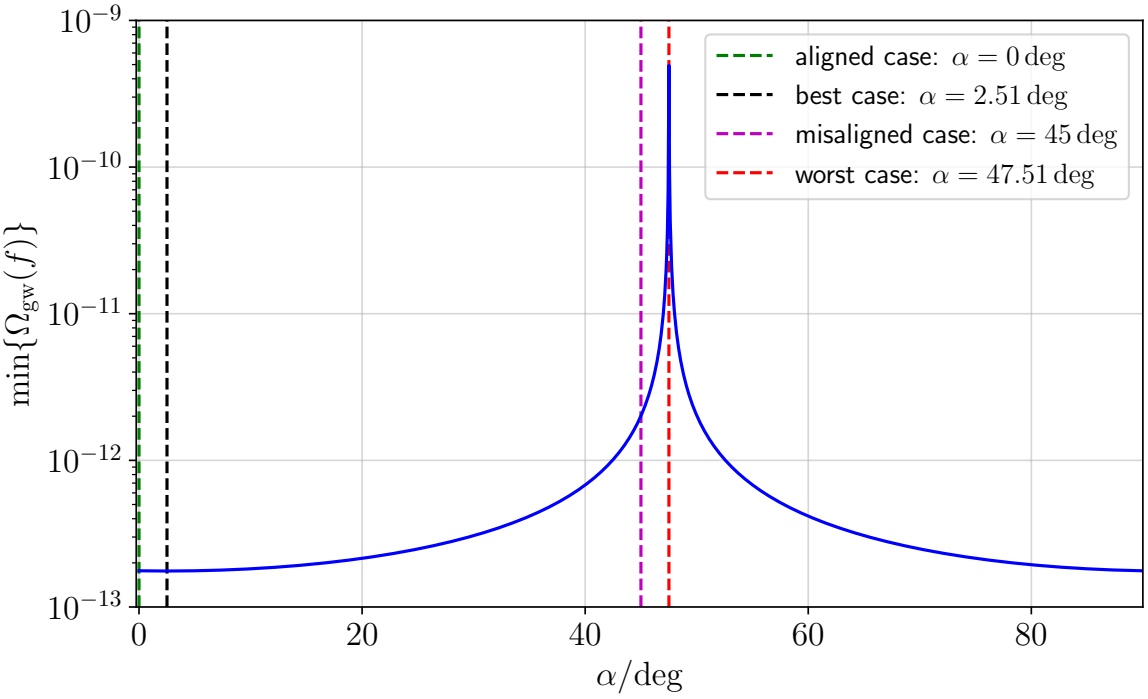

Figure 71. Peak sensitivity to the stochastic gravitational-wave background as a function of the angle α in the 2L-20km-HFLF-Cryo configuration. The SNR threshold used is $\rho = 1$ and the observation time is $T = 1$ yr.

To be strictly optimal the alignment of two interferometers would have the two detectors such that each had an arm along the great circle connecting them for 0 deg (which is how the two LIGO detectors are aligned), and rotating one by 45 deg for the minimal value [22]. For such a minimal alignment the overlap reduction function would be exactly zero in the limit $f\Delta x \to 0$, where Δx is the separation between the two detectors, and very small basically for all frequencies, as we see from figure 70. This would also give the best polarization separation for the CBC searches.

C Tables of figures of merit for BBHs and BNSs

To make the comparison among different geometries and ASDs easier, we provide here tables with the number of sources detected by each configuration with various cuts on the match-filtered SNR, or on measurement errors on some of the most relevant quantities, corresponding to the results shown in figures 5, 8, 9 and 10 for BBHs, and to figures 11, 14, 15 and 16 for BNS. We further show the same quantities for the networks ET+1CE and ET+2CE, corresponding to the results shown in figures 18 and 19.

In particular, in table 39 we show the number of detected BBH sources with different cuts in SNR, ranging from 8 to 200; in table 40 with cuts on the relative error on the luminosity distance and the 90% sky localisation [notice that the parameter estimation analysis has been performed only for the events detected with SNR $\geq$ 12]; and in table 41 with cuts on the relative error on the detector-frame chirp mass and the error on the spin magnitude of the primary object.

JCAP07(2023)068

Configuration	SNR ≥ 8	SNR ≥ 12	SNR ≥ 50	SNR ≥ 100	SNR ≥ 200
Δ-10km-HFLF-Cryo	103 528	87 568	13 674	2298	282
Δ-15km-HFLF-Cryo	111 231	101 308	26 092	5730	759
2L-15km-45°-HFLF-Cryo	107 661	97 205	23 491	4933	644
2L-20km-45°-HFLF-Cryo	110 698	103 773	34 009	8828	1267
2L-15km-0°-HFLF-Cryo	104 935	94 015	24 088	5143	642
2L-20km-0°-HFLF-Cryo	106 417	98 274	32 915	8551	1246
Δ-10km-HF	87 125	65 092	5595	773	98
Δ-15km-HF	102 149	85 698	13 697	2360	292
2L-15km-45°-HF	97 881	81 210	12 089	1987	248
2L-20km-45°-HF	105 032	93 050	20 551	4144	515
2L-15km-0°-HF	89 707	73 696	10 688	1732	201
2L-20km-0°-HF	104 558	92 308	21 970	4540	569
Δ-10km-HFLF-Cryo+CE-40km	115 179	110 118	44 676	12 590	1805
2L-15km-45°-HFLF-Cryo+CE-40km	116 328	112 661	50 947	15 545	2355
2L-15km-0°-HFLF-Cryo+CE-40km	114 816	110 265	49 034	14 820	2243
Δ-10km-HFLF-Cryo+2CE	117 045	113 910	52 092	16 109	2505
2L-15km-45°-HFLF-Cryo+2CE	117 436	115 166	57 678	19 028	3126
2L-15km-0°-HFLF-Cryo+2CE	116 639	113 597	55 218	17 849	2917
LVKI-O5	8603	2861	47	4	2

Table 39. Summary table of the number of BBH detections with various cuts in SNR for the considered ET geometries and ASDs, also in combination with one 40 km CE detector or two CE detectors and for a LVKI network during O5.

In table 42 we report the number of BNS sources detected with different cuts in SNR, in table 43 with cuts on the luminosity distance relative error and 90% sky localisation area,[54] and in table 44 with cuts on the relative errors on the chirp mass and adimensional tidal deformability parameter $\tilde{\Lambda}$ [defined in eq. (3.1)].

[54]Some differences with the results shown in tables 1 and 2 are due to the different choices for the cut in SNR for the parameter estimation analysis; in section 3 (to which the result of this appendix refer) was used SNR $\geq$ 12, while in section 4 the threshold was lowered to SNR $\geq$ 8 because of the increased statistical significance provided by to the coincidence with an electromagnetic counterpart. As can be seen from table 42, passing from one cut to the other, the number of detections changes by more than factor of 2, in particular for the HF-only configurations. Part of the discrepancy is also due to the different inversion procedure adopted in the two sections, as already outlined in footnote 9, with some events being discarded in the results presented here and in section 3, while their Fisher matrices are regularized in the ones reported in section 4, resulting in higher numbers.

JCAP07(2023)068

Configuration	$\Delta d_L/d_L \leq 0.1$	$\Delta d_L/d_L \leq 0.01$	$\Delta\Omega_{90\%} \leq 50\,\mathrm{deg}^2$	$\Delta\Omega_{90\%} \leq 10\,\mathrm{deg}^2$
Δ-10km-HFLF-Cryo	10 969	28	6064	914
Δ-15km-HFLF-Cryo	17 321	77	10 470	2273
2L-15km-45°-HFLF-Cryo	22 237	202	10 304	2124
2L-20km-45°-HFLF-Cryo	28 801	365	14 920	3648
2L-15km-0°-HFLF-Cryo	13 865	79	3030	374
2L-20km-0°-HFLF-Cryo	17 008	144	4706	608
Δ-10km-HF	3919	6	2409	281
Δ-15km-HF	8083	26	5156	817
2L-15km-45°-HF	11 193	56	5263	835
2L-20km-45°-HF	16 155	113	8448	1566
2L-15km-0°-HF	4111	17	1054	120
2L-20km-0°-HF	9693	57	2936	362
Δ-10km-HFLF-Cryo+CE-40km	80 676	2901	69 268	29 924
2L-15km-45°-HFLF-Cryo+CE-40km	82 358	4301	73 164	36 457
2L-15km-0°-HFLF-Cryo+CE-40km	64 471	2995	57 497	25 782
Δ-10km-HFLF-Cryo+2CE	101 912	5250	90 889	46 744
2L-15km-45°-HFLF-Cryo+2CE	104 289	7006	95 387	54 640
2L-15km-0°-HFLF-Cryo+2CE	93 832	5824	85 267	45 429
LVKI-O5	767	1	1607	599

Table 40. Same as table 39, for BBH sources, with cuts on the relative error on the luminosity distance and on the 90% sky localisation area.

Configuration	$\Delta\mathcal{M}_c/\mathcal{M}_c \leq 10^{-3}$	$\Delta\mathcal{M}_c/\mathcal{M}_c \leq 10^{-4}$	$\Delta\chi_1 \leq 0.05$	$\Delta\chi_1 \leq 0.01$
Δ-10km-HFLF-Cryo	48 922	4549	27 877	2811
Δ-15km-HFLF-Cryo	64 469	7703	41 612	4856
2L-15km-45°-HFLF-Cryo	58 371	6456	35 943	3958
2L-20km-45°-HFLF-Cryo	67 999	9073	45 666	5706
2L-15km-0°-HFLF-Cryo	57 330	6472	33 236	3653
2L-20km-0°-HFLF-Cryo	63 154	8279	40 068	4935
Δ-10km-HF	21 146	1580	11 715	1438
Δ-15km-HF	32 643	2818	19 956	2564
2L-15km-45°-HF	28 442	2405	16 382	2025
2L-20km-45°-HF	36 969	3547	23 205	2940
2L-15km-0°-HF	25 863	2146	13 669	1652
2L-20km-0°-HF	38 537	3740	23 065	2935
Δ-10km-HFLF-Cryo+CE-40km	73 785	8901	54 789	6649
2L-15km-45°-HFLF-Cryo+CE-40km	79 425	11 187	60 709	7988
2L-15km-0°-HFLF-Cryo+CE-40km	77 772	10 885	57 471	7519
Δ-10km-HFLF-Cryo+2CE	79 895	10 523	62 826	8226
2L-15km-45°-HFLF-Cryo+2CE	84 507	12 703	68 382	9557
2L-15km-0°-HFLF-Cryo+2CE	82 473	12 307	65 287	9012
LVKI-O5	78	1	155	20

Table 41. Same as table 39, for BBH sources, with cuts on the relative error on the detector-frame chirp mass and on the error on the spin magnitude of the primary object.

JCAP07(2023)068

Configuration	SNR ≥ 8	SNR ≥ 12	SNR ≥ 50	SNR ≥ 100	SNR ≥ 150
Δ-10km-HFLF-Cryo	107 902	36 985	458	57	19
Δ-15km-HFLF-Cryo	213 583	89 910	1206	159	38
2L-15km-45°-HFLF-Cryo	190 528	77 458	1052	134	33
2L-20km-45°-HFLF-Cryo	275 595	129 821	2018	243	64
2L-15km-0°-HFLF-Cryo	192 030	78 675	1040	136	33
2L-20km-0°-HFLF-Cryo	274 395	132 486	2048	250	65
Δ-10km-HF	44 713	13 410	166	18	9
Δ-15km-HF	116 349	41 181	516	55	17
2L-15km-45°-HF	101 550	34 956	447	52	15
2L-20km-45°-HF	176 396	70 441	961	115	32
2L-15km-0°-HF	103 539	35 817	443	57	17
2L-20km-0°-HF	184 799	74 805	989	124	37
Δ-10km-HFLF-Cryo+CE-40km	348 434	177 925	2836	312	87
2L-15km-45°-HFLF-Cryo+CE-40km	392 680	212 260	3677	418	116
2L-15km-0°-HFLF-Cryo+CE-40km	402 234	220 023	3770	414	119
Δ-10km-HFLF-Cryo+2CE	406 630	220 725	3961	436	120
2L-15km-45°-HFLF-Cryo+2CE	442 526	252 136	4900	559	152
2L-15km-0°-HFLF-Cryo+2CE	448 798	258 615	4974	531	162
LVKI-O5	250	71	3	0	0

Table 42. Same as table 39 for BNS sources.

Configuration	$\Delta d_L/d_L \leq 0.3$	$\Delta d_L/d_L \leq 0.1$	$\Delta\Omega_{90\%} \leq 100\,\mathrm{deg}^2$	$\Delta\Omega_{90\%} \leq 10\,\mathrm{deg}^2$
Δ-10km-HFLF-Cryo	748	52	184	8
Δ-15km-HFLF-Cryo	1756	153	479	23
2L-15km-45°-HFLF-Cryo	4328	479	559	25
2L-20km-45°-HFLF-Cryo	7821	919	1028	43
2L-15km-0°-HFLF-Cryo	774	48	293	12
2L-20km-0°-HFLF-Cryo	1499	104	565	23
Δ-10km-HF	4	1	4	0
Δ-15km-HF	7	1	11	1
2L-15km-45°-HF	126	12	11	0
2L-20km-45°-HF	262	22	24	1
2L-15km-0°-HF	20	1	11	1
2L-20km-0°-HF	28	2	24	1
Δ-10km-HFLF-Cryo+CE-40km	32 053	4100	54 994	2427
2L-15km-45°-HFLF-Cryo+CE-40km	45 252	7949	75 828	3838
2L-15km-0°-HFLF-Cryo+CE-40km	16 999	2079	29 821	1515
Δ-10km-HFLF-Cryo+2CE	72 335	13 630	112 705	6570
2L-15km-45°-HFLF-Cryo+2CE	89 877	19 129	145 272	9841
2L-15km-0°-HFLF-Cryo+2CE	78 798	14 909	125 640	7592
LVKI-O5	12	1	51	31

Table 43. Same as table 40 for BNS sources.

JCAP07(2023)068

Configuration	$\Delta\mathcal{M}_c/\mathcal{M}_c \leq 10^{-3}$	$\Delta\mathcal{M}_c/\mathcal{M}_c \leq 10^{-4}$	$\Delta\tilde{\Lambda}/\tilde{\Lambda} \leq 0.1$	$\Delta\tilde{\Lambda}/\tilde{\Lambda} \leq 0.05$
Δ-10km-HFLF-Cryo	35 127	18 401	1040	96
Δ-15km-HFLF-Cryo	84 835	39 607	2783	227
2L-15km-45°-HFLF-Cryo	68 391	36 645	2463	200
2L-20km-45°-HFLF-Cryo	115 695	59 051	5189	386
2L-15km-0°-HFLF-Cryo	67 023	29 813	2225	179
2L-20km-0°-HFLF-Cryo	113 726	49 445	4703	374
Δ-10km-HF	10 831	687	248	21
Δ-15km-HF	31 663	1548	667	45
2L-15km-45°-HF	25 058	2033	634	47
2L-20km-45°-HF	50 464	3644	1494	90
2L-15km-0°-HF	22 839	1463	445	36
2L-20km-0°-HF	42 731	2292	780	72
Δ-10km-HFLF-Cryo+CE-40km	171 997	46 008	2669	243
2L-15km-45°-HFLF-Cryo+CE-40km	197 631	66 214	4753	400
2L-15km-0°-HFLF-Cryo+CE-40km	198 171	63 219	4488	371
Δ-10km-HFLF-Cryo+2CE	216 875	58 522	3847	337
2L-15km-45°-HFLF-Cryo+2CE	244 198	80 406	6319	535
2L-15km-0°-HFLF-Cryo+2CE	250 033	79 746	6106	505
LVKI-O5	54	2	2	0

Table 44. Same as table 41, for BNS sources, with cuts on the relative error on the detector-frame chirp mass and on the relative error on the tidal deformability parameter $\tilde{\Lambda}$.

JCAP07(2023)068

D Correlation between parameters for typical events

In this appendix we discuss the correlation between parameters, in the BBH parameter estimation. This is instructive to obtain a physical understanding of some of the results presented in the main text. In particular, we wish to understand why the 15 km triangle and the 15 km 2L at 45° have performances very similar for the reconstruction of all parameters, except for luminosity distance, where the 15 km 2L at 45° is clearly superior, see figure 5 and tables 40, 41. To this purpose, we consider in detail some selected events (the correlation patterns that we will discuss are in fact generic). We select some BBH event with very high SNR, so that the Fisher matrix analysis is expected to be more reliable. As a first example we consider, in our ensemble of detected events, a 'light' BBH event (that we denote as "event 1") with source-frame masses $m_1 \simeq 7.9 M_\odot$, $m_2 = 7.6 M_\odot$, at a distance $d_L \simeq 0.30$ Gpc ($z \simeq 0.065$). Due to its close distance, its SNR is very high, and is 513 in the 15 km triangle and 478 in the 15 km 2L at 45°.

In figure 72 we show the correlation between some parameters. For readability, within the 15-dimensional parameter space that we use for BBHs, we restrict to the most interesting correlations, and we compare the results for the 15 km 2L at 45° with the 15 km triangle, both in their full HFLF-cryo configuration. The interesting point is that, in the correlation of various parameters with the luminosity distance, the contours for the 15 km triangle (red) are in general more tilted than the blue contour referring to the 15 km 2L at 45°. In figure 72 we see this in the correlation with all the parameters shown. This implies that, when one marginalizes over these parameters, the same error on these parameters induces a larger marginalized error on d_L. We see indeed that, for all parameters except d_L, for this event the marginalized errors are the same for the 15 km triangle and the 15 km 2L at 45°, while the marginalized distribution for d_L is narrower for the 15 km 2L at 45°. Observe that this happens despite the fact that, for this event, the SNR in the triangle was higher than in the 15 km 2L at 45°.

Figure 73 shows the analogous results for an event ("event 2") with source-frame masses $m_1 \simeq 29.0 M_\odot$, $m_2 = 24.6 M_\odot$, at a distance $d_L \simeq 1.19$ Gpc ($z \simeq 0.23$). Its SNR is again very high, 424 in the 15 km triangle and 318 in the 15 km 2L at 45°. As we reminded in section 2, the differences in the SNR between configurations, alone, is not a good indicator of the relative performances of parameter estimation (the most obvious example being that, on an ensemble of events, a 2L parallel configuration has higher SNR but worse angular localization than a 2L at 45°). This is also clearly visible from this plot: in this case, despite the larger SNR in the 15 km triangle, most parameters are significantly better estimated by the 15 km 2L at 45°. We also see that, again, the correlation contours of d_L with various parameters are more tilted in the triangle case, contributing to enlarging the marginalized posterior of d_L. This effect is also particularly evident, for this event, in the correlation between θ and ϕ.

JCAP07(2023)068

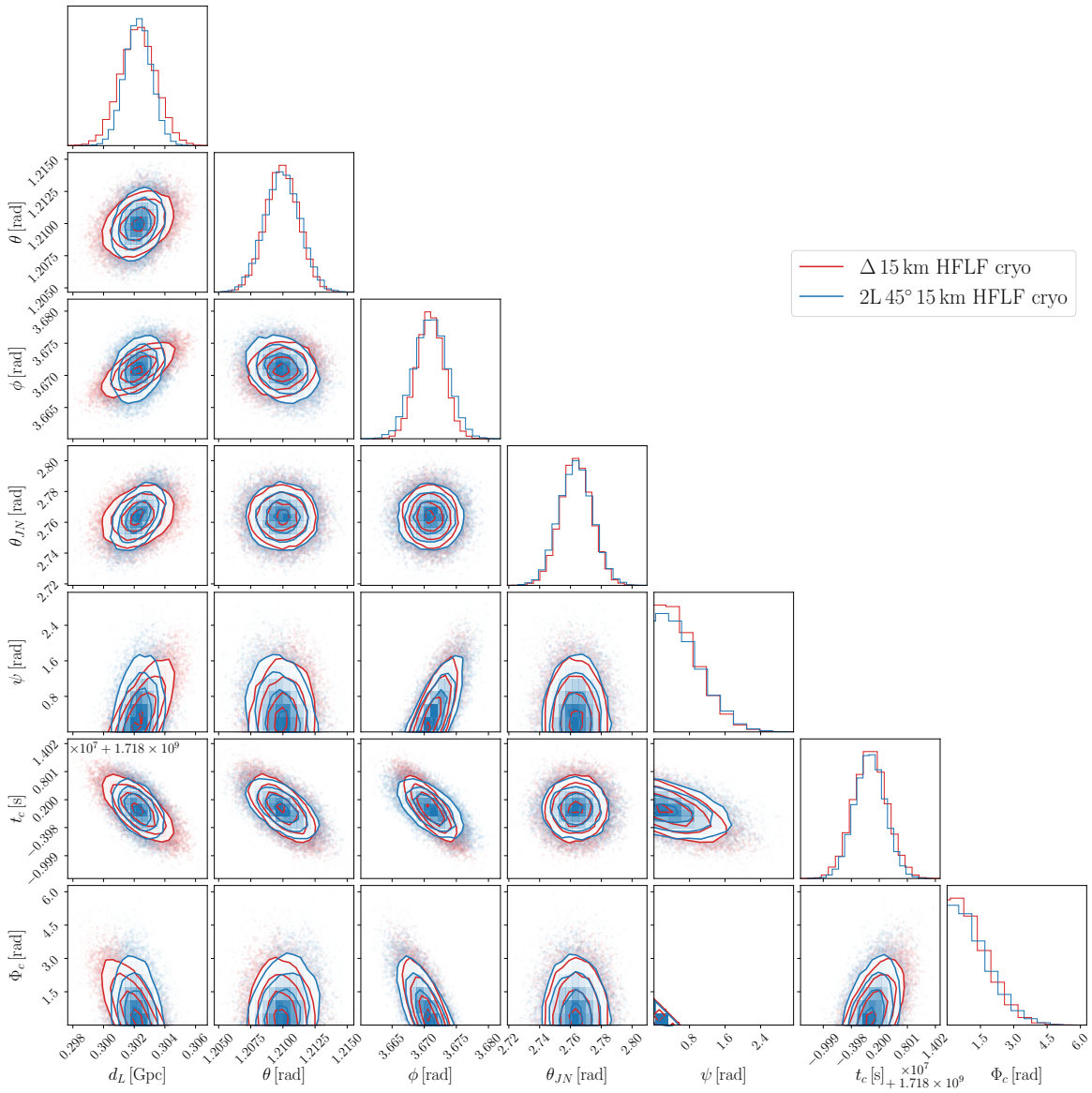

Figure 72. A corner plot showing the correlations between various parameters for a BBH event with light masses and very close distance ("event 1", see the text).

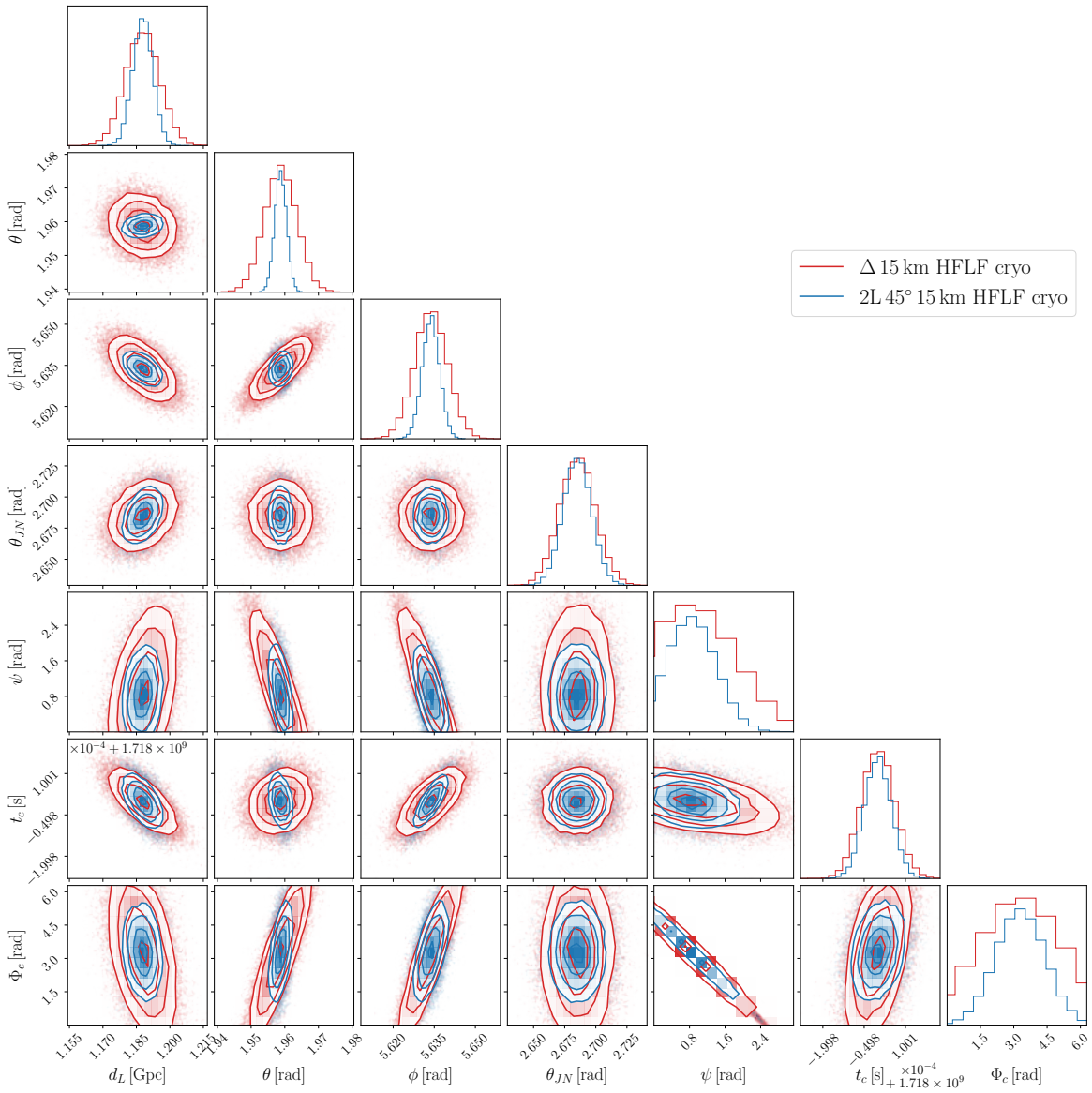

Figure 73. As in figure 72 for a BBH event with heavier masses and greater distance ("event 2", see the text).

JCAP07(2023)068

Acronyms

3G Third Generation. 2

AGWB Astrophysical Gravitational Wave Background. 50

ASD Amplitude Spectral Density. 6

BAO Barionic Acoustic Oscillation. 98

BBH Binary Black Hole. 1

BNS Binary Neutron Star. 1

CBC Compact Binary Coalescence. 5

CDO Compact Dark Object. 126

CE Cosmic Explorer. 2

CGWB Cosmological Gravitational Wave Background. 50

CIB Cosmic Infrared Background. 51

CMB Cosmic Microwave Background. 51

CSD Cross-power Spectral Density. 57

CW Continuous Wave. 117

DE Dark Energy. 95

DM Dark Matter. 88

ECO Exotic Compact Object. 73

EM Electromagnetic. 39

EoS Equation of State. 39

FAR False Alarm Rate. 129

FOPT First-Order Phase Transition. 114

FoV Field of View. 24

FRW Friedmann-Robertson-Walker. 100

GR General Relativity. 15

GRB Gamma Ray Burst. 3

GW Gravitational Wave. 1

JCAP07(2023)068

GWTC Gravitational Wave Transient Catalog. 89

HF High-Frequency. 2

HMNS Hypermassive Neutron Star. 84

IMBH Intermediate Mass Black Hole. 15

IMR Inspiral Merger Ringdown. 107

ISB Instrument Science Board. 4

ISCO Innermost Stable Circular Orbit. 75

KN Kilonova. 39

LF Low-Frequency. 2

LSST Large Synoptic Survey Telescope. 96

LVC LIGO-Virgo Collaboration. 1

LVKI LIGO Hanford, LIGO Livingston, Virgo, KAGRA, LIGO India. 6

NN Newtonian Noise. 56

NR Numerical Relativity. 84

NSBH Neutron Star-Black Hole. 1

ORF Overlap Reduction Function. 148

OSB Observational Science Board. 2

PBH Primordial Black Hole. 88

PLS Power Law Sensitivity. 3

PN Post Newtonian. 10

PSD Power Spectral Density. 57

QNM Quasinormal Mode. 68

SFH Star Formation History. 55

SGWB Stochastic Gravitational Wave Background. 50

SMNS Supramassive Neutron Star. 84

SN Supernova. 98

SNR Signal-to-Noise Ratio. 7

JCAP07(2023)068

SXI Soft X-ray Imager. 47

tCW Transient Continuous Wave. 117

TOV Tolman-Oppenheimer-Volkoff. 79

UV Ultra Violet. 42

VRO Vera Rubin Observatory. 48

XGIS X/Gamma-ray Imaging Spectrometer. 44

References

[1] LIGO Scientific and Virgo collaborations, *Observation of gravitational waves from a binary black hole merger*, *Phys. Rev. Lett.* **116** (2016) 061102 [arXiv:1602.03837] [INSPIRE].

[2] LIGO Scientific and Virgo collaborations, *GW*170817*: observation of gravitational waves from a binary neutron star inspiral*, *Phys. Rev. Lett.* **119** (2017) 161101 [arXiv:1710.05832] [INSPIRE].

[3] LIGO Scientific et al. collaborations, *Gravitational waves and gamma-rays from a binary neutron star merger: GW*170817 *and GRB* 170817*A*, *Astrophys. J. Lett.* **848** (2017) L13 [arXiv:1710.05834] [INSPIRE].

[4] LIGO Scientific et al. collaborations, *Multi-messenger observations of a binary neutron star merger*, *Astrophys. J. Lett.* **848** (2017) L12 [arXiv:1710.05833] [INSPIRE].

[5] LIGO Scientific and Virgo collaborations, *GWTC*-2*: compact binary coalescences observed by LIGO and Virgo during the first half of the third observing run*, *Phys. Rev. X* **11** (2021) 021053 [arXiv:2010.14527] [INSPIRE].

[6] LIGO Scientific et al. collaborations, *GWTC*-3*: compact binary coalescences observed by LIGO and Virgo during the second part of the third observing run*, arXiv:2111.03606 [INSPIRE].

[7] KAGRA et al. collaborations, *Population of merging compact binaries inferred using gravitational waves through GWTC*-3, *Phys. Rev. X* **13** (2023) 011048 [arXiv:2111.03634] [INSPIRE].

[8] LIGO Scientific et al. collaborations, *Tests of general relativity with GWTC*-3, arXiv:2112.06861 [INSPIRE].

[9] LIGO Scientific et al. collaborations, *Constraints on the cosmic expansion history from GWTC*-3, *Astrophys. J.* **949** (2023) 76 [arXiv:2111.03604] [INSPIRE].

[10] S. Hild, S. Chelkowski and A. Freise, *Pushing towards the ET sensitivity using 'conventional' technology*, arXiv:0810.0604 [INSPIRE].

[11] M. Punturo et al., *The Einstein Telescope: a third-generation gravitational wave observatory*, *Class. Quant. Grav.* **27** (2010) 194002 [INSPIRE].

[12] S. Hild et al., *Sensitivity studies for third-generation gravitational wave observatories*, *Class. Quant. Grav.* **28** (2011) 094013 [arXiv:1012.0908] [INSPIRE].

[13] D. Reitze et al., *Cosmic explorer: the U.S. contribution to gravitational-wave astronomy beyond LIGO*, *Bull. Am. Astron. Soc.* **51** (2019) 035 [arXiv:1907.04833] [INSPIRE].

[14] M. Evans et al., *A horizon study for cosmic explorer: science, observatories, and community*, arXiv:2109.09882 [INSPIRE].

JCAP07(2023)068

[15] M. Maggiore et al., *Science case for the Einstein Telescope*, *JCAP* **03** (2020) 050 [arXiv:1912.02622] [INSPIRE].

[16] B. Sathyaprakash et al., *Scientific objectives of Einstein Telescope*, *Class. Quant. Grav.* **29** (2012) 124013 [*Erratum ibid.* **30** (2013) 079501] [arXiv:1206.0331] [INSPIRE].

[17] F. Iacovelli, M. Mancarella, S. Foffa and M. Maggiore, *Forecasting the detection capabilities of third-generation gravitational-wave detectors using GWFAST*, *Astrophys. J.* **941** (2022) 208 [arXiv:2207.02771] [INSPIRE].

[18] S. Ronchini et al., *Perspectives for multimessenger astronomy with the next generation of gravitational-wave detectors and high-energy satellites*, *Astron. Astrophys.* **665** (2022) A97 [arXiv:2204.01746] [INSPIRE].

[19] S. Borhanian and B.S. Sathyaprakash, *Listening to the universe with next generation ground-based gravitational-wave detectors*, arXiv:2202.11048 [INSPIRE].

[20] V. Kalogera et al., *The next generation global gravitational wave observatory: the science book*, arXiv:2111.06990 [INSPIRE].

[21] E.E. Flanagan, *The sensitivity of the laser interferometer gravitational wave observatory (LIGO) to a stochastic background, and its dependence on the detector orientations*, *Phys. Rev. D* **48** (1993) 2389 [astro-ph/9305029] [INSPIRE].

[22] N. Christensen, *Optimal detection strategies for measuring the stochastic gravitational radiation background with laser interferometric antennas*, *Phys. Rev. D* **55** (1997) 448 [INSPIRE].

[23] KAGRA et al. collaborations, *Prospects for observing and localizing gravitational-wave transients with advanced LIGO, advanced Virgo and KAGRA*, *Living Rev. Rel.* **21** (2018) 3 [arXiv:1304.0670] [INSPIRE].

[24] M. Bailes et al., *Gravitational-wave physics and astronomy in the* 2020*s and* 2030*s*, *Nature Rev. Phys.* **3** (2021) 344 [INSPIRE].

[25] J.G. Rollins, E. Hall, C. Wipf and L. McCuller, *pygwinc: gravitational wave interferometer noise calculator*, Astrophysics Source Code Library, record ascl:2007.020 July 2020.

[26] P. Jaranowski, A. Krolak and B.F. Schutz, *Data analysis of gravitational — wave signals from spinning neutron stars.* 1. *The signal and its detection*, *Phys. Rev. D* **58** (1998) 063001 [gr-qc/9804014] [INSPIRE].

[27] LIGO Scientific collaboration, *Exploring the sensitivity of next generation gravitational wave detectors*, *Class. Quant. Grav.* **34** (2017) 044001 [arXiv:1607.08697] [INSPIRE].

[28] L. London et al., *First higher-multipole model of gravitational waves from spinning and coalescing black-hole binaries*, *Phys. Rev. Lett.* **120** (2018) 161102 [arXiv:1708.00404] [INSPIRE].

[29] E.D. Hall and M. Evans, *Metrics for next-generation gravitational-wave detectors*, *Class. Quant. Grav.* **36** (2019) 225002 [arXiv:1902.09485] [INSPIRE].

[30] S. Borhanian, *GWBENCH: a novel Fisher information package for gravitational-wave benchmarking*, *Class. Quant. Grav.* **38** (2021) 175014 [arXiv:2010.15202] [INSPIRE].

[31] U. Dupletsa et al., *gwfish: a simulation software to evaluate parameter-estimation capabilities of gravitational-wave detector networks*, *Astron. Comput.* **42** (2023) 100671 [arXiv:2205.02499] [INSPIRE].

[32] F. Iacovelli, M. Mancarella, S. Foffa and M. Maggiore, *GWFAST: a Fisher information matrix python code for third-generation gravitational-wave detectors*, *Astrophys. J. Supp.* **263** (2022) 2 [arXiv:2207.06910] [INSPIRE].

JCAP07(2023)068

[33] M.L. Chan, C. Messenger, I.S. Heng and M. Hendry, *Binary neutron star mergers and third generation detectors: localization and early warning*, *Phys. Rev. D* **97** (2018) 123014 [arXiv:1803.09680] [INSPIRE].

[34] Y. Li et al., *Exploring the sky localization and early warning capabilities of third generation gravitational wave detectors in three-detector network configurations*, *Phys. Rev. D* **105** (2022) 043010 [arXiv:2109.07389] [INSPIRE].

[35] M. Pieroni, A. Ricciardone and E. Barausse, *Detectability and parameter estimation of stellar origin black hole binaries with next generation gravitational wave detectors*, *Sci. Rep.* **12** (2022) 17940 [arXiv:2203.12586] [INSPIRE].

[36] M. Vallisneri, *Use and abuse of the Fisher information matrix in the assessment of gravitational-wave parameter-estimation prospects*, *Phys. Rev. D* **77** (2008) 042001 [gr-qc/0703086] [INSPIRE].

[37] C.L. Rodriguez, B. Farr, W.M. Farr and I. Mandel, *Inadequacies of the Fisher information matrix in gravitational-wave parameter estimation*, *Phys. Rev. D* **88** (2013) 084013 [arXiv:1308.1397] [INSPIRE].

[38] G. Pratten et al., *Computationally efficient models for the dominant and subdominant harmonic modes of precessing binary black holes*, *Phys. Rev. D* **103** (2021) 104056 [arXiv:2004.06503] [INSPIRE].

[39] S. Khan et al., *Frequency-domain gravitational waves from nonprecessing black-hole binaries. II. A phenomenological model for the advanced detector era*, *Phys. Rev. D* **93** (2016) 044007 [arXiv:1508.07253] [INSPIRE].

[40] T. Dietrich et al., *Improving the NRTidal model for binary neutron star systems*, *Phys. Rev. D* **100** (2019) 044003 [arXiv:1905.06011] [INSPIRE].

[41] A. Buonanno, Y.-B. Chen and M. Vallisneri, *Detecting gravitational waves from precessing binaries of spinning compact objects: adiabatic limit*, *Phys. Rev. D* **67** (2003) 104025 [*Erratum ibid.* **74** (2006) 029904] [gr-qc/0211087] [INSPIRE].

[42] L. Wade et al., *Systematic and statistical errors in a bayesian approach to the estimation of the neutron-star equation of state using advanced gravitational wave detectors*, *Phys. Rev. D* **89** (2014) 103012 [arXiv:1402.5156] [INSPIRE].

[43] M. Mapelli, N. Giacobbo, E. Ripamonti and M. Spera, *The cosmic merger rate of stellar black hole binaries from the Illustris simulation*, *Mon. Not. Roy. Astron. Soc.* **472** (2017) 2422 [arXiv:1708.05722] [INSPIRE].

[44] N. Giacobbo, M. Mapelli and M. Spera, *Merging black hole binaries: the effects of progenitor's metallicity, mass-loss rate and Eddington factor*, *Mon. Not. Roy. Astron. Soc.* **474** (2018) 2959 [arXiv:1711.03556] [INSPIRE].

[45] P. Kroupa, *The initial mass function and its variation*, *ASP Conf. Ser.* **285** (2002) 86 [astro-ph/0102155] [INSPIRE].

[46] H. Sana et al., *Binary interaction dominates the evolution of massive stars*, *Science* **337** (2012) 444 [arXiv:1207.6397] [INSPIRE].

[47] N. Giacobbo and M. Mapelli, *The impact of electron-capture supernovae on merging double neutron stars*, *Mon. Not. Roy. Astron. Soc.* **482** (2019) 2234 [arXiv:1805.11100] [INSPIRE].

[48] M. Mapelli et al., *Impact of the rotation and compactness of progenitors on the mass of black holes*, *Astrophys. J.* **888** (2020) 76 [arXiv:1909.01371] [INSPIRE].

[49] C.L. Fryer et al., *Compact remnant mass function: dependence on the explosion mechanism and metallicity*, *Astrophys. J.* **749** (2012) 91 [arXiv:1110.1726] [INSPIRE].

JCAP07(2023)068

[50] N. Giacobbo and M. Mapelli, *Revising natal kick prescriptions in population synthesis simulations*, arXiv:1909.06385 [DOI:10.3847/1538-4357/ab7335] [INSPIRE].

[51] J.R. Hurley, C.A. Tout and O.R. Pols, *Evolution of binary stars and the effect of tides on binary populations*, *Mon. Not. Roy. Astron. Soc.* **329** (2002) 897 [astro-ph/0201220] [INSPIRE].

[52] F. Santoliquido et al., *The cosmic merger rate density of compact objects: impact of star formation, metallicity, initial mass function and binary evolution*, *Mon. Not. Roy. Astron. Soc.* **502** (2021) 4877 [arXiv:2009.03911] [INSPIRE].

[53] M. Mapelli et al., *Hierarchical black hole mergers in young, globular and nuclear star clusters: the effect of metallicity, spin and cluster properties*, *Mon. Not. Roy. Astron. Soc.* **505** (2021) 339 [arXiv:2103.05016] [INSPIRE].

[54] M. Mapelli et al., *The cosmic evolution of binary black holes in young, globular, and nuclear star clusters: rates, masses, spins, and mixing fractions*, *Mon. Not. Roy. Astron. Soc.* **511** (2022) 5797 [arXiv:2109.06222] [INSPIRE].

[55] LIGO Scientific et al. collaborations, *Localization and broadband follow-up of the gravitational-wave transient GW150914*, *Astrophys. J. Lett.* **826** (2016) L13 [arXiv:1602.08492] [INSPIRE].

[56] CTA Consortium collaboration, *Introducing the CTA concept*, *Astropart. Phys.* **43** (2013) 3 [INSPIRE].

[57] K. Nandra et al., *The hot and energetic universe: a white paper presenting the science theme motivating the Athena+ mission*, arXiv:1306.2307 [INSPIRE].

[58] LSST collaboration, *LSST: from science drivers to reference design and anticipated data products*, *Astrophys. J.* **873** (2019) 111 [arXiv:0805.2366] [INSPIRE].

[59] J.P. Gardner et al., *The James Webb space telescope*, *Space Sci. Rev.* **123** (2006) 485 [astro-ph/0606175] [INSPIRE].

[60] R. Gilmozzi and J. Spyromilio, *The 42 m European ELT: status*, *Proc. SPIE* **7012** (2008) 701219.

[61] A. Weltman et al., *Fundamental physics with the Square Kilometre Array*, *Publ. Astron. Soc. Austral.* **37** (2020) e002 [arXiv:1810.02680] [INSPIRE].

[62] S.R. Kulkarni et al., *Science with the Ultraviolet Explorer (UVEX)*, arXiv:2111.15608 [INSPIRE].

[63] THESEUS collaboration, *The THESEUS space mission: science goals, requirements and mission concept*, *Exper. Astron.* **52** (2021) 183 [arXiv:2104.09531] [INSPIRE].

[64] HERMES-SP and HERMES-TP collaborations, *The HERMES-technologic and scientific pathfinder*, *Proc. SPIE* **11444** (2020) 114441R [arXiv:2101.03078] [INSPIRE].

[65] A. De Angelis et al., *Gamma-ray astrophysics in the MeV range: the ASTROGAM concept and beyond*, *Exper. Astron.* **51** (2021) 1225 [arXiv:2102.02460] [INSPIRE].

[66] AMEGO collaboration, *All-sky Medium Energy Gamma-ray Observatory: exploring the extreme multimessenger universe*, arXiv:1907.07558 [INSPIRE].

[67] B. Zhang, *Gamma-ray burst prompt emission*, *Int. J. Mod. Phys. D* **23** (2014) 1430002 [arXiv:1402.7022] [INSPIRE].

[68] S. Banerjee et al., *Simulations of early kilonova emission from neutron star mergers*, *Astrophys. J.* **901** (2020) 29 [arXiv:2008.05495] [INSPIRE].

[69] A. Asif et al., *Design of the ULTRASAT UV camera*, arXiv:2108.01493 [DOI:10.1117/12.2594253] [INSPIRE].

JCAP07(2023)068

[70] B. Dorsman et al., *Prospects of gravitational-wave follow-up through a wide-field ultraviolet satellite: a Dorado case study*, *Astrophys. J.* **944** (2023) 126 [arXiv:2206.09696] [INSPIRE].

[71] B. Banerjee et al., *Pre-merger alert to detect the very-high-energy prompt emission from binary neutron-star mergers: Einstein Telescope and Cherenkov Telescope Array synergy*, arXiv:2212.14007 [INSPIRE].

[72] CTA CONSORTIUM collaboration, *Introducing the CTA concept*, *Astropart. Phys.* **43** (2013) 3 [INSPIRE].

[73] C. Meegan et al., *The Fermi gamma-ray burst monitor*, *Astrophys. J.* **702** (2009) 791 [arXiv:0908.0450] [INSPIRE].

[74] Y.G. LI et al., *The GECAM and its payload*, *Scientia Sinica Phys. Mech. Astron.* **50** (2020) 129508.

[75] B. Patricelli et al., *Prospects for multimessenger detection of binary neutron star mergers in the fourth LIGO-Virgo-KAGRA observing run*, *Mon. Not. Roy. Astron. Soc.* **513** (2022) 4159 [*Erratum ibid.* **514** (2022) 3395] [arXiv:2204.12504] [INSPIRE].

[76] A. Colombo et al., *Multi-messenger observations of binary neutron star mergers in the O4 run*, *Astrophys. J.* **937** (2022) 79 [arXiv:2204.07592] [INSPIRE].

[77] G. Oganesyan et al., *Structured jets and X-ray plateaus in gamma-ray burst phenomena*, *Astrophys. J.* **893** (2020) 88 [arXiv:1904.08786] [INSPIRE].

[78] S. Ascenzi et al., *High-latitude emission from the structured jet of γ-ray bursts observed off-axis*, *Astron. Astrophys.* **641** (2020) A61 [arXiv:2004.12215] [INSPIRE].

[79] A. Perego, D. Radice and S. Bernuzzi, *AT* 2017*gfo: an anisotropic and three-component Kilonova counterpart of GW*170817, *Astrophys. J. Lett.* **850** (2017) L37 [arXiv:1711.03982] [INSPIRE].

[80] I. Andreoni et al., *Target-of-opportunity observations of gravitational-wave events with Vera C. Rubin observatory*, *Astrophys. J. Supp.* **260** (2022) 18 [arXiv:2111.01945] [INSPIRE].

[81] P.S. Cowperthwaite, V.A. Villar, D.M. Scolnic and E. Berger, *LSST target-of-opportunity observations of gravitational wave events: essential and efficient*, *Astrophys. J.* **874** (2019) 88 [arXiv:1811.03098] [INSPIRE].

[82] LSST collaboration, *Target of opportunity observations of gravitational wave events with LSST*, arXiv:1812.04051 [INSPIRE].

[83] M. Maggiore, *Gravitational wave experiments and early universe cosmology*, *Phys. Rept.* **331** (2000) 283 [gr-qc/9909001] [INSPIRE].

[84] C. Caprini and D.G. Figueroa, *Cosmological backgrounds of gravitational waves*, *Class. Quant. Grav.* **35** (2018) 163001 [arXiv:1801.04268] [INSPIRE].

[85] M. Maggiore, *Gravitational waves. Volume* 2*: astrophysics and cosmology*, Oxford University Press, Oxford, U.K. (2018).

[86] R. Durrer, *The cosmic microwave background*, Cambridge University Press, Cambridge, U.K. (2008) [DOI:10.1017/CBO9780511817205] [INSPIRE].

[87] M.G. Hauser and E. Dwek, *The cosmic infrared background: measurements and implications*, *Ann. Rev. Astron. Astrophys.* **39** (2001) 249 [astro-ph/0105539] [INSPIRE].

[88] C. Caprini et al., *Reconstructing the spectral shape of a stochastic gravitational wave background with LISA*, *JCAP* **11** (2019) 017 [arXiv:1906.09244] [INSPIRE].

[89] R. Flauger et al., *Improved reconstruction of a stochastic gravitational wave background with LISA*, *JCAP* **01** (2021) 059 [arXiv:2009.11845] [INSPIRE].

JCAP07(2023)068

[90] C.R. Contaldi, *Anisotropies of gravitational wave backgrounds: a line of sight approach*, *Phys. Lett. B* **771** (2017) 9 [arXiv:1609.08168] [INSPIRE].

[91] M. Geller, A. Hook, R. Sundrum and Y. Tsai, *Primordial anisotropies in the gravitational wave background from cosmological phase transitions*, *Phys. Rev. Lett.* **121** (2018) 201303 [arXiv:1803.10780] [INSPIRE].

[92] N. Bartolo et al., *Anisotropies and non-Gaussianity of the cosmological gravitational wave background*, *Phys. Rev. D* **100** (2019) 121501 [arXiv:1908.00527] [INSPIRE].

[93] N. Bartolo et al., *Characterizing the cosmological gravitational wave background: anisotropies and non-Gaussianity*, *Phys. Rev. D* **102** (2020) 023527 [arXiv:1912.09433] [INSPIRE].

[94] G. Cusin, C. Pitrou and J.-P. Uzan, *The signal of the gravitational wave background and the angular correlation of its energy density*, *Phys. Rev. D* **97** (2018) 123527 [arXiv:1711.11345] [INSPIRE].

[95] G. Cusin, C. Pitrou and J.-P. Uzan, *Anisotropy of the astrophysical gravitational wave background: analytic expression of the angular power spectrum and correlation with cosmological observations*, *Phys. Rev. D* **96** (2017) 103019 [arXiv:1704.06184] [INSPIRE].

[96] G. Cusin, I. Dvorkin, C. Pitrou and J.-P. Uzan, *First predictions of the angular power spectrum of the astrophysical gravitational wave background*, *Phys. Rev. Lett.* **120** (2018) 231101 [arXiv:1803.03236] [INSPIRE].

[97] G. Cusin, I. Dvorkin, C. Pitrou and J.-P. Uzan, *Properties of the stochastic astrophysical gravitational wave background: astrophysical sources dependencies*, *Phys. Rev. D* **100** (2019) 063004 [arXiv:1904.07797] [INSPIRE].

[98] K.Z. Yang, V. Mandic, C. Scarlata and S. Banagiri, *Searching for cross-correlation between stochastic gravitational wave background and galaxy number counts*, *Mon. Not. Roy. Astron. Soc.* **500** (2020) 1666 [arXiv:2007.10456] [INSPIRE].

[99] A.C. Jenkins, M. Sakellariadou, T. Regimbau and E. Slezak, *Anisotropies in the astrophysical gravitational-wave background: predictions for the detection of compact binaries by LIGO and Virgo*, *Phys. Rev. D* **98** (2018) 063501 [arXiv:1806.01718] [INSPIRE].

[100] A.C. Jenkins, R. O'Shaughnessy, M. Sakellariadou and D. Wysocki, *Anisotropies in the astrophysical gravitational-wave background: the impact of black hole distributions*, *Phys. Rev. Lett.* **122** (2019) 111101 [arXiv:1810.13435] [INSPIRE].

[101] A.C. Jenkins and M. Sakellariadou, *Anisotropies in the stochastic gravitational-wave background: formalism and the cosmic string case*, *Phys. Rev. D* **98** (2018) 063509 [arXiv:1802.06046] [INSPIRE].

[102] G. Cusin, I. Dvorkin, C. Pitrou and J.-P. Uzan, *Stochastic gravitational wave background anisotropies in the mHz band: astrophysical dependencies*, *Mon. Not. Roy. Astron. Soc.* **493** (2020) L1 [arXiv:1904.07757] [INSPIRE].

[103] A.C. Jenkins and M. Sakellariadou, *Shot noise in the astrophysical gravitational-wave background*, *Phys. Rev. D* **100** (2019) 063508 [arXiv:1902.07719] [INSPIRE].

[104] A.C. Jenkins, J.D. Romano and M. Sakellariadou, *Estimating the angular power spectrum of the gravitational-wave background in the presence of shot noise*, *Phys. Rev. D* **100** (2019) 083501 [arXiv:1907.06642] [INSPIRE].

[105] G. Cusin, R. Durrer and P.G. Ferreira, *Polarization of a stochastic gravitational wave background through diffusion by massive structures*, *Phys. Rev. D* **99** (2019) 023534 [arXiv:1807.10620] [INSPIRE].

[106] D. Bertacca et al., *Projection effects on the observed angular spectrum of the astrophysical stochastic gravitational wave background*, *Phys. Rev. D* **101** (2020) 103513 [arXiv:1909.11627] [INSPIRE].

JCAP07(2023)068

[107] C. Pitrou, G. Cusin and J.-P. Uzan, *Unified view of anisotropies in the astrophysical gravitational-wave background*, *Phys. Rev. D* **101** (2020) 081301 [arXiv:1910.04645] [INSPIRE].

[108] D. Alonso, G. Cusin, P.G. Ferreira and C. Pitrou, *Detecting the anisotropic astrophysical gravitational wave background in the presence of shot noise through cross-correlations*, *Phys. Rev. D* **102** (2020) 023002 [arXiv:2002.02888] [INSPIRE].

[109] N. Bellomo et al., *CLASS_GWB: robust modeling of the astrophysical gravitational wave background anisotropies*, *JCAP* **06** (2022) 030 [arXiv:2110.15059] [INSPIRE].

[110] P. Adshead et al., *Multimessenger cosmology: correlating cosmic microwave background and stochastic gravitational wave background measurements*, *Phys. Rev. D* **103** (2021) 023532 [arXiv:2004.06619] [INSPIRE].

[111] A. Ricciardone et al., *Cross-correlating astrophysical and cosmological gravitational wave backgrounds with the cosmic microwave background*, *Phys. Rev. Lett.* **127** (2021) 271301 [arXiv:2106.02591] [INSPIRE].

[112] G. Galloni et al., *Test of the statistical isotropy of the universe using gravitational waves*, *JCAP* **09** (2022) 046 [arXiv:2202.12858] [INSPIRE].

[113] G. Capurri et al., *Intensity and anisotropies of the stochastic gravitational wave background from merging compact binaries in galaxies*, *JCAP* **11** (2021) 032 [arXiv:2103.12037] [INSPIRE].

[114] G. Cusin and G. Tasinato, *Doppler boosting the stochastic gravitational wave background*, *JCAP* **08** (2022) 036 [arXiv:2201.10464] [INSPIRE].

[115] L. Valbusa Dall'Armi, A. Ricciardone and D. Bertacca, *The dipole of the astrophysical gravitational-wave background*, *JCAP* **11** (2022) 040 [arXiv:2206.02747] [INSPIRE].

[116] S. Mastrogiovanni, C. Bonvin, G. Cusin and S. Foffa, *Detection and estimation of the cosmic dipole with the Einstein Telescope and cosmic explorer*, *Mon. Not. Roy. Astron. Soc.* **521** (2023) 984 [arXiv:2209.11658] [INSPIRE].

[117] D. Alonso et al., *Noise angular power spectrum of gravitational wave background experiments*, *Phys. Rev. D* **101** (2020) 124048 [arXiv:2005.03001] [INSPIRE].

[118] G. Mentasti and M. Peloso, *ET sensitivity to the anisotropic stochastic gravitational wave background*, *JCAP* **03** (2021) 080 [arXiv:2010.00486] [INSPIRE].

[119] G. Mentasti, C. Contaldi and M. Peloso, *Prospects for detecting anisotropies and polarization of the stochastic gravitational wave background with ground-based detectors*, arXiv:2304.06640 [INSPIRE].

[120] T. Regimbau et al., *A mock data challenge for the Einstein gravitational-wave telescope*, *Phys. Rev. D* **86** (2012) 122001 [arXiv:1201.3563] [INSPIRE].

[121] C. Périgois et al., *Gravitational background from dynamical binaries and detectability with 2G detectors*, *Phys. Rev. D* **105** (2022) 103032 [arXiv:2112.01119] [INSPIRE].

[122] S.S. Bavera et al., *Stochastic gravitational-wave background as a tool for investigating multi-channel astrophysical and primordial black-hole mergers*, *Astron. Astrophys.* **660** (2022) A26 [arXiv:2109.05836] [INSPIRE].

[123] V. Bromm and R.B. Larson, *The first stars*, *Ann. Rev. Astron. Astrophys.* **42** (2004) 79 [astro-ph/0311019] [INSPIRE].

[124] T. Hartwig et al., *Gravitational waves from the remnants of the first stars*, *Mon. Not. Roy. Astron. Soc.* **460** (2016) L74 [arXiv:1603.05655] [INSPIRE].

[125] T. Kinugawa, A. Miyamoto, N. Kanda and T. Nakamura, *The detection rate of inspiral and quasi-normal modes of Population III binary black holes which can confirm or refute the general relativity in the strong gravity region*, *Mon. Not. Roy. Astron. Soc.* **456** (2016) 1093 [arXiv:1505.06962] [INSPIRE].

JCAP07(2023)068

[126] K. Belczynski et al., *On the likelihood of detecting gravitational waves from Population III compact object binaries*, *Mon. Not. Roy. Astron. Soc.* **471** (2017) 4702 [arXiv:1612.01524] [INSPIRE].

[127] B. Liu and V. Bromm, *Gravitational waves from Population III binary black holes formed by dynamical capture*, *Mon. Not. Roy. Astron. Soc.* **495** (2020) 2475 [arXiv:2003.00065] [INSPIRE].

[128] A. Tanikawa et al., *Merger rate density of binary black holes through isolated Population I, II, III and extremely metal-poor binary star evolution*, *Astrophys. J.* **926** (2022) 83 [arXiv:2110.10846] [INSPIRE].

[129] C. Périgois, C. Belczynski, T. Bulik and T. Regimbau, *StarTrack predictions of the stochastic gravitational-wave background from compact binary mergers*, *Phys. Rev. D* **103** (2021) 043002 [arXiv:2008.04890] [INSPIRE].

[130] K. Martinovic, C. Perigois, T. Regimbau and M. Sakellariadou, *Footprints of Population III stars in the gravitational-wave background*, *Astrophys. J.* **940** (2022) 29 [arXiv:2109.09779] [INSPIRE].

[131] K. Inayoshi, K. Kashiyama, E. Visbal and Z. Haiman, *Gravitational wave background from Population III binary black holes consistent with cosmic reionization*, *Mon. Not. Roy. Astron. Soc.* **461** (2016) 2722 [arXiv:1603.06921] [INSPIRE].

[132] I. Kowalska, T. Bulik and K. Belczynski, *Gravitational wave background from Population III binaries*, *Astron. Astrophys.* **541** (2012) A120 [arXiv:1202.3346] [INSPIRE].

[133] Y. Suwa, T. Takiwaki, K. Kotake and K. Sato, *Gravitational wave background from Population III stars*, *Astrophys. J. Lett.* **665** (2007) L43 [arXiv:0706.3495] [INSPIRE].

[134] N. Christensen, *Stochastic gravitational wave backgrounds*, *Rept. Prog. Phys.* **82** (2019) 016903 [arXiv:1811.08797] [INSPIRE].

[135] K. Janssens et al., *Correlated* 1–1000 *Hz magnetic field fluctuations from lightning over earth-scale distances and their impact on gravitational wave searches*, *Phys. Rev. D* **107** (2023) 022004 [arXiv:2209.00284] [INSPIRE].

[136] F. Badaracco and J. Harms, *Optimization of seismometer arrays for the cancellation of Newtonian noise from seismic body waves*, *Class. Quant. Grav.* **36** (2019) 145006 [arXiv:1903.07936] [INSPIRE].

[137] T. Andric and J. Harms, *Simulations of gravitoelastic correlations for the Sardinian candidate site of the Einstein Telescope*, *J. Geophys. Res.* **125** (2020) e2020JB020401.

[138] M.D. Giovanni et al., *A seismological study of the Sos Enattos Area — the Sardinia candidate site for the Einstein Telescope*, *Seismological Res. Lett.* **92** (2020) 352.

[139] M. Bader et al., *Newtonian-noise characterization at Terziet in Limburg — the Euregio Meuse-Rhine candidate site for Einstein Telescope*, *Class. Quant. Grav.* **39** (2022) 025009 [INSPIRE].

[140] S. Koley et al., *Surface and underground seismic characterization at Terziet in Limburg — the Euregio Meuse-Rhine candidate site for Einstein Telescope*, *Class. Quant. Grav.* **39** (2022) 025008 [INSPIRE].

[141] K. Janssens et al., *Impact of correlated seismic and correlated Newtonian noise on the Einstein Telescope*, *Phys. Rev. D* **106** (2022) 042008 [arXiv:2206.06809] [INSPIRE].

[142] E.T.S.C.E. Team, *Design report update* 2020 *for the Einstein Telescope*, https://apps.et-gw.eu/tds/?content=3&r=17245.

[143] S. Shani-Kadmiel, F. Linde, L. Evers and B. Vink, *Einstein Telescope seismic campaigns*, https://www.fdsn.org/networks/detail/3T_2020/ (2020) [DOI:10.7914/SN/3T_2020].

JCAP07(2023)068

[144] V. Mandic et al., *A 3D broadband seismometer array experiment at the Homestake mine*, *Seismol. Res. Lett.* **89** (2018) 2420.

[145] E. Thrane and J.D. Romano, *Sensitivity curves for searches for gravitational-wave backgrounds*, *Phys. Rev. D* **88** (2013) 124032 [arXiv:1310.5300] [INSPIRE].

[146] LIGO Scientific, Virgo and KAGRA collaborations, *Data for upper limits on the isotropic gravitational-wave background from advanced LIGO's and advanced Virgo's third observing run*, version 5, https://dcc.ligo.org/G2001287/public, April 2022.

[147] KAGRA et al. collaborations, *Upper limits on the isotropic gravitational-wave background from advanced LIGO and advanced Virgo's third observing run*, *Phys. Rev. D* **104** (2021) 022004 [arXiv:2101.12130] [INSPIRE].

[148] J. Peterson, *Observation and modeling of seismic background noise*, *Open-file report* **93-322** (1993).

[149] B. Goncharov, A.H. Nitz and J. Harms, *Utilizing the null stream of the Einstein Telescope*, *Phys. Rev. D* **105** (2022) 122007 [arXiv:2204.08533] [INSPIRE].

[150] K. Janssens et al., *Formalism for power spectral density estimation for non-identical and correlated noise using the null channel in Einstein Telescope*, *Eur. Phys. J. Plus* **138** (2023) 352 [*Erratum ibid.* **138** (2023) 446] [arXiv:2205.00416] [INSPIRE].

[151] M. Coughlin et al., *Limiting the effects of earthquakes on gravitational-wave interferometers*, *Class. Quant. Grav.* **34** (2017) 044004 [arXiv:1611.09812] [INSPIRE].

[152] Virgo collaboration, *The Virgo O3 run and the impact of the environment*, *Class. Quant. Grav.* **39** (2022) 235009 [arXiv:2203.04014] [INSPIRE].

[153] W.O. Schumann, *Über die strahlungslosen Eigenschwingungen einer leitenden Kugel, die von einer Luftschicht und einer Ionosphärenhülle umgeben ist* (in German), *Z. Naturforschung A* **7** (1952) 149.

[154] W.O. Schumann, *Über die Dämpfung der elektromagnetischen Eigenschwingungen des Systems Erde — Luft — Ionosphäre* (in German), *Z. Naturforschung A* **7** (1952) 250.

[155] I. Fiori et al., *The hunt for environmental noise in Virgo during the third observing run*, *Galaxies* **8** (2020) 82 [INSPIRE].

[156] K. Janssens et al., *Impact of Schumann resonances on the Einstein Telescope and projections for the magnetic coupling function*, *Phys. Rev. D* **104** (2021) 122006 [*Erratum ibid.* **105** (2022) 109904] [arXiv:2110.14730] [INSPIRE].

[157] F. Amann et al., *Site-selection criteria for the Einstein Telescope*, *Rev. Sci. Instrum.* **91** (2020) 9 [arXiv:2003.03434] [INSPIRE].

[158] A. Cirone et al., *Magnetic coupling to the advanced Virgo payloads and its impact on the low frequency sensitivity*, *Rev. Sci. Instrum.* **89** (2018) 114501 [arXiv:1807.06278] [INSPIRE].

[159] D.J. Boccippio, S.J. Goodman and S. Heckman, *Regional differences in tropical lightning distributions*, *J. Appl. Meteor.* **39** (2000) 2231.

[160] M.W. Coughlin et al., *Measurement and subtraction of Schumann resonances at gravitational-wave interferometers*, *Phys. Rev. D* **97** (2018) 102007 [arXiv:1802.00885] [INSPIRE].

[161] A. Cirone et al., *Investigation of magnetic noise in advanced Virgo*, *Class. Quant. Grav.* **36** (2019) 225004 [arXiv:1908.11174] [INSPIRE].

[162] AdvLIGO collaboration, *Environmental noise in advanced LIGO detectors*, *Class. Quant. Grav.* **38** (2021) 145001 [arXiv:2101.09935] [INSPIRE].

[163] R.P. Kerr, *Gravitational field of a spinning mass as an example of algebraically special metrics*, *Phys. Rev. Lett.* **11** (1963) 237 [INSPIRE].

JCAP07(2023)068

[164] B. Carter, *Axisymmetric black hole has only two degrees of freedom*, *Phys. Rev. Lett.* **26** (1971) 331 [INSPIRE].

[165] D.C. Robinson, *Uniqueness of the Kerr black hole*, *Phys. Rev. Lett.* **34** (1975) 905 [INSPIRE].

[166] P.T. Chrusciel, J. Lopes Costa and M. Heusler, *Stationary black holes: uniqueness and beyond*, *Living Rev. Rel.* **15** (2012) 7 [arXiv:1205.6112] [INSPIRE].

[167] I. Kamaretsos, M. Hannam, S. Husa and B.S. Sathyaprakash, *Black-hole hair loss: learning about binary progenitors from ringdown signals*, *Phys. Rev. D* **85** (2012) 024018 [arXiv:1107.0854] [INSPIRE].

[168] I. Kamaretsos, M. Hannam and B. Sathyaprakash, *Is black-hole ringdown a memory of its progenitor?*, *Phys. Rev. Lett.* **109** (2012) 141102 [arXiv:1207.0399] [INSPIRE].

[169] S. Gossan, J. Veitch and B.S. Sathyaprakash, *Bayesian model selection for testing the no-hair theorem with black hole ringdowns*, *Phys. Rev. D* **85** (2012) 124056 [arXiv:1111.5819] [INSPIRE].

[170] X. Jiménez Forteza, S. Bhagwat, P. Pani and V. Ferrari, *Spectroscopy of binary black hole ringdown using overtones and angular modes*, *Phys. Rev. D* **102** (2020) 044053 [arXiv:2005.03260] [INSPIRE].

[171] I. Ota and C. Chirenti, *Overtones or higher harmonics? Prospects for testing the no-hair theorem with gravitational wave detections*, *Phys. Rev. D* **101** (2020) 104005 [arXiv:1911.00440] [INSPIRE].

[172] I. Ota and C. Chirenti, *Black hole spectroscopy horizons for current and future gravitational wave detectors*, *Phys. Rev. D* **105** (2022) 044015 [arXiv:2108.01774] [INSPIRE].

[173] X.J. Forteza, S. Bhagwat, S. Kumar and P. Pani, *Novel ringdown amplitude-phase consistency test*, *Phys. Rev. Lett.* **130** (2023) 021001 [arXiv:2205.14910] [INSPIRE].

[174] K.D. Kokkotas and B.G. Schmidt, *Quasinormal modes of stars and black holes*, *Living Rev. Rel.* **2** (1999) 2 [gr-qc/9909058] [INSPIRE].

[175] E. Berti, V. Cardoso and A.O. Starinets, *Quasinormal modes of black holes and black branes*, *Class. Quant. Grav.* **26** (2009) 163001 [arXiv:0905.2975] [INSPIRE].

[176] E. Berti, V. Cardoso and C.M. Will, *On gravitational-wave spectroscopy of massive black holes with the space interferometer LISA*, *Phys. Rev. D* **73** (2006) 064030 [gr-qc/0512160] [INSPIRE].

[177] E. Berti, J. Cardoso, V. Cardoso and M. Cavaglia, *Matched-filtering and parameter estimation of ringdown waveforms*, *Phys. Rev. D* **76** (2007) 104044 [arXiv:0707.1202] [INSPIRE].

[178] O. Dreyer et al., *Black hole spectroscopy: testing general relativity through gravitational wave observations*, *Class. Quant. Grav.* **21** (2004) 787 [gr-qc/0309007] [INSPIRE].

[179] S. Bhagwat, C. Pacilio, E. Barausse and P. Pani, *Landscape of massive black-hole spectroscopy with LISA and the Einstein Telescope*, *Phys. Rev. D* **105** (2022) 124063 [arXiv:2201.00023] [INSPIRE].

[180] E. Barausse, V. Morozova and L. Rezzolla, *On the mass radiated by coalescing black-hole binaries*, *Astrophys. J.* **758** (2012) 63 [*Erratum ibid.* **786** (2014) 76] [arXiv:1206.3803] [INSPIRE].

[181] F. Hofmann, E. Barausse and L. Rezzolla, *The final spin from binary black holes in quasi-circular orbits*, *Astrophys. J. Lett.* **825** (2016) L19 [arXiv:1605.01938] [INSPIRE].

[182] V. Varma et al., *High-accuracy mass, spin, and recoil predictions of generic black-hole merger remnants*, *Phys. Rev. Lett.* **122** (2019) 011101 [arXiv:1809.09125] [INSPIRE].

[183] J. Meidam et al., *Testing the no-hair theorem with black hole ringdowns using TIGER*, *Phys. Rev. D* **90** (2014) 064009 [arXiv:1406.3201] [INSPIRE].

JCAP07(2023)068

[184] H. Yang et al., *Black hole spectroscopy with coherent mode stacking*, *Phys. Rev. Lett.* **118** (2017) 161101 [arXiv:1701.05808] [INSPIRE].

[185] A. Maselli, P. Pani, L. Gualtieri and E. Berti, *Parametrized ringdown spin expansion coefficients: a data-analysis framework for black-hole spectroscopy with multiple events*, *Phys. Rev. D* **101** (2020) 024043 [arXiv:1910.12893] [INSPIRE].

[186] G.F. Giudice, M. McCullough and A. Urbano, *Hunting for dark particles with gravitational waves*, *JCAP* **10** (2016) 001 [arXiv:1605.01209] [INSPIRE].

[187] V. Cardoso and P. Pani, *Testing the nature of dark compact objects: a status report*, *Living Rev. Rel.* **22** (2019) 4 [arXiv:1904.05363] [INSPIRE].

[188] J. Abedi, N. Afshordi, N. Oshita and Q. Wang, *Quantum black holes in the sky*, *Universe* **6** (2020) 43 [arXiv:2001.09553] [INSPIRE].

[189] S.D. Mathur, *The fuzzball proposal for black holes: an elementary review*, *Fortsch. Phys.* **53** (2005) 793 [hep-th/0502050] [INSPIRE].

[190] I. Bena, E.J. Martinec, S.D. Mathur and N.P. Warner, *Snowmass white paper: micro- and macro-structure of black holes*, arXiv:2203.04981 [INSPIRE].

[191] P. Jetzer, *Boson stars*, *Phys. Rept.* **220** (1992) 163 [INSPIRE].

[192] S.L. Liebling and C. Palenzuela, *Dynamical boson stars*, *Living Rev. Rel.* **26** (2023) 1 [arXiv:1202.5809] [INSPIRE].

[193] E. Maggio, P. Pani and G. Raposo, *Testing the nature of dark compact objects with gravitational waves*, arXiv:2105.06410 [DOI:10.1007/978-981-15-4702-7_29-1] [INSPIRE].

[194] V. Cardoso, E. Franzin and P. Pani, *Is the gravitational-wave ringdown a probe of the event horizon?*, *Phys. Rev. Lett.* **116** (2016) 171101 [*Erratum ibid.* **117** (2016) 089902] [arXiv:1602.07309] [INSPIRE].

[195] V. Cardoso and P. Pani, *Tests for the existence of black holes through gravitational wave echoes*, *Nature Astron.* **1** (2017) 586 [arXiv:1709.01525] [INSPIRE].

[196] J. Westerweck et al., *Low significance of evidence for black hole echoes in gravitational wave data*, *Phys. Rev. D* **97** (2018) 124037 [arXiv:1712.09966] [INSPIRE].

[197] R.K.L. Lo, T.G.F. Li and A.J. Weinstein, *Template-based gravitational-wave echoes search using Bayesian model selection*, *Phys. Rev. D* **99** (2019) 084052 [arXiv:1811.07431] [INSPIRE].

[198] N. Uchikata et al., *Searching for black hole echoes from the LIGO-Virgo catalog GWTC-1*, *Phys. Rev. D* **100** (2019) 062006 [arXiv:1906.00838] [INSPIRE].

[199] K.W. Tsang et al., *A morphology-independent search for gravitational wave echoes in data from the first and second observing runs of advanced LIGO and advanced Virgo*, *Phys. Rev. D* **101** (2020) 064012 [arXiv:1906.11168] [INSPIRE].

[200] E. Maggio, A. Testa, S. Bhagwat and P. Pani, *Analytical model for gravitational-wave echoes from spinning remnants*, *Phys. Rev. D* **100** (2019) 064056 [arXiv:1907.03091] [INSPIRE].

[201] R.O. Hansen, *Multipole moments of stationary space-times*, *J. Math. Phys.* **15** (1974) 46 [INSPIRE].

[202] N.V. Krishnendu, K.G. Arun and C.K. Mishra, *Testing the binary black hole nature of a compact binary coalescence*, *Phys. Rev. Lett.* **119** (2017) 091101 [arXiv:1701.06318] [INSPIRE].

[203] N. Loutrel, R. Brito, A. Maselli and P. Pani, *Inspiraling compact objects with generic deformations*, *Phys. Rev. D* **105** (2022) 124050 [arXiv:2203.01725] [INSPIRE].

JCAP07(2023)068

[204] M. Favata, *Conservative corrections to the innermost stable circular orbit (ISCO) of a Kerr black hole: a new gauge-invariant post-Newtonian ISCO condition, and the ISCO shift due to test-particle spin and the gravitational self-force*, *Phys. Rev. D* **83** (2011) 024028 [arXiv:1010.2553] [INSPIRE].

[205] T. Binnington and E. Poisson, *Relativistic theory of tidal Love numbers*, *Phys. Rev. D* **80** (2009) 084018 [arXiv:0906.1366] [INSPIRE].

[206] T. Damour and A. Nagar, *Relativistic tidal properties of neutron stars*, *Phys. Rev. D* **80** (2009) 084035 [arXiv:0906.0096] [INSPIRE].

[207] N. Gürlebeck, *No-hair theorem for black holes in astrophysical environments*, *Phys. Rev. Lett.* **114** (2015) 151102 [arXiv:1503.03240] [INSPIRE].

[208] P. Pani, *I-Love-Q relations for gravastars and the approach to the black-hole limit*, *Phys. Rev. D* **92** (2015) 124030 [*Erratum ibid.* **95** (2017) 049902] [arXiv:1506.06050] [INSPIRE].

[209] N. Uchikata, S. Yoshida and P. Pani, *Tidal deformability and I-Love-Q relations for gravastars with polytropic thin shells*, *Phys. Rev. D* **94** (2016) 064015 [arXiv:1607.03593] [INSPIRE].

[210] R.A. Porto, *The tune of love and the nature(ness) of spacetime*, *Fortsch. Phys.* **64** (2016) 723 [arXiv:1606.08895] [INSPIRE].

[211] V. Cardoso et al., *Testing strong-field gravity with tidal Love numbers*, *Phys. Rev. D* **95** (2017) 084014 [*Addendum ibid.* **95** (2017) 089901] [arXiv:1701.01116] [INSPIRE].

[212] S.B. Giddings, S. Koren and G. Treviño, *Exploring strong-field deviations from general relativity via gravitational waves*, *Phys. Rev. D* **100** (2019) 044005 [arXiv:1904.04258] [INSPIRE].

[213] N. Sennett et al., *Distinguishing boson stars from black holes and neutron stars from tidal interactions in inspiraling binary systems*, *Phys. Rev. D* **96** (2017) 024002 [arXiv:1704.08651] [INSPIRE].

[214] L.R. Weih, M. Hanauske and L. Rezzolla, *Postmerger gravitational-wave signatures of phase transitions in binary mergers*, *Phys. Rev. Lett.* **124** (2020) 171103 [arXiv:1912.09340] [INSPIRE].

[215] A. Bauswein et al., *Identifying a first-order phase transition in neutron star mergers through gravitational waves*, *Phys. Rev. Lett.* **122** (2019) 061102 [arXiv:1809.01116] [INSPIRE].

[216] Z. Carson, A.W. Steiner and K. Yagi, *Future prospects for constraining nuclear matter parameters with gravitational waves*, *Phys. Rev. D* **100** (2019) 023012 [arXiv:1906.05978] [INSPIRE].

[217] C. Pacilio, A. Maselli, M. Fasano and P. Pani, *Ranking Love numbers for the neutron star equation of state: the need for third-generation detectors*, *Phys. Rev. Lett.* **128** (2022) 101101 [arXiv:2104.10035] [INSPIRE].

[218] R. Smith et al., *Bayesian inference for gravitational waves from binary neutron star mergers in third generation observatories*, *Phys. Rev. Lett.* **127** (2021) 081102 [arXiv:2103.12274] [INSPIRE].

[219] P.K. Gupta et al., *Determining the equation of state of neutron stars with Einstein Telescope using tidal effects and r-mode excitations from a population of binary inspirals*, arXiv:2205.01182 [INSPIRE].

[220] M. Breschi et al., *Kilohertz gravitational waves from binary neutron star mergers: inference of postmerger signals with the Einstein Telescope*, arXiv:2205.09979 [INSPIRE].

[221] A. Puecher et al., *Unraveling information about supranuclear-dense matter from the complete binary neutron star coalescence process using future gravitational-wave detector networks*, *Phys. Rev. D* **107** (2023) 124009 [arXiv:2210.09259] [INSPIRE].

JCAP07(2023)068

[222] M. Wijngaarden et al., *Probing neutron stars with the full premerger and postmerger gravitational wave signal from binary coalescences*, *Phys. Rev. D* **105** (2022) 104019 [arXiv:2202.09382] [INSPIRE].

[223] L. Baiotti and L. Rezzolla, *Binary neutron star mergers: a review of Einstein's richest laboratory*, *Rept. Prog. Phys.* **80** (2017) 096901 [arXiv:1607.03540] [INSPIRE].

[224] B. Wei et al., *Novel relativistic mean field Lagrangian guided by pseudo-spin symmetry restoration*, *Chin. Phys. C* **44** (2020) 074107 [INSPIRE].

[225] C.-J. Xia et al., *Unified nuclear matter equations of state constrained by the in-medium balance in density-dependent covariant density functionals*, *Phys. Rev. C* **105** (2022) 045803 [arXiv:2201.12053] [INSPIRE].

[226] C.-J. Xia et al., *Unified neutron star EOSs and neutron star structures in RMF models*, *Commun. Theor. Phys.* **74** (2022) 095303 [arXiv:2208.12893] [INSPIRE].

[227] J. Margueron, R. Hoffmann Casali and F. Gulminelli, *Equation of state for dense nucleonic matter from metamodeling. I. Foundational aspects*, *Phys. Rev. C* **97** (2018) 025805 [arXiv:1708.06894] [INSPIRE].

[228] S. De et al., *Tidal deformabilities and radii of neutron stars from the observation of GW*170817, *Phys. Rev. Lett.* **121** (2018) 091102 [*Erratum ibid.* **121** (2018) 259902] [arXiv:1804.08583] [INSPIRE].

[229] N. Kunert et al., *Quantifying modeling uncertainties when combining multiple gravitational-wave detections from binary neutron star sources*, *Phys. Rev. D* **105** (2022) L061301 [arXiv:2110.11835] [INSPIRE].

[230] T. Carreau, F. Gulminelli and J. Margueron, *Bayesian analysis of the crust-core transition with a compressible liquid-drop model*, *Eur. Phys. J. A* **55** (2019) 188 [arXiv:1902.07032] [INSPIRE].

[231] D. Barba-González, C. Albertus and M.Á. Pérez-García, *Crystallization in single- and multicomponent neutron star crusts*, *Phys. Rev. C* **106** (2022) 065806 [arXiv:2207.14323] [INSPIRE].

[232] C. Drischler, K. Hebeler and A. Schwenk, *Asymmetric nuclear matter based on chiral two- and three-nucleon interactions*, *Phys. Rev. C* **93** (2016) 054314 [arXiv:1510.06728] [INSPIRE].

[233] H.D. Thi, C. Mondal and F. Gulminelli, *The nuclear matter density functional under the nucleonic hypothesis*, *Universe* **7** (2021) 373 [arXiv:2109.09675] [INSPIRE].

[234] LIGO Scientific and Virgo collaborations, *Properties of the binary neutron star merger GW*170817, *Phys. Rev. X* **9** (2019) 011001 [arXiv:1805.11579] [INSPIRE].

[235] B. Zackay, L. Dai and T. Venumadhav, *Relative binning and fast likelihood evaluation for gravitational wave parameter estimation*, arXiv:1806.08792 [INSPIRE].

[236] L. Dai, T. Venumadhav and B. Zackay, *Parameter estimation for GW*170817 *using relative binning*, arXiv:1806.08793 [INSPIRE].

[237] N. Leslie, L. Dai and G. Pratten, *Mode-by-mode relative binning: fast likelihood estimation for gravitational waveforms with spin-orbit precession and multiple harmonics*, *Phys. Rev. D* **104** (2021) 123030 [arXiv:2109.09872] [INSPIRE].

[238] A. Puecher, A. Samajdar and T. Dietrich, *Measuring tidal effects with the Einstein Telescope: a design study*, in preparation (2022).

[239] E.R. Most et al., *Signatures of quark-hadron phase transitions in general-relativistic neutron-star mergers*, *Phys. Rev. Lett.* **122** (2019) 061101 [arXiv:1807.03684] [INSPIRE].

[240] D.M. Siegel, R. Ciolfi, A.I. Harte and L. Rezzolla, *Magnetorotational instability in relativistic hypermassive neutron stars*, *Phys. Rev. D* **87** (2013) 121302 [arXiv:1302.4368] [INSPIRE].

JCAP07(2023)068

[241] M.G. Alford et al., *Viscous dissipation and heat conduction in binary neutron-star mergers*, *Phys. Rev. Lett.* **120** (2018) 041101 [arXiv:1707.09475] [INSPIRE].

[242] D. Radice, *General-relativistic large-eddy simulations of binary neutron star mergers*, *Astrophys. J. Lett.* **838** (2017) L2 [arXiv:1703.02046] [INSPIRE].

[243] M. Shibata and K. Kiuchi, *Gravitational waves from remnant massive neutron stars of binary neutron star merger: viscous hydrodynamics effects*, *Phys. Rev. D* **95** (2017) 123003 [arXiv:1705.06142] [INSPIRE].

[244] R. De Pietri et al., *Convective excitation of inertial modes in binary neutron star mergers*, *Phys. Rev. Lett.* **120** (2018) 221101 [arXiv:1802.03288] [INSPIRE].

[245] A. Bauswein, T.W. Baumgarte and H.-T. Janka, *Prompt merger collapse and the maximum mass of neutron stars*, *Phys. Rev. Lett.* **111** (2013) 131101 [arXiv:1307.5191] [INSPIRE].

[246] S. Köppel, L. Bovard and L. Rezzolla, *A general-relativistic determination of the threshold mass to prompt collapse in binary neutron star mergers*, *Astrophys. J. Lett.* **872** (2019) L16 [arXiv:1901.09977] [INSPIRE].

[247] M. Agathos et al., *Inferring prompt black-hole formation in neutron star mergers from gravitational-wave data*, *Phys. Rev. D* **101** (2020) 044006 [arXiv:1908.05442] [INSPIRE].

[248] A. Bauswein and H.-T. Janka, *Measuring neutron-star properties via gravitational waves from binary mergers*, *Phys. Rev. Lett.* **108** (2012) 011101 [arXiv:1106.1616] [INSPIRE].

[249] K. Takami, L. Rezzolla and L. Baiotti, *Spectral properties of the post-merger gravitational-wave signal from binary neutron stars*, *Phys. Rev. D* **91** (2015) 064001 [arXiv:1412.3240] [INSPIRE].

[250] J.A. Clark, A. Bauswein, N. Stergioulas and D. Shoemaker, *Observing gravitational waves from the post-merger phase of binary neutron star coalescence*, *Class. Quant. Grav.* **33** (2016) 085003 [arXiv:1509.08522] [INSPIRE].

[251] K.W. Tsang, T. Dietrich and C. Van Den Broeck, *Modeling the postmerger gravitational wave signal and extracting binary properties from future binary neutron star detections*, *Phys. Rev. D* **100** (2019) 044047 [arXiv:1907.02424] [INSPIRE].

[252] M. Breschi et al., *Kilohertz gravitational waves from binary neutron star mergers: numerical-relativity informed postmerger model*, arXiv:2205.09112 [INSPIRE].

[253] T. Dietrich et al., *Matter imprints in waveform models for neutron star binaries: tidal and self-spin effects*, *Phys. Rev. D* **99** (2019) 024029 [arXiv:1804.02235] [INSPIRE].

[254] K. Kiuchi et al., *Sub-radian-accuracy gravitational waves from coalescing binary neutron stars in numerical relativity. II. Systematic study on the equation of state, binary mass, and mass ratio*, *Phys. Rev. D* **101** (2020) 084006 [arXiv:1907.03790] [INSPIRE].

[255] M. Oguri, *Effect of gravitational lensing on the distribution of gravitational waves from distant binary black hole mergers*, *Mon. Not. Roy. Astron. Soc.* **480** (2018) 3842 [arXiv:1807.02584] [INSPIRE].

[256] M.C. Artale et al., *Host galaxies of merging compact objects: mass, star formation rate, metallicity and colours*, *Mon. Not. Roy. Astron. Soc.* **487** (2019) 1675 [arXiv:1903.00083] [INSPIRE].

[257] F. Santoliquido et al., *The cosmic merger rate density of compact objects: impact of star formation, metallicity, initial mass function and binary evolution*, *Mon. Not. Roy. Astron. Soc.* **502** (2021) 4877 [arXiv:2009.03911] [INSPIRE].

[258] M. Mapelli et al., *Hierarchical black hole mergers in young, globular and nuclear star clusters: the effect of metallicity, spin and cluster properties*, *Mon. Not. Roy. Astron. Soc.* **505** (2021) 339 [arXiv:2103.05016] [INSPIRE].

JCAP07(2023)068

[259] T. Regimbau and S.A. Hughes, *Gravitational-wave confusion background from cosmological compact binaries: implications for future terrestrial detectors*, *Phys. Rev. D* **79** (2009) 062002 [arXiv:0901.2958] [INSPIRE].

[260] C. Van Den Broeck, *Astrophysics, cosmology, and fundamental physics with compact binary coalescence and the Einstein Telescope*, *J. Phys. Conf. Ser.* **484** (2014) 012008 [arXiv:1303.7393] [INSPIRE].

[261] A.M. Green and B.J. Kavanagh, *Primordial black holes as a dark matter candidate*, *J. Phys. G* **48** (2021) 043001 [arXiv:2007.10722] [INSPIRE].

[262] B. Carr, K. Kohri, Y. Sendouda and J. Yokoyama, *Constraints on primordial black holes*, *Rept. Prog. Phys.* **84** (2021) 116902 [arXiv:2002.12778] [INSPIRE].

[263] S. Bird et al., *Did LIGO detect dark matter?*, *Phys. Rev. Lett.* **116** (2016) 201301 [arXiv:1603.00464] [INSPIRE].

[264] S. Clesse and J. García-Bellido, *The clustering of massive primordial black holes as dark matter: measuring their mass distribution with advanced LIGO*, *Phys. Dark Univ.* **15** (2017) 142 [arXiv:1603.05234] [INSPIRE].

[265] M. Sasaki, T. Suyama, T. Tanaka and S. Yokoyama, *Primordial black hole scenario for the gravitational-wave event GW150914*, *Phys. Rev. Lett.* **117** (2016) 061101 [*Erratum ibid.* **121** (2018) 059901] [arXiv:1603.08338] [INSPIRE].

[266] S. Wang, Y.-F. Wang, Q.-G. Huang and T.G.F. Li, *Constraints on the primordial black hole abundance from the first advanced LIGO observation run using the stochastic gravitational-wave background*, *Phys. Rev. Lett.* **120** (2018) 191102 [arXiv:1610.08725] [INSPIRE].

[267] Y. Ali-Haïmoud, E.D. Kovetz and M. Kamionkowski, *Merger rate of primordial black-hole binaries*, *Phys. Rev. D* **96** (2017) 123523 [arXiv:1709.06576] [INSPIRE].

[268] Z.-C. Chen and Q.-G. Huang, *Merger rate distribution of primordial-black-hole binaries*, *Astrophys. J.* **864** (2018) 61 [arXiv:1801.10327] [INSPIRE].

[269] M. Raidal, C. Spethmann, V. Vaskonen and H. Veermäe, *Formation and evolution of primordial black hole binaries in the early universe*, *JCAP* **02** (2019) 018 [arXiv:1812.01930] [INSPIRE].

[270] V. Vaskonen and H. Veermäe, *Lower bound on the primordial black hole merger rate*, *Phys. Rev. D* **101** (2020) 043015 [arXiv:1908.09752] [INSPIRE].

[271] V. De Luca, G. Franciolini, P. Pani and A. Riotto, *Primordial black holes confront LIGO/Virgo data: current situation*, *JCAP* **06** (2020) 044 [arXiv:2005.05641] [INSPIRE].

[272] S. Bhagwat et al., *The importance of priors on LIGO-Virgo parameter estimation: the case of primordial black holes*, *JCAP* **01** (2021) 037 [arXiv:2008.12320] [INSPIRE].

[273] A. Hall, A.D. Gow and C.T. Byrnes, *Bayesian analysis of LIGO-Virgo mergers: primordial vs. astrophysical black hole populations*, *Phys. Rev. D* **102** (2020) 123524 [arXiv:2008.13704] [INSPIRE].

[274] V. De Luca, V. Desjacques, G. Franciolini and A. Riotto, *The clustering evolution of primordial black holes*, *JCAP* **11** (2020) 028 [arXiv:2009.04731] [INSPIRE].

[275] K.W.K. Wong et al., *Constraining the primordial black hole scenario with Bayesian inference and machine learning: the GWTC-2 gravitational wave catalog*, *Phys. Rev. D* **103** (2021) 023026 [arXiv:2011.01865] [INSPIRE].

[276] G. Hütsi, M. Raidal, V. Vaskonen and H. Veermäe, *Two populations of LIGO-Virgo black holes*, *JCAP* **03** (2021) 068 [arXiv:2012.02786] [INSPIRE].

JCAP07(2023)068

[277] K. Kritos et al., *The astro-primordial black hole merger rates: a reappraisal*, *JCAP* **05** (2021) 039 [arXiv:2012.03585] [INSPIRE].

[278] H. Deng, *A possible mass distribution of primordial black holes implied by LIGO-Virgo*, *JCAP* **04** (2021) 058 [arXiv:2101.11098] [INSPIRE].

[279] R. Kimura, T. Suyama, M. Yamaguchi and Y.-L. Zhang, *Reconstruction of primordial power spectrum of curvature perturbation from the merger rate of primordial black hole binaries*, *JCAP* **04** (2021) 031 [arXiv:2102.05280] [INSPIRE].

[280] V. De Luca, G. Franciolini, P. Pani and A. Riotto, *Bayesian evidence for both astrophysical and primordial black holes: mapping the GWTC-2 catalog to third-generation detectors*, *JCAP* **05** (2021) 003 [arXiv:2102.03809] [INSPIRE].

[281] Z.-C. Chen, C. Yuan and Q.-G. Huang, *Confronting the primordial black hole scenario with the gravitational-wave events detected by LIGO-Virgo*, *Phys. Lett. B* **829** (2022) 137040 [arXiv:2108.11740] [INSPIRE].

[282] G. Franciolini et al., *Searching for a subpopulation of primordial black holes in LIGO-Virgo gravitational-wave data*, *Phys. Rev. D* **105** (2022) 083526 [arXiv:2105.03349] [INSPIRE].

[283] S. Mukherjee and J. Silk, *Can we distinguish astrophysical from primordial black holes via the stochastic gravitational wave background?*, *Mon. Not. Roy. Astron. Soc.* **506** (2021) 3977 [arXiv:2105.11139] [INSPIRE].

[284] X. Wang, Y.-L. Zhang, R. Kimura and M. Yamaguchi, *Reconstruction of power spectrum of primordial curvature perturbations on small scales from primordial black hole binaries scenario of LIGO/VIRGO detection*, *Sci. China Phys. Mech. Astron.* **66** (2023) 260462 [arXiv:2209.12911] [INSPIRE].

[285] G. Franciolini, K. Kritos, E. Berti and J. Silk, *Primordial black hole mergers from three-body interactions*, *Phys. Rev. D* **106** (2022) 083529 [arXiv:2205.15340] [INSPIRE].

[286] L.-M. Zheng et al., *Towards a reliable reconstruction of the power spectrum of primordial curvature perturbation on small scales from GWTC-3*, *Phys. Lett. B* **838** (2023) 137720 [arXiv:2212.05516] [INSPIRE].

[287] C.T. Byrnes, E.J. Copeland and A.M. Green, *Primordial black holes as a tool for constraining non-Gaussianity*, *Phys. Rev. D* **86** (2012) 043512 [arXiv:1206.4188] [INSPIRE].

[288] P. Boldrini et al., *Cusp-to-core transition in low-mass dwarf galaxies induced by dynamical heating of cold dark matter by primordial black holes*, *Mon. Not. Roy. Astron. Soc.* **492** (2020) 5218 [arXiv:1909.07395] [INSPIRE].

[289] G. Bertone et al., *Primordial black holes as silver bullets for new physics at the weak scale*, *Phys. Rev. D* **100** (2019) 123013 [arXiv:1905.01238] [INSPIRE].

[290] M. Volonteri, *Formation of supermassive black holes*, *Astron. Astrophys. Rev.* **18** (2010) 279 [arXiv:1003.4404] [INSPIRE].

[291] G. Franciolini, I. Musco, P. Pani and A. Urbano, *From inflation to black hole mergers and back again: gravitational-wave data-driven constraints on inflationary scenarios with a first-principle model of primordial black holes across the QCD epoch*, *Phys. Rev. D* **106** (2022) 123526 [arXiv:2209.05959] [INSPIRE].

[292] T. Nakamura et al., *Pre-DECIGO can get the smoking gun to decide the astrophysical or cosmological origin of GW150914-like binary black holes*, *PTEP* **2016** (2016) 093E01 [arXiv:1607.00897] [INSPIRE].

[293] Z.-C. Chen and Q.-G. Huang, *Distinguishing primordial black holes from astrophysical black holes by Einstein Telescope and cosmic explorer*, *JCAP* **08** (2020) 039 [arXiv:1904.02396] [INSPIRE].

JCAP07(2023)068

[294] S.M. Koushiappas and A. Loeb, *Maximum redshift of gravitational wave merger events*, *Phys. Rev. Lett.* **119** (2017) 221104 [arXiv:1708.07380] [INSPIRE].

[295] R. Schneider et al., *Gravitational waves signals from the collapse of the first stars*, *Mon. Not. Roy. Astron. Soc.* **317** (2000) 385 [astro-ph/9909419] [INSPIRE].

[296] R. Schneider, A. Ferrara, P. Natarajan and K. Omukai, *First stars, very massive black holes and metals*, *Astrophys. J.* **571** (2002) 30 [astro-ph/0111341] [INSPIRE].

[297] R. Schneider et al., *Low-mass relics of early star formation*, *Nature* **422** (2003) 869 [astro-ph/0304254] [INSPIRE].

[298] V. Bromm, *High-redshift gamma-ray bursts from Population III progenitors*, *Astrophys. J.* **642** (2006) 382 [astro-ph/0509303] [INSPIRE].

[299] L. Tornatore, S. Borgani, K. Dolag and F. Matteucci, *Chemical enrichment of galaxy clusters from hydrodynamical simulations*, *Mon. Not. Roy. Astron. Soc.* **382** (2007) 1050 [arXiv:0705.1921] [INSPIRE].

[300] M. Trenti and M. Stiavelli, *The formation rates of Population III stars and chemical enrichment of halos during the reionization era*, *Astrophys. J.* **694** (2009) 879 [arXiv:0901.0711] [INSPIRE].

[301] R.S. de Souza, N. Yoshida and K. Ioka, *Population III.1 and III.2 gamma-ray bursts: constraints on the event rate for future radio and X-ray surveys*, *Astron. Astrophys.* **533** (2011) A32 [arXiv:1105.2395] [INSPIRE].

[302] P. Mocz et al., *Galaxy formation with BECDM — II. Cosmic filaments and first galaxies*, *Mon. Not. Roy. Astron. Soc.* **494** (2020) 2027 [arXiv:1911.05746] [INSPIRE].

[303] T. Kinugawa et al., *Possible indirect confirmation of the existence of Pop III massive stars by gravitational wave*, *Mon. Not. Roy. Astron. Soc.* **442** (2014) 2963 [arXiv:1402.6672] [INSPIRE].

[304] K. Inayoshi, R. Hirai, T. Kinugawa and K. Hotokezaka, *Formation pathway of Population III coalescing binary black holes through stable mass transfer*, *Mon. Not. Roy. Astron. Soc.* **468** (2017) 5020 [arXiv:1701.04823] [INSPIRE].

[305] B. Liu and V. Bromm, *The Population III origin of GW*190521, *Astrophys. J. Lett.* **903** (2020) L40 [arXiv:2009.11447] [INSPIRE].

[306] T. Kinugawa, T. Nakamura and H. Nakano, *Chirp mass and spin of binary black holes from first star remnants*, *Mon. Not. Roy. Astron. Soc.* **498** (2020) 3946 [arXiv:2005.09795] [INSPIRE].

[307] A. Tanikawa et al., *Merger rate density of Population III binary black holes below, above, and in the pair-instability mass gap*, *Astrophys. J.* **910** (2021) 30 [arXiv:2008.01890] [INSPIRE].

[308] N. Singh, T. Bulik, K. Belczynski and A. Askar, *Exploring compact binary populations with the Einstein Telescope*, *Astron. Astrophys.* **667** (2022) A2 [arXiv:2112.04058] [INSPIRE].

[309] K.K.Y. Ng et al., *On the single-event-based identification of primordial black hole mergers at cosmological distances*, *Astrophys. J. Lett.* **931** (2022) L12 [arXiv:2108.07276] [INSPIRE].

[310] G. Franciolini et al., *How to assess the primordial origin of single gravitational-wave events with mass, spin, eccentricity, and deformability measurements*, *Phys. Rev. D* **105** (2022) 063510 [arXiv:2112.10660] [INSPIRE].

[311] M. Martinelli et al., *Dancing in the dark: detecting a population of distant primordial black holes*, *JCAP* **08** (2022) 006 [arXiv:2205.02639] [INSPIRE].

[312] K.K.Y. Ng et al., *Measuring properties of primordial black hole mergers at cosmological distances: effect of higher order modes in gravitational waves*, *Phys. Rev. D* **107** (2023) 024041 [arXiv:2210.03132] [INSPIRE].

JCAP07(2023)068

[313] K.K.Y. Ng et al., *Constraining high-redshift stellar-mass primordial black holes with next-generation ground-based gravitational-wave detectors*, *Astrophys. J. Lett.* **933** (2022) L41 [arXiv:2204.11864] [INSPIRE].

[314] V. De Luca, G. Franciolini, P. Pani and A. Riotto, *The evolution of primordial black holes and their final observable spins*, *JCAP* **04** (2020) 052 [arXiv:2003.02778] [INSPIRE].

[315] V. De Luca et al., *The initial spin probability distribution of primordial black holes*, *JCAP* **05** (2019) 018 [arXiv:1903.01179] [INSPIRE].

[316] V. De Luca, G. Franciolini, P. Pani and A. Riotto, *The minimum testable abundance of primordial black holes at future gravitational-wave detectors*, *JCAP* **11** (2021) 039 [arXiv:2106.13769] [INSPIRE].

[317] G. Franciolini et al., *Searching for primordial black holes with the Einstein Telescope: impact of design and systematics*, in preparation (2022).

[318] M. Sasaki, T. Suyama, T. Tanaka and S. Yokoyama, *Primordial black holes — perspectives in gravitational wave astronomy*, *Class. Quant. Grav.* **35** (2018) 063001 [arXiv:1801.05235] [INSPIRE].

[319] S. Clesse and J. Garcia-Bellido, *GW*190425*, GW*190521 *and GW*190814*: three candidate mergers of primordial black holes from the QCD epoch*, *Phys. Dark Univ.* **38** (2022) 101111 [arXiv:2007.06481] [INSPIRE].

[320] V. De Luca et al., *GW*190521 *mass gap event and the primordial black hole scenario*, *Phys. Rev. Lett.* **126** (2021) 051101 [arXiv:2009.01728] [INSPIRE].

[321] G. Franciolini and P. Pani, *Searching for mass-spin correlations in the population of gravitational-wave events: the GWTC-3 case study*, *Phys. Rev. D* **105** (2022) 123024 [arXiv:2201.13098] [INSPIRE].

[322] S. Shandera, D. Jeong and H.S.G. Gebhardt, *Gravitational waves from binary mergers of subsolar mass dark black holes*, *Phys. Rev. Lett.* **120** (2018) 241102 [arXiv:1802.08206] [INSPIRE].

[323] S. Barsanti, V. De Luca, A. Maselli and P. Pani, *Detecting subsolar-mass primordial black holes in extreme mass-ratio inspirals with LISA and Einstein Telescope*, *Phys. Rev. Lett.* **128** (2022) 111104 [arXiv:2109.02170] [INSPIRE].

[324] O. Pujolas, V. Vaskonen and H. Veermäe, *Prospects for probing gravitational waves from primordial black hole binaries*, *Phys. Rev. D* **104** (2021) 083521 [arXiv:2107.03379] [INSPIRE].

[325] H.-K. Guo, K. Sinha and C. Sun, *Probing boson stars with extreme mass ratio inspirals*, *JCAP* **09** (2019) 032 [arXiv:1904.07871] [INSPIRE].

[326] T. Nakamura, M. Sasaki, T. Tanaka and K.S. Thorne, *Gravitational waves from coalescing black hole MACHO binaries*, *Astrophys. J. Lett.* **487** (1997) L139 [astro-ph/9708060] [INSPIRE].

[327] K. Ioka, T. Chiba, T. Tanaka and T. Nakamura, *Black hole binary formation in the expanding universe: three body problem approximation*, *Phys. Rev. D* **58** (1998) 063003 [astro-ph/9807018] [INSPIRE].

[328] I. Mandel and A. Farmer, *Merging stellar-mass binary black holes*, *Phys. Rept.* **955** (2022) 1 [arXiv:1806.05820] [INSPIRE].

[329] M.J. Benacquista and J.M.B. Downing, *Relativistic binaries in globular clusters*, *Living Rev. Rel.* **16** (2013) 4 [arXiv:1110.4423] [INSPIRE].

JCAP07(2023)068

[330] Y.-B. Bae, C. Kim and H.M. Lee, *Compact binaries ejected from globular clusters as gravitational wave sources*, *Mon. Not. Roy. Astron. Soc.* **440** (2014) 2714 [arXiv:1308.1641] [INSPIRE].

[331] C.L. Rodriguez, P. Amaro-Seoane, S. Chatterjee and F.A. Rasio, *Post-Newtonian dynamics in dense star clusters: highly-eccentric, highly-spinning, and repeated binary black hole mergers*, *Phys. Rev. Lett.* **120** (2018) 151101 [arXiv:1712.04937] [INSPIRE].

[332] M. Zevin et al., *Eccentric black hole mergers in dense star clusters: the role of binary-binary encounters*, *Astrophys. J.* **871** (2019) 91 [arXiv:1810.00901] [INSPIRE].

[333] K. Kritos, V. Strokov, V. Baibhav and E. Berti, *Rapster: a fast code for dynamical formation of black-hole binaries in dense star clusters*, arXiv:2210.10055 [INSPIRE].

[334] A. Nishizawa, E. Berti, A. Klein and A. Sesana, *eLISA eccentricity measurements as tracers of binary black hole formation*, *Phys. Rev. D* **94** (2016) 064020 [arXiv:1605.01341] [INSPIRE].

[335] A. Nishizawa, A. Sesana, E. Berti and A. Klein, *Constraining stellar binary black hole formation scenarios with eLISA eccentricity measurements*, *Mon. Not. Roy. Astron. Soc.* **465** (2017) 4375 [arXiv:1606.09295] [INSPIRE].

[336] M. Zevin et al., *Implications of eccentric observations on binary black hole formation channels*, *Astrophys. J. Lett.* **921** (2021) L43 [arXiv:2106.09042] [INSPIRE].

[337] M. Favata et al., *Constraining the orbital eccentricity of inspiralling compact binary systems with advanced LIGO*, *Phys. Rev. D* **105** (2022) 023003 [arXiv:2108.05861] [INSPIRE].

[338] A. Buonanno et al., *Comparison of post-Newtonian templates for compact binary inspiral signals in gravitational-wave detectors*, *Phys. Rev. D* **80** (2009) 084043 [arXiv:0907.0700] [INSPIRE].

[339] P. Ajith, *Addressing the spin question in gravitational-wave searches: waveform templates for inspiralling compact binaries with nonprecessing spins*, *Phys. Rev. D* **84** (2011) 084037 [arXiv:1107.1267] [INSPIRE].

[340] C.K. Mishra, A. Kela, K.G. Arun and G. Faye, *Ready-to-use post-Newtonian gravitational waveforms for binary black holes with nonprecessing spins: an update*, *Phys. Rev. D* **93** (2016) 084054 [arXiv:1601.05588] [INSPIRE].

[341] B. Moore, M. Favata, K.G. Arun and C.K. Mishra, *Gravitational-wave phasing for low-eccentricity inspiralling compact binaries to 3PN order*, *Phys. Rev. D* **93** (2016) 124061 [arXiv:1605.00304] [INSPIRE].

[342] B.F. Schutz, *Determining the Hubble constant from gravitational wave observations*, *Nature* **323** (1986) 310 [INSPIRE].

[343] D.E. Holz and S.A. Hughes, *Using gravitational-wave standard sirens*, *Astrophys. J.* **629** (2005) 15 [astro-ph/0504616] [INSPIRE].

[344] N. Dalal, D.E. Holz, S.A. Hughes and B. Jain, *Short GRB and binary black hole standard sirens as a probe of dark energy*, *Phys. Rev. D* **74** (2006) 063006 [astro-ph/0601275] [INSPIRE].

[345] C.L. MacLeod and C.J. Hogan, *Precision of Hubble constant derived using black hole binary absolute distances and statistical redshift information*, *Phys. Rev. D* **77** (2008) 043512 [arXiv:0712.0618] [INSPIRE].

[346] S. Nissanke et al., *Exploring short gamma-ray bursts as gravitational-wave standard sirens*, *Astrophys. J.* **725** (2010) 496 [arXiv:0904.1017] [INSPIRE].

[347] C. Cutler and D.E. Holz, *Ultra-high precision cosmology from gravitational waves*, *Phys. Rev. D* **80** (2009) 104009 [arXiv:0906.3752] [INSPIRE].

JCAP07(2023)068

[348] C. Messenger and J. Read, *Measuring a cosmological distance-redshift relationship using only gravitational wave observations of binary neutron star coalescences*, *Phys. Rev. Lett.* **108** (2012) 091101 [arXiv:1107.5725] [INSPIRE].

[349] S.R. Taylor, J.R. Gair and I. Mandel, *Hubble without the Hubble: cosmology using advanced gravitational-wave detectors alone*, *Phys. Rev. D* **85** (2012) 023535 [arXiv:1108.5161] [INSPIRE].

[350] S.R. Taylor and J.R. Gair, *Cosmology with the lights off: standard sirens in the Einstein Telescope era*, *Phys. Rev. D* **86** (2012) 023502 [arXiv:1204.6739] [INSPIRE].

[351] W. Del Pozzo, T.G.F. Li and C. Messenger, *Cosmological inference using only gravitational wave observations of binary neutron stars*, *Phys. Rev. D* **95** (2017) 043502 [arXiv:1506.06590] [INSPIRE].

[352] H.-Y. Chen, M. Fishbach and D.E. Holz, *A two per cent Hubble constant measurement from standard sirens within five years*, *Nature* **562** (2018) 545 [arXiv:1712.06531] [INSPIRE].

[353] S.M. Feeney et al., *Prospects for resolving the Hubble constant tension with standard sirens*, *Phys. Rev. Lett.* **122** (2019) 061105 [arXiv:1802.03404] [INSPIRE].

[354] R. Gray et al., *Cosmological inference using gravitational wave standard sirens: a mock data analysis*, *Phys. Rev. D* **101** (2020) 122001 [arXiv:1908.06050] [INSPIRE].

[355] W.M. Farr, M. Fishbach, J. Ye and D. Holz, *A future percent-level measurement of the Hubble expansion at redshift* 0.8 *with advanced LIGO*, *Astrophys. J. Lett.* **883** (2019) L42 [arXiv:1908.09084] [INSPIRE].

[356] O.A. Hannuksela, T.E. Collett, M. Çalışkan and T.G.F. Li, *Localizing merging black holes with sub-arcsecond precision using gravitational-wave lensing*, *Mon. Not. Roy. Astron. Soc.* **498** (2020) 3395 [arXiv:2004.13811] [INSPIRE].

[357] B. Wang, Z. Zhu, A. Li and W. Zhao, *Comprehensive analysis of the tidal effect in gravitational waves and implication for cosmology*, *Astrophys. J. Suppl.* **250** (2020) 6 [arXiv:2005.12875] [INSPIRE].

[358] S. Mukherjee, B.D. Wandelt, S.M. Nissanke and A. Silvestri, *Accurate precision cosmology with redshift unknown gravitational wave sources*, *Phys. Rev. D* **103** (2021) 043520 [arXiv:2007.02943] [INSPIRE].

[359] A. Finke et al., *Cosmology with LIGO/Virgo dark sirens: Hubble parameter and modified gravitational wave propagation*, *JCAP* **08** (2021) 026 [arXiv:2101.12660] [INSPIRE].

[360] C. Ye and M. Fishbach, *Cosmology with standard sirens at cosmic noon*, *Phys. Rev. D* **104** (2021) 043507 [arXiv:2103.14038] [INSPIRE].

[361] D. Chatterjee et al., *Cosmology with love: measuring the Hubble constant using neutron star universal relations*, *Phys. Rev. D* **104** (2021) 083528 [arXiv:2106.06589] [INSPIRE].

[362] A. Finke et al., *Probing modified gravitational wave propagation with strongly lensed coalescing binaries*, *Phys. Rev. D* **104** (2021) 084057 [arXiv:2107.05046] [INSPIRE].

[363] A. Finke et al., *Modified gravitational wave propagation and the binary neutron star mass function*, *Phys. Dark Univ.* **36** (2022) 100994 [arXiv:2108.04065] [INSPIRE].

[364] A. Palmese, C.R. Bom, S. Mucesh and W.G. Hartley, *A standard siren measurement of the Hubble constant using gravitational-wave events from the first three LIGO/Virgo observing runs and the DESI legacy survey*, *Astrophys. J.* **943** (2023) 56 [arXiv:2111.06445] [INSPIRE].

[365] M. Mancarella, E. Genoud-Prachex and M. Maggiore, *Cosmology and modified gravitational wave propagation from binary black hole population models*, *Phys. Rev. D* **105** (2022) 064030 [arXiv:2112.05728] [INSPIRE].

JCAP07(2023)068

[366] S.-J. Jin, T.-N. Li, J.-F. Zhang and X. Zhang, *Precisely measuring the Hubble constant and dark energy using only gravitational-wave dark sirens*, arXiv:2202.11882 [INSPIRE].

[367] S. Mukherjee, A. Krolewski, B.D. Wandelt and J. Silk, *Cross-correlating dark sirens and galaxies: measurement of H_0 from GWTC-3 of LIGO-Virgo-KAGRA*, arXiv:2203.03643 [INSPIRE].

[368] T. Ghosh, B. Biswas and S. Bose, *Simultaneous inference of neutron star equation of state and the Hubble constant with a population of merging neutron stars*, *Phys. Rev. D* **106** (2022) 123529 [arXiv:2203.11756] [INSPIRE].

[369] B. Shiralilou et al., *Measuring Hubble constant with dark neutron star-black hole mergers*, arXiv:2207.11792 [INSPIRE].

[370] M. Mancarella et al., *Gravitational-wave cosmology with dark sirens: state of the art and perspectives for 3G detectors*, *PoS* **ICHEP2022** (2022) 127 [arXiv:2211.15512] [INSPIRE].

[371] J.R. Gair et al., *The hitchhiker's guide to the galaxy catalog approach for dark siren gravitational-wave cosmology*, *Astron. J.* **166** (2023) 22 [arXiv:2212.08694] [INSPIRE].

[372] E. Belgacem et al., *Cosmology and dark energy from joint gravitational wave-GRB observations*, *JCAP* **08** (2019) 015 [arXiv:1907.01487] [INSPIRE].

[373] LIGO Scientific and Virgo collaborations, *A standard siren measurement of the Hubble constant from GW170817 without the electromagnetic counterpart*, *Astrophys. J. Lett.* **871** (2019) L13 [arXiv:1807.05667] [INSPIRE].

[374] DES et al. collaborations, *First measurement of the Hubble constant from a dark standard siren using the dark energy survey galaxies and the LIGO/Virgo binary-black-hole merger GW170814*, *Astrophys. J. Lett.* **876** (2019) L7 [arXiv:1901.01540] [INSPIRE].

[375] LIGO Scientific et al. collaborations, *A gravitational-wave measurement of the Hubble constant following the second observing run of advanced LIGO and Virgo*, *Astrophys. J.* **909** (2021) 218 [arXiv:1908.06060] [INSPIRE].

[376] DES collaboration, *A statistical standard siren measurement of the Hubble constant from the LIGO/Virgo gravitational wave compact object merger GW190814 and dark energy survey galaxies*, *Astrophys. J. Lett.* **900** (2020) L33 [arXiv:2006.14961] [INSPIRE].

[377] J.M. Ezquiaga, *Hearing gravity from the cosmos: GWTC-2 probes general relativity at cosmological scales*, *Phys. Lett. B* **822** (2021) 136665 [arXiv:2104.05139] [INSPIRE].

[378] K. Leyde et al., *Current and future constraints on cosmology and modified gravitational wave friction from binary black holes*, *JCAP* **09** (2022) 012 [arXiv:2202.00025] [INSPIRE].

[379] A. Balaudo et al., *Prospects of testing late-time cosmology with weak lensing of gravitational waves and galaxy surveys*, *JCAP* **06** (2023) 050 [arXiv:2210.06398] [INSPIRE].

[380] B.S. Sathyaprakash, B.F. Schutz and C. Van Den Broeck, *Cosmography with the Einstein Telescope*, *Class. Quant. Grav.* **27** (2010) 215006 [arXiv:0906.4151] [INSPIRE].

[381] W. Zhao, C. Van Den Broeck, D. Baskaran and T.G.F. Li, *Determination of dark energy by the Einstein Telescope: comparing with CMB, BAO and SNIa observations*, *Phys. Rev. D* **83** (2011) 023005 [arXiv:1009.0206] [INSPIRE].

[382] M. Kalomenopoulos, S. Khochfar, J. Gair and S. Arai, *Mapping the inhomogeneous universe with standard sirens: degeneracy between inhomogeneity and modified gravity theories*, *Mon. Not. Roy. Astron. Soc.* **503** (2021) 3179 [arXiv:2007.15020] [INSPIRE].

[383] Planck collaboration, *Planck 2018 results. VI. Cosmological parameters*, *Astron. Astrophys.* **641** (2020) A6 [*Erratum ibid.* **652** (2021) C4] [arXiv:1807.06209] [INSPIRE].

[384] LIGO Scientific et al. collaborations, *A gravitational-wave standard siren measurement of the Hubble constant*, *Nature* **551** (2017) 85 [arXiv:1710.05835] [INSPIRE].

JCAP07(2023)068

[385] A.G. Riess et al., *Large Magellanic Cloud Cepheid standards provide a 1% foundation for the determination of the Hubble constant and stronger evidence for physics beyond ΛCDM*, *Astrophys. J.* **876** (2019) 85 [arXiv:1903.07603] [INSPIRE].

[386] K.C. Wong et al., *H0LiCOW — XIII. A 2.4 per cent measurement of H_0 from lensed quasars: 5.3σ tension between early- and late-universe probes*, *Mon. Not. Roy. Astron. Soc.* **498** (2020) 1420 [arXiv:1907.04869] [INSPIRE].

[387] PLANCK collaboration, *Planck 2018 results. VI. Cosmological parameters*, *Astron. Astrophys.* **641** (2020) A6 [*Erratum ibid.* **652** (2021) C4] [arXiv:1807.06209] [INSPIRE].

[388] DES collaboration, *Dark Energy Survey year 1 results: constraints on extended cosmological models from galaxy clustering and weak lensing*, *Phys. Rev. D* **99** (2019) 123505 [arXiv:1810.02499] [INSPIRE].

[389] M. Chevallier and D. Polarski, *Accelerating universes with scaling dark matter*, *Int. J. Mod. Phys. D* **10** (2001) 213 [gr-qc/0009008] [INSPIRE].

[390] E.V. Linder, *Exploring the expansion history of the universe*, *Phys. Rev. Lett.* **90** (2003) 091301 [astro-ph/0208512] [INSPIRE].

[391] E. Belgacem, Y. Dirian, S. Foffa and M. Maggiore, *Modified gravitational-wave propagation and standard sirens*, *Phys. Rev. D* **98** (2018) 023510 [arXiv:1805.08731] [INSPIRE].

[392] E. Belgacem, Y. Dirian, S. Foffa and M. Maggiore, *Gravitational-wave luminosity distance in modified gravity theories*, *Phys. Rev. D* **97** (2018) 104066 [arXiv:1712.08108] [INSPIRE].

[393] M. Maggiore, *Phantom dark energy from nonlocal infrared modifications of general relativity*, *Phys. Rev. D* **89** (2014) 043008 [arXiv:1307.3898] [INSPIRE].

[394] E. Belgacem et al., *Nonlocal gravity and gravitational-wave observations*, *JCAP* **11** (2019) 022 [arXiv:1907.02047] [INSPIRE].

[395] E. Belgacem et al., *Gravity in the infrared and effective nonlocal models*, *JCAP* **04** (2020) 010 [arXiv:2001.07619] [INSPIRE].

[396] I.D. Saltas, I. Sawicki, L. Amendola and M. Kunz, *Anisotropic stress as a signature of nonstandard propagation of gravitational waves*, *Phys. Rev. Lett.* **113** (2014) 191101 [arXiv:1406.7139] [INSPIRE].

[397] L. Lombriser and A. Taylor, *Breaking a dark degeneracy with gravitational waves*, *JCAP* **03** (2016) 031 [arXiv:1509.08458] [INSPIRE].

[398] L. Amendola, I. Sawicki, M. Kunz and I.D. Saltas, *Direct detection of gravitational waves can measure the time variation of the Planck mass*, *JCAP* **08** (2018) 030 [arXiv:1712.08623] [INSPIRE].

[399] A. Nishizawa, *Generalized framework for testing gravity with gravitational-wave propagation. I. Formulation*, *Phys. Rev. D* **97** (2018) 104037 [arXiv:1710.04825] [INSPIRE].

[400] S. Arai and A. Nishizawa, *Generalized framework for testing gravity with gravitational-wave propagation. II. Constraints on Horndeski theory*, *Phys. Rev. D* **97** (2018) 104038 [arXiv:1711.03776] [INSPIRE].

[401] A. Nishizawa and S. Arai, *Generalized framework for testing gravity with gravitational-wave propagation. III. Future prospect*, *Phys. Rev. D* **99** (2019) 104038 [arXiv:1901.08249] [INSPIRE].

[402] LISA COSMOLOGY WORKING GROUP collaboration, *Testing modified gravity at cosmological distances with LISA standard sirens*, *JCAP* **07** (2019) 024 [arXiv:1906.01593] [INSPIRE].

[403] M. Maggiore, *Gravitational waves. Volume 1: theory and experiments*, Oxford University Press, Oxford, U.K. (2007) [DOI:10.1093/acprof:oso/9780198570745.001.0001] [INSPIRE].

JCAP07(2023)068

[404] E. Belgacem, S. Foffa, M. Maggiore and T. Yang, *Gaussian processes reconstruction of modified gravitational wave propagation*, *Phys. Rev. D* **101** (2020) 063505 [arXiv:1911.11497] [INSPIRE].

[405] M. Maggiore, *Nonlocal infrared modifications of gravity. A review*, *Fundam. Theor. Phys.* **187** (2017) 221 [arXiv:1606.08784] [INSPIRE].

[406] S. Mastrogiovanni et al., *Gravitational wave friction in light of GW170817 and GW190521*, *JCAP* **02** (2021) 043 [arXiv:2010.04047] [INSPIRE].

[407] C. Messenger et al., *Source redshifts from gravitational-wave observations of binary neutron star mergers*, *Phys. Rev. X* **4** (2014) 041004 [arXiv:1312.1862] [INSPIRE].

[408] T.G.F. Li, W. Del Pozzo and C. Messenger, *Measuring the redshift of standard sirens using the neutron star deformability*, in the proceedings of the 13th *Marcel Grossmann meeting on recent developments in theoretical and experimental general relativity, astrophysics and relativistic field theories*, (2015), p. 2019 [DOI:10.1142/9789814623995_0346] [arXiv:1303.0855] [INSPIRE].

[409] A.F. Heavens et al., *Generalized Fisher matrices*, *Mon. Not. Roy. Astron. Soc.* **445** (2014) 1687 [arXiv:1404.2854] [INSPIRE].

[410] P. Ajith and S. Bose, *Estimating the parameters of non-spinning binary black holes using ground-based gravitational-wave detectors: statistical errors*, *Phys. Rev. D* **79** (2009) 084032 [arXiv:0901.4936] [INSPIRE].

[411] S. Borhanian et al., *Dark sirens to resolve the Hubble-Lemaître tension*, *Astrophys. J. Lett.* **905** (2020) L28 [arXiv:2007.02883] [INSPIRE].

[412] L.P. Singer et al., *Going the distance: mapping host galaxies of LIGO and Virgo sources in three dimensions using local cosmography and targeted follow-up*, *Astrophys. J. Lett.* **829** (2016) L15 [arXiv:1603.07333] [INSPIRE].

[413] A.G. Riess et al., *A comprehensive measurement of the local value of the Hubble constant with* $1\,km\,s^{-1}\,Mpc^{-1}$ *uncertainty from the Hubble Space Telescope and the SH0ES team*, *Astrophys. J. Lett.* **934** (2022) L7 [arXiv:2112.04510] [INSPIRE].

[414] C.J. Krüger and F. Foucart, *Estimates for disk and ejecta masses produced in compact binary mergers*, *Phys. Rev. D* **101** (2020) 103002 [arXiv:2002.07728] [INSPIRE].

[415] G. Raaijmakers et al., *The challenges ahead for multimessenger analyses of gravitational waves and kilonova: a case study on GW190425*, *Astrophys. J.* **922** (2021) 269 [arXiv:2102.11569] [INSPIRE].

[416] R. Jeannerot, J. Rocher and M. Sakellariadou, *How generic is cosmic string formation in SUSY GUTs*, *Phys. Rev. D* **68** (2003) 103514 [hep-ph/0308134] [INSPIRE].

[417] T. Damour and A. Vilenkin, *Gravitational wave bursts from cosmic strings*, *Phys. Rev. Lett.* **85** (2000) 3761 [gr-qc/0004075] [INSPIRE].

[418] LIGO Scientific et al. collaborations, *Constraints on cosmic strings using data from the third advanced LIGO-Virgo observing run*, *Phys. Rev. Lett.* **126** (2021) 241102 [arXiv:2101.12248] [INSPIRE].

[419] J.J. Blanco-Pillado, K.D. Olum and B. Shlaer, *The number of cosmic string loops*, *Phys. Rev. D* **89** (2014) 023512 [arXiv:1309.6637] [INSPIRE].

[420] L. Lorenz, C. Ringeval and M. Sakellariadou, *Cosmic string loop distribution on all length scales and at any redshift*, *JCAP* **10** (2010) 003 [arXiv:1006.0931] [INSPIRE].

[421] A. Kosowsky, M.S. Turner and R. Watkins, *Gravitational radiation from colliding vacuum bubbles*, *Phys. Rev. D* **45** (1992) 4514 [INSPIRE].

[422] A. Mazumdar and G. White, *Review of cosmic phase transitions: their significance and experimental signatures*, *Rept. Prog. Phys.* **82** (2019) 076901 [arXiv:1811.01948] [INSPIRE].

JCAP07(2023)068

[423] M.B. Hindmarsh, M. Lüben, J. Lumma and M. Pauly, *Phase transitions in the early universe*, *SciPost Phys. Lect. Notes* **24** (2021) 1 [arXiv:2008.09136] [INSPIRE].

[424] C. Caprini et al., *Science with the space-based interferometer eLISA. II: gravitational waves from cosmological phase transitions*, *JCAP* **04** (2016) 001 [arXiv:1512.06239] [INSPIRE].

[425] J. Ellis, M. Lewicki, J.M. No and V. Vaskonen, *Gravitational wave energy budget in strongly supercooled phase transitions*, *JCAP* **06** (2019) 024 [arXiv:1903.09642] [INSPIRE].

[426] L. Delle Rose, G. Panico, M. Redi and A. Tesi, *Gravitational waves from supercool axions*, *JHEP* **04** (2020) 025 [arXiv:1912.06139] [INSPIRE].

[427] B. Zhou et al., *Compact binary foreground subtraction in next-generation ground-based observatories*, arXiv:2209.01221 [INSPIRE].

[428] B. Zhou et al., *Subtracting compact binary foregrounds to search for subdominant gravitational-wave backgrounds in next-generation ground-based observatories*, arXiv:2209.01310 [INSPIRE].

[429] K. Martinovic, P.M. Meyers, M. Sakellariadou and N. Christensen, *Simultaneous estimation of astrophysical and cosmological stochastic gravitational-wave backgrounds with terrestrial detectors*, *Phys. Rev. D* **103** (2021) 043023 [arXiv:2011.05697] [INSPIRE].

[430] K. Riles, *Searches for continuous-wave gravitational radiation*, *Living Rev. Rel.* **26** (2023) 3 [arXiv:2206.06447] [INSPIRE].

[431] O.J. Piccinni, *Status and perspectives of continuous gravitational wave searches*, *Galaxies* **10** (2022) 72 [arXiv:2202.01088] [INSPIRE].

[432] R. Tenorio, D. Keitel and A.M. Sintes, *Search methods for continuous gravitational-wave signals from unknown sources in the advanced-detector era*, *Universe* **7** (2021) 474 [arXiv:2111.12575] [INSPIRE].

[433] C. Palomba, *Gravitational radiation from young magnetars: preliminary results*, *Astron. Astrophys.* **367** (2001) 525.

[434] L. Stella, S. Dall'Osso, G.L. Israel and A. Vecchio, *Gravitational radiation from newborn magnetars*, *Astrophys. J. Lett.* **634** (2005) L165 [astro-ph/0511068] [INSPIRE].

[435] S.K. Lander and D.I. Jones, *Magnetar birth: rotation rates and gravitational-wave emission*, *Mon. Not. Roy. Astron. Soc.* **494** (2020) 4838 [arXiv:1910.14336] [INSPIRE].

[436] S. Dall'Osso and L. Stella, *Millisecond magnetars*, *Astrophys. Space Sci. Libr.* **465** (2021) 245 [arXiv:2103.10878] [INSPIRE].

[437] G. Bertone et al., *Gravitational wave probes of dark matter: challenges and opportunities*, *SciPost Phys. Core* **3** (2020) 007 [arXiv:1907.10610] [INSPIRE].

[438] R. Brito, V. Cardoso and P. Pani, *Superradiance: new frontiers in black hole physics*, *Lect. Notes Phys.* **906** (2015) 1 [arXiv:1501.06570] [INSPIRE].

[439] A. Pierce, K. Riles and Y. Zhao, *Searching for dark photon dark matter with gravitational wave detectors*, *Phys. Rev. Lett.* **121** (2018) 061102 [arXiv:1801.10161] [INSPIRE].

[440] A.L. Miller et al., *Probing planetary-mass primordial black holes with continuous gravitational waves*, *Phys. Dark Univ.* **32** (2021) 100836 [arXiv:2012.12983] [INSPIRE].

[441] C.M. Will, *The confrontation between general relativity and experiment*, *Living Rev. Rel.* **17** (2014) 4 [arXiv:1403.7377] [INSPIRE].

[442] LIGO Scientific et al. collaborations, *Searches for gravitational waves from known pulsars at two harmonics in the second and third LIGO-Virgo observing runs*, *Astrophys. J.* **935** (2022) 1 [arXiv:2111.13106] [INSPIRE].

JCAP07(2023)068

[443] KAGRA et al. collaborations, *All-sky search for continuous gravitational waves from isolated neutron stars using advanced LIGO and advanced Virgo O3 data*, *Phys. Rev. D* **106** (2022) 102008 [arXiv:2201.00697] [INSPIRE].

[444] LIGO SCIENTIFIC et al. collaborations, *Narrowband searches for continuous and long-duration transient gravitational waves from known pulsars in the LIGO-Virgo third observing run*, *Astrophys. J.* **932** (2022) 133 [arXiv:2112.10990] [INSPIRE].

[445] LIGO SCIENTIFIC et al. collaborations, *Searches for continuous gravitational waves from young supernova remnants in the early third observing run of advanced LIGO and Virgo*, *Astrophys. J.* **921** (2021) 80 [arXiv:2105.11641] [INSPIRE].

[446] KAGRA et al. collaborations, *Search for continuous gravitational wave emission from the Milky Way center in O3 LIGO-Virgo data*, *Phys. Rev. D* **106** (2022) 042003 [arXiv:2204.04523] [INSPIRE].

[447] J.A. Morales and C.J. Horowitz, *Neutron star crust can support a large ellipticity*, *Mon. Not. Roy. Astron. Soc.* **517** (2022) 5610 [arXiv:2209.03222] [INSPIRE].

[448] G. Woan et al., *Evidence for a minimum ellipticity in millisecond pulsars*, *Astrophys. J. Lett.* **863** (2018) L40 [arXiv:1806.02822] [INSPIRE].

[449] J. Soldateschi and N. Bucciantini, *Detectability of continuous gravitational waves from magnetically deformed neutron stars*, *Galaxies* **9** (2021) 101 [arXiv:2110.06039] [INSPIRE].

[450] P. Astone et al., *Method for all-sky searches of continuous gravitational wave signals using the frequency-Hough transform*, *Phys. Rev. D* **90** (2014) 042002 [arXiv:1407.8333] [INSPIRE].

[451] KAGRA et al. collaborations, *Search for gravitational waves from Scorpius X-1 with a hidden Markov model in O3 LIGO data*, *Phys. Rev. D* **106** (2022) 062002 [arXiv:2201.10104] [INSPIRE].

[452] LIGO SCIENTIFIC et al. collaborations, *All-sky search for gravitational wave emission from scalar boson clouds around spinning black holes in LIGO O3 data*, *Phys. Rev. D* **105** (2022) 102001 [arXiv:2111.15507] [INSPIRE].

[453] C.D. Bochenek, V. Ravi and D. Dong, *Localized FRBs are consistent with magnetar progenitors formed in core-collapse supernovae*, *Astrophys. J.* **907** (2021) L31 [arXiv:2009.13030] [INSPIRE].

[454] N. Jordana-Mitjans et al., *A short gamma-ray burst from a protomagnetar remnant*, *Astrophys. J.* **939** (2022) 106 [arXiv:2211.05810] [INSPIRE].

[455] B. Margalit and B.D. Metzger, *Constraining the maximum mass of neutron stars from multi-messenger observations of GW*170817, *Astrophys. J. Lett.* **850** (2017) L19 [arXiv:1710.05938] [INSPIRE].

[456] A. Bauswein, O. Just, H.-T. Janka and N. Stergioulas, *Neutron-star radius constraints from GW*170817 *and future detections*, *Astrophys. J. Lett.* **850** (2017) L34 [arXiv:1710.06843] [INSPIRE].

[457] L. Rezzolla, E.R. Most and L.R. Weih, *Using gravitational-wave observations and quasi-universal relations to constrain the maximum mass of neutron stars*, *Astrophys. J. Lett.* **852** (2018) L25 [arXiv:1711.00314] [INSPIRE].

[458] D. Radice, A. Perego, F. Zappa and S. Bernuzzi, *GW*170817*: joint constraint on the neutron star equation of state from multimessenger observations*, *Astrophys. J. Lett.* **852** (2018) L29 [arXiv:1711.03647] [INSPIRE].

[459] LIGO SCIENTIFIC and VIRGO collaborations, *GW*170814*: a three-detector observation of gravitational waves from a binary black hole coalescence*, *Phys. Rev. Lett.* **119** (2017) 141101 [arXiv:1709.09660] [INSPIRE].

JCAP07(2023)068

[460] LIGO Scientific and Virgo collaborations, *GW*170817*: measurements of neutron star radii and equation of state*, *Phys. Rev. Lett.* **121** (2018) 161101 [arXiv:1805.11581] [INSPIRE].

[461] D. Kasen et al., *Origin of the heavy elements in binary neutron-star mergers from a gravitational wave event*, *Nature* **551** (2017) 80 [arXiv:1710.05463] [INSPIRE].

[462] J. Granot, D. Guetta and R. Gill, *Lessons from the short GRB* 170817*A: the first gravitational-wave detection of a binary neutron star merger*, *Astrophys. J. Lett.* **850** (2017) L24 [arXiv:1710.06407] [INSPIRE].

[463] J. Granot, R. Gill, D. Guetta and F. De Colle, *Off-axis emission of short GRB jets from double neutron star mergers and GRB* 170817*A*, *Mon. Not. Roy. Astron. Soc.* **481** (2018) 1597 [arXiv:1710.06421] [INSPIRE].

[464] D. Pooley, P. Kumar, J.C. Wheeler and B. Grossan, *GW*170817 *most likely made a black hole*, *Astrophys. J. Lett.* **859** (2018) L23 [arXiv:1712.03240] [INSPIRE].

[465] T. Matsumoto, K. Ioka, S. Kisaka and E. Nakar, *Is the macronova in GW*170817 *powered by the central engine?*, *Astrophys. J.* **861** (2018) 55 [arXiv:1802.07732] [INSPIRE].

[466] Y.-W. Yu, L.-D. Liu and Z.-G. Dai, *A long-lived remnant neutron star after GW*170817 *inferred from its associated kilonova*, *Astrophys. J.* **861** (2018) 114 [arXiv:1711.01898] [INSPIRE].

[467] S. Ai et al., *The allowed parameter space of a long-lived neutron star as the merger remnant of GW*170817, *Astrophys. J.* **860** (2018) 57 [arXiv:1802.00571] [INSPIRE].

[468] J.-J. Geng et al., *Brightening X-ray/optical/radio emission of GW*170817*/SGRB* 170817*A: evidence for an electron-positron wind from the central engine?*, *Astrophys. J. Lett.* **856** (2018) L33 [arXiv:1803.07219] [INSPIRE].

[469] S.-Z. Li, L.-D. Liu, Y.-W. Yu and B. Zhang, *What powered the optical transient AT*2017*gfo associated with GW*170817*?*, *Astrophys. J. Lett.* **861** (2018) L12 [arXiv:1804.06597] [INSPIRE].

[470] LIGO Scientific and Virgo collaborations, *Search for post-merger gravitational waves from the remnant of the binary neutron star merger GW*170817, *Astrophys. J. Lett.* **851** (2017) L16 [arXiv:1710.09320] [INSPIRE].

[471] LIGO Scientific and Virgo collaborations, *Search for gravitational waves from a long-lived remnant of the binary neutron star merger GW*170817, *Astrophys. J.* **875** (2019) 160 [arXiv:1810.02581] [INSPIRE].

[472] E. Thrane et al., *Long gravitational-wave transients and associated detection strategies for a network of terrestrial interferometers*, *Phys. Rev. D* **83** (2011) 083004 [arXiv:1012.2150] [INSPIRE].

[473] A. Mytidis et al., *Sensitivity study using machine learning algorithms on simulated r-mode gravitational wave signals from newborn neutron stars*, *Phys. Rev. D* **99** (2019) 024024 [arXiv:1508.02064] [INSPIRE].

[474] A. Miller et al., *Method to search for long duration gravitational wave transients from isolated neutron stars using the generalized frequency-Hough transform*, *Phys. Rev. D* **98** (2018) 102004 [arXiv:1810.09784] [INSPIRE].

[475] L. Sun and A. Melatos, *Application of hidden Markov model tracking to the search for long-duration transient gravitational waves from the remnant of the binary neutron star merger GW*170817, *Phys. Rev. D* **99** (2019) 123003 [arXiv:1810.03577] [INSPIRE].

[476] M. Oliver, D. Keitel and A.M. Sintes, *Adaptive transient Hough method for long-duration gravitational wave transients*, *Phys. Rev. D* **99** (2019) 104067 [arXiv:1901.01820] [INSPIRE].

JCAP07(2023)068

[477] A.L. Miller et al., *How effective is machine learning to detect long transient gravitational waves from neutron stars in a real search?*, *Phys. Rev. D* **100** (2019) 062005 [arXiv:1909.02262] [INSPIRE].

[478] S. Dall'Osso, L. Stella and C. Palomba, *Neutron star bulk viscosity, "spin-flip" and GW emission of newly born magnetars*, *Mon. Not. Roy. Astron. Soc.* **480** (2018) 1353 [arXiv:1806.11164] [INSPIRE].

[479] K. Gill et al., *Prospects for gravitational wave searches for core-collapse supernovae within the local universe*, *APS April Meeting Abstracts* **2017** (2017) C3001.

[480] C. Kouveliotou et al., *An X-ray pulsar with a superstrong magnetic field in the soft gamma-ray repeater SGR* 1806-20, *Nature* **393** (1998) 235 [INSPIRE].

[481] P. Beniamini, K. Hotokezaka, A. van der Horst and C. Kouveliotou, *Formation rates and evolution histories of magnetars*, *Mon. Not. Roy. Astron. Soc.* **487** (2019) 1426 [arXiv:1903.06718] [INSPIRE].

[482] G. Bertone and D. Hooper, *History of dark matter*, *Rev. Mod. Phys.* **90** (2018) 045002 [arXiv:1605.04909] [INSPIRE].

[483] S. D'Antonio et al., *Semicoherent analysis method to search for continuous gravitational waves emitted by ultralight boson clouds around spinning black holes*, *Phys. Rev. D* **98** (2018) 103017 [arXiv:1809.07202] [INSPIRE].

[484] R.D. Peccei and H.R. Quinn, *CP conservation in the presence of instantons*, *Phys. Rev. Lett.* **38** (1977) 1440 [INSPIRE].

[485] A. Arvanitaki et al., *String axiverse*, *Phys. Rev. D* **81** (2010) 123530 [arXiv:0905.4720] [INSPIRE].

[486] A. Arvanitaki and S. Dubovsky, *Exploring the string axiverse with precision black hole physics*, *Phys. Rev. D* **83** (2011) 044026 [arXiv:1004.3558] [INSPIRE].

[487] A. Arvanitaki, M. Baryakhtar and X. Huang, *Discovering the QCD axion with black holes and gravitational waves*, *Phys. Rev. D* **91** (2015) 084011 [arXiv:1411.2263] [INSPIRE].

[488] M. Baryakhtar, R. Lasenby and M. Teo, *Black hole superradiance signatures of ultralight vectors*, *Phys. Rev. D* **96** (2017) 035019 [arXiv:1704.05081] [INSPIRE].

[489] M. Isi, L. Sun, R. Brito and A. Melatos, *Directed searches for gravitational waves from ultralight bosons*, *Phys. Rev. D* **99** (2019) 084042 [*Erratum ibid.* **102** (2020) 049901] [arXiv:1810.03812] [INSPIRE].

[490] M. Baryakhtar, M. Galanis, R. Lasenby and O. Simon, *Black hole superradiance of self-interacting scalar fields*, *Phys. Rev. D* **103** (2021) 095019 [arXiv:2011.11646] [INSPIRE].

[491] C. Palomba et al., *Direct constraints on ultra-light boson mass from searches for continuous gravitational waves*, *Phys. Rev. Lett.* **123** (2019) 171101 [arXiv:1909.08854] [INSPIRE].

[492] L. Sun, R. Brito and M. Isi, *Search for ultralight bosons in Cygnus X-1 with advanced LIGO*, *Phys. Rev. D* **101** (2020) 063020 [*Erratum ibid.* **102** (2020) 089902] [arXiv:1909.11267] [INSPIRE].

[493] P.W. Graham et al., *Dark matter direct detection with accelerometers*, *Phys. Rev. D* **93** (2016) 075029 [arXiv:1512.06165] [INSPIRE].

[494] D. Carney et al., *Ultralight dark matter detection with mechanical quantum sensors*, *New J. Phys.* **23** (2021) 023041 [arXiv:1908.04797] [INSPIRE].

[495] J.M. Armaleo, D. López Nacir and F.R. Urban, *Searching for spin-2 ULDM with gravitational waves interferometers*, *JCAP* **04** (2021) 053 [arXiv:2012.13997] [INSPIRE].

[496] R.T. Co, L.J. Hall and K. Harigaya, *QCD axion dark matter with a small decay constant*, *Phys. Rev. Lett.* **120** (2018) 211602 [arXiv:1711.10486] [INSPIRE].

JCAP07(2023)068

[497] R.T. Co, A. Pierce, Z. Zhang and Y. Zhao, *Dark photon dark matter produced by axion oscillations*, *Phys. Rev. D* **99** (2019) 075002 [arXiv:1810.07196] [INSPIRE].

[498] H.-K. Guo, K. Riles, F.-W. Yang and Y. Zhao, *Searching for dark photon dark matter in LIGO O1 data*, *Commun. Phys.* **2** (2019) 155 [arXiv:1905.04316] [INSPIRE].

[499] S. Morisaki et al., *Improved sensitivity of interferometric gravitational wave detectors to ultralight vector dark matter from the finite light-traveling time*, *Phys. Rev. D* **103** (2021) L051702 [arXiv:2011.03589] [INSPIRE].

[500] Y. Michimura et al., *Ultralight vector dark matter search with auxiliary length channels of gravitational wave detectors*, *Phys. Rev. D* **102** (2020) 102001 [arXiv:2008.02482] [INSPIRE].

[501] S.M. Vermeulen et al., *Direct limits for scalar field dark matter from a gravitational-wave detector*, arXiv:2103.03783 [DOI:10.1038/s41586-021-04031-y] [INSPIRE].

[502] Y.V. Stadnik and V.V. Flambaum, *Enhanced effects of variation of the fundamental constants in laser interferometers and application to dark matter detection*, *Phys. Rev. A* **93** (2016) 063630 [arXiv:1511.00447] [INSPIRE].

[503] Y.V. Stadnik and V.V. Flambaum, *Searching for dark matter and variation of fundamental constants with laser and maser interferometry*, *Phys. Rev. Lett.* **114** (2015) 161301 [arXiv:1412.7801] [INSPIRE].

[504] H. Grote and Y.V. Stadnik, *Novel signatures of dark matter in laser-interferometric gravitational-wave detectors*, *Phys. Rev. Res.* **1** (2019) 033187 [arXiv:1906.06193] [INSPIRE].

[505] E. Hall and N. Aggarwal, *Advanced LIGO, LISA, and cosmic explorer as dark matter transducers*, arXiv:2210.17487 [INSPIRE].

[506] A.L. Miller et al., *Probing new light gauge bosons with gravitational-wave interferometers using an adapted semicoherent method*, *Phys. Rev. D* **103** (2021) 103002 [arXiv:2010.01925] [INSPIRE].

[507] LIGO Scientific et al. collaborations, *Distinguishing between dark-matter interactions with gravitational-wave detectors*, *Phys. Rev. D* **105** (2022) 103035 [arXiv:2204.03814] [INSPIRE].

[508] LIGO Scientific et al. collaborations, *Constraints on dark photon dark matter using data from LIGO's and Virgo's third observing run*, *Phys. Rev. D* **105** (2022) 063030 [arXiv:2105.13085] [INSPIRE].

[509] K. Nagano, T. Fujita, Y. Michimura and I. Obata, *Axion dark matter search with interferometric gravitational wave detectors*, *Phys. Rev. Lett.* **123** (2019) 111301 [arXiv:1903.02017] [INSPIRE].

[510] K. Nagano et al., *Axion dark matter search using arm cavity transmitted beams of gravitational wave detectors*, *Phys. Rev. D* **104** (2021) 062008 [arXiv:2106.06800] [INSPIRE].

[511] H.-K. Guo and A. Miller, *Searching for mini extreme mass ratio inspirals with gravitational-wave detectors*, arXiv:2205.10359 [INSPIRE].

[512] A.L. Miller, N. Aggarwal, S. Clesse and F. De Lillo, *Constraints on planetary and asteroid-mass primordial black holes from continuous gravitational-wave searches*, *Phys. Rev. D* **105** (2022) 062008 [arXiv:2110.06188] [INSPIRE].

[513] Y. Guersel and M. Tinto, *Near optimal solution to the inverse problem for gravitational wave bursts*, *Phys. Rev. D* **40** (1989) 3884 [INSPIRE].

[514] I.C.F. Wong and T.G.F. Li, *Signal space in the triangular network of the Einstein Telescope*, *Phys. Rev. D* **105** (2022) 084002 [arXiv:2108.05108] [INSPIRE].

[515] J. Harms, *Terrestrial gravity fluctuations*, *Living Rev. Rel.* **22** (2019) 6 [INSPIRE].

JCAP07(2023)068

[516] S. Wu and A.H. Nitz, *Mock data study for next-generation ground-based detectors: the performance loss of matched filtering due to correlated confusion noise*, *Phys. Rev. D* **107** (2023) 063022 [arXiv:2209.03135] [INSPIRE].

[517] S. Sachdev, T. Regimbau and B.S. Sathyaprakash, *Subtracting compact binary foreground sources to reveal primordial gravitational-wave backgrounds*, *Phys. Rev. D* **102** (2020) 024051 [arXiv:2002.05365] [INSPIRE].

[518] M. Was et al., *On the background estimation by time slides in a network of gravitational wave detectors*, *Class. Quant. Grav.* **27** (2010) 015005 [arXiv:0906.2120] [INSPIRE].

[519] M. Cabero, A. Mahabal and J. McIver, *GWSkyNet: a real-time classifier for public gravitational-wave candidates*, *Astrophys. J. Lett.* **904** (2020) L9 [arXiv:2010.11829] [INSPIRE].

[520] S. Chatterji et al., *Coherent network analysis technique for discriminating gravitational-wave bursts from instrumental noise*, *Phys. Rev. D* **74** (2006) 082005 [gr-qc/0605002] [INSPIRE].

[521] B.F. Schutz and B.S. Sathyaprakash, *Self-calibration of networks of gravitational wave detectors*, arXiv:2009.10212 [INSPIRE].

[522] L. Sun et al., *Characterization of systematic error in advanced LIGO calibration*, *Class. Quant. Grav.* **37** (2020) 225008 [arXiv:2005.02531] [INSPIRE].

[523] Z. Pan and H. Yang, *Improving the detection sensitivity to primordial stochastic gravitational waves with reduced astrophysical foregrounds*, *Phys. Rev. D* **107** (2023) 123036 [arXiv:2301.04529] [INSPIRE].

[524] aLIGO collaboration, *Sensitivity and performance of the advanced LIGO detectors in the third observing run*, *Phys. Rev. D* **102** (2020) 062003 [arXiv:2008.01301] [INSPIRE].

[525] R. Brustein, M. Gasperini, M. Giovannini and G. Veneziano, *Relic gravitational waves from string cosmology*, *Phys. Lett. B* **361** (1995) 45 [hep-th/9507017] [INSPIRE].

[526] A. Buonanno, M. Maggiore and C. Ungarelli, *Spectrum of relic gravitational waves in string cosmology*, *Phys. Rev. D* **55** (1997) 3330 [gr-qc/9605072] [INSPIRE].

[527] J.L. Cook and L. Sorbo, *Particle production during inflation and gravitational waves detectable by ground-based interferometers*, *Phys. Rev. D* **85** (2012) 023534 [*Erratum ibid.* **86** (2012) 069901] [arXiv:1109.0022] [INSPIRE].

[528] J.D. Romano and N.J. Cornish, *Detection methods for stochastic gravitational-wave backgrounds: a unified treatment*, *Living Rev. Rel.* **20** (2017) 2 [arXiv:1608.06889] [INSPIRE].

[529] L. Valbusa Dall'Armi, A. Nishizawa, A. Ricciardone and S. Matarrese, *Circular polarization of the astrophysical gravitational wave background*, arXiv:2301.08205 [INSPIRE].

[530] V. Domcke et al., *Measuring the net circular polarization of the stochastic gravitational wave background with interferometers*, *JCAP* **05** (2020) 028 [arXiv:1910.08052] [INSPIRE].

[531] K. Martinovic, C. Badger, M. Sakellariadou and V. Mandic, *Searching for parity violation with the LIGO-Virgo-KAGRA network*, *Phys. Rev. D* **104** (2021) L081101 [arXiv:2103.06718] [INSPIRE].

JCAP07(2023)068